学位論文
核子対あたり重心系エネルギー 5.02 TeV 陽子–陽子及び鉛–鉛原子核衝突における中性中間子と直接光子測定

Measurement of neutral mesons and direct photons in pp and Pb–Pb collisions at $\sqrt{s_{\rm NN}} = 5.02$ TeV

2019 年 1 月博士 (理学) 申請

関畑　大貴 (D150900)
広島大学大学院 理学研究科 物理科学専攻
クォーク物理学研究室

January 31, 2019

Ph.D Thesis

Measurement of neutral mesons and direct photons in pp and Pb–Pb collisions at $\sqrt{s_{\rm NN}} = 5.02$ TeV

Daiki Sekihata (D150900)
Graduate School of Science in Hiroshima University
Department of Physical Science
Experimental Quark Physics Laboratory
January 31, 2019

Abstract

The new state of matter, called quark-gluon plasma (QGP), created by the high-energy heavy-ion collision has been studied for more than 40 years. Partons originating from initial hard scatterings lose their energy in the hot and dense QCD medium, which results in suppression of hadron production at high transverse momentum (p_{T}), compared to pp collisions at the same center-of-mass energy $\sqrt{s_{\mathrm{NN}}}$. Light flavor particles are excellent probes to study the suppression in a wide p_{T} range with high precision. Especially, neutral mesons such as π^0 and η mesons that decay into two photons can be reconstructed and identified by a fine-segmented electro-magnetic calorimeter in a wide p_{T} range.

In this thesis, the suppression of π^0 and η mesons in Pb–Pb collisions at the highest energy $\sqrt{s_{\mathrm{NN}}} = 5.02$ TeV is reported. By increasing the collision energy, p_{T} spectra of π^0 meson become harder than that at $\sqrt{s_{\mathrm{NN}}} = 2.76$ TeV in both pp and Pb–Pb collisions. Nevertheless, the suppression of π^0 meson in Pb–Pb collisions compared to pp collisions is the same level, which is by a factor of up to 8. This indicates the larger energy-loss at the higher collision energy. Comparing light and heavy flavor hadrons, namely π^0 and D mesons, the suppression of D mesons at low p_{T} is weaker than that of π^0 meson. This is interpreted as the smaller energy-loss for charm quarks than for up, down quarks. The suppression pattern of η meson seems to be similar to $K^{\pm}$ meson consisting of a strange quark, though uncertainties for the η meson measurement is large.

Direct photons that are defined as photons not originating from hadron decays are also discussed in this thesis. Direct photons are unique probes to study the space-time evolution of the QGP, since they are not involved in strong interaction and can carry information when they are produced. When focusing on direct photons, π^0 and η mesons contribute as huge backgrounds. To subtract decay photon yields, the cocktail simulation where p_{T} spectra of neutral mesons are inputs has been performed. Direct photon spectra or upper limits at the 90% of confidence level have been extracted. Finally, R_{AA} of direct photons has been determined and is consistent with unity at high p_{T} which justifies the measurement. On the other hand, the excess beyond the pQCD calculation is observed at low p_{T} by a factor of up to 4 in central Pb–Pb collisions. This indicates thermal photon emissions from the hot and dense QCD medium. The obtained effective temperature T_{eff} is 345 ± 222(total unc.) MeV in Pb–Pb collisions at $\sqrt{s_{\mathrm{NN}}} = 5.02$ TeV for centrality 0-10%. This is the first measurement and setting upper limits on direct photons in pp and Pb–Pb collisions at $\sqrt{s_{\mathrm{NN}}} = 5.02$ TeV.

Contents

List of Figures

List of Tables

1 Introduction

Our main goal in high-energy heavy-ion collisions is to understand properties, such as energy density, temperature, transport coefficient, order of the phase transition e.t.c., of the quark-gluon plasma (QGP), which is the state of deconfined quarks and gluons from hadrons. These research for the QGP will provide phenomenological knowledge of fundamental Quantum Chromo-Dynamics (QCD).

1.1 Quantum Chromo-Dynamics (QCD)

The Quantum Chromo-Dynamics is a fundamental non-Abelian SU(3) gauge theory to describe strong interaction. The strong interaction is mediated by gluons between elementary particles which have color charge (red, blue and green). As gluon also has color, self-interaction among gluons can be induced. On the other hand, in Quantum Electro-Dynamics (QED), photon is neutral gauge boson and mediates electric charge with coupling constant $\alpha_{\rm QED} = 1/137$. Hence, photons do not interact themselves. This is a main difference between QCD and QED. One of the most important point of QCD is that the strong interaction among quarks and gluons becomes weaker at high energy (i.e. large momentum transfer Q^2). This behavior is called "asymptotic freedom". The strong coupling constant α_s at large Q^2 can be approximated as :

$$\alpha_s(Q^2) \approx \frac{12\pi}{(33 - 2N_f)\ln{(Q^2/\lambda^2_{\rm QCD})}}, \tag{1}$$

where N_f is the number of quark flavors ($N_f \leq 6$), $\lambda_{\rm QCD}$ is called QCD scale, which is typically 200 MeV. Therefore, $\alpha_s(Q^2)$ becomes smaller and perturbative calculation is applicable at large Q^2. The confinement can be also expressed by a following phenomenological potential:

$$V(r) = -\frac{4}{3}\frac{\alpha_s}{r} + kr, \tag{2}$$

where $1/r$ term is dominant at small distance which is similar to Coulomb potential and kr is related to the confinement of quarks in hadrons. When one wants to separate two quarks, the potential energy kr increases and tends to produce a new $q\bar{q}$ pair. This results in two shorter strings. Finally, extracting single quark is not possible and new colorless hadrons will be produced.

1.2 Quark-gluon plasma (QGP)

The confined state of quarks and gluons in hadrons can be broken at the extremely high temperature or high density of many body systems of hadrons. This leads a transition from hadronic phase to the deconfined state of partons. The deconfined state of partons is called "quark-gluon plasma (QGP)" proposed by Bjorken [1]. Numerical calculations based on the lattice QCD are performed. Step-like behavior of ε/T^4 at $T = T_{\rm C}$ is clearly seen in Figure 1. This is interpreted as the transition from the hadronic phase to the QGP at the critical temperature $T_{\rm C} = 150 \sim 200$ MeV due to increase of degrees of freedom related to deconfined quarks and gluons from hadrons. In addition, recent lattice QCD calculations also predict crossover transition [2, 3].
Figure 2 shows a schematic phase diagram of QCD matter. The horizontal axis represents the net baryon density normalized to the normal nucleus, the vertical axis indicates the temperature. It is thought that the QGP has existed in the early universe at a few micro seconds after Big-Bang.

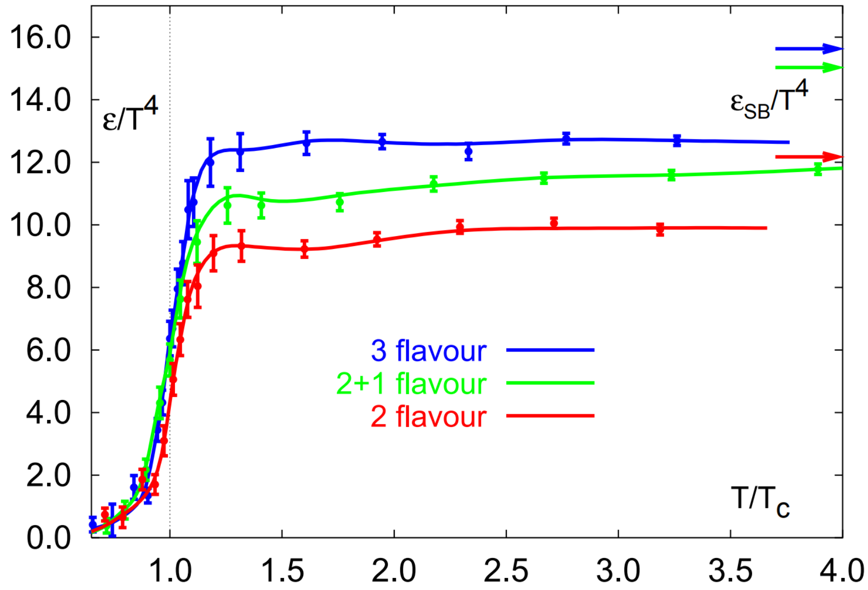

Figure 1: The energy density ε divided by 4th power of the temperature T^4 predicted by lattice QCD [4].

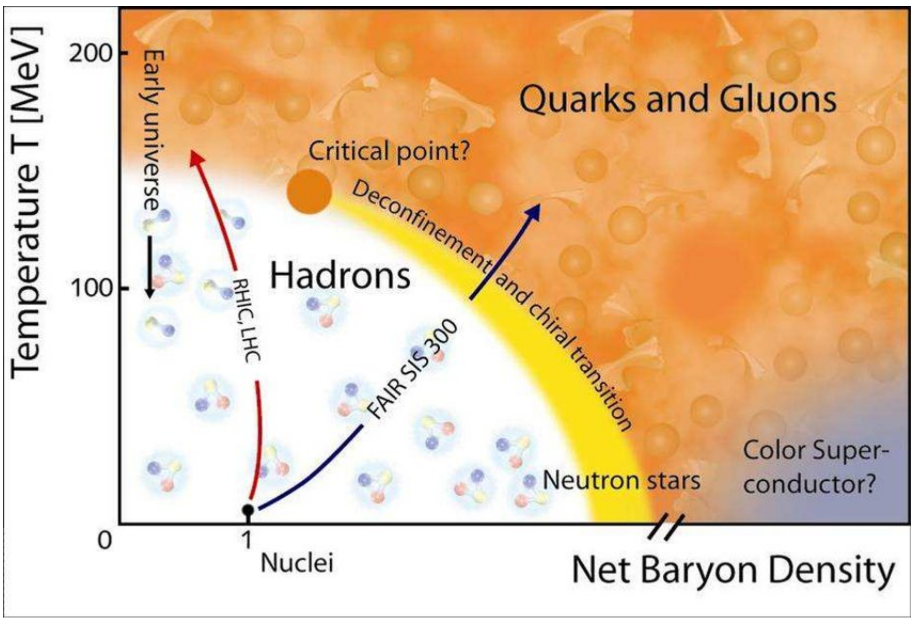

Figure 2: A schematic phase diagram of QCD matter [5].

1.3 High-energy heavy-ion collisions

High-energy heavy-ion collisions provide an unique opportunity to study strongly interacting matter, namely the QGP. In high-energy heavy-ion collisions, two Lorentz-contracted nuclei interact at the geometrical overlap region (Figure 3). A distance between the center of each nuclei is called "impact parameter" b. Nucleons participating the interaction are "participants" and the others are "spectators". The impact parameter b is not directly measured, but can be simulated by the Glauber model calculation [6]. Then it provides the number of participant N_{part} and the number of binary nucleon-nucleon collisions N_{coll}. N_{part} is related to the volume of the interaction region. The number of particles produced at the later stage of collisions is roughly scaled by N_{part}. On the other hand, the number of particles produced by initial hard scatterings is basically scaled by N_{coll}.

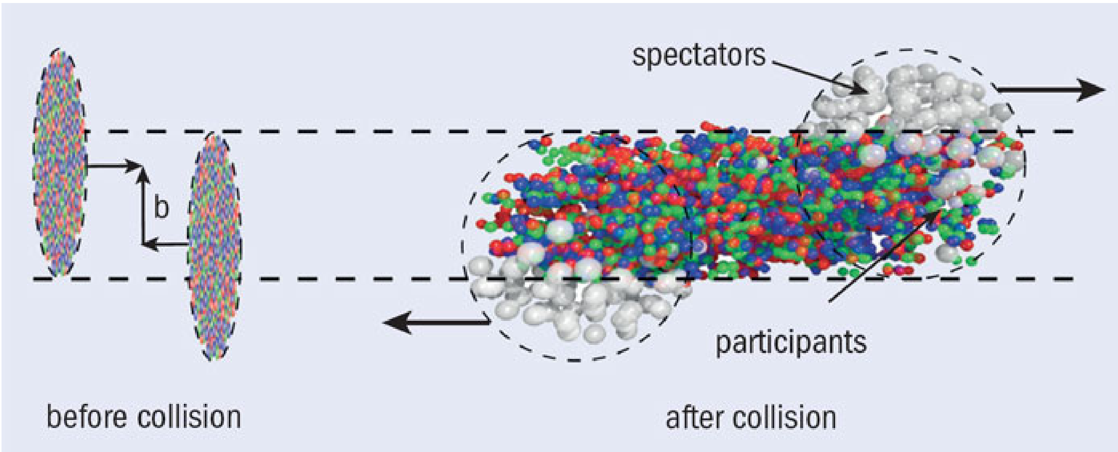

Figure 3: A schematic view of collision geometry in high-energy heavy-ion collisions [7].

As shown by Figure 4, the space-time evolution of the QCD matter created by heavy-ion collisions pass through various phases.

1. Pre-equilibrium ($0 < t < \tau_0$)
   Two accelerated nuclei collide with each other at $t = 0$ and high energy is released in a tiny volume. Multiple parton scatterings lead local equilibrium of the hot and dense matter.

2. QGP phase ($\tau_0 < t < \tau_{\mathrm{C}}$)
   The QGP phase is formed at $t = \tau_0$, if energy density is higher than a value necessary for the transition ($\varepsilon > 1$ GeV/fm^3). Its evolution can be described by hydrodynamics and the temperature becomes cooler.

3. Mixed phase between QGP and hadron gas ($\tau_{\mathrm{C}} < t < \tau_{\mathrm{H}}$)
   The mixed phase consisting of quarks, gluons and hadrons can exist only if the phase transition is at first order. When the temperature reaches the transition temperature T_{C}, hadronization will start. Eventually, inelastic scattering of hadrons stops. This temperature is called "chemical freeze-out temperature".

4. Hadron gas ($\tau_{\mathrm{H}} < t < \tau_{\mathrm{F}}$)
   Hadronization processes finishes here, but still keep interaction as momentum exchange by elastic scatterings. At the end, elastic scattering ceases, too. This temperature is called "kinetic freeze-out temperature". After the kinetic freeze-out, hadrons fly to our detectors.

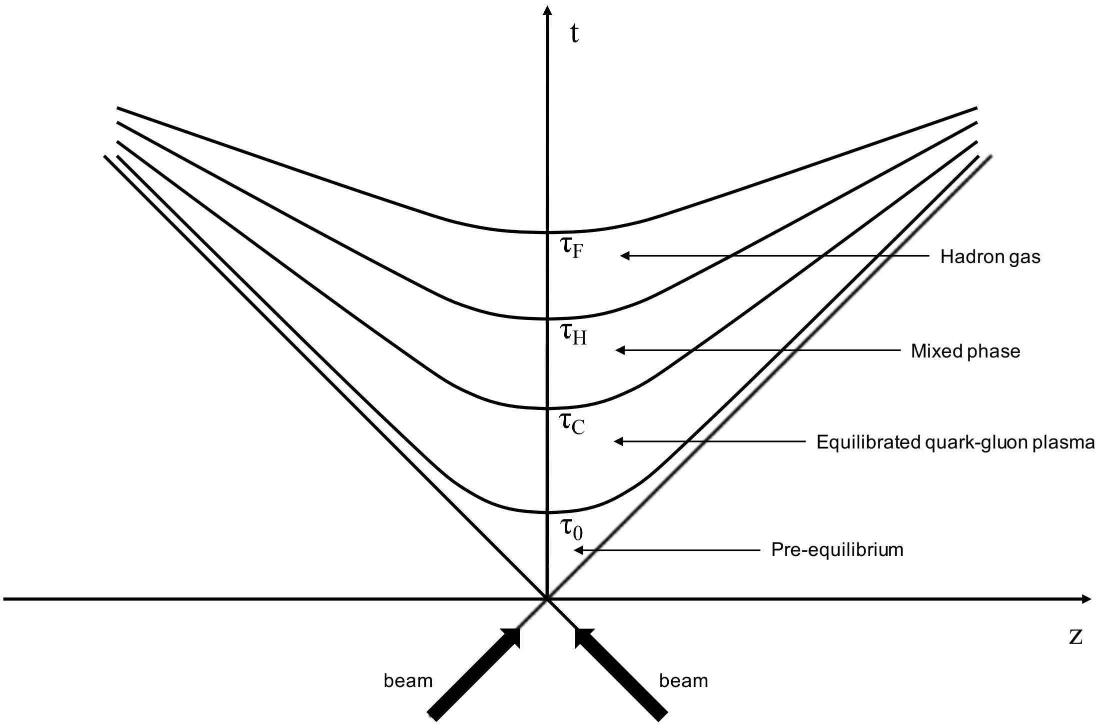

Figure 4: A schematic view of space-time evolution of the matter in high-energy heavy-ion collisions

1.4 Suppression of high p_{T} hadrons

Partons originating from initial hard scatterings lose their energy in the hot and dense medium, which results in modification of p_{T} spectra of hadrons. Light flavor hadrons are excellent probes to study the hadron suppression with high precision, because their statistics is large. It has been reported that the suppression of hadron yields compared to those in pp collisions scaled by N_{coll}, quantified by the nuclear modification factor R_{AA} (Eq. 4), is up to by a factor of 5 in Au–Au collisions at $\sqrt{s_{\mathrm{NN}}} = 0.2$ TeV at RHIC [8, 9]. It is by a factor of up to 8 in Pb–Pb collisions at $\sqrt{s_{\mathrm{NN}}} = 2.76$ TeV in LHC Run1 (2009–2013) [10, 11, 12]. At the latest during LHC Run2 (2015–2018), the LHC provided Pb–Pb collisions at $\sqrt{s_{\mathrm{NN}}} = 5.02$ TeV, which is the highest collision energy in the world. In this thesis, neutral meson (π^0 and η mesons) are focused on. Its advantage is that π^0 and η mesons can be reconstructed via their 2γ decays with a fine-segmented electro-magnetic calorimeter in a wide transverse momentum (p_{T}) range. In addition, photons decayed from neutral mesons are huge backgrounds, which have to be subtracted from inclusive photons, for the direct photons measurement described in section 1.5 later.

1.4.1 Particle production in hadron colliders at high p_{T}

First of all, the particle production at high p_{T} was measured by CERN-ISR in pp collisions at different energies (23, 45 and 62 GeV) [14]. Figure 5 shows the production cross section of charged hadrons in pp collisions at 23, 53, 546 and $p\bar{p}$ collisions at $\sqrt{s} = 1800$ GeV. The invariant differential cross section of charged hadrons is described by an exponential function $\exp(-a \cdot p_{\mathrm{T}})$ at low p_{T} region, while a power-law behavior p_{T}^{-n} is seen at high p_{T}. Moreover, the power-law parameter n is lower at higher collision energies, resulting in harder slope of p_{T} spectra at high p_{T}.

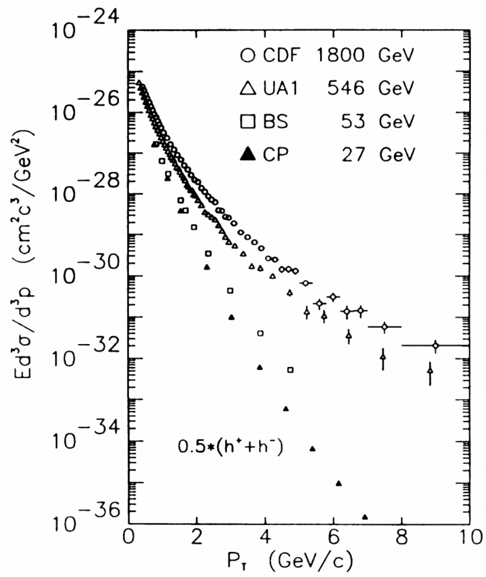

Figure 5: The production cross section of charged hadrons in pp collisions [13].

The hard scattering occurs in the initial stage of pp and heavy-ion collisions and can be calculated by perturbative QCD (pQCD) based on factorization theorem. Figure 6 shows a schematic diagram of parton interaction $a + b \to c + x$ in hadronic collisions. The production cross section is defined as :

$$d\sigma^{pp \to h_C X} = dx_a dx_b dz_c \cdot f_a(x_a, \mu_F) \cdot f_a(x_a, \mu_F) \times d\sigma_{a+b \to c+x}(\alpha_s(\mu_R)) \times D_c(z_c, \mu_F), \quad (3)$$

where $f_{a(b)}(x_{a(b)}, \mu_F)$ is called parton distribution function (PDF) which is probability to find a parton $a(b)$ at its momentum fraction at $x_{a(b)}$ in a proton $A(B)$.
There, $x_{a(b)}$ = momentum of parton $a(b)$/momentum of proton $A(B)$. $d\sigma_{a+b \to c+x}(\alpha_s(\mu_R))$ is a production cross section of parton c from scattering between parton a and b. $D_c(z_c, \mu_F)$ is fragmentation function (FF) which describes probability to hadronize into a hadron h_C from a parton c at momentum fraction z_c, where z_c = momentum of h_C/momentum of parton c. μ_F: factorization scale and μ_R: re-normalization scale are dummy parameters introduced to avoid divergence in theoretical calculations. Usually, they are fixed to transverse momentum of the particle ($\mu_F = \mu_R = p_{\mathrm{T}}$) in calculations.

1.4.2 Nuclear modification factor R_{AA}

One of ideas to observe medium-induced effects is to compare particle yields between A–A collision and pp collisions. Due to the large number of partons in A–A collisions, particle yields in A–A collisions is normalized by the number of binary nucleon-nucleon collisions N_{coll}. If there are medium-induced effects in A–A collisions, particle yields in A–A collisions may be different from N_{coll} scaling. The medium-induced effects to high p_{T} particles is quantified by a ratio of particle yields in A–A collisions to that in pp collisions at the same center-of-mass energy $\sqrt{s_{\mathrm{NN}}}$, called R_{AA}:

$$R_{\mathrm{AA}} = \frac{d^2N/dp_{\mathrm{T}}dy|_{\mathrm{AA}}}{T_{\mathrm{AA}} \times d^2\sigma/dp_{\mathrm{T}}dy|_{\mathrm{pp}}} = \frac{d^2N/dp_{\mathrm{T}}dy|_{\mathrm{AA}}}{N_{\mathrm{coll}} \times d^2N/dp_{\mathrm{T}}dy|_{\mathrm{pp}}}, \quad (4)$$

where $d^2N/dp_{\mathrm{T}}dy|_{\mathrm{AA}}$ is differential particle yields in A–A collisions, $d^2\sigma/dp_{\mathrm{T}}dy|_{\mathrm{pp}}$ is differential production cross section in pp collisions and T_{AA} is called nuclear overlap function which is

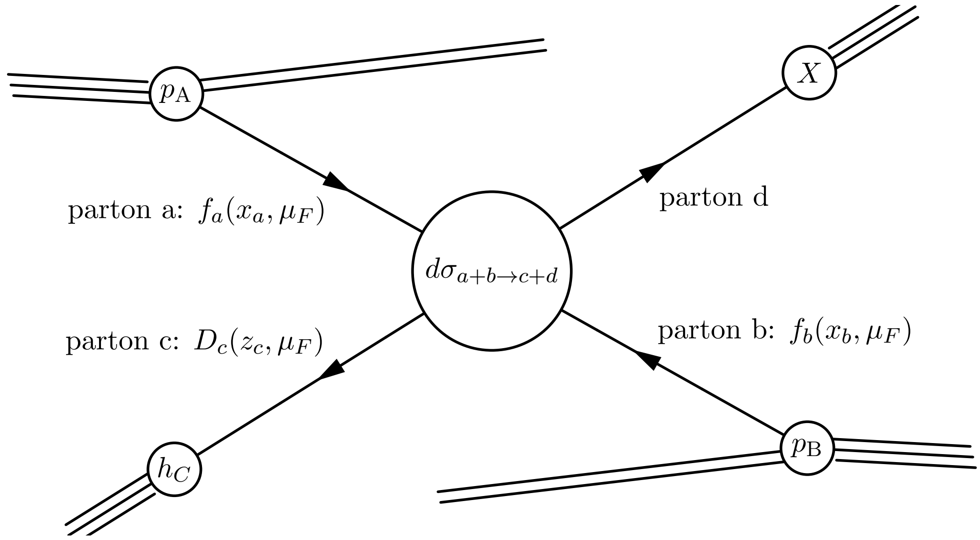

Figure 6: A schematic diagram $a + b \to c + d$, where hadron X represents anything else.

connected to the average number of inelastic collisions by $T_{\mathrm{AA}} = N_{\mathrm{coll}}/\sigma_{\mathrm{pp}}^{\mathrm{INEL}}$. In case of no medium-induced effects, $R_{AA} = 1$ at high p_{T}. Hence, R_{AA} is an excellent probe to see medium-induced effects. As of 2018, it has been known that $R_{\mathrm{AA}} < 1$ for hadrons, $R_{\mathrm{AA}} = 1$ for electro-weak bosons $(\gamma, W^{\pm}/Z)$ respectively.

1.4.3 Cold nuclear matter effects

In order to understand hadron suppression in A–A compared to pp ($R_{\mathrm{AA}} < 1$), it is important to test particle productions in p–A collisions where the hot and dense QCD medium is not likely created. Possible effects to modify particle yields are multiple soft scatterings or different parton distribution function in a nucleus, which are generally called “cold nuclear matter effects”.

Cronin effect It was observed that the production cross section in p–A collisions is not scaled by mass number A of the target nucleus [15] at ISR in 1970, compared to that in pp collisions. They got these results by incident proton beam at 200, 300 and 400 GeV to fixed Be, Ti and W targets. They found production cross section in p–A collisions as a function of p_{T} and A can be expressed by :

$$E\frac{d^3\sigma}{dp^3}(p_{\mathrm{T}}, A) = E\frac{d^3\sigma}{dp^3}(p_{\mathrm{T}}, 1) \times A^{\alpha(p_{\mathrm{T}})}, \quad (5)$$

where power $\alpha > 1$ for $p_{\mathrm{T}} > 2$ GeV as shown by Figure. 7. Thus, an enhancement of particle yields in p–A collisions compared to the expectation from pp collisions was observed. This effect is refereed as “Cronin effect” and interpreted as multiple soft scatterings of incoming nucleons, which cause an additional p_{T} broadening of particles.

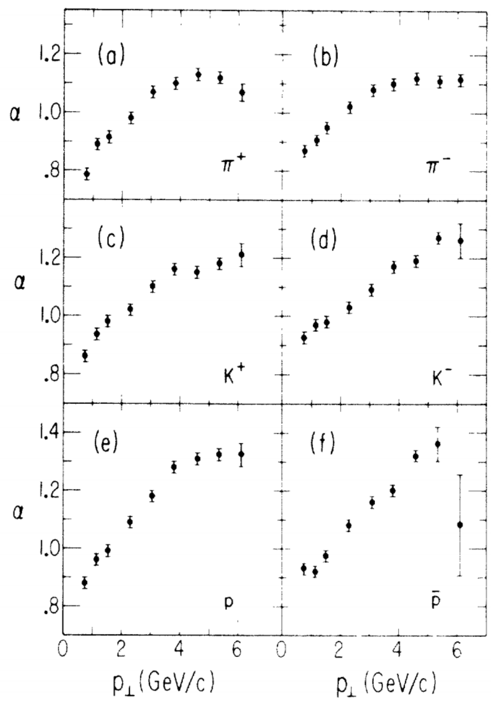

Figure 7: Power parameter α vs. p_{T} [15].

Nuclear shadowing Another initial effect is different parton distribution function in a nucleus. European Muon Collaboration (EMC) firstly reported that nuclear structure function in a nucleus is different from that in a free proton by deep inelastic scattering (DIS) with μ–Fe(d) collisions [17]. This results in different parton distribution function in a nucleus from one in a free proton. Figure 8 shows the ratio of nuclear structure function in a heavier ion to that in a Carbon ion measured by New Muon Collaboration (NMC) [16]. $F_2^{\mathrm{A}}/F_2^{\mathrm{C}} < 1$ at $x < 0.07$ refereed as "shadowing", $F_2^{\mathrm{A}}/F_2^{\mathrm{C}} > 1$ at $0.07 < x < 0.3$ refereed as "anti-shadowing" and there is a dip at $0.3 < x$ called "EMC effect". The relevant x of a parton can be estimated from transverse momentum p_{T} of a leading hadron which carries the largest momentum fraction of the original scattered parton by means of :

$$x \approx \frac{2p_{\mathrm{T}}}{\sqrt{s_{\mathrm{NN}}}} \tag{6}$$

At LHC energies $\sqrt{s_{\mathrm{NN}}} = 2.76 \sim 5.5$ TeV and leading $p_{\mathrm{T}}^h \sim O(100)$ GeV, hence $x < 0.05$ where the shadowing effect is the most relevant.

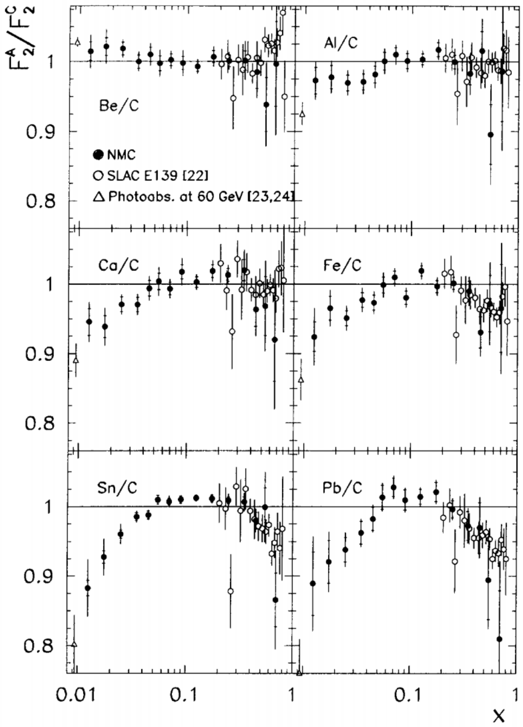

Figure 8: The ratio of nuclear structure function in heavy nuclei to one in Carbon [16].

1.4.4 Parton energy-loss

One possible explanation for $R_{\mathrm{AA}} < 1$ is parton energy-loss in interaction with the hot and dense QCD medium. By traversing the QCD medium, the parton loses its energy by elastic scattering or gluon radiation. Initially, only radiative energy-loss in static QCD medium (non-moving constituents) was assumed in theoretical models such as GLV [18, 19], DGLV [20], BDMPS[21, 22] till $\sim$ 2008. The radiative energy is similar to Bremsstrahlung of an electron in an electro-magnetic field. However, these calculation gave disagreement with experimental results. Then, one of theoretical models have included radiative energy-loss in dynamical QCD medium (moving constituents) [23, 24]. Currently, it is considered that radiative and elastic energy-losses are comparable in dynamical QCD medium [25, 26]. Theoretical models shown in this thesis are described below.

DREENA-C [25] and DREENA-B [26] Descriptions are taken from [25, 26]. DREENA stands for Dynamical Radiative and Elastic ENergy loss Approach and C denotes the constant-temperature QCD medium and B stands for Bjorken expansion of the QCD medium. They aim to calculate the nuclear modification factor R_{AA} and the azimuthal anisotropy v_2 simultaneously in their framework. First, let T be an averaged temperature of the medium, L be an averaged path-length traversed by particles and $\Delta E/E$ be fractional energy-loss. In a simple case for the purpose of these estimations, it is assumed that

$$\Delta E/E \approx \eta T L, \tag{7}$$

where η is a proportionality factor. The nuclear modification $R_{\rm AA}$ is commonly estimated [27] as :

$$R_{\rm AA} \approx \left(1 - \frac{1}{2}\frac{\Delta E}{E}\right)^{n-2}, \tag{8}$$

where n is the steepness of the initial momentum distribution function. Here, different path-length between in-plain ($L_{\rm in} = L - \Delta L$) and out-of-plain ($L_{\rm in} = L - \Delta L$) is introduced. For the constant-temperature QCD medium, the nuclear modification factor $R_{\rm AA}$ can be expressed as :

$$R_{\rm AA} \approx \frac{1}{2}(R_{\rm AA}^{\rm in} + R_{\rm AA}^{\rm out}) \approx 1 - \xi TL, \tag{9}$$

The azimuthal anisotropy v_2 can be :

$$v_2 \approx \frac{1}{2}\frac{R_{\rm AA}^{\rm in} - R_{\rm AA}^{\rm out}}{R_{\rm AA}^{\rm in} + R_{\rm AA}^{\rm out}} \approx \frac{\xi T \Delta L}{2} \tag{10}$$

For the evolving system, the average temperature along in-plane is higher than that along out-of-plane ($T_{\rm in} = T + \Delta T$ and $T_{\rm out} = T - \Delta T$). In this case,

$$R_{\rm AA} \approx 1 - \xi TL, \tag{11}$$

and

$$v_2 \approx \frac{\xi T \Delta L - \xi \Delta T L}{2} \tag{12}$$

Therefore, DREENA-B and -C predict the similar $R_{\rm AA}$, while the smaller v_2 is predicted by DREENA-B. Only $R_{\rm AA}$ is compared to experimental data in this thesis.

1.5 Direct photons production

The direct photon is an unique tool to study space-time evolution of the hot and dense matter. Direct photons are defined as photons not originating from hadron decays, for example $\pi^0 \to \gamma\gamma$, $\eta \to \gamma\gamma$ and so on. Because they are not involved in the strong interaction, they carry undistorted information at the time of their productions. Moreover, direct photons are divided into to two sources. One is "thermal photon" originating from the thermal radiation from the hot and dense medium. An averaged temperature $T_{\rm eff}$ of locally equilibrated medium over the all space-time evolution can be measured by the $p_{\rm T}$ spectrum of thermal photons, assuming the Boltzmann distribution $A \times \exp(-p_{\rm T}/T_{\rm eff})$. The previous measurement by PHENIX at RHIC reported $T_{\rm eff} = 221 \pm 19(\rm stat.) \pm 19(\rm syst.)$ MeV [28, 29] via virtual photons and $T_{\rm eff} = 239 \pm 25(\rm stat.) \pm 7(\rm syst.)$ MeV [30] via real photons in 0-20 % central Au–Au collisions at $\sqrt{s_{\rm NN}} = 0.2$ TeV. In ALICE, $T_{\rm eff} = 294 \pm 12(\rm stat.) \pm 47(\rm syst.)$ MeV [31] in 0-20 % central Pb–Pb collisions at $\sqrt{s_{\rm NN}} = 2.76$ TeV. The other one is "prompt photon" produced by initial hard scatterings between partons. The prompt photon is a powerful probe to test pQCD calculations. Thermal photons are dominant at low $p_{\rm T}$ ($1 < p_{\rm T} < 3$) regime, while prompt photons exhibit at high $p_{\rm T}$. Figure 9 illustrates Feynman diagrams for direct photon productions. Thermal photons are also emitted from a hot hadron gas (HHG), which is the last stage of collisions. Main constituents of the hot hadron gas are pions and ρ mesons. They produce photon as $\pi^{\pm}\rho \to \pi^{\pm}\gamma$, $\pi^+\pi^- \to \rho\gamma$ and $\rho \to \pi^+\pi^-\gamma$.

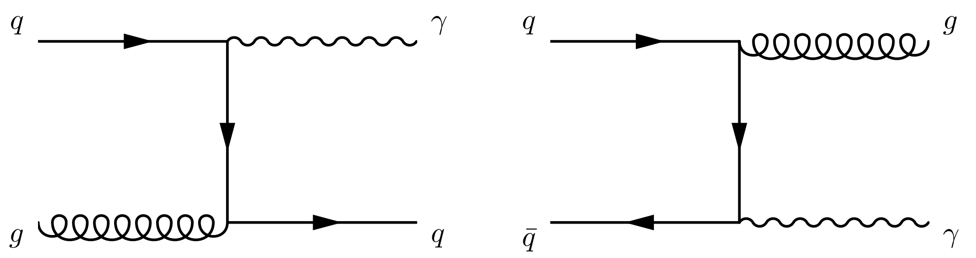

(a) Compton scattering of quark–gluon (b) Annihilation of quark–anti-quark

Figure 9: Feynman diagrams for direct photon productions

1.5.1 Pioneers of the direct photon measurement

WA80

The first attempt to measure thermal photons was performed by the WA80 (West Area) collaboration [32, 33]. WA80 is a fixed-target experiment at the SPS in CERN colliding ^{16}O and ^{32}S beam at 200A GeV with Au. They reported upper limits on the direct photon yield at the 90% confidence level in central ^{32}S–Au collisions by employing a statistical subtraction method, as shown by Figure 10b. It is a technique to subtract decay photon yields simulated by known sources (e.g. $\pi^0 \to \gamma\gamma$, $\eta \to \gamma\gamma$ e.t.c.) from inclusive photon yields. The dotted curve is the calculated thermal photon production from a QGP by reference [34]. The solid curve is the expected thermal photon production from a hot hadron gas by reference [34]. The dashed curve is also thermal emissions from a hot hadron gas taken from reference [35]. This was the important step, as hadron gas scenarios were excluded by their upper limits.

WA98

WA98 [36, 37] is also a fixed-target experiment upgraded from WA80. The improvement was a lead glass calorimeter which has excellent energy resolution. The WA98 collaboration has measured direct photon yields in central 158A GeV Pb–Pb collisions for the first time. They used the same statistical subtraction method explained above. Figure 11a shows excess of direct photons beyond decay photons from known sources. The upper (lower) panel is for peripheral (central) collisions. If the ratio is greater than unity beyond statistical (bar at each point) and systematic (shaded band around unity) uncertainties, there are direct photons. Figure 11b shows invariant yields of direct photons in central 158A GeV Pb–Pb collisions. Clear direct photon signals were observed at $p_{\mathrm{T}} > 1.5$ GeVc. Downward arrows indicate upper limits at 90% confidence level.

1.5.2 Direct photon puzzle

The PHENIX collaboration at RHIC reported not only the invariant yield [30], but also the azimuthal anisotropy $v_2 = \langle \cos(2\Delta\varphi) \rangle$ of direct photons [38] at low p_{T} as shown by Figure 12. It was surprisingly a big discovery of the large v_2 of direct photons. The observed large v_2 together with the large direct photon yield contradicts our interpretations. The large direct photon yield are produced at the very early stage, when the temperature of the medium is the highest where the collective flow of the medium is small. Contrary to this, the large v_2 suggests that photons are produced at the very late stage of the collision, when the collective flow of the system is fully developed where the temperature and the corresponding thermal emission rate is

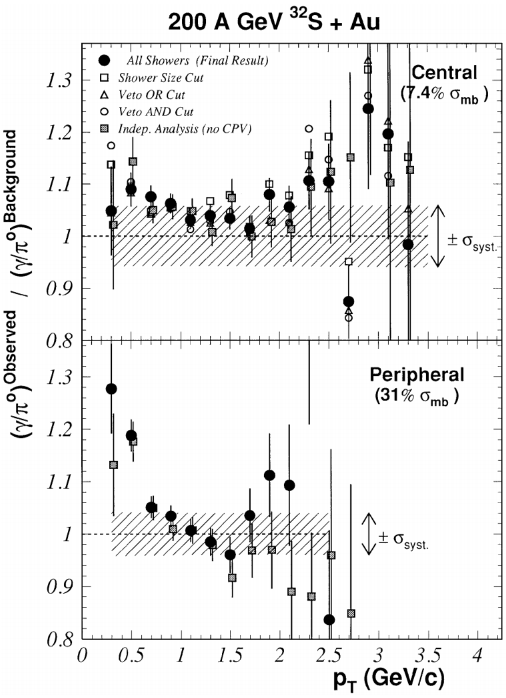

(a) The ratio $\frac{(\gamma/\pi^0)^{\text{obs}}}{(\gamma/\pi^0)^{\text{bkgd}}}$.

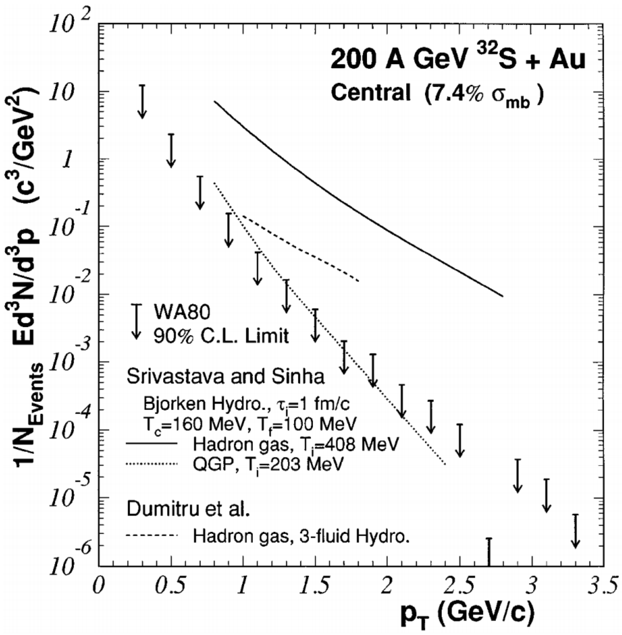

(b) Upper limits at the 90% confidence level on invariant yields of direct photons in central collisions.

Figure 10: Results from WA80 [33].

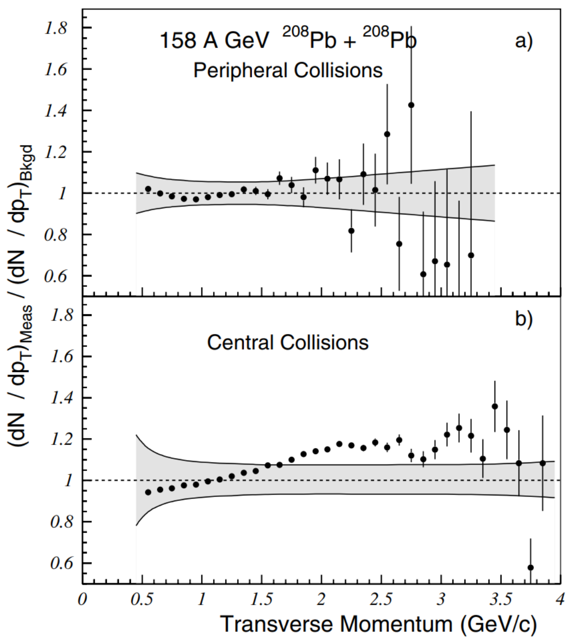

(a) The ratio of measured inclusive photon yields to calculated decay photon yields.

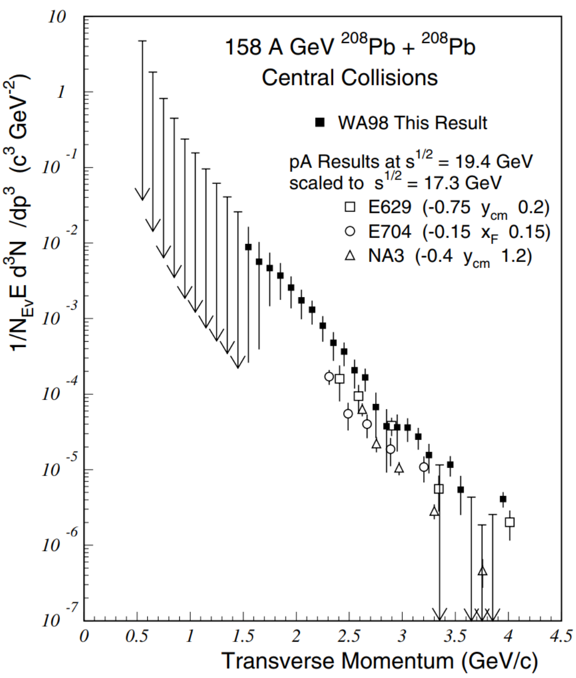

(b) Invariant yields of direct photons in central collisions.

Figure 11: Results from WA98 [37].

small. Hence, there is difficultly in theoretical models to describe the large yield and the large v_2 for direct photons at the same time. This is called "direct photon puzzle", which is not solved yet as of now. On the other hand, due to the large uncertainty, there is not direct photon puzzle at the LHC energy (Figure 13).

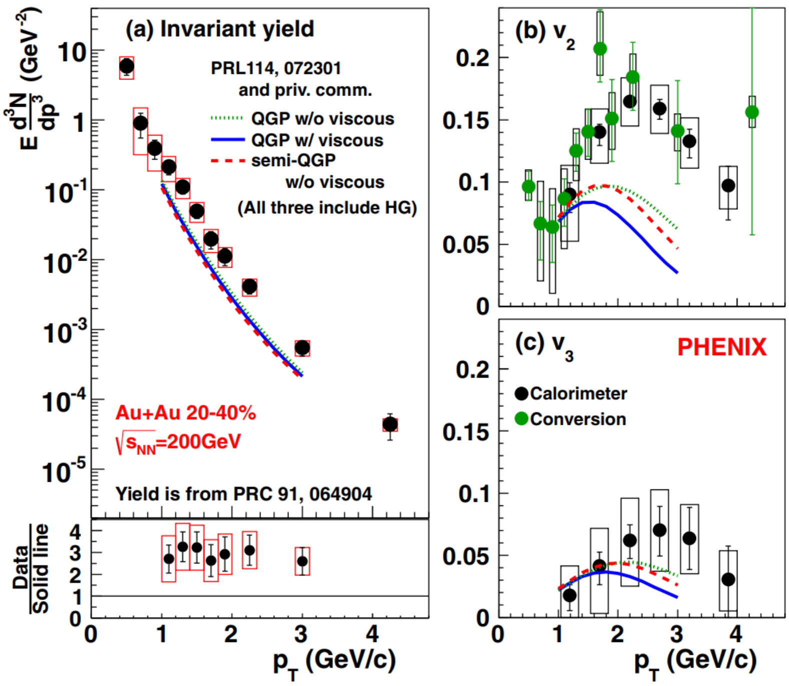

Figure 12: Direct photon yields and flow in 20-40 % Au–Au collisions at $\sqrt{s_{\rm NN}} = 0.2$ TeV with PHENIX [30, 38].

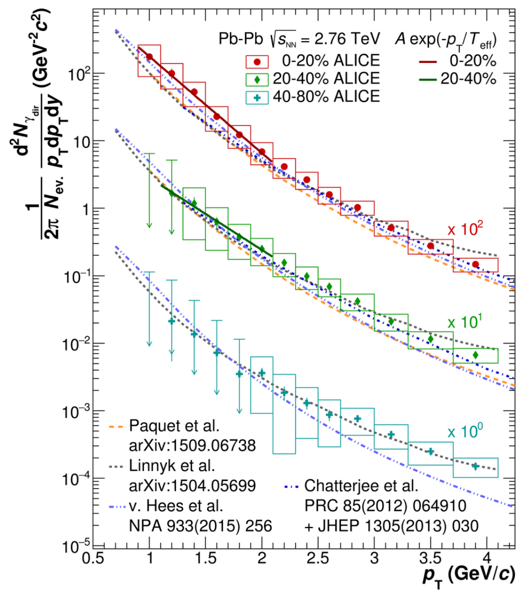

(a) Invariant yields.

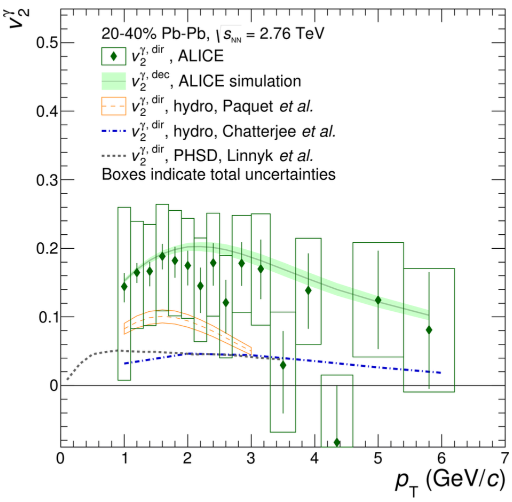

(b) The azimuthal anisotropy v_2.

Figure 13: Direct photon yields and v_2 in 20-40% Pb–Pb collisions at $\sqrt{s_{\rm NN}} = 5.02$ TeV with ALICE [31, 39].

1.6 Organization of this thesis

Neutral mesons (π^0, η) and direct photon $\gamma^{\rm dir}$ production in pp and Pb–Pb collisions at $\sqrt{s_{\rm NN}}$ = 5.02 TeV in ALICE with the PHOS detector are described. This thesis is organized by following. The LHC and ALICE detectors are introduced in Chapter 2. Data sets and its quality assurance for this thesis are written in Chapter 3. Chapter 4 introduces analysis method for neutral mesons measurements. Systematic uncertainties of neutral mesons measurements are summarized in Chapter 5. Results of neutral mesons measurements are discussed in Chapter 6. After that, analysis method for direct photons are given in Chapter 7. Systematic uncertainties of inclusive and direct photons measurements are summarized in Chapter 8. Results of photons measurements are discussed in Chapter 9. Finally, the conclusion of this thesis is in Chapter 10.

2 The LHC and the ALICE apparatus

This section is aimed at basic informations about the LHC accelerator at CERN and the ALICE detectors which are relevant to this thesis.

2.1 The Large Hadron Collider (LHC)

Descriptions about the LHC are taken from these references [40, 41, 42]. The Large Hadron Collider (LHC) is located at CERN across the border between France and Switzerland. The LHC underground tunnel was previously hosted by the Large Electron Positron (LEP) collider. It is the most powerful particle accelerator in the world, whose circumference length is 27 km. The LHC can collide protons at a center-of-mass energy up to 14 TeV and Pb ions up to 5.5 TeV per nucleon.

First, protons are produced from Hydrgen gas by stripping electrons in an electic field. They are accelerated through LINear ACcelerator 2 (LINAC2) up to 50 MeV and injected to a booster for Proton Synchrotoron (PS). At the booster for PS, they are accelerated up to 1.4 GeV. PS accelerates proton beams up to 25 GeV, then sends them to Super Proton Synchrotron (SPS) where they are futher accelerated up to 450 GeV. Finally, proton beams are delivered to the LHC ring and accelerated up to 6500. The designed maximum energy is 7000 GeV per beam, but it is operated at 6500 GeV during Run2 which means center-of-mass energy is at 13 TeV.

Lead (Pb) ions are produced by heating slid ^{208}Pb to make a vapour [43]. Ion beams are accelerated up to 4.2 MeV per nucleon by LINear ACcelerator 3 (LINAC3). Low Energy Ion Ring (LIER) takes them from LINAC3 and accelerates to 72 MeV/n. The rest of path is the same as proton beams, but beam energy is 5.9 GeV/n at the PS, 177 GeV/n at the SPS, 2510 GeV/n at the LHC.

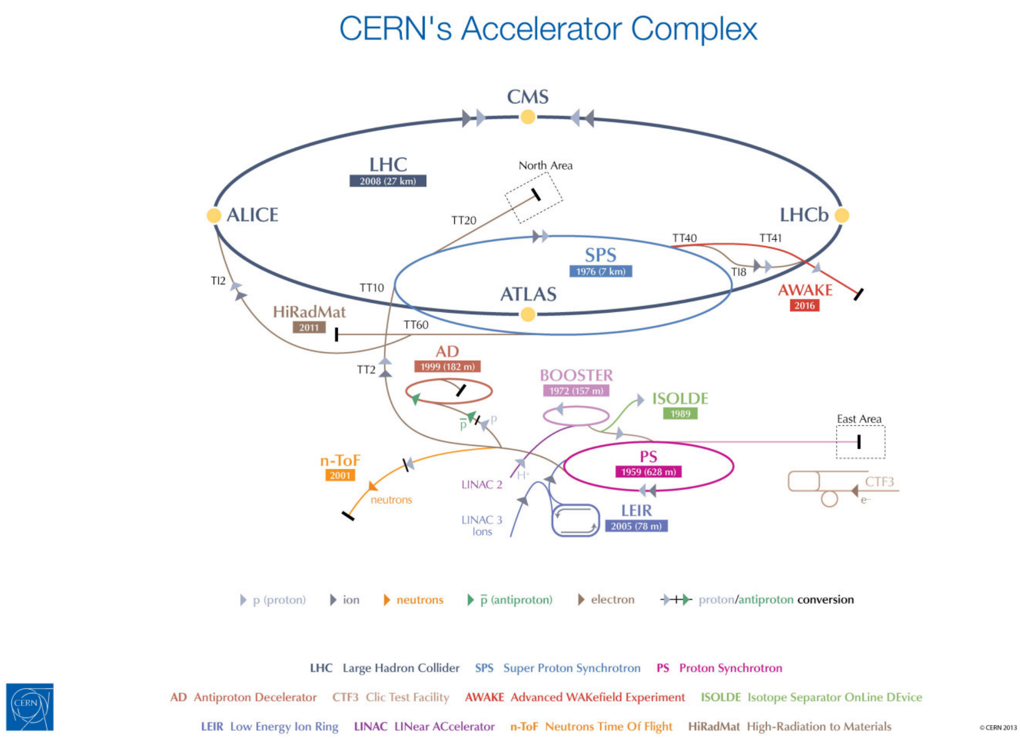

Figure 14: CERN accelerator complex [44].

2.2 ALICE apparatus

Detectors descriptions are taken from these references [45, 46].

2.2.1 Overview of ALICE apparatus

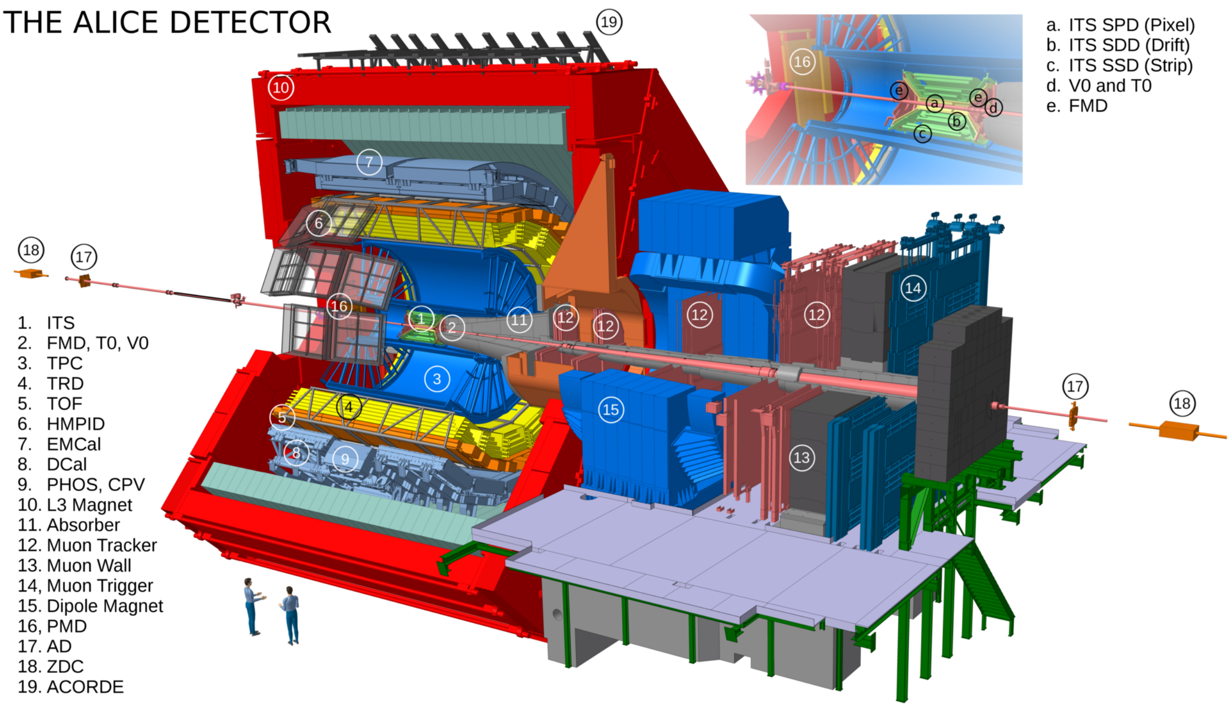

Figure 15: Overview of ALICE detectors in Run2

From the inner side of the central barrel, Inner Tracking System (ITS) which is six layers of silicon tracker and Time Projection Chamber (TPC) which also provides particle identification (PID) by ionization energy loss dE/dx are installed. They are central tracking systems to measure momenta of charged particles under a solenoid magnet $B = 0.5$ T in ALICE. Two type of electro-magnetic calorimeters (Photon Spectrometer (PHOS) and EMCal/DCal) are located from 4.6/4.4 m from a interaction point to measure photon and electron energy and its hit position. In addition to them, there are several PID detectors such as Time of Flight (TOF), High Momentum Particle Identification Detector (HMPID), Transition Radiation Detector (TRD) at mid-rapidity. Trigger detectors (VZERO, T0) are installed to study event property (e.g. event plane and multiplicity) at forward and backward rapidity. Zero Degree Calorimeter (ZDC) at forward and backward rapidity is used to reject events induced by beam-gas interactions. Muon tracker and trigger are installed at only forward rapidity under a dipole magnet $B = 0.7$ T. Hereafter, V0A(C) denotes VZERO detector at A(C)-side, same for T0. In ALICE, A-side is for $\eta > 0$ and C-side is for $\eta < 0$.

2.2.2 Basic kinematic variables in ALICE coordinate

The coordinate system in ALICE for emitted particles from the interaction point (IP) is right-handed Cartesian coordinate system (x,y,z). The point (0,0,0) is the center of ALICE detectors. The beam axis is in parallel to the z-axis and the x-y plane is transverse to the beam(z-) axis. The positive direction of x-axis is defined as the direction from the IP to the center of the LHC ring. The positive direction of y-axis is upward. More often, a spherical coordinate system

(r,θ,φ) is used. The azimuthal angle around the beam(z-) axis $\varphi = \arctan(y/x)$, the polar angle from beam(z-) axis $\theta = \arctan(\sqrt{x^2+y^2}/z)$, and the distance from the IP $r = \sqrt{x^2+y^2+z^2}$. The azimuthal angle φ in the transverse plane starts from $\varphi = 0$ pointing to $x = 0$, the center of the LHC ring. Rapidity y of a particle is defined as :

$$y = \frac{1}{2}\ln\left(\frac{E+p_z}{E-p_z}\right),$$

where E is energy of the particle, p_z is momentum along the z-axis. Pseudo-rapidity η, the relativistic limit of rapidity y, is also used to point the particle position.

$$\eta = -\ln\left(\tan\left(\frac{\theta}{2}\right)\right)$$

Furthermore, to be Lorentz-invariant in high-energy particle physics, transverse momentum p_{T} which is momentum along the transverse plane is defined as :

$$p_{\mathrm{T}} = p\sin\theta = \sqrt{p_x^2+p_y^2}$$

Especially, p_{T} is important variable, as it is given by collisions.
The distance in $\eta - \varphi$ plane ΔR is used for jet reconstruction and particle isolation as :

$$\Delta R = \sqrt{\Delta\eta^2+\Delta\varphi^2}$$
$$\Delta\eta = \eta_i - \eta_j$$
$$\Delta\varphi = \varphi_i - \varphi_j,$$

where $\eta_{i(j)}$, $\varphi_{i(j)}$ represent the position of particle $i(j)$.

2.2.3 Trigger detectors

VZERO The VZERO detector [47] consisting of 32×2 plastic scintillators covers $-3.7 < \eta < -1.7$ V0C and $2.8 < \eta < 5.1$ V0A. This detector provides minimum-bias (MB) triggers V0OR/V0AND. V0OR (INT5) requires at least one hit on either V0A or V0C. V0AND (INT7) requires at least one hit on each V0A and V0C. The VZERO detector also measures event multiplicity and event plane in Pb–Pb collisions.

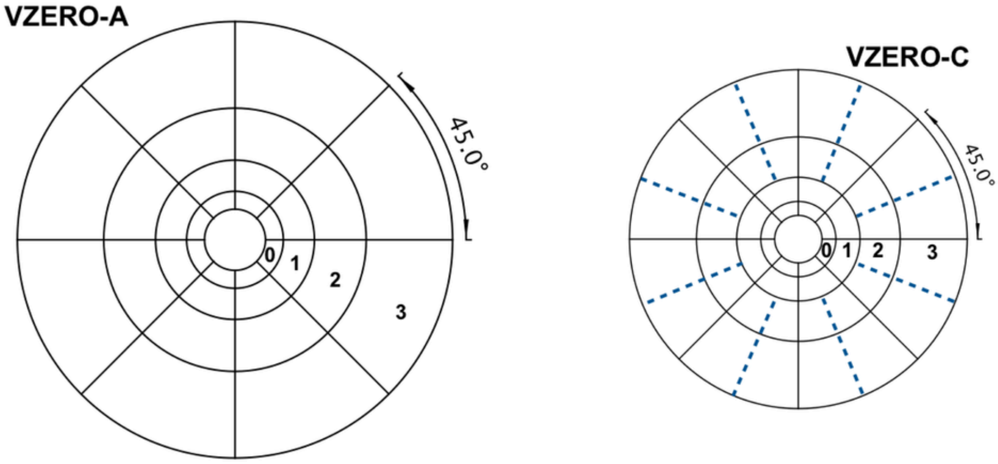

Figure 16: Sketches of V0A and V0C arrays [48].

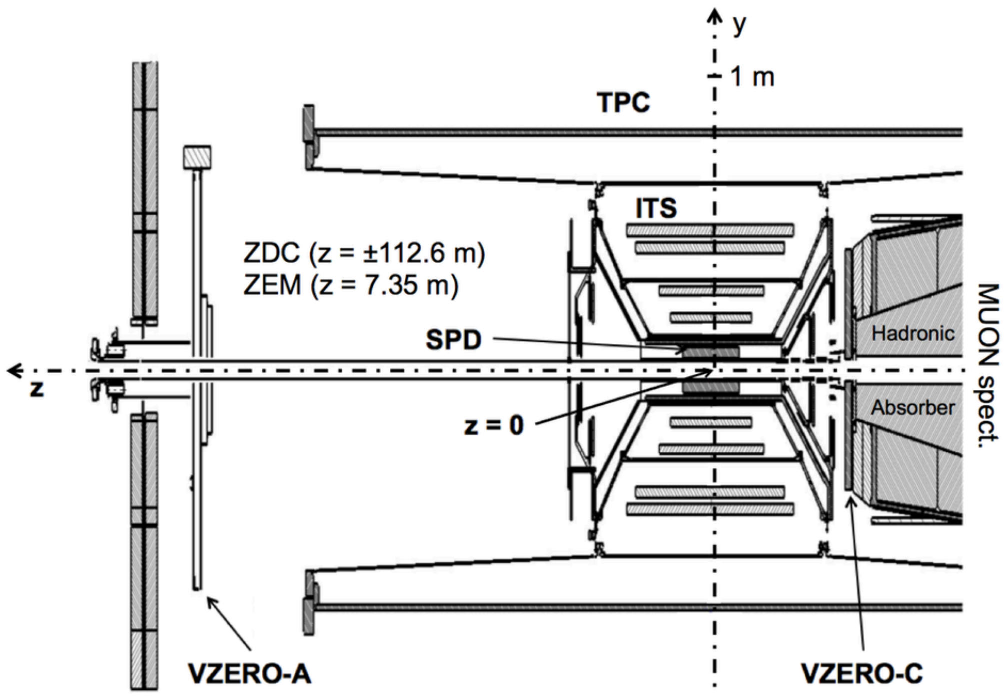

Figure 17: Position of VZERO (A-C) arrays and ITS around the beam pipe [48].

It also rejects beam-gas interactions by collision timing. As shown by Figure.19, three event classes are observed: collisions at (8.3 ns,14.3 ns), beam-gas interactions at (-14.3 ns,-8.3 ns) and (14.3 ns,8.3 ns).

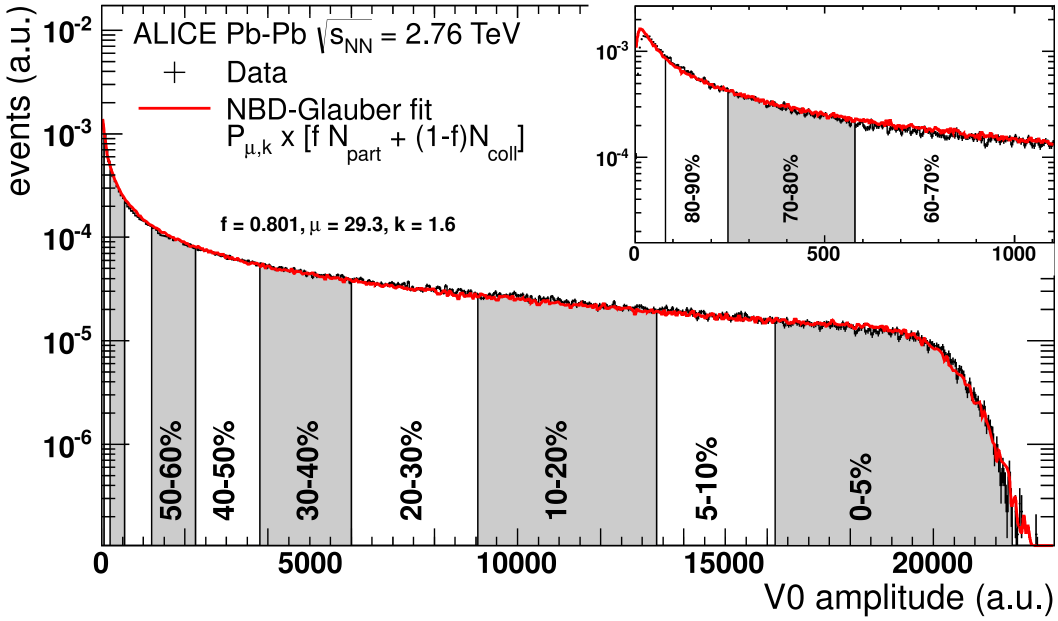

Figure 18: V0 (V0A + V0C) amplitude distribution [46].

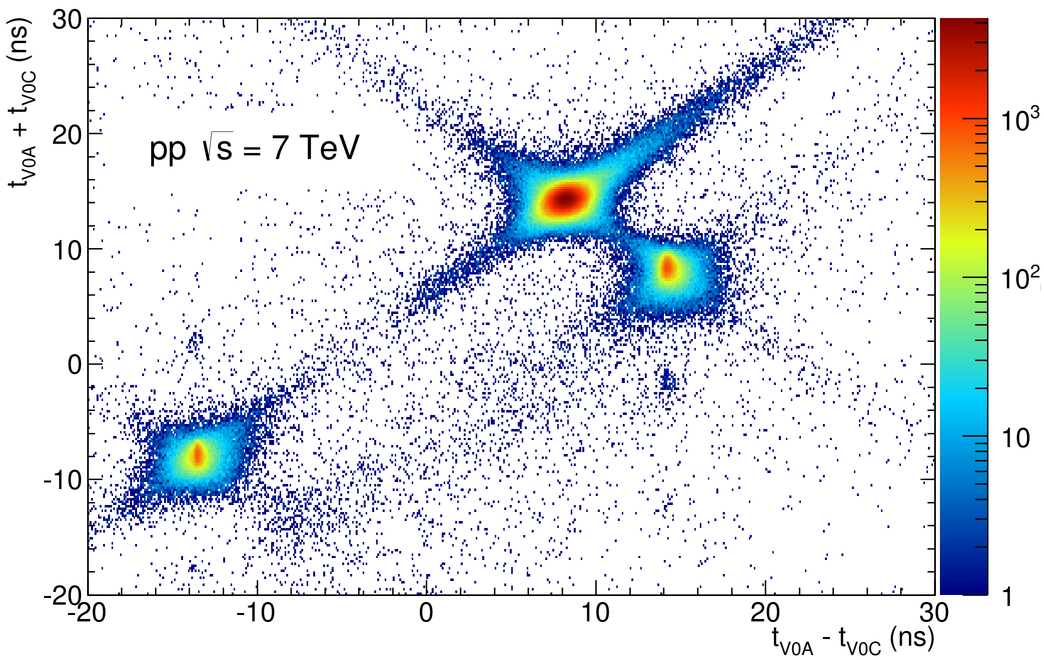

Figure 19: Correlation between the sum and the difference of hit timing of V0A and V0C [46].

T0 The T0 detector [47], quartz Cherenkov detector, measures collision timing and the position of the interaction along the beam line precisely. It also delivers luminosity at IP2 to LHC operators. The acceptance of the T0 detector is $-3.3 < \eta < -3.0$ for T0C and $4.6 < \eta < 4.9$ for T0A.

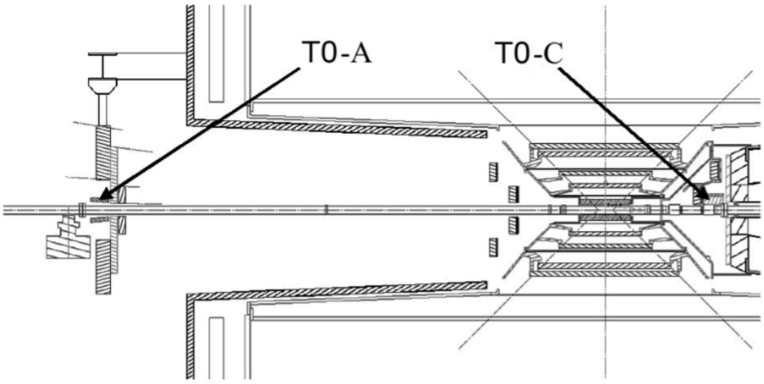

Figure 20: Positions of T0A and T0C [49].

2.2.4 Central Tracking System

Inner Tracking System (ITS) The ITS detector [51] is inner-most silicon tracker to reconstruct a primary vertex of a collision and momenta of charged particles. The coverage of the ITS is $|\eta| < 0.9$ and 2π in azimuth. It consists of three different types that are Silicon Pixel Detector (SPD), Silicon Strip Detector (SSD) and Silicon Drift Detector (SDD) from inner to outer layer. Each of them has two layers. SSD and SDD also provide ionization energy loss dE/dx for PID at low transverse momentum.

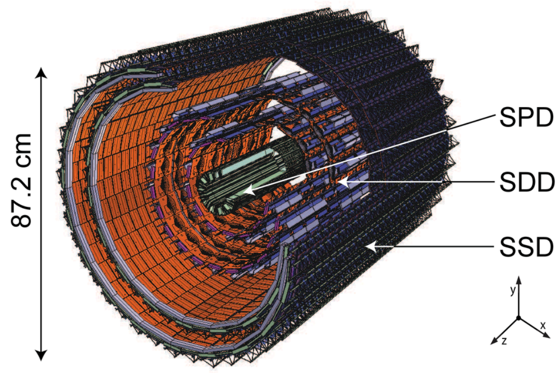

Figure 21: The layout of ITS [50].

Time Projection Chamber (TPC) TPC [54] is the main tracking detector which measures momenta of charged particles and ionization energy loss dE/dx for PID in ALICE. Advantages of TPC are great spatial resolution under high multiplicity environment $N_{\mathrm{ch}} \sim O(10^3)$ produced by Pb–Pb collisions and strong PID performance. The coverage is $|\eta| < 0.9$, 2π in azimuth and its radius is between 85 and 250 cm around the beam axis.

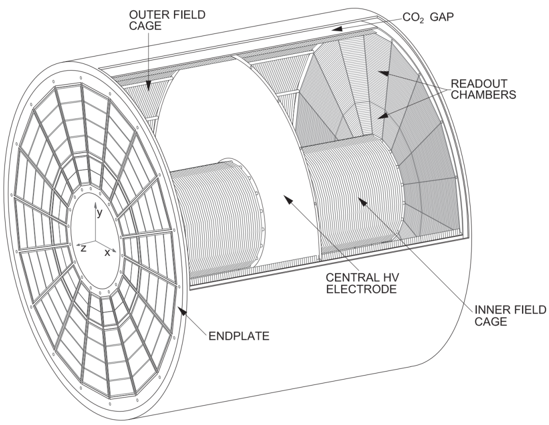

Figure 23: The layout of TPC [52, 53].

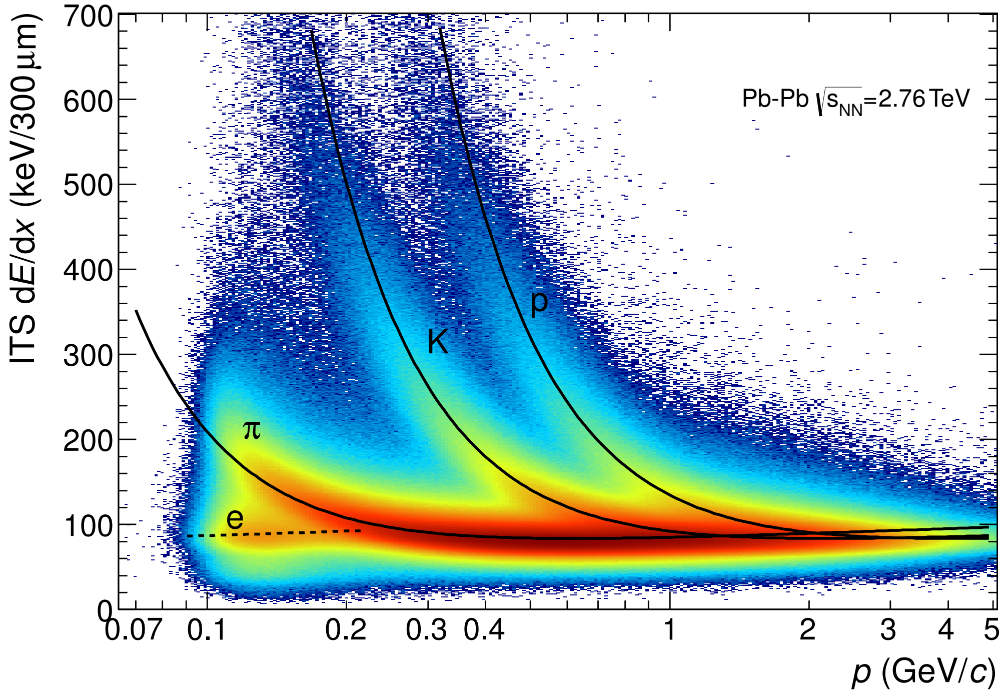

Figure 22: dE/dx measured in ITS standalone as a function momentum of charged particle [46].

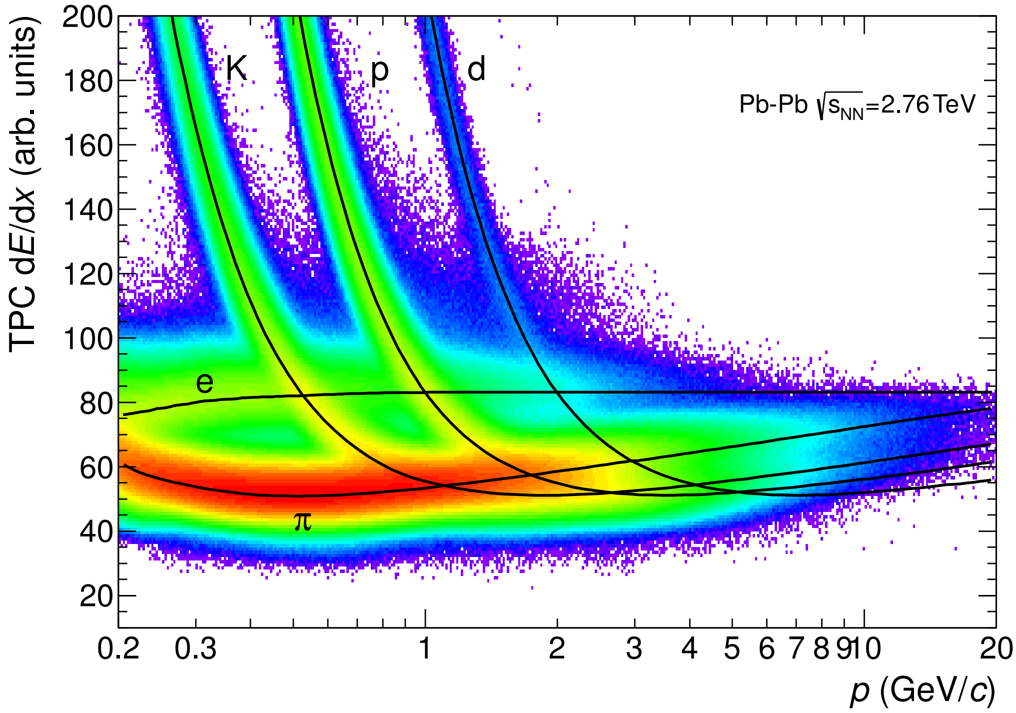

Figure 24: dE/dx measured in TPC as a function momentum of charged particle [46].

2.2.5 Electro-magnetic calorimeters

Photon Spectrometer (PHOS) PHOS [55, 45] is the main detector in this thesis. PHOS is a homogeneous electro-magnetic calorimeter located from 4.6 m from the interaction point. It consists of fine-segmented 12,544 $PbWO_4$ crystals readout by Avalanche Photo Diode (APD)s, operated at -25 degrees Celcius. A Moliere radius of the $PbWO_4$ crystal is 2.2 cm which allows us to distinguish two photons decayed from π^0 at high p_{T} with a small opening angle. A radiation length X_0 is 0.89 cm and a density is 8.29 g/cm^3 for the $PbWO_4$ crystal. Volume of one crystal is $2.2 \times 2.2 \times 18$ cm^3, which corresponds to 20 X_0. The acceptance of the PHOS detector is $|\eta| < 0.12$, $250^\circ < \varphi < 320^\circ$, $\Delta\varphi = 20^\circ$ for one module. The energy resolution as a function of energy E in GeV is [56] :

$$\frac{\sigma_E}{E}\ (\%) = \sqrt{\left(\frac{0.013}{E}\right)^2 + \left(\frac{0.036}{\sqrt{E}}\right)^2 + (0.0112)^2}$$

The position resolution as a function of energy E in GeV is [55] :

$$\sigma_{x,z}\ (\text{mm}) = \sqrt{\left(\frac{3.26}{\sqrt{E}}\right)^2 + 0.44^2}$$

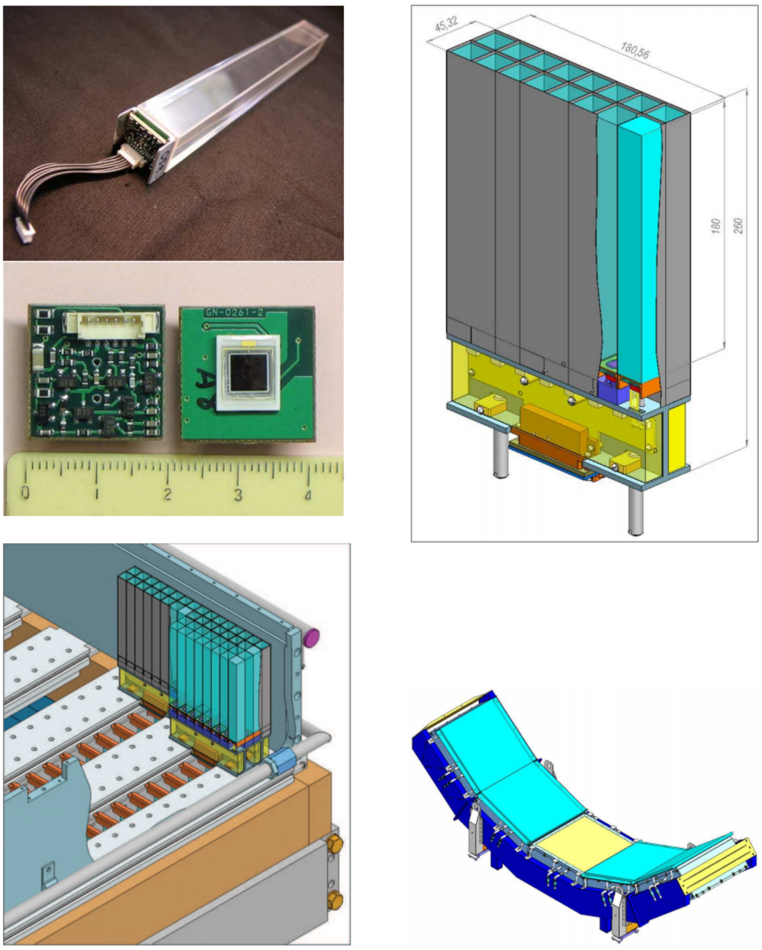

Figure 25: Elements of the PHOS detector.

PHOS is constructed as shown by Figure 25. The $PbWO_4$ crystal readout by the APD for one element on top left, one strip unit has 8×2 elements on to right. One module consists of $64 \times 56 = 3584$ elements on bottom left. Finally, there are three and a half modules are installed in ALICE. (A half module have been installed since 2015.) The PHOS detector provides Level-0 and Level-1 triggers to select events containing high energy deposition in the area of 4×4 cells on PHOS. Energy thresholds of triggers are configurable and were set to 4 GeV (L0) in pp collisions at $\sqrt{s}$ = 5.02 TeV (2017) and 8 GeV (L1 High), 4 GeV (L1 Midium) in Pb–Pb collisions at $\sqrt{s_{\mathrm{NN}}}$ = 5.02 TeV (2015). The latency of the L0 and the L1 trigger is 1.2 and 7 μs respectively [57].

2.2.6 Other detectors

ALICE detectors that are not relevant to this thesis (ACORDE, AD, CPV, EMCal, FMD, HMPID, MCH, MTR, PMD, TOF, TRD, ZDC) are explained in [45, 46].

3 Data sets

The detailed event selection, cluster selection on PHOS and quality of data are described in this section.

3.1 Data sets in pp collisions at $\sqrt{s} = 5.02$ TeV

Minimum-bias events and PHOS triggered events have been analyzed in this these. The integrated luminosity used in this analysis is 19 nb^{-1} for Minimum-bias and 550 nb^{-1} for PHOS L0 triggered events respectively.

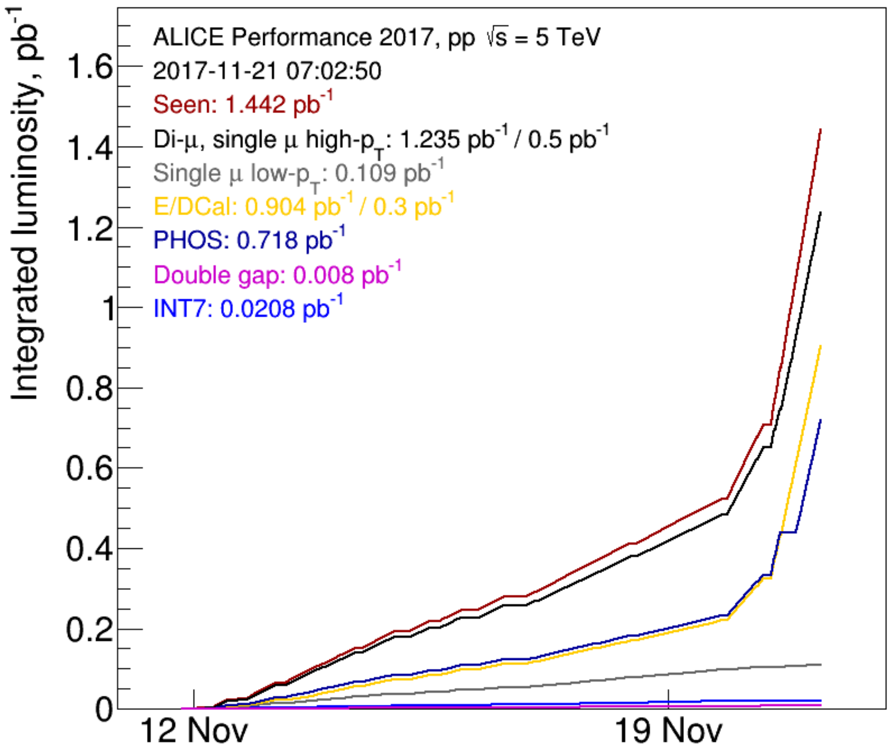

Figure 26: The integrated luminosity in pp collisions at $\sqrt{s} = 5.02$ TeV taken in 2017.

Run lists

LHC17p

282343, 282342, 282341, 282340, 282314, 282313, 282312, 282309, 282307, 282306, 282305, 282304, 282303, 282302, 282247, 282230, 282229, 282227, 282224, 282206, 282189, 282147, 282146, 282127, 282126, 282125, 282123, 282122, 282120, 282119, 282118, 282099, 282098, 282078, 282051, 282050, 282031, 282030, 282025, 282021, 282016, 282008.

LHC17q

282441, 282440, 282439, 282437, 282399, 282398, 282393, 282392, 282391, 282367, 282366, 282365.

In LHC17q, MB events were recorded in only 282367, 282366, 282365.

Monte-Carlo simulation samples

LHC17l3b PYTHIA8 for LHC17p-q ($\sim$ 200 M events)

LHC17j3[a,b,c][1,2] single particle simulation (π^0, η, γ) for LHC17pq (main efficiency for correction in LHC17pq)

Event selection

physics selection (reject beam-gas interactions)

the number of charged track associated with the primary vertex > 0

pileup rejection by SPD

$|Z_{\mathrm{vtx}}| < 10$ cm

Minimal cluster selection

$E_{\mathrm{cluster}} > 0.2$ GeV (to extract photon signal as much as possible at low energy)

M02 > 0.1 cm for only E > 1 GeV (to extract photon signal as much as possible at low energy)

M20 > 0.1 cm for only E > 2 GeV (to extract photon signal as much as possible at low energy)

M20 < 2.0 cm (to remove clusters whose size is too large)

|TOF| < 12.5 ns in real data (to remove photons from other bunch crossings)

The total number of events after these event selection is about 975 M MB events and 1.0 M PHOS triggered events. A cluster means "a group of cells". Photons interact with $PbWO_4$ crystals and generate electro-magnetic showers, depositing energy in a group of cells around the impact point of each photon. This group of cells is defined as a cluster. The sum of amplitudes measured in each cell in the cluster is proportional to the initial photon energy. The center of gravity in cell coordinates weighted by the cell energy logarithmically defines the hit position. Second moments ($M20$, $M02$) of the cluster is used to discriminate electro-magnetic or hadronic showers [58, 59].

3.1.1 Quality assessment of MB data

The minimum-bias (MB) trigger configuration was V0AND (INT7 in Figure.26) in this data taking period. As a first check of PHOS data, an average cluster energy and an average number of hits are plotted. The average values are stable in all runs. π^0 peak parameters are plotted run-by-run to verify that PHOS was stable in this period. As a result, M1,2,3 are all stable. Especially, π^0 peak could not be seen well on M4, because M4 has limited detector acceptance. A peak position in M1,2,3 are consistent within statistical error bar. There are poor statistics in some runs where π^0 peak is not so clear. M4 was excluded from the beginning because a systematic uncertainty of material budget is large in front of M4 due to TOF + TRD, which is not suitable for the precise photon measurement.

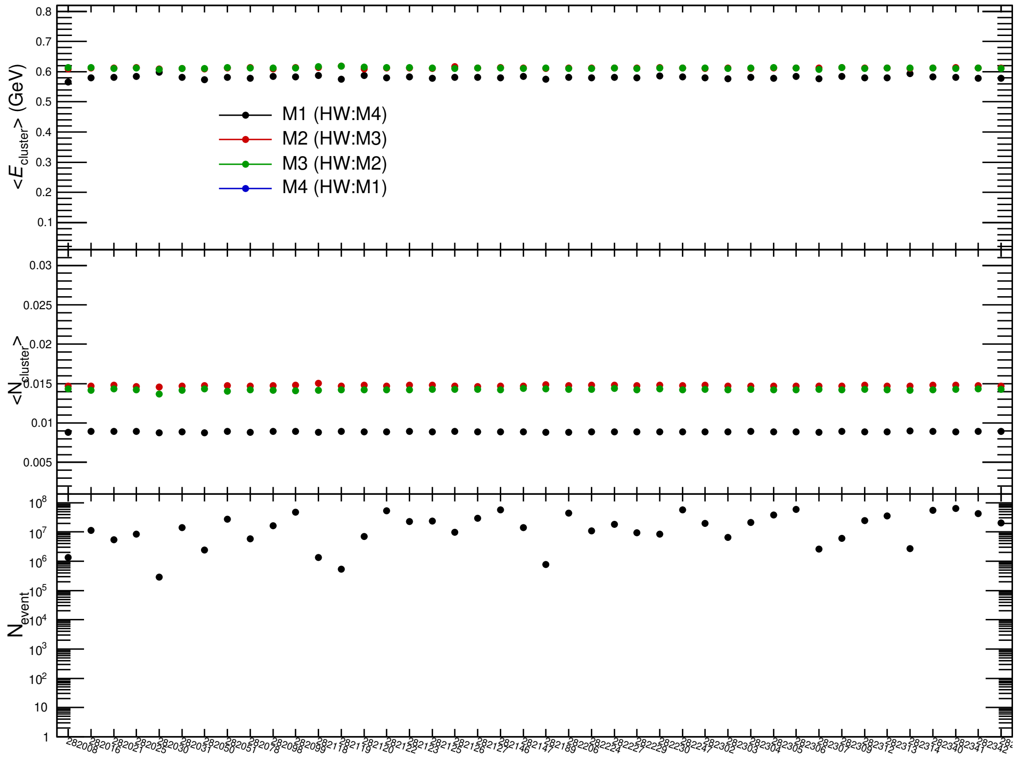

Figure 27: The average cluster energy and number of hits in each run on PHOS in LHC17p pass1.

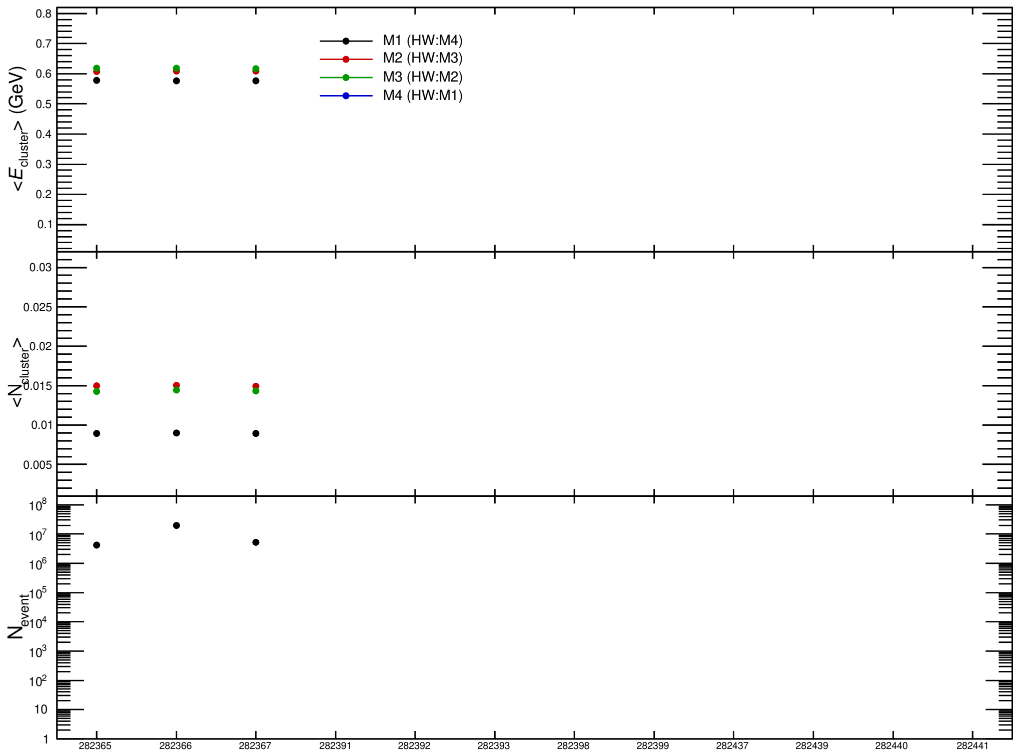

Figure 28: The average cluster energy and number of hits in each run on PHOS in LHC17q pass1.

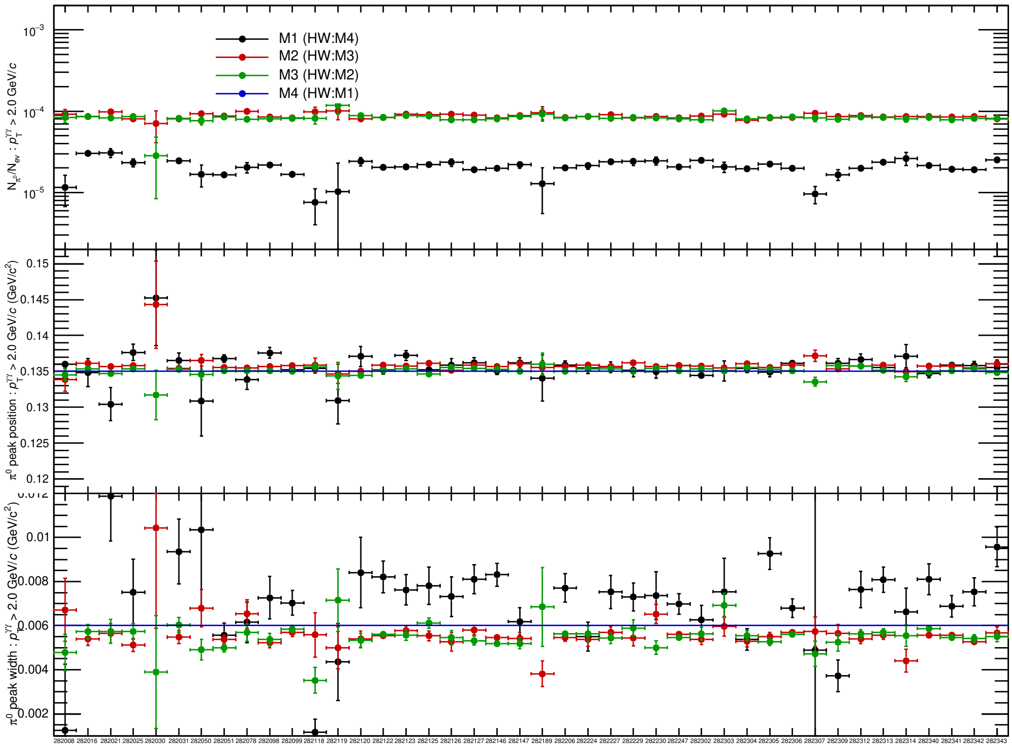

Figure 29: π^0 yield, peak position and sigma in each run in LHC17p pass1.

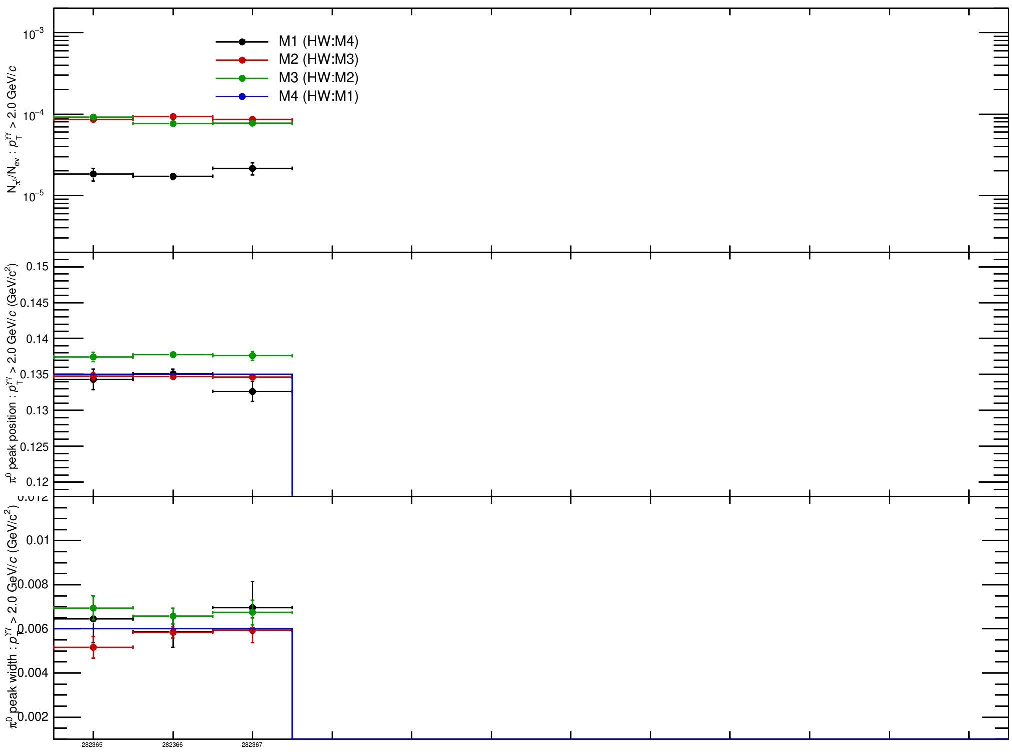

Figure 30: π^0 yield, peak position and sigma in each run in LHC17q pass1.

3.1.2 Quality assessment of PHOS triggered data

In addition to minimal event selection described above, at least one high energy hit on PHOS is required for the PHOS trigger. Additional quality assessments were performed in case of PHOS triggered data. PHOS L0 trigger decision is taken by each TRU by the sliding window algorithm. If analogue sum of 2×2 FastORs ($= 4 \times 4$ cells) is greater than the threshold, PHOS L0 trigger fires. On the other hand, PHOS L1 trigger decision is taken by STU. STU stands for Summary Trigger Unit and it is new trigger device since Run2. STU summarizes all TRU information and scan them by the same sliding window algorithm beyond TRU borders. Thanks to STU, PHOS L1 trigger can detect high energy hits between borders of TRUs, while L0 can not. At first, one has to check distance between a fired TRU channel and cluster hit positions in X and Z coordinate respectively. Since TRU stores cell indices at the bottom-left of fired channels, a typical distance is expected to be [-3,0] in X and [-3,0] in Z. Figure 31 proves that the typical distance is [-3,0] in X and [-3,0] in Z. Based on this fact, a matching criterion between a fired TRU channel and a cluster is set to [-3,0] in X and [-3,0] in Z respectively. The dead TRUs are in white (Figure 31,32). PHOS triggered events must contain at least one cluster which matches the fired TRU channel decided by the criterion based on the distance between fired TRU channels and clusters. Fig.32 shows energy distribution in PHOS L0 triggered events. The matching efficiency is close to 100% above the trigger threshold at 4 GeV in pp collisions at $\sqrt{s} = 5.02$ TeV (LHC17pq). The rejection factor of the PHOS L0 trigger in pp collisions at $\sqrt{s} = 5.02$ TeV is stable at 30.6 k as shown by Figure 33.

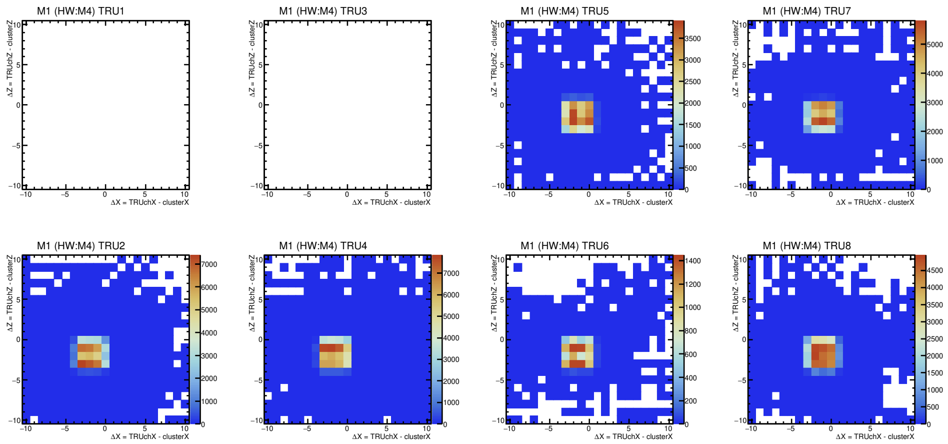

(a) The distance between fired TRU channels and cluster position on M1 in LHC17pq.

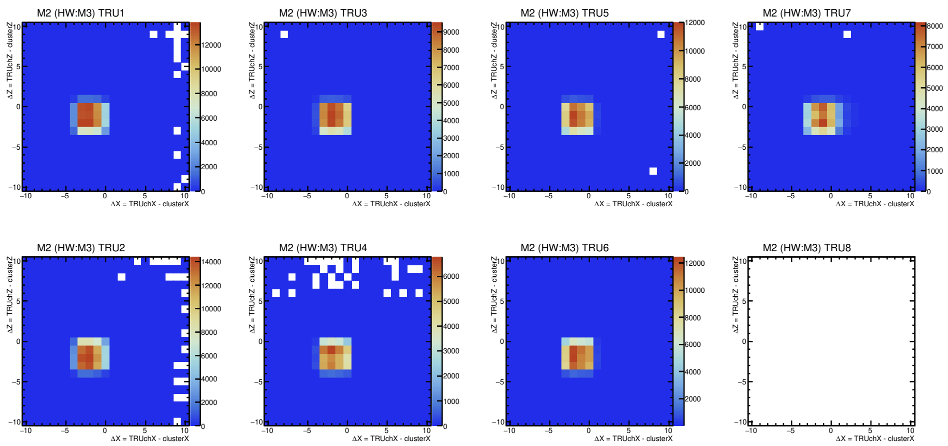

(b) The distance between fired TRU channels and cluster position on M2 in LHC17pq.

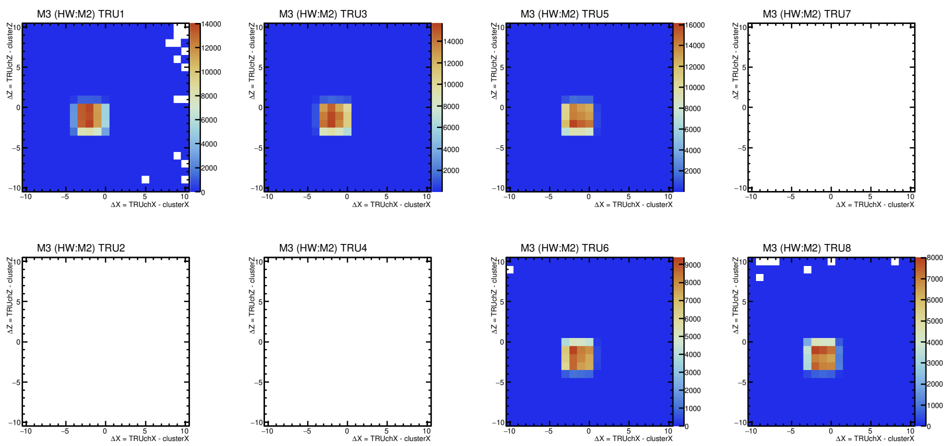

(c) The distance between fired TRU channels and cluster position on M3 in LHC17pq.

Figure 31: The distance between fired TRU channels and cluster position in different module for $E_{\text{cluster}} > 4$ GeV in LHC17pq.

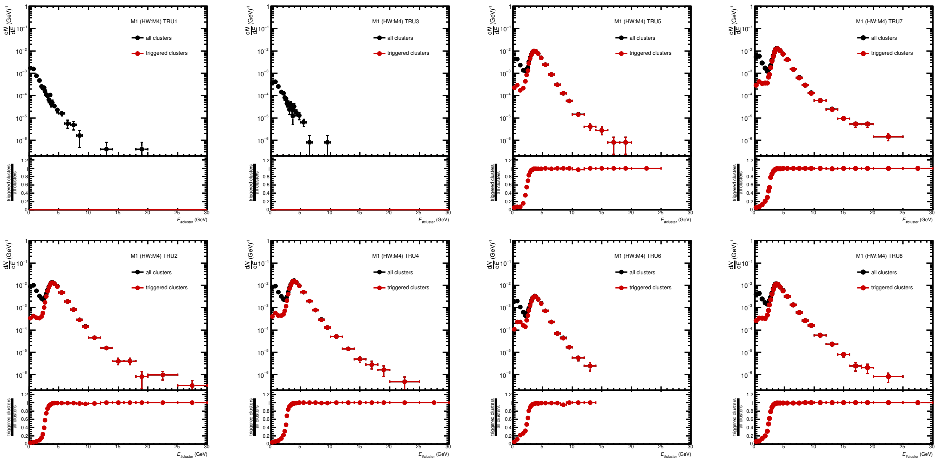

(a) Energy distribution on M1 in LHC17pq.

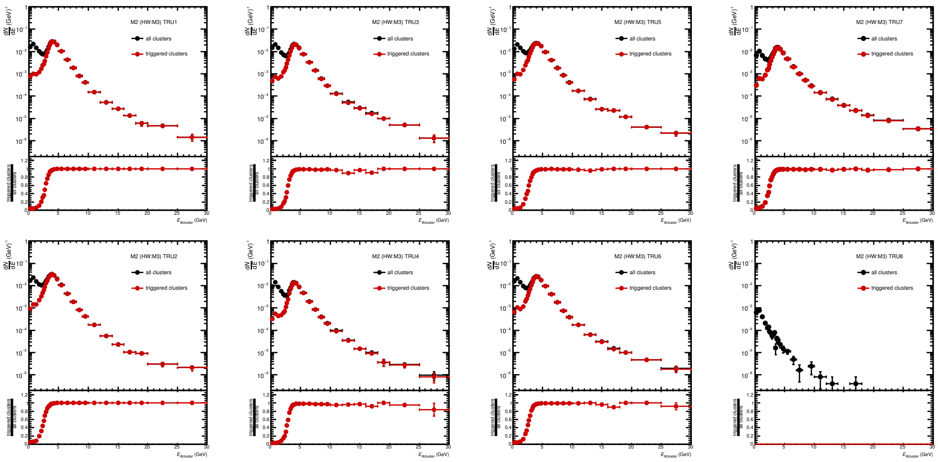

(b) Energy distribution on M2 in LHC17pq.

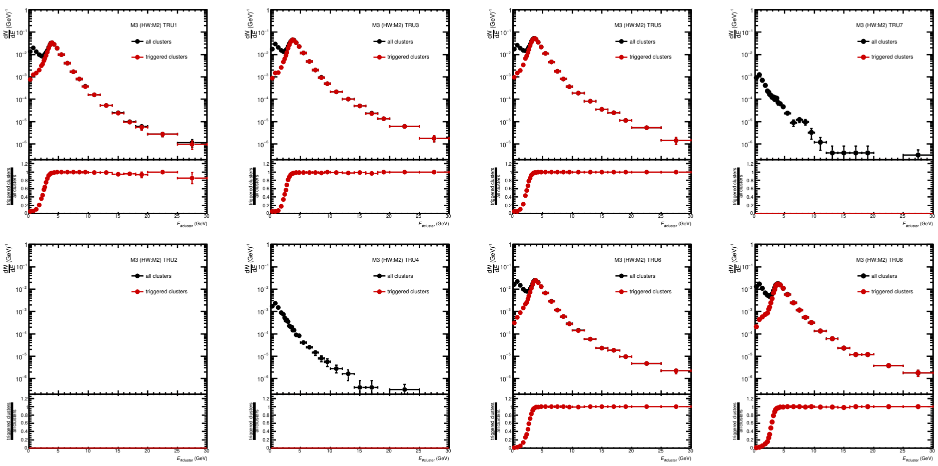

(c) Energy distribution on M3 in LHC17pq.

Figure 32: Energy distribution of all clusters and triggered clusters and ratios in LHC17pq.

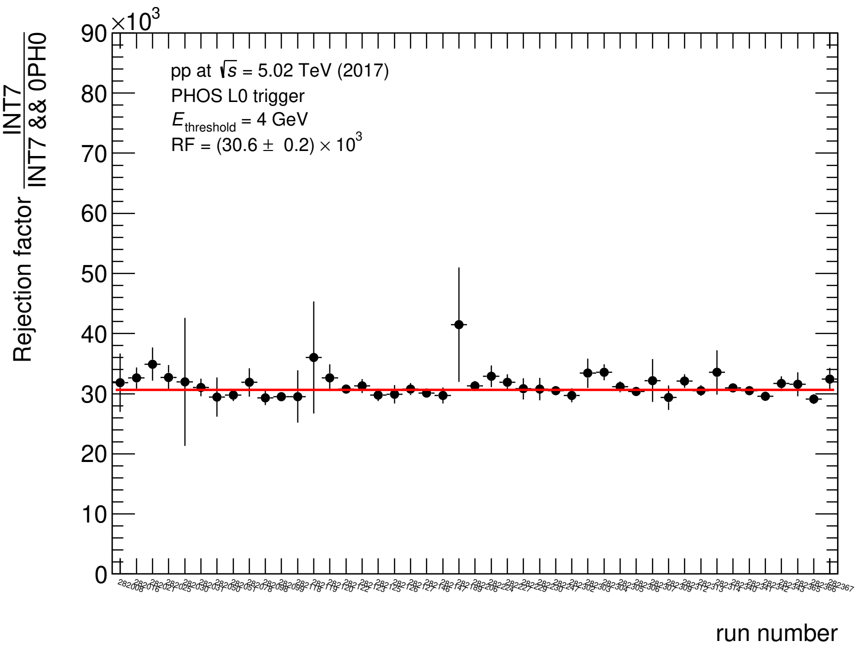

Figure 33: The rejection factor of PHOS L0 trigger (run-by-run) in pp collisions at $\sqrt{s} = 5.02$ TeV

3.2 Data sets in Pb–Pb collisions at $\sqrt{s_{\mathrm{NN}}} = 5.02$ TeV

The integrated luminosity used in this analysis is 12 μb^{-1} for Minimum-bias and 70 μb^{-1} for PHOS L1 triggered events respectively.

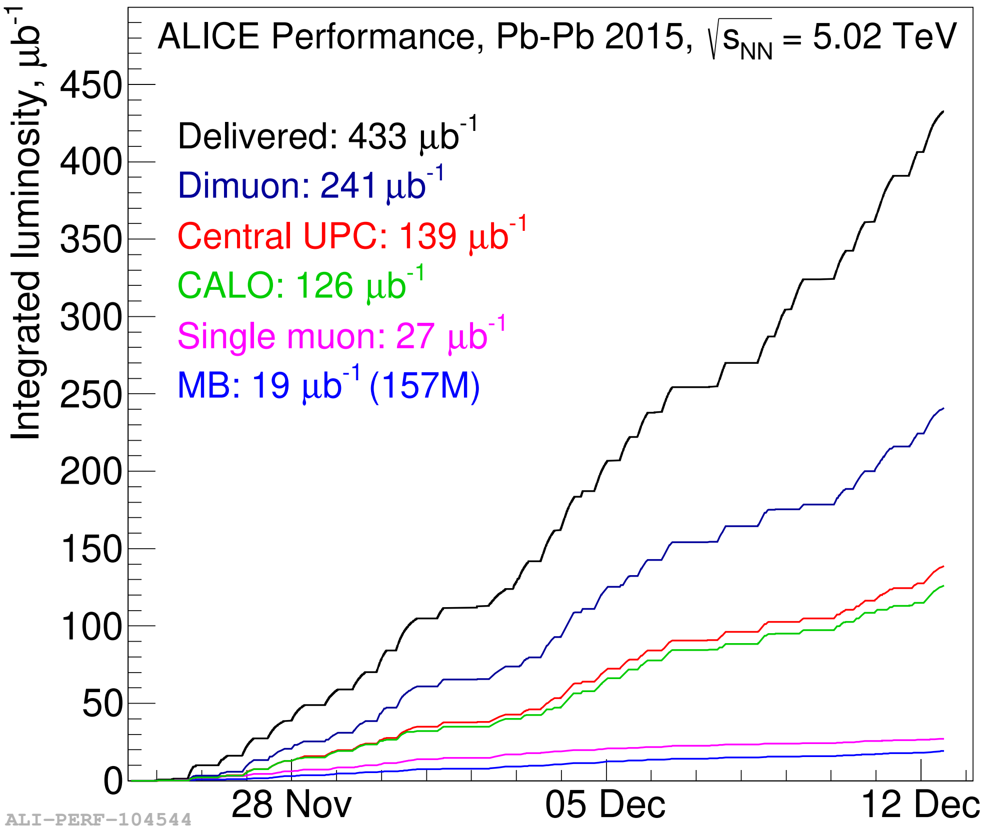

Figure 34: The integrated luminosity in Pb–Pb collisions at $\sqrt{s_{\mathrm{NN}}} = 5.02$ TeV taken in 2015.

Run lists

LHC15o

pass1

246982, 246980, 246937, 246930, 246928, 246867, 246865, 246855, 246851, 246847, 246846, 246845, 246844, 246810, 246809, 246808, 246807, 246805, 246804, 246766, 246765, 246763, 246760, 246759, 246758, 246757, 246751, 246750, 246676, 246675, 246495, 246493, 246488, 246487, 246434, 246431, 246428, 246424, 246275, 246271, 246225, 246222, 246217, 246185, 246182, 246181, 246180, 246178, 246153, 246152, 246151, 246148, 246115, 246113, 246089, 246087, 246049, 246048, 246042, 246037, 246036, 246012, 246003, 246001, 245963, 245954, 245952, 245949, 245923, 245831, 245829, 245705, 245702, 245700, 245692, 245683.

pass1_pidfix

245545, 245544, 245543, 245542, 245540, 245535, 245507, 245505, 245504, 245501, 245497, 245496, 245454, 245453, 245452, 245450, 245446, 245441, 245439, 245410, 245409, 245407, 245401, 245397, 245396, 245353, 245349, 245347, 245346, 245345, 245343, 245259, 245233, 245232, 245231, 245152, 245151, 245146, 245145

low_IR pass5

246392, 246391, 246390, 245068, 245066, 245064, 244983, 244982, 244980, 244975, 244918

Monte-Carlo simulation samples

LHC16g1[,a,b,c] HIJING for LHC15o ($\sim$ 10 M events)

LHC17i7[a,b,c][1,2] single particle simulation (π^0, η, γ) for LHC15o (main efficiency for correction in LHC15o)

Event selection

physics selection (reject beam-gas interactions)

the number of charged track associated with the primary vertex > 0

pileup rejection by SPD

$|Z_{\mathrm{vtx}}| < 10$ cm

centrality estimator : V0 multiplicity (V0M)

Minimal cluster selection

$E_{\mathrm{cluster}} > 0.2$ GeV (to extract photon signal as much as possible at low energy)

M02 > 0.1 cm for only E > 1 GeV (to extract photon signal as much as possible at low energy)

M20 > 0.1 cm for only E > 2 GeV (to extract photon signal as much as possible at low energy)

M20 < 2.0 cm (to remove too large size cluster)

|TOF| < 50.0 ns in real data (to remove photons from other bunch crossings)

3.2.1 Quality assessment of MB data

The minimum-bias (MB) trigger configuration was V0AND (MB in Figure.34) in this data taking period. As a first check of PHOS data, an average cluster energy and an average number of hits are plotted here. Average values stay stable in all runs. π^0 peak parameters are plotted (Figure.38, Figure.39 and Figure.40) run-by-run to verify that PHOS was stable in this period. As a result, M1,2,3 are all stable. Especially, π^0 peak could not be seen well on M4, because M4 has limited detector acceptance. A peak position in M1,2,3 are consistent within statistical error bar. There are poor statistics in some runs where π^0 peak is not so clear. Note that M4 was excluded from analyses in Pb–Pb, too.

3.2.2 Quality assessment of PHOS triggered data

In this data taking period (LHC15o), 2 different L1 triggers that are high (L1H) and medium (L1M) threshold triggers were active. As it has been known that PHOS L1 triggers on M3 did not work because of poor matching efficiency between trigger units and readout units from the begenning of analyses in this data taking perid, Since STU stores cell indices at the top-left of fired channels, a typical distance is expected to be [-3,0] in X and [-1,2] in Z. Based on Figure 41 and 42, a matching criterion between a fired TRU channel and a cluster is set to [-3,0] in X and [-3,0] in Z for module 1 and [-3,0] in X and [-1,2] in Z for module 2. M3 is excluded from trigger analyses in Pb–Pb collisions at $\sqrt{s_{\mathrm{NN}}} = 5.02$ TeV. The matching efficiency is close to 100% above the trigger thresholds at 4 GeV for medium (L1M) and 8 GeV for high (L1H) in Pb–Pb collisions at $\sqrt{s_{\mathrm{NN}}} = 5.02$ TeV (LHC15o). The rejection factor of PHOS L1 triggers in Pb–Pb collisions at $\sqrt{s_{\mathrm{NN}}} = 5.02$ TeV is stable at 9.66 k for L1H and 0.835 k for L1M as shown by Figure 45. According to Figure 45a, runs 245233, 245439 and 246391 have small rejection, which means the L1H trigger have fired too often. Thus, these 3 runs were excluded from PHOS L1 trigger analyses.

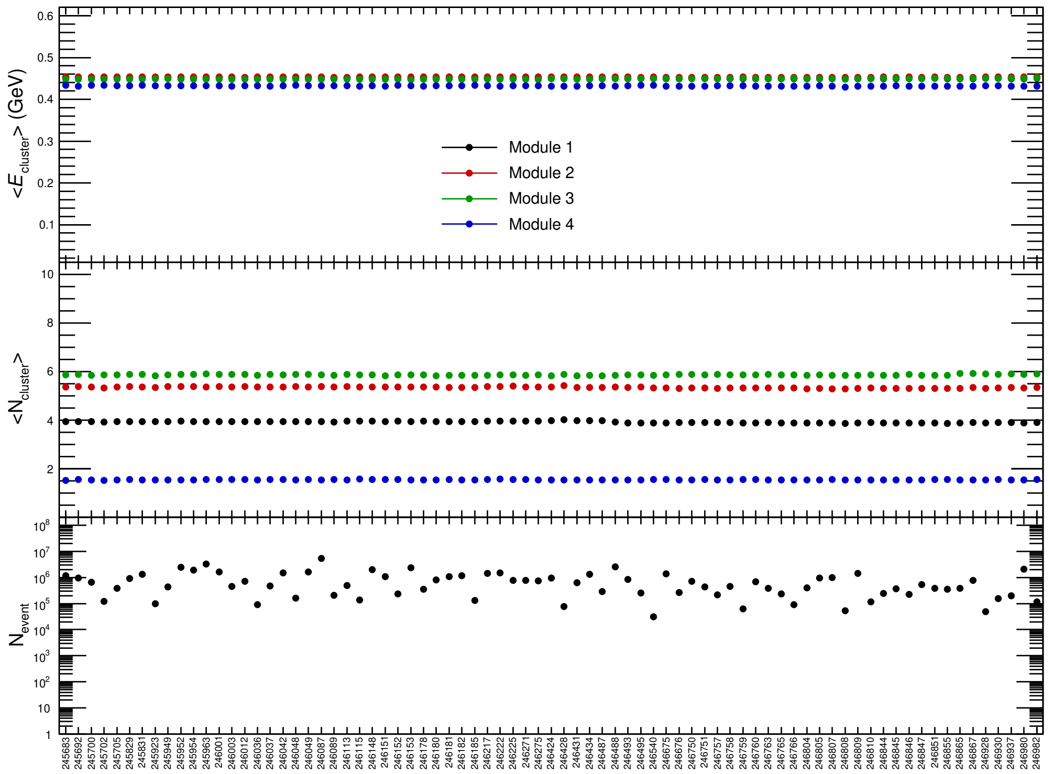

Figure 35: The average cluster energy and number of hits in each run on PHOS in LHC15o pass1.

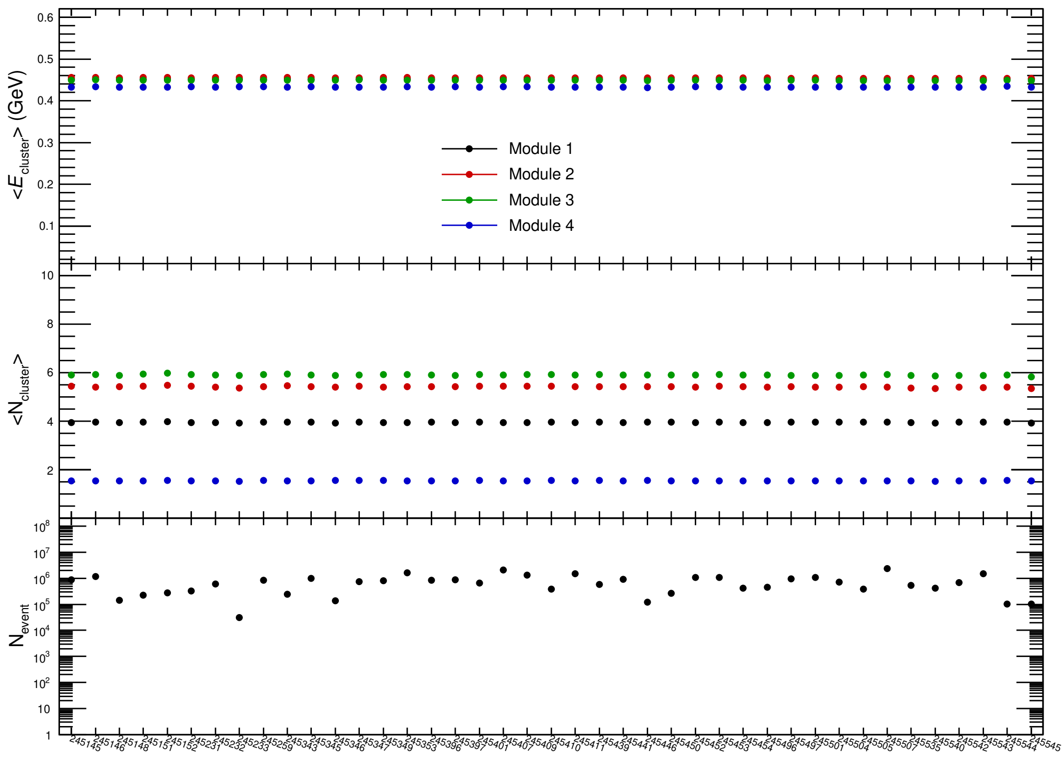

Figure 36: The average cluster energy and number of hits in each run on PHOS in LHC15o pass1_pidfix.

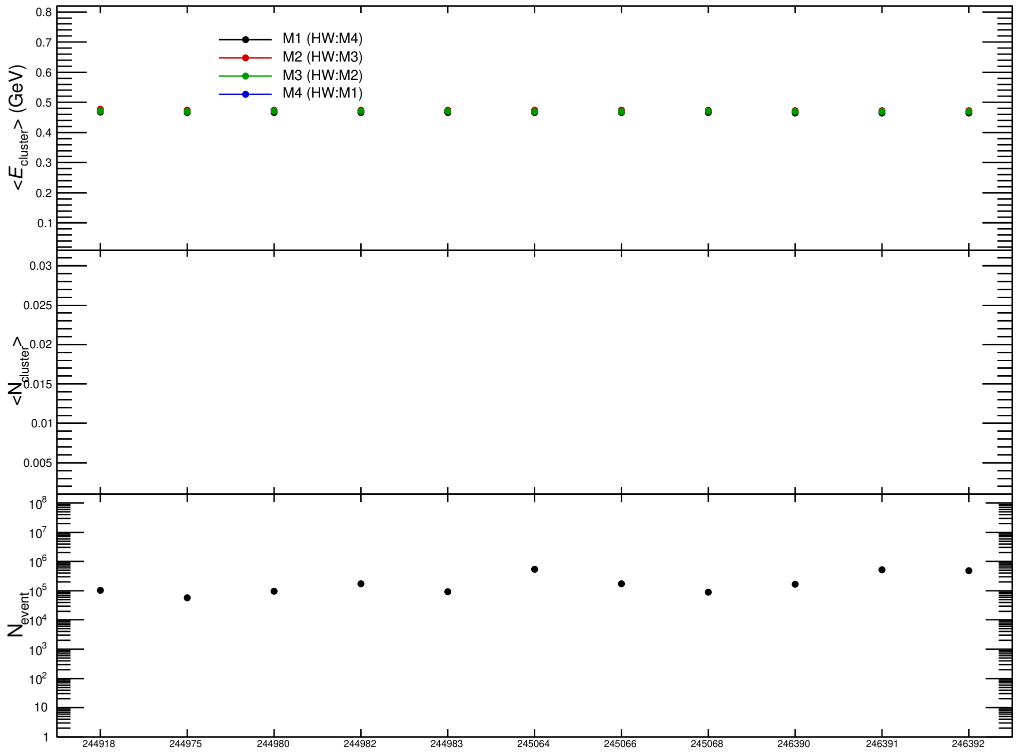

Figure 37: The average cluster energy and number of hits in each run on PHOS in LHC15o lowIR pass5.

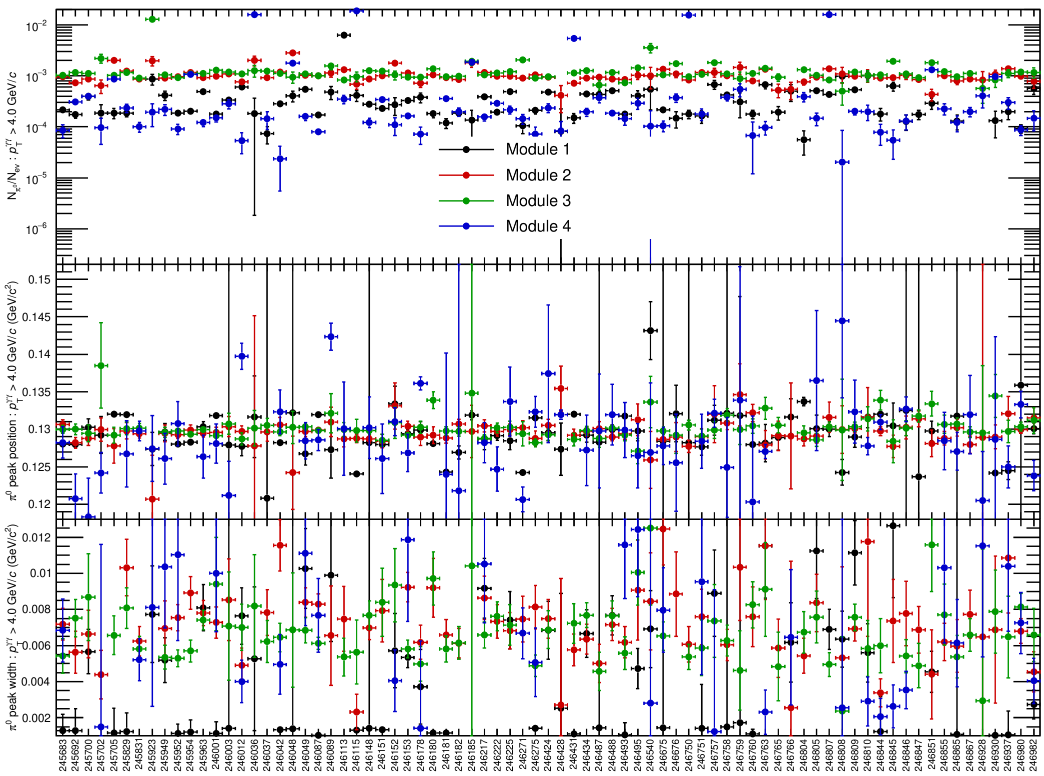

Figure 38: π^0 yield, peak position and sigma in each run in LHC15o pass1.

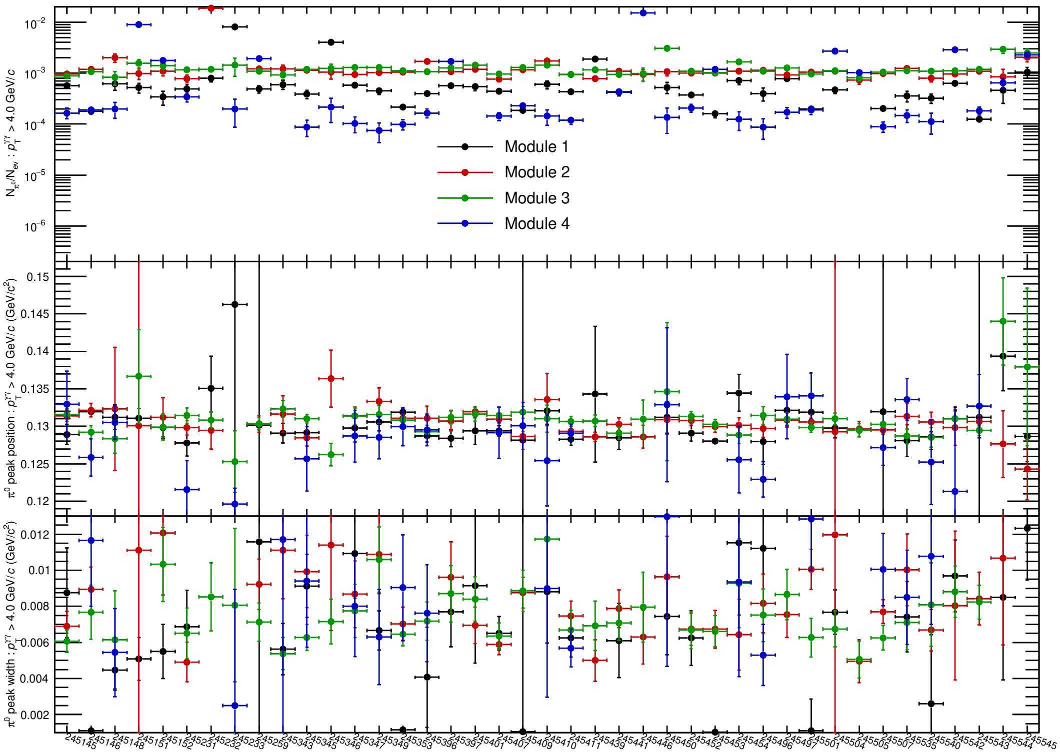

Figure 39: π^0 yield, peak position and sigma in each run in LHC15o pass1_pidfix.

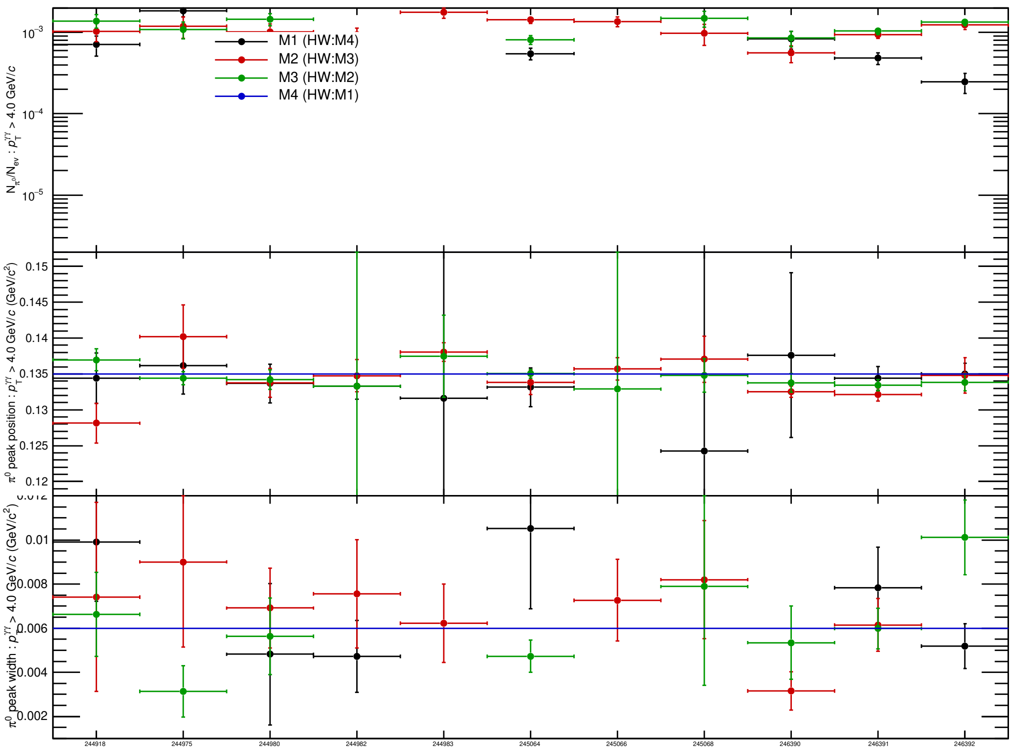

Figure 40: π^0 yield, peak position and sigma in each run in LHC15o lowIR pass5.

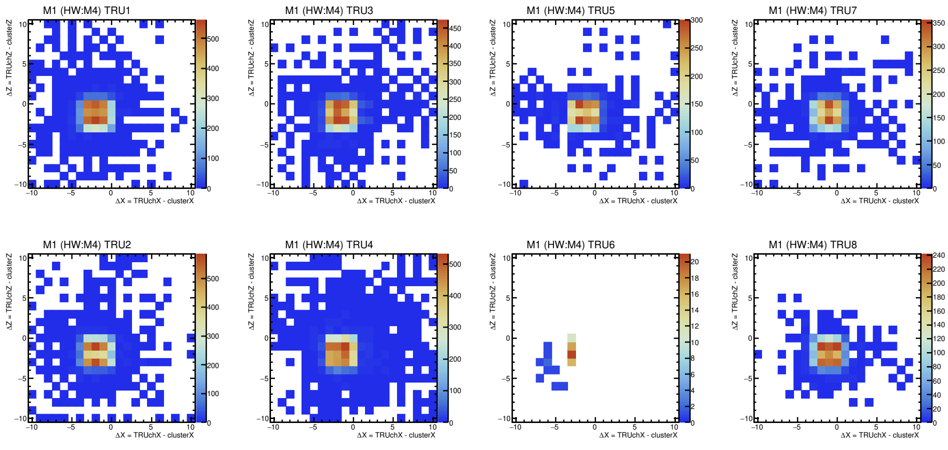

(a) Module 1.

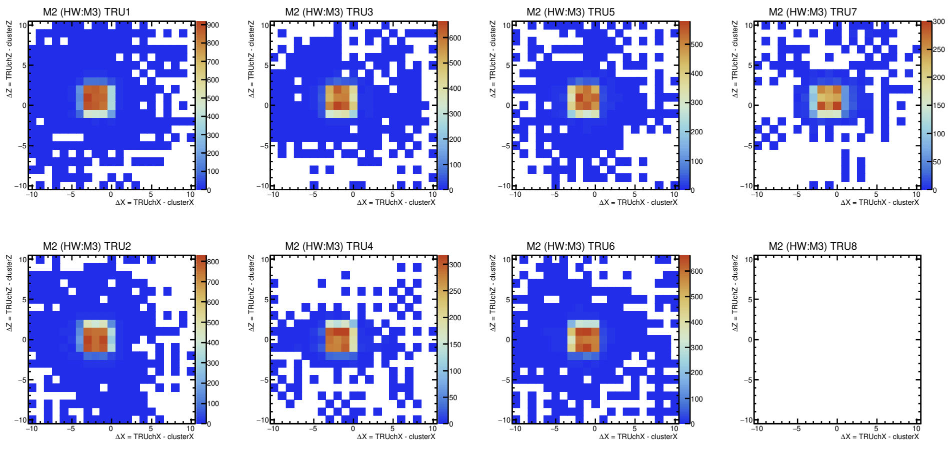

(b) Module 2.

Figure 41: The distance between fired TRU channels and cluster position on different modules for L1H at $E_{\text{cluster}} > 8$ GeV in Pb–Pb collisions at $\sqrt{s_{\text{NN}}} = 5.02$ TeV

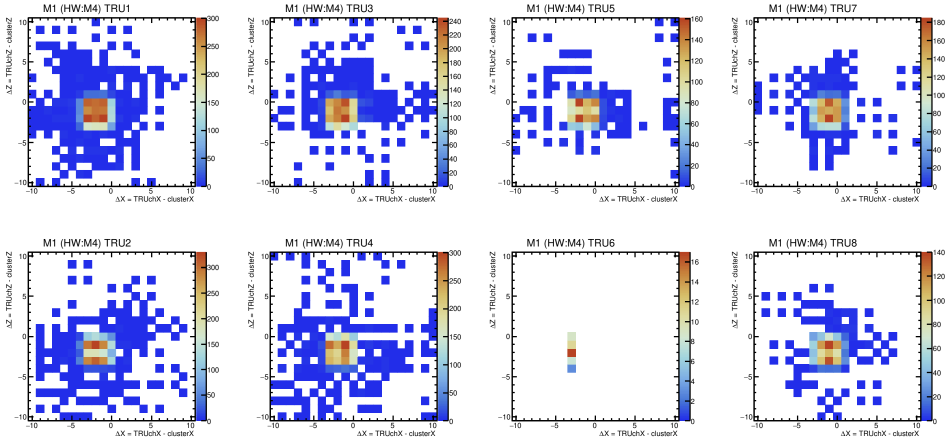

(a) Module 1.

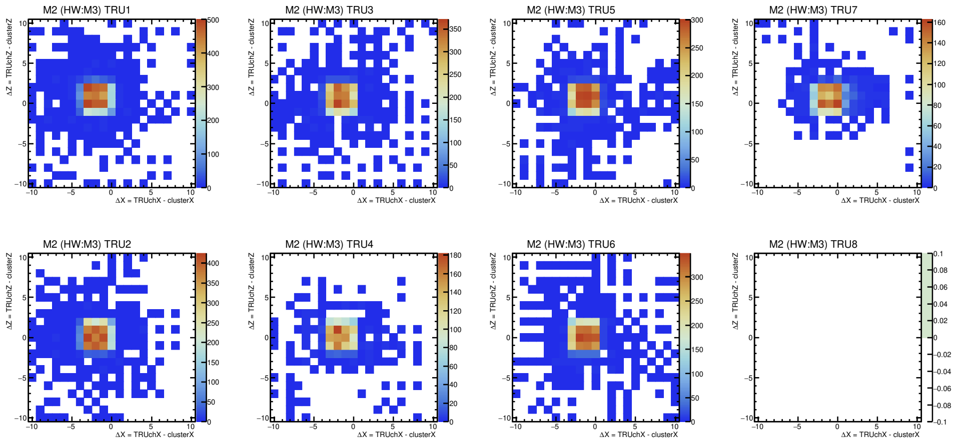

(b) Module 2.

Figure 42: The distance between fired TRU channels and cluster position on different modules for L1M at $E_{\text{cluster}} > 4$ GeV in Pb–Pb collisions at $\sqrt{s_{\text{NN}}} = 5.02$ TeV

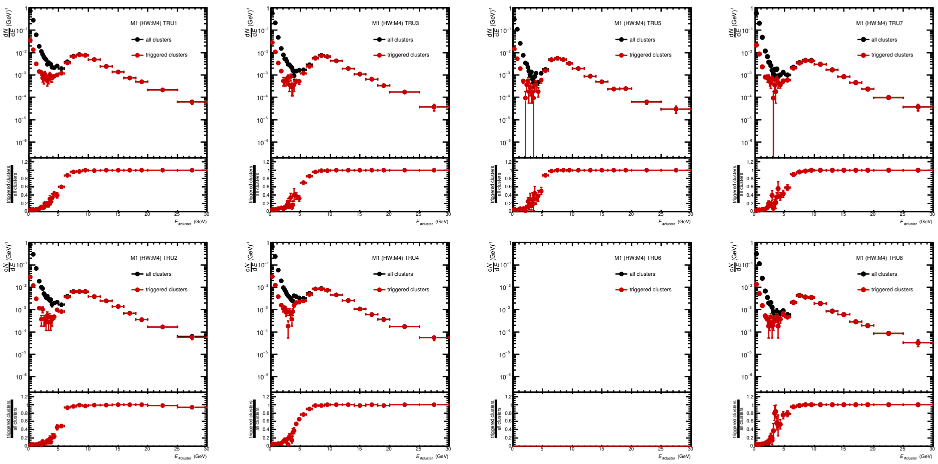

(a) Module 1.

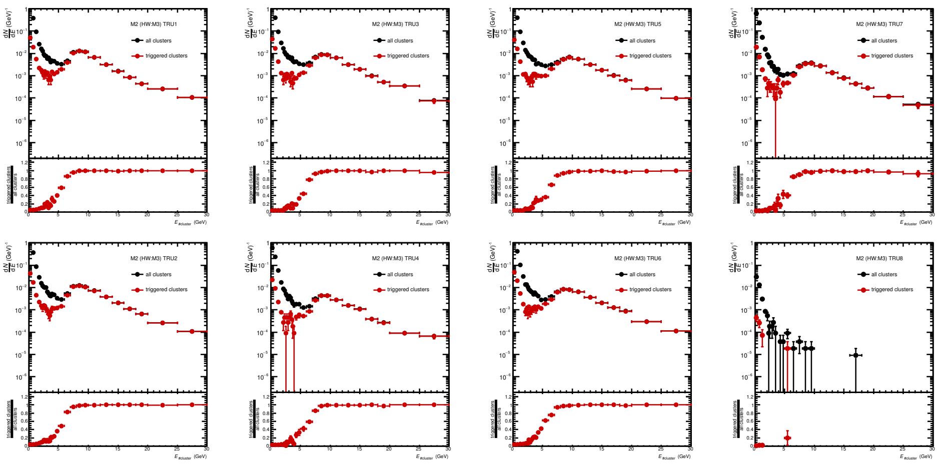

(b) Module 2.

Figure 43: Energy distribution of all clusters and triggered clusters and ratios on different modules for L1H in Pb–Pb collisions at $\sqrt{s_{\mathrm{NN}}} = 5.02$ TeV

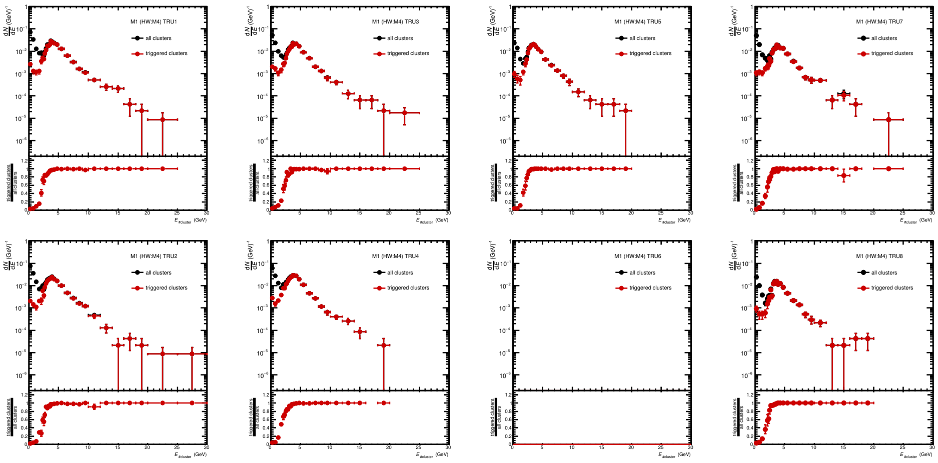

(a) Module 1.

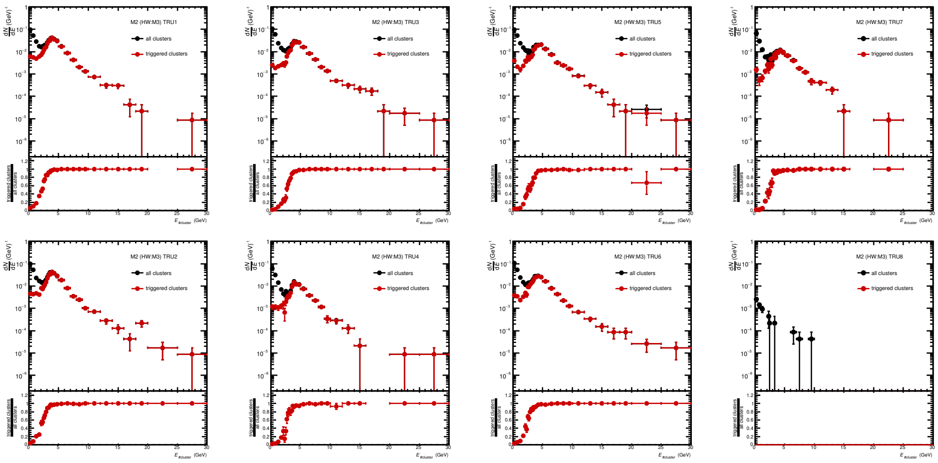

(b) Module 2.

Figure 44: Energy distribution of all clusters and triggered clusters and ratios on different modules for L1M in Pb–Pb collisions at $\sqrt{s_{\rm NN}}$ = 5.02 TeV

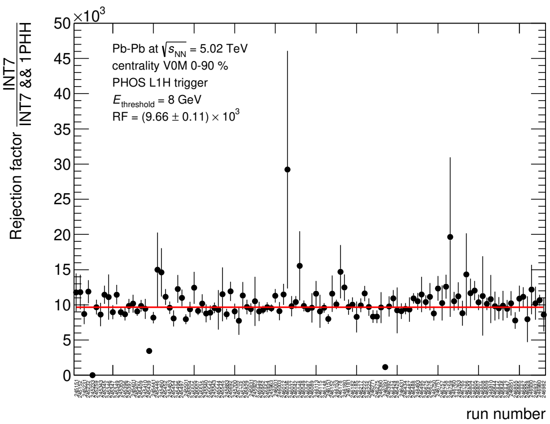

(a) PHOS L1H trigger

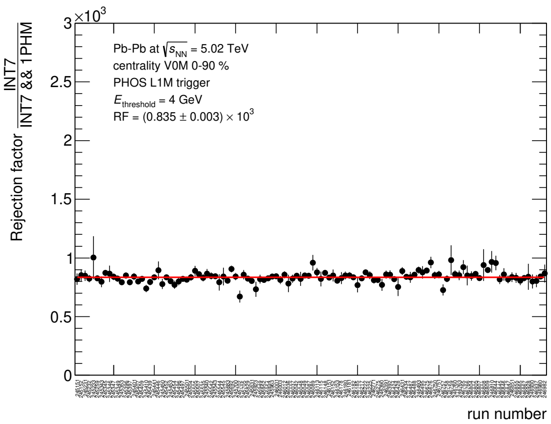

(b) PHOS L1M trigger

Figure 45: The rejection factor of PHOS L1 trigger (run-by-run) in Pb–Pb collisions at $\sqrt{s_{\rm NN}}$ = 5.02 TeV

4 Analyses of neutral mesons

Procedure to measure production cross section of neutral mesons are described in this section. At first, an analysis strategy to give an overview of analyses is summarized in 4.1. Since photon identification is a key of this thesis, criteria for photon selection is in 4.2. The detailed explanation about analyses in pp and Pb–Pb are in section 4.3 and 4.4, respectively.

4.1 Analysis strategy

The PHOS detector is used to measure energies and positions of produced photons. The minimum-bias trigger is V0AND which requires at least 1 hit on each V0A and V0C. Neutral mesons (π^0 and η) are reconstructed by invariant mass method defined by Eq. 13, which is based on 4-momentum conservation between a particle and its decay products.

$$M_{\gamma\gamma} = \sqrt{2E_1E_2(1-\cos\theta_{12})}, \tag{13}$$

where $E_{1/2}$ is energy of photon1/2, θ_{12} is opening angle between photon1 and photon2. The invariant mass reconstruction is performed over all possible combinations in each event. Raw yields of neutral mesons are obtained by counting histogram entries around 135 MeV/c^2 for π^0 and 547 MeV/c^2 for η respectively. The background is subtracted by mixed-event technique (a first photon is taken from a current event and a second photon is from another event). 4-momentum of particles never conserves in this technique and this gives us only background. Same procedure is performed in M.C. simulation. Since generated particle is known in simulation, an acceptance $\times$ reconstruction efficiency ε can be measured by :

$$\text{acc.} \times \text{rec. efficiency } \varepsilon = \frac{\text{Number of reconstructed particles on PHOS}}{\text{Number of generated particles in } |y| < 0.5 \text{ and } 2\pi \text{ in azimuth}} \tag{14}$$

Finally, a production cross section of particle is given by :

$$E\frac{d^3\sigma}{dp^3} = \frac{1}{2\pi} \times \frac{1}{p_{\rm T}}\frac{dN}{dp_{\rm T}} \times \frac{1}{\Delta y} \times \frac{1}{\varepsilon} \times \frac{1}{L_{\rm int}}, \tag{15}$$

where $\frac{dN}{dp_{\rm T}}$ is transverse momentum-($p_{\rm T}$-)differential raw yield of particle and $L_{\rm int} = \frac{N_{\rm ev}}{\sigma_{\rm pp}^{\rm V0AND}}$ is an integrated luminosity. The cross section of V0AND trigger $\sigma_{\rm pp}^{\rm V0AND} = 51.2 \pm 1.2$ mb and the total inelastic cross section $\sigma_{\rm pp}^{\rm INEL} = 67.6 \pm 0.6$ mb [60] in pp collisions at $\sqrt{s} = 5.02$ TeV. In case of rare-triggered data (e.g. high-energy photon trigger in PHOS), the particle yields have to be further normalized by a trigger rejection factor (RF).

$$\text{RF} = \frac{\text{MB}}{\text{MB \& rare-trigger input}} \tag{16}$$

$$L_{\rm int} = \frac{N_{\rm ev}}{\sigma_{\rm pp}^{\rm V0AND}} \times \text{RF} \tag{17}$$

Once neutral mesons yields are measured in both pp and Pb–Pb collisions, the nuclear modification factor $R_{\rm AA}$ for each particle is measured based on.4.

4.2 Photon identification

There are two types of photon identification cut to clusters measured by PHOS. They are Charged Particle Veto (CPV) and shower shape cut called dispersion cut.

4.2.1 CPV cut

This cut is to reject charged particles. As photon is neutral and can not be tracked, photon hits on PHOS should not match extrapolated tracks from ITS/TPC. Hence, if a distance in the $x - z$ plane between a cluster and an extrapolated track is closer than a certain threshold, the cluster is rejected.

4.2.2 Dispersion cut

This cut is to select electro-magnetic clusters by an elliptic shape of the electro-magnetic shower evolution in $PbWO_4$ crystals. It is characterized by eigenvalues in a cluster [58, 59] :

$$M02\ (\mathrm{cm}) = \frac{1}{2}\left(\sigma_{xx}^2 + \sigma_{zz}^2 + \sqrt{(\sigma_{xx}^2 - \sigma_{zz}^2)^2 + 4\sigma_{xz}^4}\right) \text{ for long axis}$$
$$M20\ (\mathrm{cm}) = \frac{1}{2}\left(\sigma_{xx}^2 + \sigma_{zz}^2 - \sqrt{(\sigma_{xx}^2 - \sigma_{zz}^2)^2 + 4\sigma_{xz}^4}\right) \text{ for short axis,}$$

where $\sigma_{xz}^2 = \langle xz \rangle - \langle x \rangle \langle z \rangle$, $\langle x \rangle = \frac{1}{w_{\mathrm{total}}} \sum_i w_i x_i$ is the weighted average over all cells in a cluster. The weight w_i is given by $w_i = \max(0, 4.5 + \ln(E_i/E))$, where E_i is cell energy at i and $w_{\mathrm{total}} = \sum_i w_i$. Clusters are required to pass a criterion based on correlation between $M02$ and $M20$ as a function of the energy. Especially for clusters at low energy, simple minimum and maximum thresholds to N_{cell} and $M02$ as a function of their energy are imposed, instead of the dispersion cut. N_{cell} is the number of cells in a cluster (i.e. how many cells a cluster consists of). In order to save photon clusters at low energy, these criteria are loose for low energy clusters where the evolution of the electro-magnetic shower is poor.

4.3 Analyses in pp collisions at $\sqrt{s} = 5.02$ TeV

Details of analyses in pp collisions are described here. First, neutral meson reconstruction via two photons were performed. Second, M.C. tuning to reproduce realistic peak parameters and determine efficiency. Then, various cut efficiencies (cluster timing, triggering, feed down from strange hadrons) have been evaluated.

4.3.1 Raw yield extraction

π^0 and η mesons are reconstructed via their two photons decay with invariant mass method. The neutral meson peaks are fitted by Gaussian function and integrated over the mean value $\pm 3\sigma$. Backgrounds are estimated by mixed event technique. Varying fitting ranges, functions and integral ranges are included in systematic uncertainties.

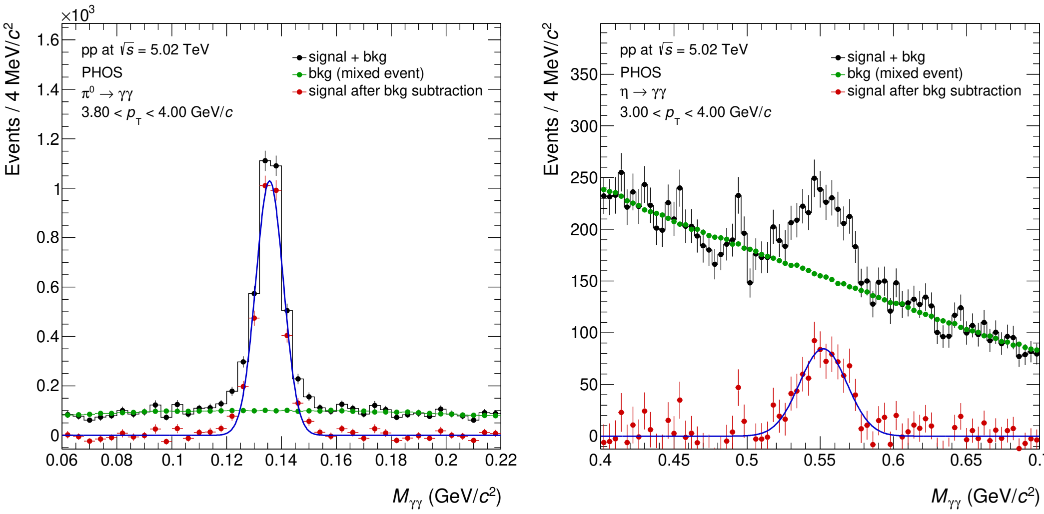

(a) π^0 peak in kINT7 (b) η peak in kINT7

Figure 46: Invariant mass distributions in pp collisions at $\sqrt{s} = 5.02$ TeV (INT7)

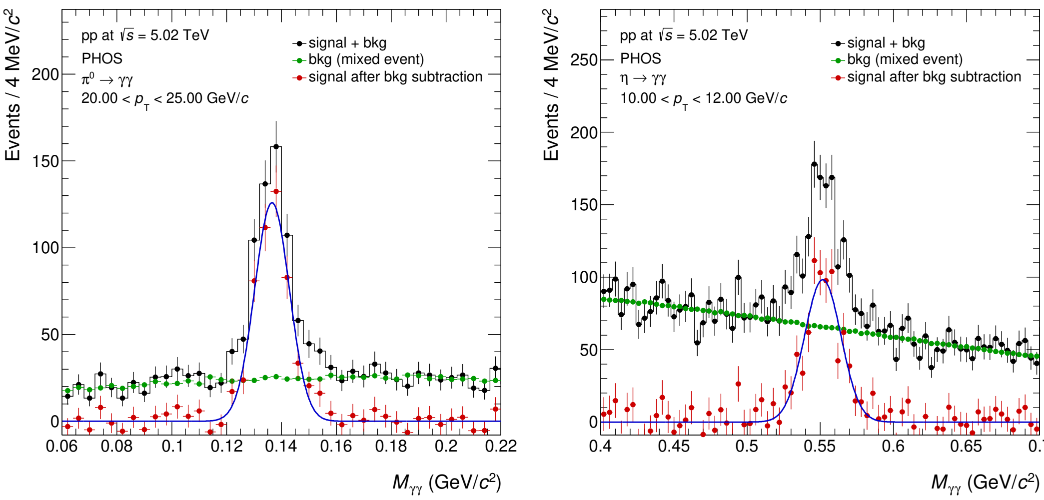

(a) π^0 peak in kPHI7 (b) η peak in kPHI7

Figure 47: Invariant mass distributions in pp collisions at $\sqrt{s} = 5.02$ TeV (PHI7)

Figure 46, 47 are invariant mass distributions for MB and L0 PHOS triggered events respectively. Neutral meson signal are clearly seen. The number of neutral meson signals is obtained by bin-counting on the invariant mass distribution at each p_{T} bin.

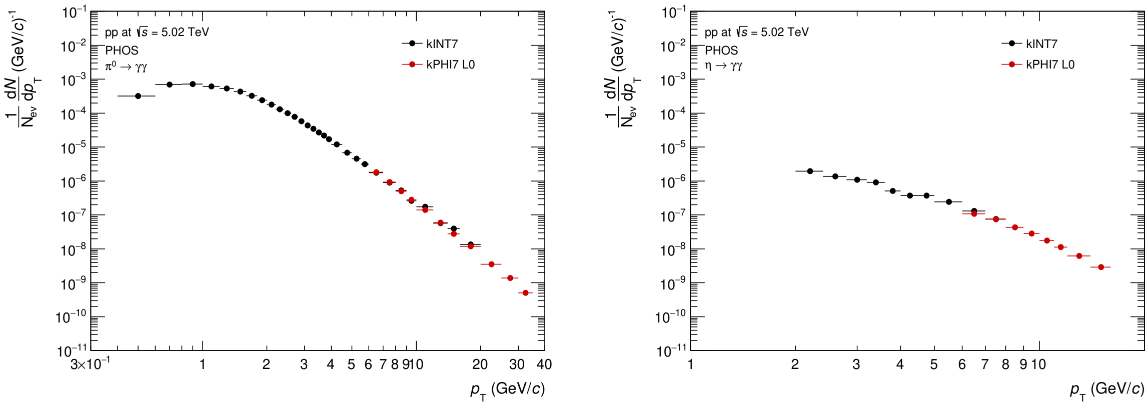

(a) Raw yields of π^0 (b) Raw yields of η

Figure 48: Raw yields of neutral mesons in pp collisions at $\sqrt{s} = 5.02$ TeV

Raw yields are plotted on Figure 48. No PID cut was applied in π^0 signal extraction in pp, while an energy asymmetry cut ($\alpha = \frac{|E_1 - E_2|}{E_1 + E_2} < 0.7$) and CoreDisp 2.5$\sigma$ only in INT7 events were applied for the η meson measurement. As η has heavier mass (547 MeV/c^2) than π^0 mass (135 MeV/c^2), the tighter cut is helpful to extract its signal.

4.3.2 Acceptance × reconstruction efficiency

The efficiency is obtained by M.C. simulation. First, M.C. simulation has to reproduce realistic peak position and width of neutral mesons by tuning energy measurement in M.C.. Figure 49, 50 show good agreement of peak parameters by Gaussian fitting to π^0 and η meson between data and M.C..

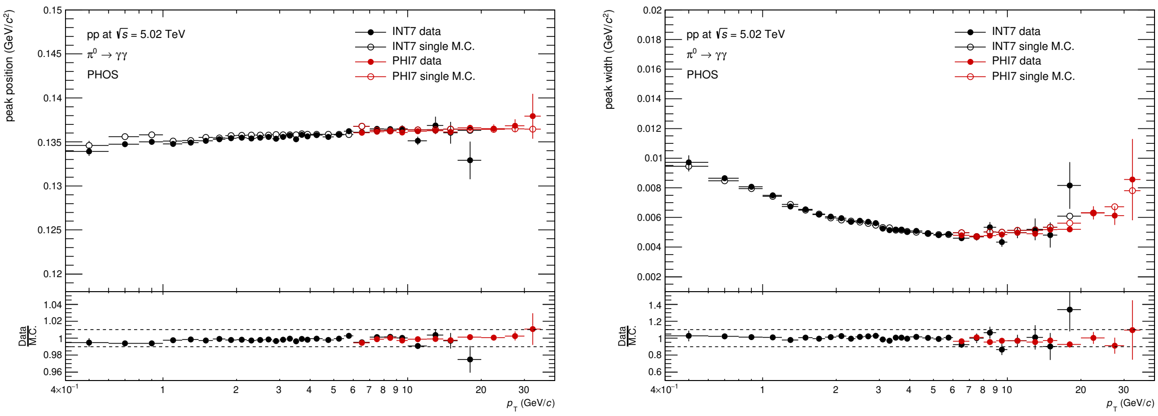

(a) π^0 peak position (b) π^0 peak width

Figure 49: π^0 peak parameters in pp collisions at $\sqrt{s} = 5.02$ TeV

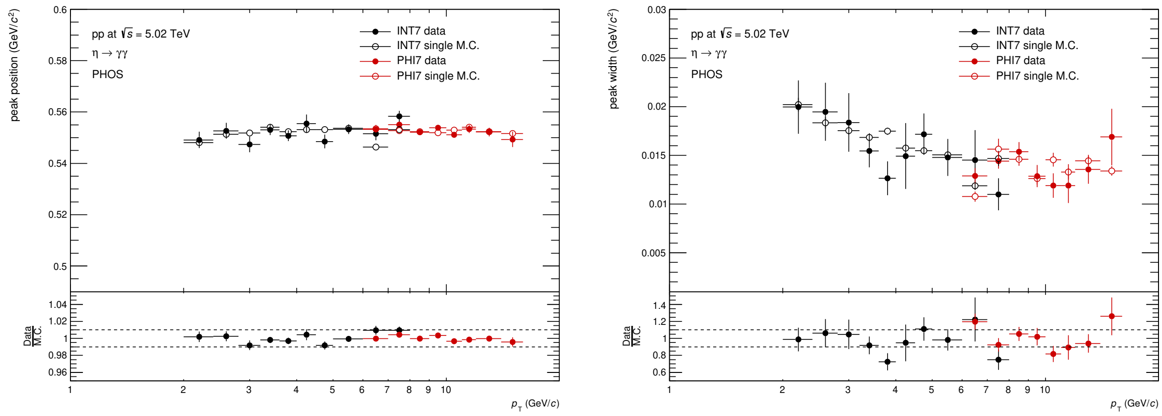

(a) η peak position (b) η peak width

Figure 50: η peak parameters in pp collisions at $\sqrt{s}$ = 5.02 TeV

Once properties of neutral meson peak are reproduced by M.C., acceptance × reconstruction efficiency has been measured based on Eq. 14.

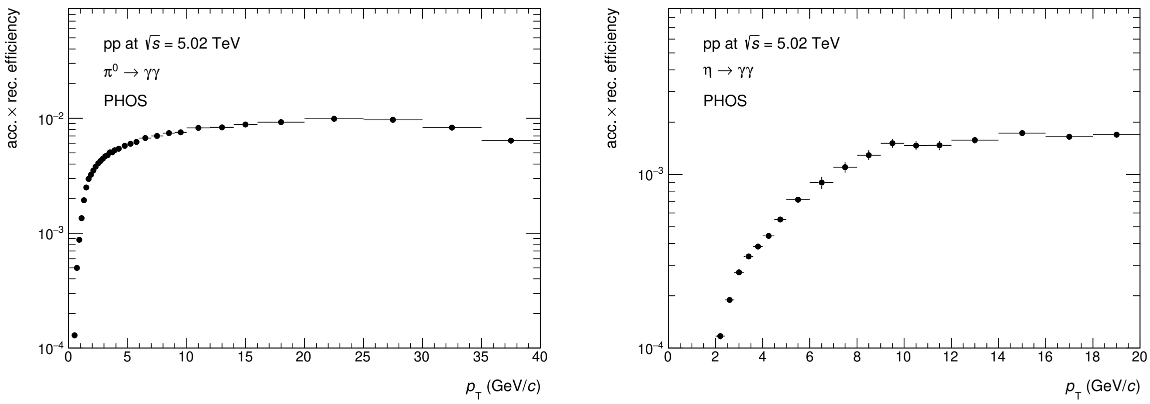

(a) acceptance × reconstruction efficiency of π^0 (b) acceptance × reconstruction efficiency of η

Figure 51: acceptance × reconstruction efficiency of neutral mesons in pp collisions at $\sqrt{s}$ = 5.02 TeV with PHOS

4.3.3 Timing cut

The bunch space of each proton beam bunch was 25 ns during LHC-Run2 operation. Timing cut ($|\mathrm{TOF}_{\mathrm{cluster}}| < 12.5$ ns) was applied at cluster level to reject clusters from other BCs. The timing of a cluster is defined as the timing of a leading cell which has the highest amplitude in APDs. TOF cut efficiency($\varepsilon_{\mathrm{TOF}}$) is defined by :

$$\varepsilon_{\mathrm{TOF}} = \frac{N_{\mathrm{TOF}\ \gamma}^{\mathrm{triggered\ BC}}}{N_{\mathrm{all}\ \gamma}^{\mathrm{triggered\ BC}}}, \quad (18)$$

where $\mathrm{N}_{\mathrm{TOF}\ \gamma}^{\mathrm{triggered\ BC}}$ is the number of photons after TOF cut in the triggered BC and $\mathrm{N}_{\mathrm{all}\ \gamma}^{\mathrm{triggered\ BC}}$ is the number of all photons in the triggered BC respectively. The efficiency is measured by data driven, called tag-and-probe method. This technique is widely applicable for any kinds of efficiency, e.g. trigger efficiency, PID cut efficiency and so on. The first photon is required to pass the timing cut (tagged photon) and reconstructing invariant mass with two photons in same events. If the reconstructed invariant mass is in the π^0 (η) meson signal window, typically $0.12 < M_{\gamma\gamma} < 0.15$ GeV/c^2 ($0.5 < M_{\gamma\gamma} < 0.6$ GeV/c^2), the second photon is called probe photon. Then, the efficiency can be measured with probe photons by :

$$\varepsilon = \frac{\text{The number of probe photons which pass criteria}}{\text{The number of all probe photons}} \tag{19}$$

The drop of TOF efficiency in Figure 52b at $E_{\text{cluster}} > 6$ GeV is due to switching high gain (HG) to low gain (LG) channels in the PHOS readout electronics. Timing resolution is worse in LG, as LG channels have lower gain. Then, the number of photons is corrected by ε_{TOF} as a function of photon energy. Since ε_{TOF} is measured as a function of photon energy, $\frac{1}{\varepsilon^1_{\text{TOF}} \times \varepsilon^2_{\text{TOF}}}$ is necessary at neutral mesons level which is reconstructed from two photons.

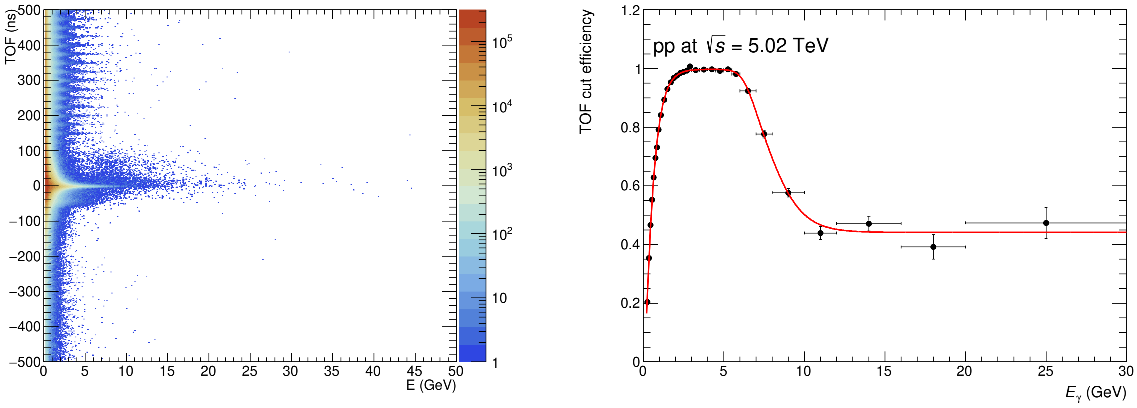

(a) TOF vs. E_{cluster}.

(b) TOF cut efficiency as a function of photon energy.

Figure 52: The cluster timing distribution and TOF cut efficiency

4.3.4 Trigger efficiency

The PHOS trigger allows us to measure high energy photons/electrons efficiently in ALICE. The energy threshold of the PHOS L0 trigger in pp collisions at $\sqrt{s}$ = 5.02 TeV (LHC17pq) period was set to 4 GeV in sum of 4×4 analogue signal (FastOR). The rejection factor is defined by :

$$\text{RF} = \frac{\text{MB}}{\text{MB \& 0PH0 and matched with cluster}}, \tag{20}$$

as shown by The PHOS trigger efficiency is measured in MB events by means of :

$$\varepsilon_{\text{trg}} = \frac{\text{Number of triggered clusters in kINT7}}{\text{Number of all clusters in kINT7}} \tag{21}$$

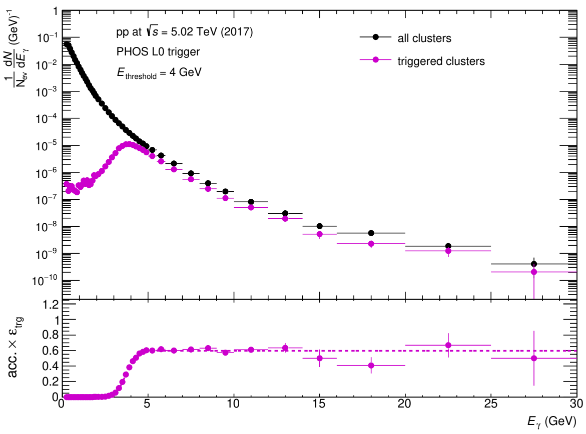

Figure 53: PHOS L0 trigger efficiency in pp collisions at $\sqrt{s} = 5.02$ TeV

Charged particle veto and dispersion cut were applied for both nominator and denominator to get high photon purity. The trigger efficiency in pp collisions at $\sqrt{s}$ = 5.02 TeV (LHC17pq) reaches 0.6 above the energy threshold. For the neutral meson reconstruction, at least one triggered cluster (logical-OR) is required in this analysis. The trigger efficiency for π^0 and η is $\varepsilon^{\mathrm{OR}}_{\mathrm{trg}} = \varepsilon^{1}_{\mathrm{trg}} + \varepsilon^{2}_{\mathrm{trg}} - \varepsilon^{1}_{\mathrm{trg}} \times \varepsilon^{2}_{\mathrm{trg}}$.

4.3.5 Feed down correction from strange hadrons

π^0 from strange hadrons decays such as $K^0_S \to \pi^0\pi^0$ (BR = 30.69%, $c\tau$ = 2.7 cm) and $\Lambda \to n\pi^0$ (BR = 35.8 %, $c\tau$ = 7.9 cm (negligible)) contribute the total number of π^0, while π^0 from primary interaction is focused on. Hence, they have to be subtracted from the total number of π^0. For this study, M.C. simulation with PYTHIA8 event generator was used to estimate this contribution. However, it is known that PYTHIA event generator does not reproduce realistic $K^\pm/\pi^\pm$ ratio. Therefore, re-weighting to K^0_S spectrum is necessary. Since $K^\pm/\pi^\pm$ ratio in pp collisions at $\sqrt{s}$ = 5.02 TeV has not been published as of January 31 2019, $K^\pm/\pi^\pm$ ratio in pp collisions at $\sqrt{s}$ = 2.76 TeV [61, 62] are taken as a reference. $K^\pm/\pi^\pm$ ratio does not depend on collision energy at ~TeV energy region [61, 63]. The feed down factor is defined as :

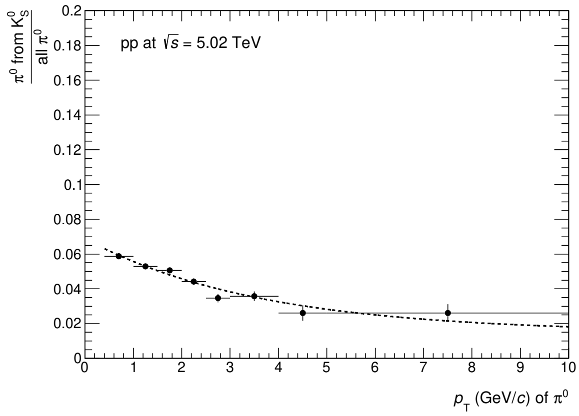

Figure 54: Feed down factor for π^0 from K^0_S in pp collisions at $\sqrt{s}$ = 5.02 TeV

$$\mathrm{FD} = \frac{\text{Number of reconstructed } \pi^0 \text{ from } K^0_S}{\text{Number of all reconstructed } \pi^0} \tag{22}$$

Figure 55 shows $K^\pm/\pi^\pm$ ratio before and after the re-weighting procedure. The FD factor is plotted on Figure 54, which is about 6% at the maximum and decreases with p_{T}.

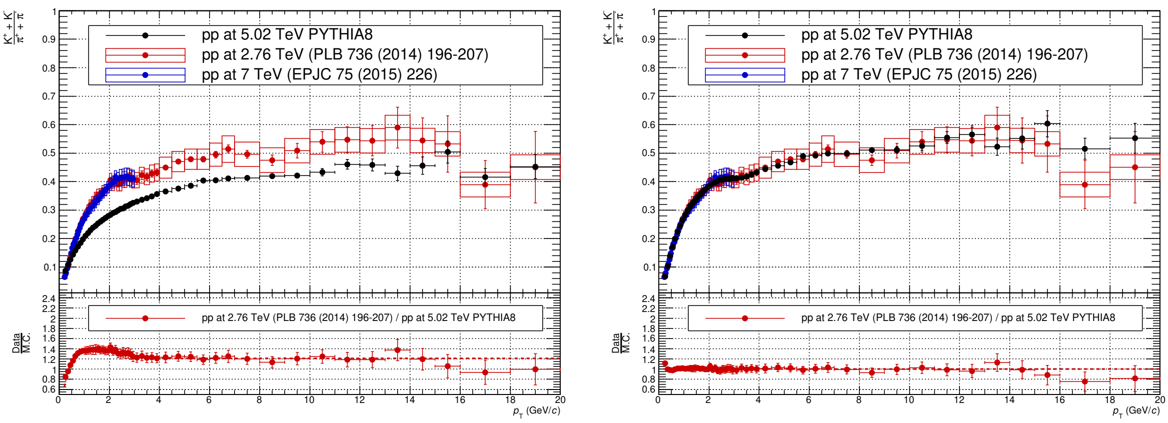

(a) $K^\pm/\pi^\pm$ ratio before re-weighting. (b) $K^\pm/\pi^\pm$ ratio after re-weighting.

Figure 55: $K^\pm/\pi^\pm$ ratio in PYTHIA8

4.4 Analyses in Pb–Pb collisions at $\sqrt{s_{\mathrm{NN}}} = 5.02$ TeV

Details of analyses in Pb–Pb collisions are described in this section. They are generally the same as in pp collisions. In addition to analyses in pp, events are classified by multiplicity on the VZERO detector called "centrality class". The centrality at 0 % indicates the highest multiplicity class and the higher value of centrality, the lower multiplicity class. There were two active L1 PHOS triggers in Pb–Pb collisions recorded in 2015. One is CINT7PHH, high energy threshold at 8 GeV for all centrality classes. The other is CPER7PHM, medium energy threshold at 4 GeV for peripheral collisions (centrality > 60%). As shown by Figure 56, the centrality distribution in Minimum-Bias events (CINT7) is well calibrated and flat. However, they are biased in PHOS triggered data. It is understood that the probability to detect a high energy photon under the high multiplicity environment is higher than that in peripheral collisions, because the number of produced photons is also large in central collisions. Trigger rejection factors for L1H and L1M are biased, too.

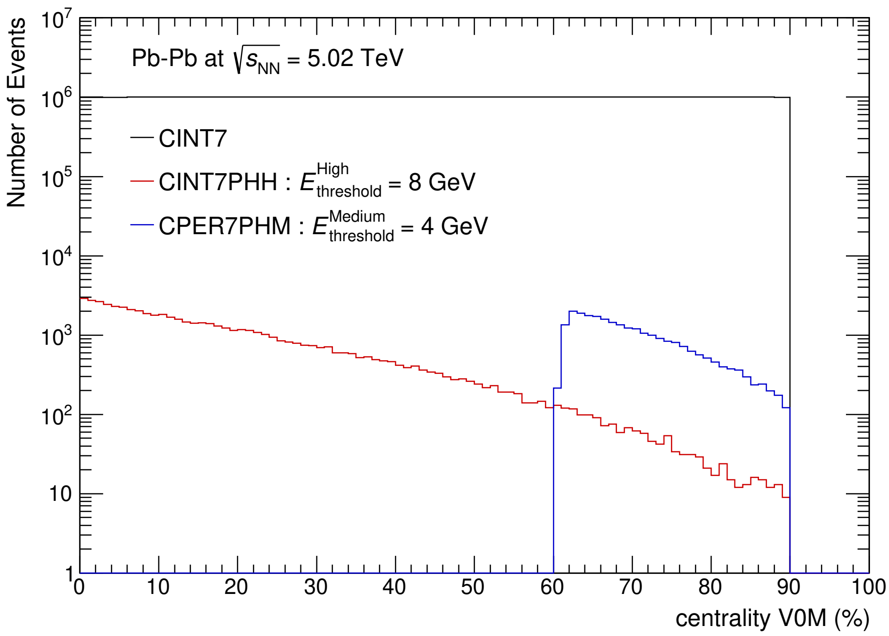

Figure 56: Centrality V0M distributions in Pb–Pb collisions at $\sqrt{s_{\mathrm{NN}}} = 5.02$ TeV (2015)

4.4.1 Raw yield extraction

Figure 57, 58 are invariant mass distributions for MB and L1 PHOS triggered events respectively. Neutral meson signal are clearly seen in all centrality classes. The number of neutral meson signals is obtained by bin-counting on the invariant mass distribution at each p_{T} bin. Raw yields are plotted on Figure 59, 60 in different centrality classes. Both CPV and core-dispersion cuts were applied to clusters in Pb–Pb collisions. Furthermore, energy asymmetry $\alpha = \frac{|E_1 - E_2|}{E_1 + E_2} < 0.8$ for π^0 and $\alpha < 0.7$ for η mesons were also applied.

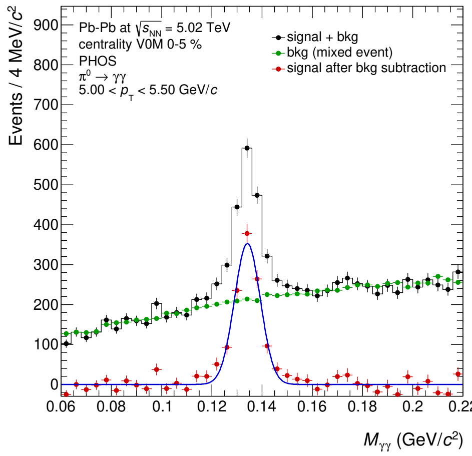

(a) π^0 peak in centrality 0-5 %

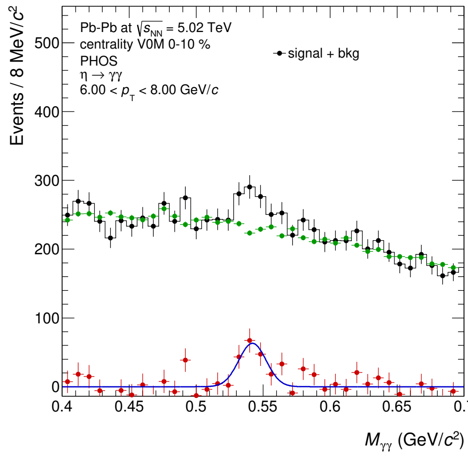

(b) η peak in centrality 0-10 %

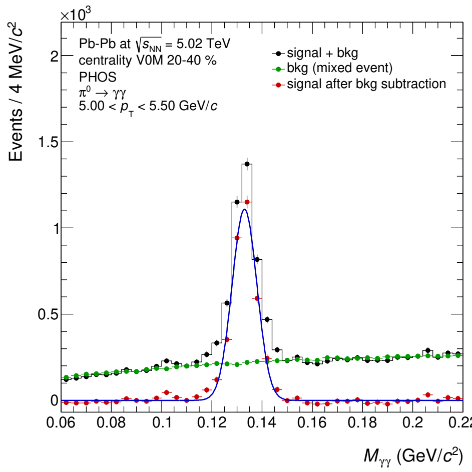

(c) π^0 peak in centrality 20-40 %

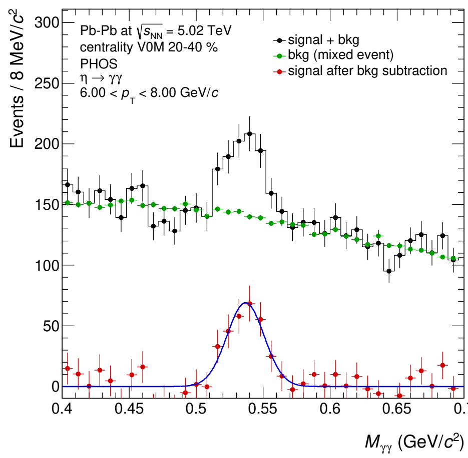

(d) η peak in centrality 20-40 %

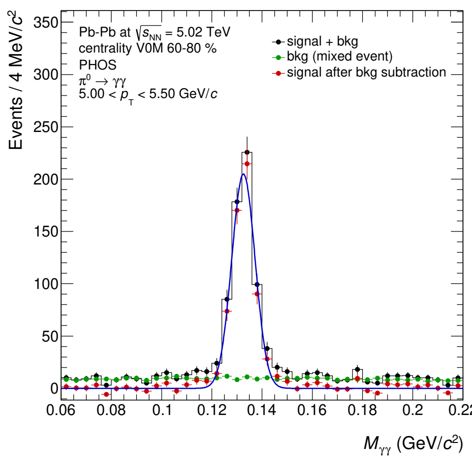

(e) π^0 peak in centrality 60-80 %

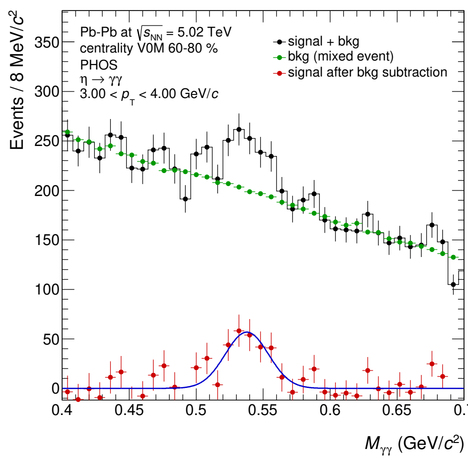

(f) η peak in centrality 60-80 %

Figure 57: Invariant mass distributions in Pb–Pb collisions at $\sqrt{s_{NN}} = 5.02$ TeV (INT7)

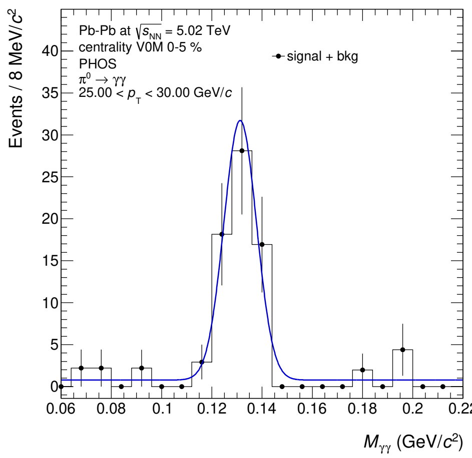

(a) π^0 peak in centrality 0-5 %

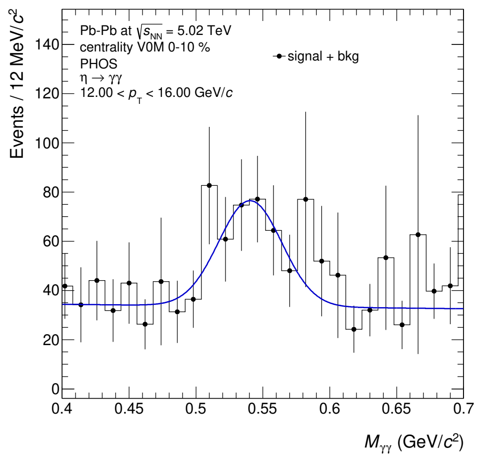

(b) η peak in centrality 0-10 %

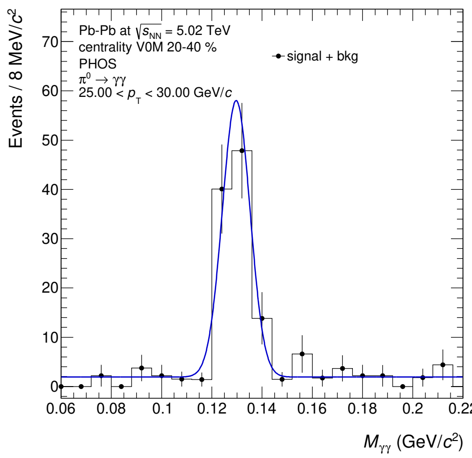

(c) π^0 peak in centrality 20-40 %

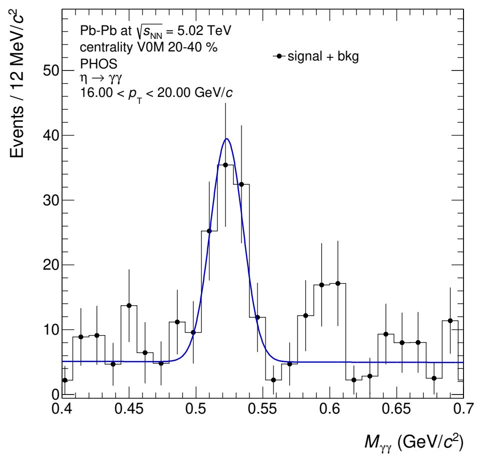

(d) η peak in centrality 20-40 %

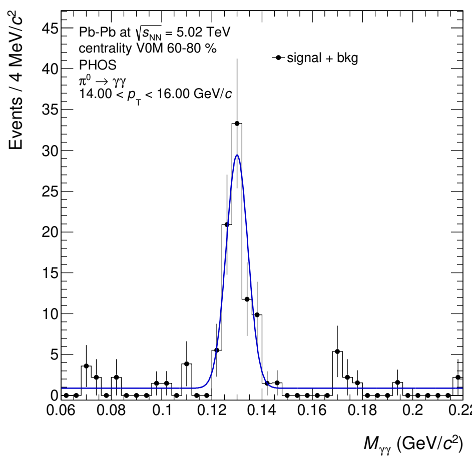

(e) π^0 peak in centrality 60-80 %

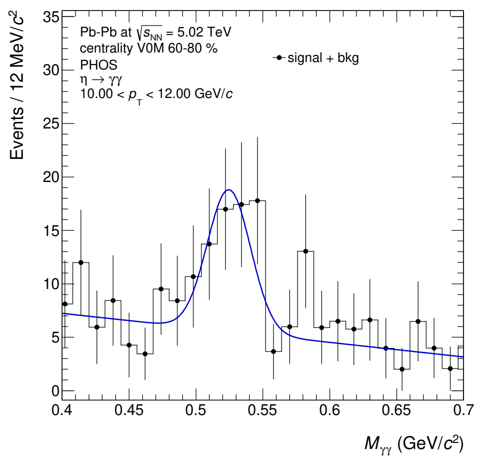

(f) η peak in centrality 60-80 %

Figure 58: Invariant mass distributions in Pb–Pb collisions at $\sqrt{s_{\mathrm{NN}}} = 5.02$ TeV (PHI7)

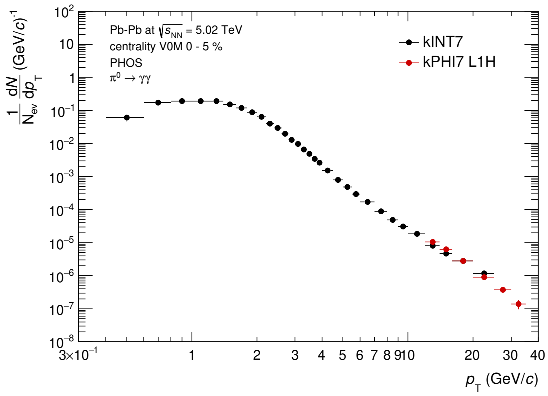

(a) centrality 0-5 %

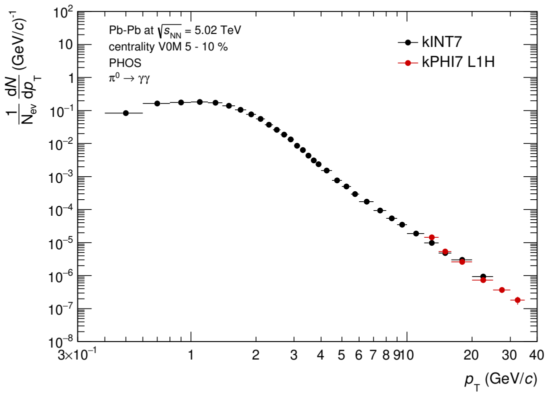

(b) centrality 5-10 %

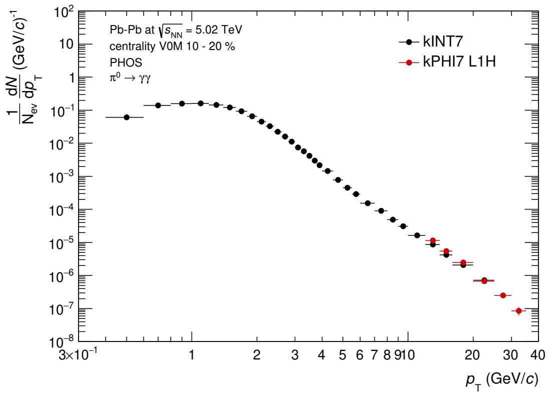

(c) centrality 10-20 %

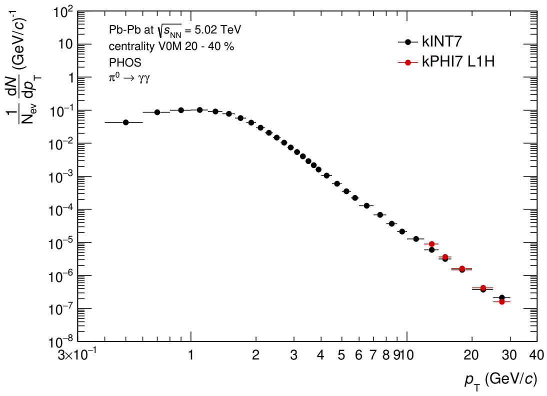

(d) centrality 20-40 %

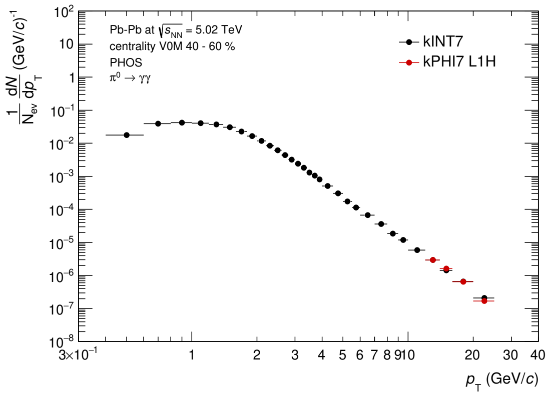

(e) centrality 40-60 %

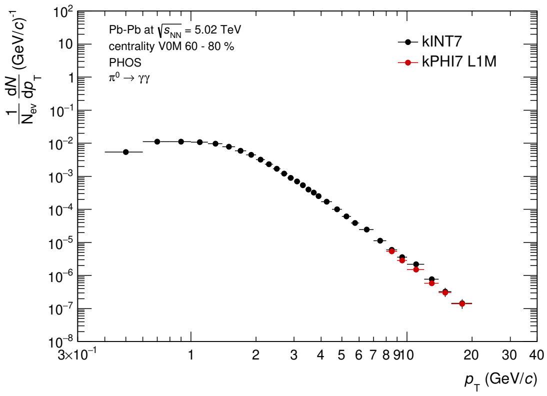

(f) centrality 60-80 %

Figure 59: Raw yields of π^0 in Pb–Pb collisions at $\sqrt{s_{NN}} = 5.02$ TeV

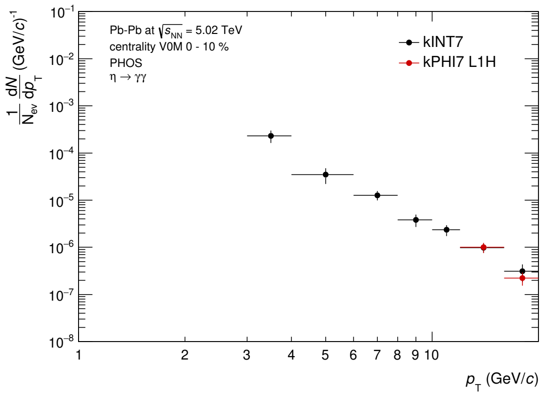

(a) centrality 0-10 %

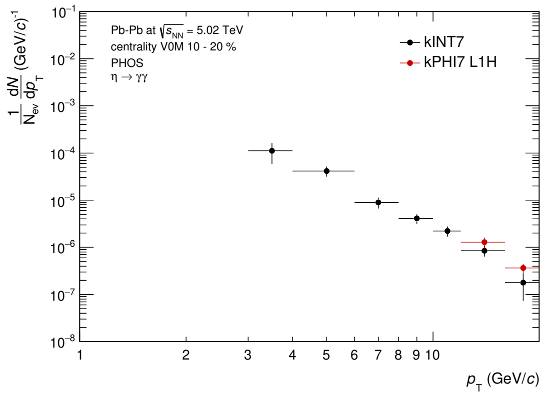

(b) centrality 10-20 %

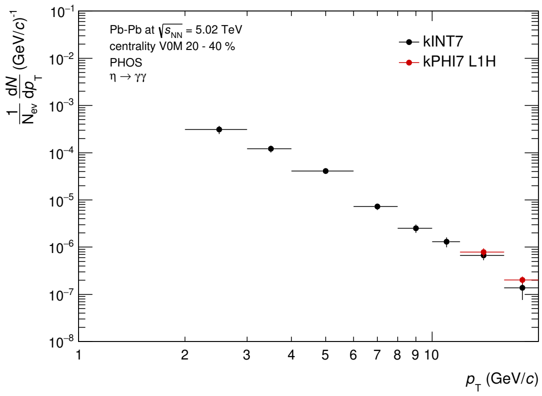

(c) centrality 20-40 %

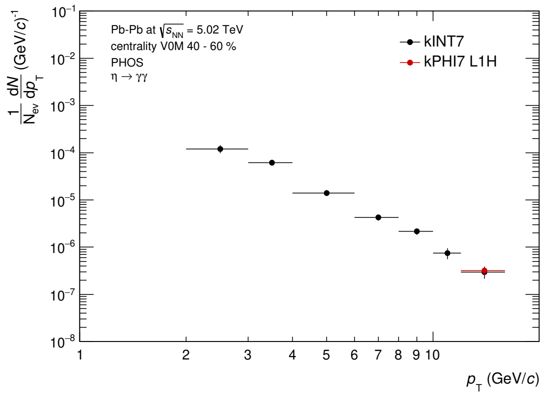

(d) centrality 40-60 %

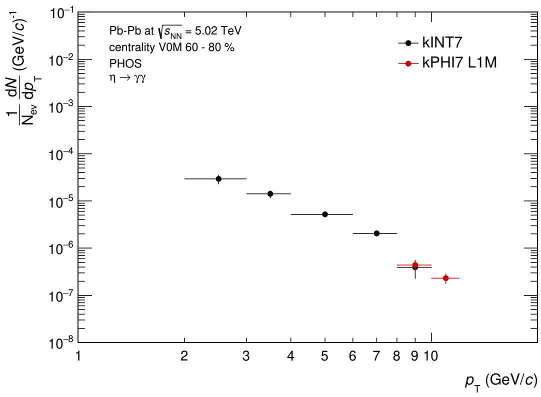

(e) centrality 60-80 %

Figure 60: Raw yields of η in Pb–Pb collisions at $\sqrt{s_{NN}} = 5.02$ TeV

4.4.2 Acceptance × reconstruction efficiency

Due to the extremely high charged particle multiplicity $dN_{\rm ch}/d\eta \approx O(10^3)$ [64, 65] in central Pb–Pb collisions, the reconstruction efficiency for photons and neutral mesons is influenced and centrality-dependent. In order to take high multiplicity environment into account, the efficiency in Pb–Pb collisions is obtained by using embedding technique. The main idea of embedding technique is to merge real data as underlying events (UE) with events from single particle simulation (π^0, η and γ) and to reconstruct data again. This allows us to study how clusters are modified under the realistic high multiplicity environment. The general procedure is following :

1. embed 1 simulated particle per 1 underlying event.
2. cell information in both UE and simulation are inversely calibrated to ADC values from cell energy. At this step, global energy scale and non-linear response of energy measurement in simulation is also inversely applied.
3. merge all cells at ADC level.
4. clusterize merged cells by the same clustering algorithm.

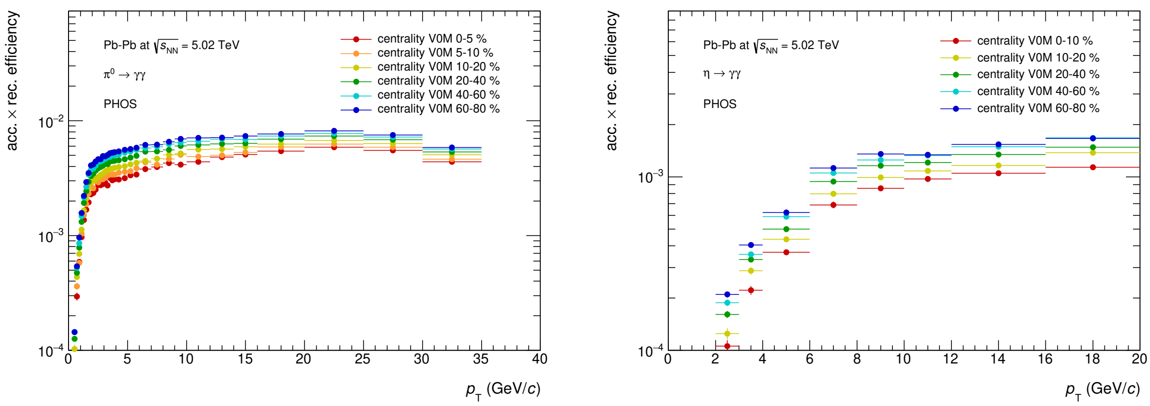

(a) acceptance × reconstruction efficiency of π^0 (b) acceptance × reconstruction efficiency of η

Figure 61: acceptance × reconstruction efficiency of neutral mesons in Pb–Pb collisions at $\sqrt{s_{\rm NN}}$ = 5.02 TeV with PHOS

As well as analyses in pp, M.C. simulation has to reproduce realistic peak position and width of neutral mesons. To avoid overlapping effect under high multiplicity environment, π^0 peak parameters were tuned in peripheral collisions. Figure 62, 63, 64, 65 are the comparison of peak parameters for π^0 and η between data and embedding M.C.. Peak parameters are in good agreement in peripheral collisions, while 1% of discrepancy in peak position is found in central collisions. The global energy scale and the non-linearity response of energy measurement in M.C. are fully detector response and should not depend on event multiplicity. Therefore, $\Delta E/E \approx 0.01$ in central collisions is attributed to an additional systematic uncertainty of the global energy scale.

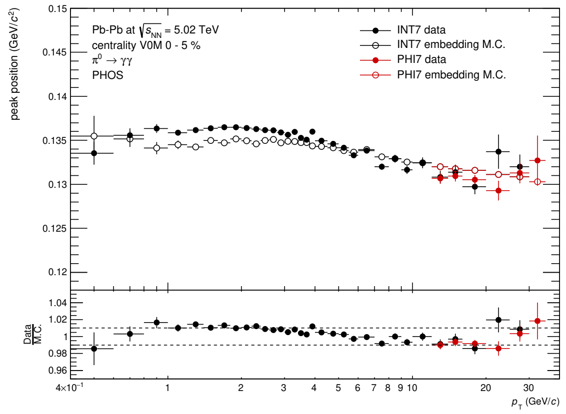

(a) centrality 0-5 %

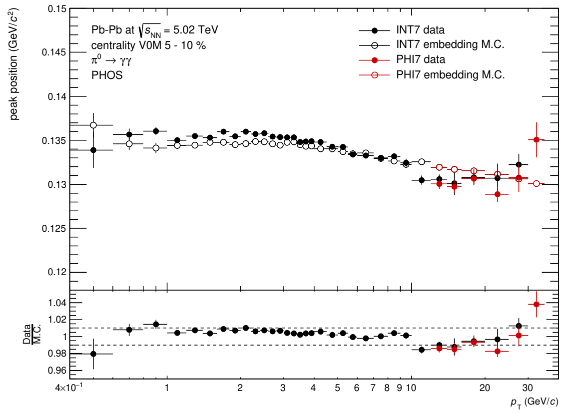

(b) centrality 5-10 %

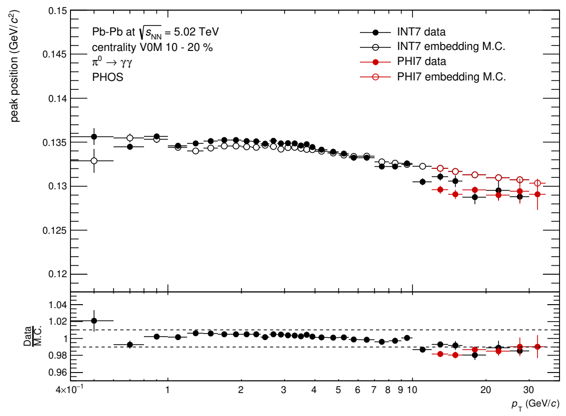

(c) centrality 10-20 %

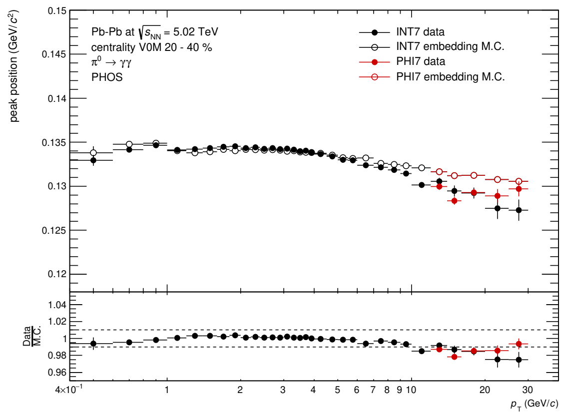

(d) centrality 20-40 %

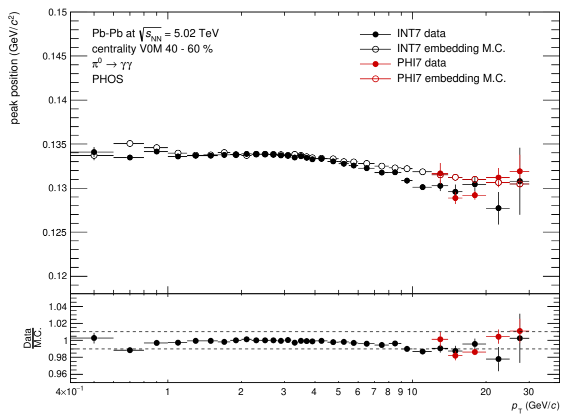

(e) centrality 40-60 %

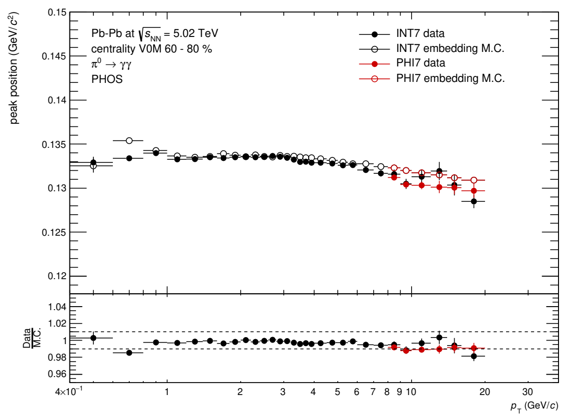

(f) centrality 60-80 %

Figure 62: π^0 peak position in Pb–Pb collisions at $\sqrt{s_{\rm NN}} = 5.02$ TeV for different centrality classes

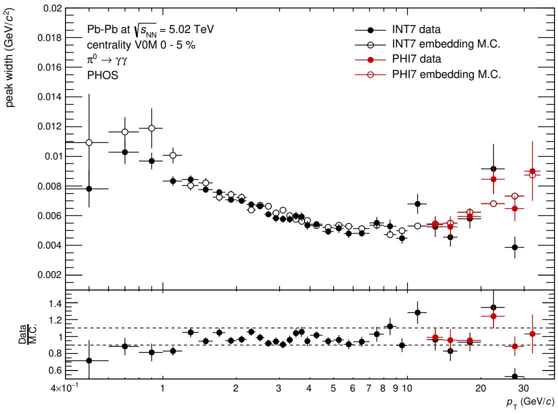

(a) centrality 0-5 %

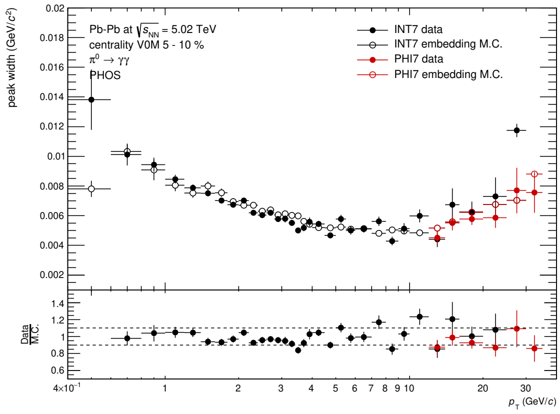

(b) centrality 5-10 %

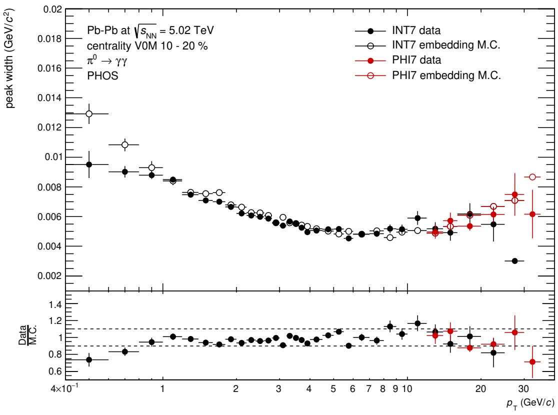

(c) centrality 10-20 %

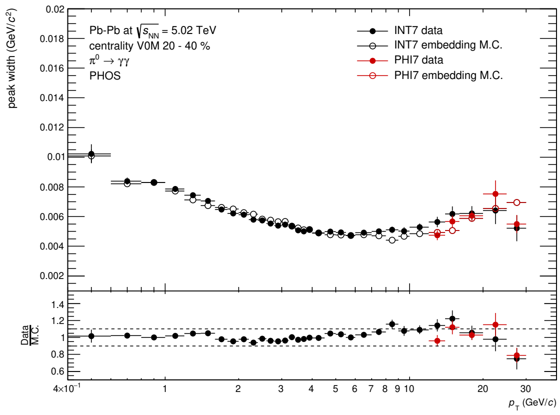

(d) centrality 20-40 %

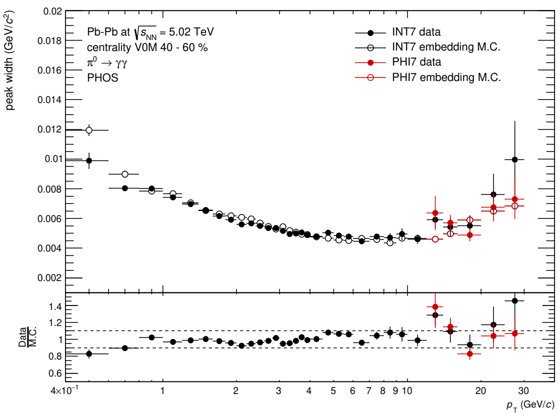

(e) centrality 40-60 %

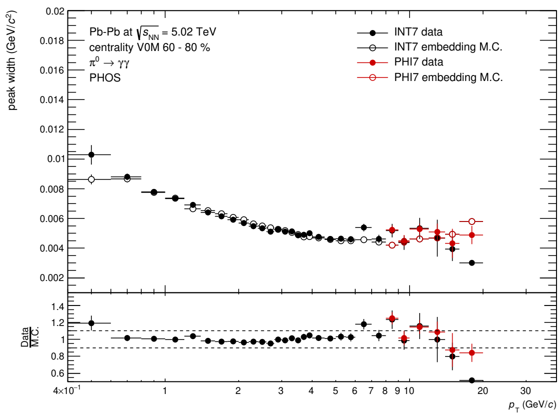

(f) centrality 60-80 %

Figure 63: π^0 peak width in Pb–Pb collisions at $\sqrt{s_{NN}}$ = 5.02 TeV for different centrality classes

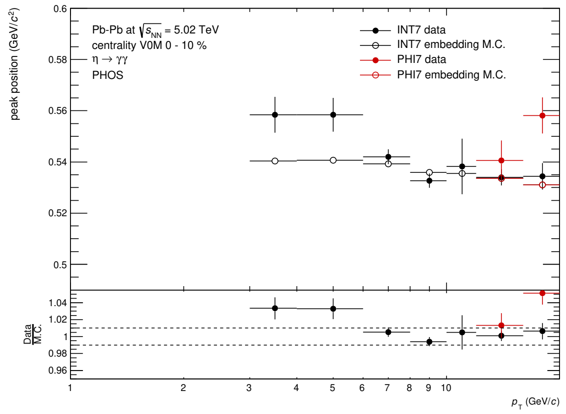

(a) centrality 0-10 %

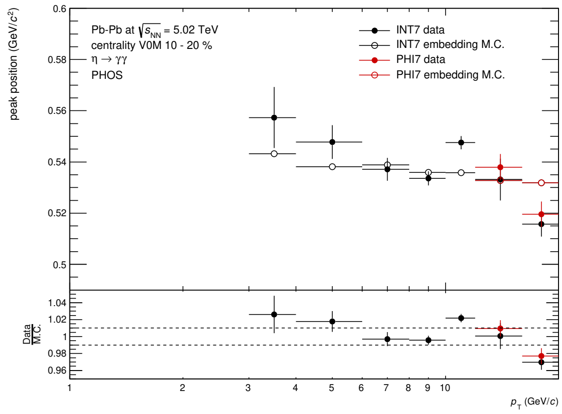

(b) centrality 10-20 %

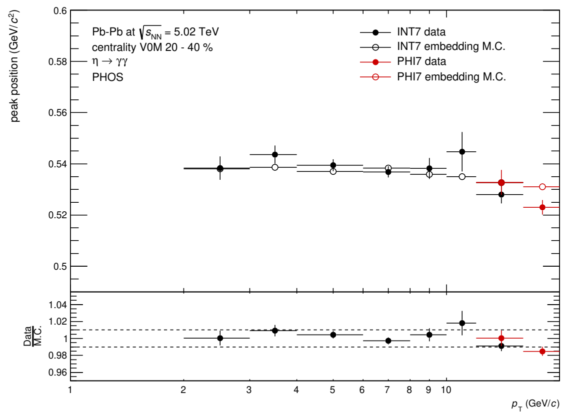

(c) centrality 20-40 %

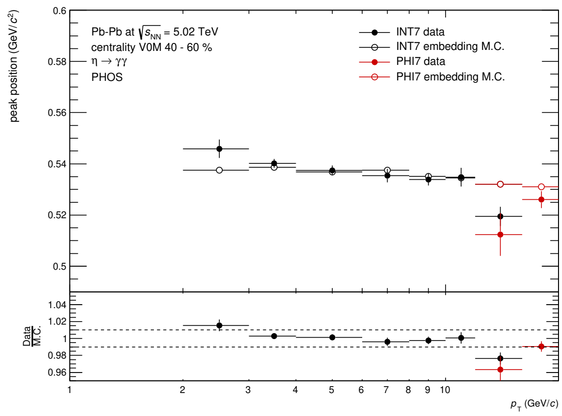

(d) centrality 40-60 %

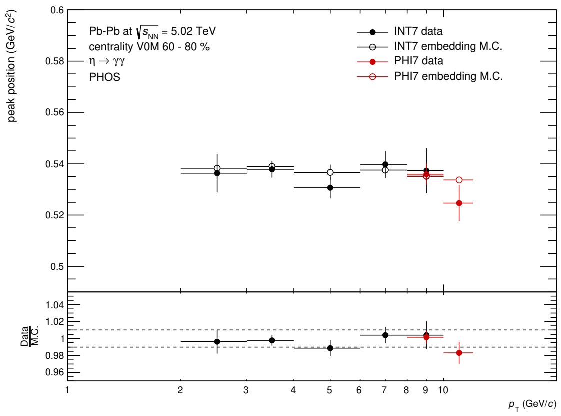

(e) centrality 60-80 %

Figure 64: η peak position in Pb–Pb collisions at $\sqrt{s_{\rm NN}}$ = 5.02 TeV for different centrality classes

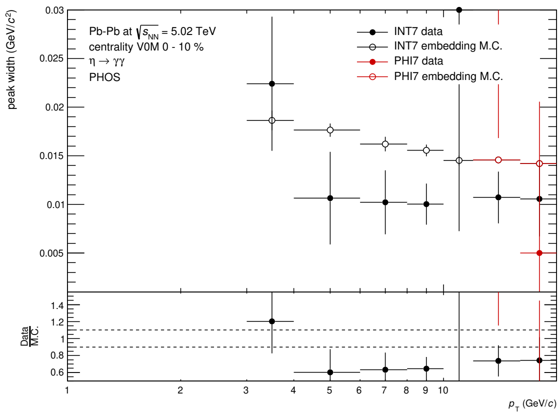

(a) centrality 0-10 %

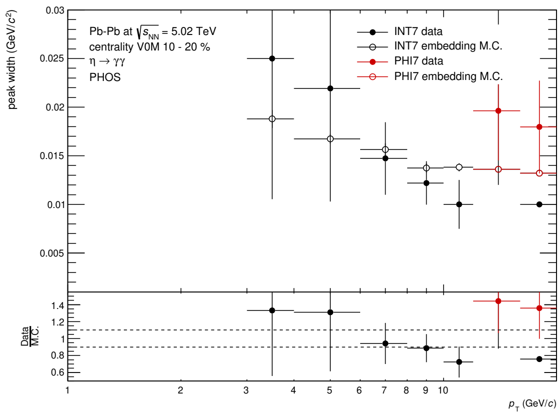

(b) centrality 10-20 %

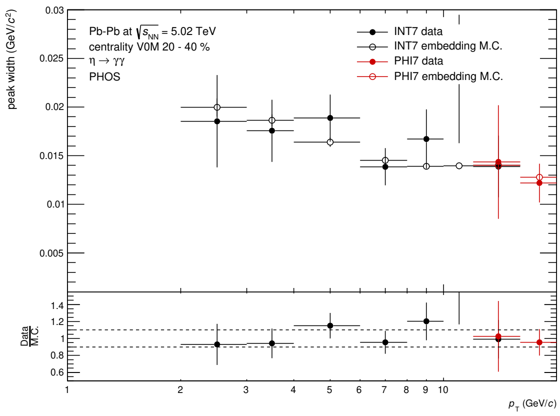

(c) centrality 20-40 %

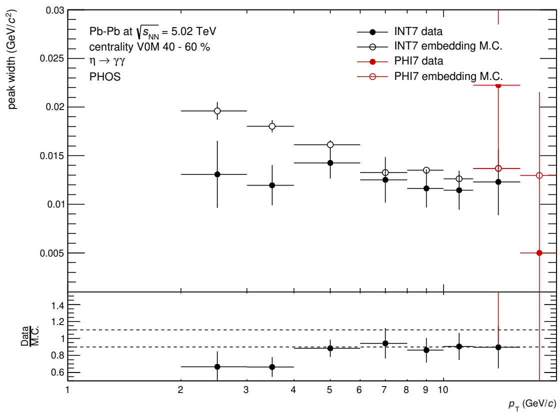

(d) centrality 40-60 %

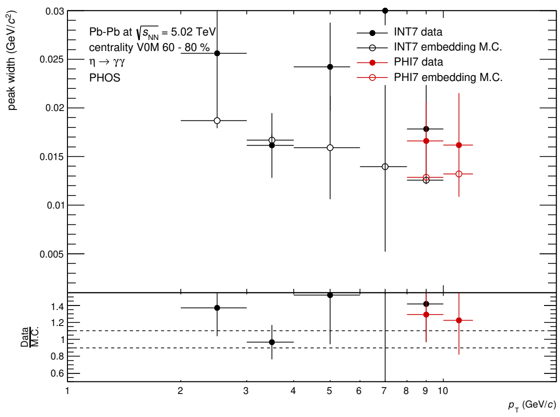

(e) centrality 60-80 %

Figure 65: η peak width in Pb–Pb collisions at $\sqrt{s_{\mathrm{NN}}}$ = 5.02 TeV for different centrality classes

4.4.3 Timing cut

The general procedure is the same as in pp, but the bunch space was 100/150/175/225 ns in Pb–Pb collisions (2015). So, the timing cut for clusters is $|\mathrm{TOF}| < 50$ ns. This wide time window leads higher TOF cut efficiency than one in pp. The drop of TOF efficiency in Figure 66b at $E_{\mathrm{cluster}} > 6$ GeV is due to switching high gain (HG) to low gain (LG) channels in the PHOS readout electronics.

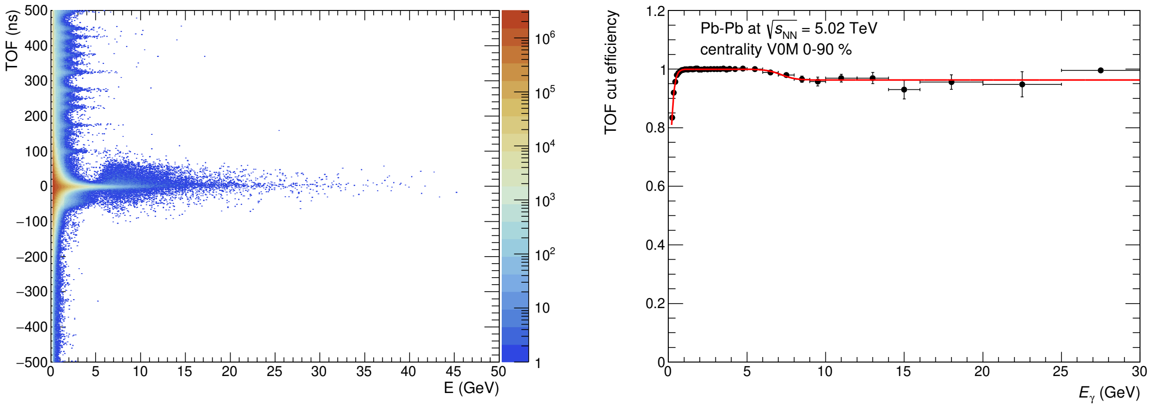

(a) TOF vs. E_{cluster}. (b) $\varepsilon_{\mathrm{TOF}}$ as a function of photon energy.

Figure 66: Timing distribution of clusters and TOF cut efficiency

4.4.4 Trigger efficiency

There were two active L1 PHOS triggers in Pb–Pb collisions recorded in 2015. One is CINT7PHH, high energy threshold at 8 GeV for all centrality classes. The other is CPER7PHM, medium energy threshold at 4 GeV for peripheral collisions (centrality > 60%). As the rejection factor strongly depends on centrality (Figure 67a), this bias was also taken into account for the event normalization. The trigger efficiency has a plateau region at 0.45 above the threshold shown by Figure 67b. The rejection factor and trigger efficiency are plotted for centrality 0-90 %, because they have been measured in MB events. This method is available, since all fired triggers information is stored even in MB events.

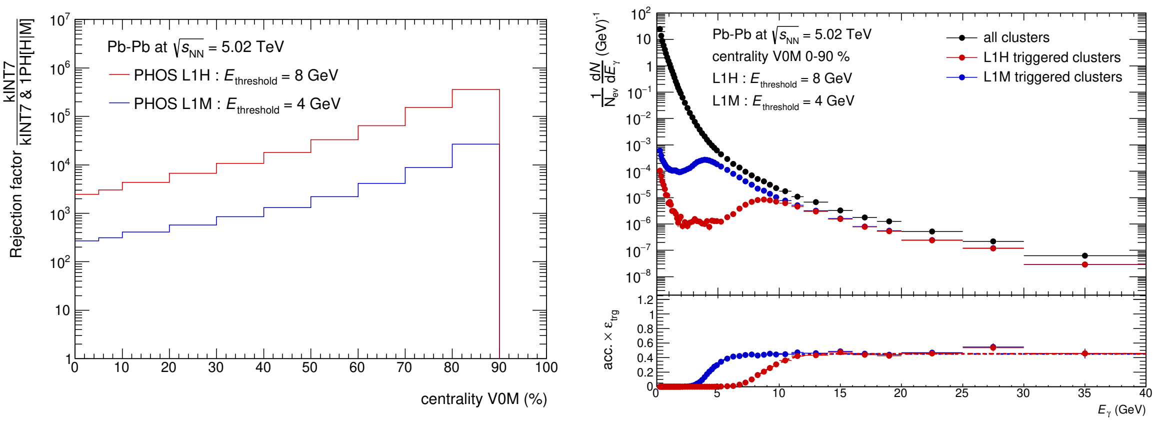

(a) The rejection factor vs. centrality (b) PHOS L1 triggers efficiencies

Figure 67: PHOS L1 triggers performance in Pb–Pb collisions at $\sqrt{s_{\mathrm{NN}}} = 5.02$ TeV

4.4.5 Feed down correction from strange hadrons

HIJING event generator was used to estimate feed down in Pb–Pb collisions. The re-weighting to K_S^0 spectrum is necessary, because it is also known that HIJING does not reproduce realistic $K^{\pm}/\pi^{\pm}$ ratio. $K^{\pm}/\pi^{\pm}$ ratio in Pb–Pb collisions at $\sqrt{s} = 2.76$ TeV [61] are taken as a reference. Figure 69, 70 show $K^{\pm}/\pi^{\pm}$ ratio before and after the re-weighting procedure. The FD factor in different centrality classes is plotted on Figure 68. It is about 11% at the maximum in central $(0-5\%)$ collisions and becomes smaller in peripheral $(60-80\%)$ collisions.

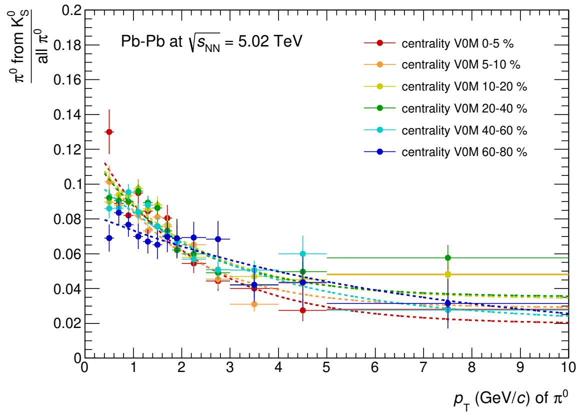

Figure 68: Feed down factor for π^0 from K_S^0 in Pb–Pb collisions at $\sqrt{s_{\mathrm{NN}}} = 5.02$ TeV

4.5 Combining MB and PHOS triggered data

Neutral meson spectra have been measured independently in minimum bias data and PHOS triggered data. Finally, they have been combined by the weighted average described in [66]. Since systematic uncertainties of global energy scale, PID, material budget, feed down in case of π^0 and acceptance of detector are common between minimum bias and PHOS triggered data, quadratic sum of uncertainties of yield extraction, TOF in INT7, trigger efficiency in PHI7 and statistical uncertainty are used as weights. The weighted average is defined as :

$$\hat{\mu} = \frac{1}{w} \sum_{i}^{n} w_i y_i, \tag{23}$$

where $w_i = \frac{1}{\sigma_i^2}$ and $w = \sum_i^n w_i$. The standard deviation of $\hat{\mu}$ is $\frac{1}{\sqrt{w}}$.

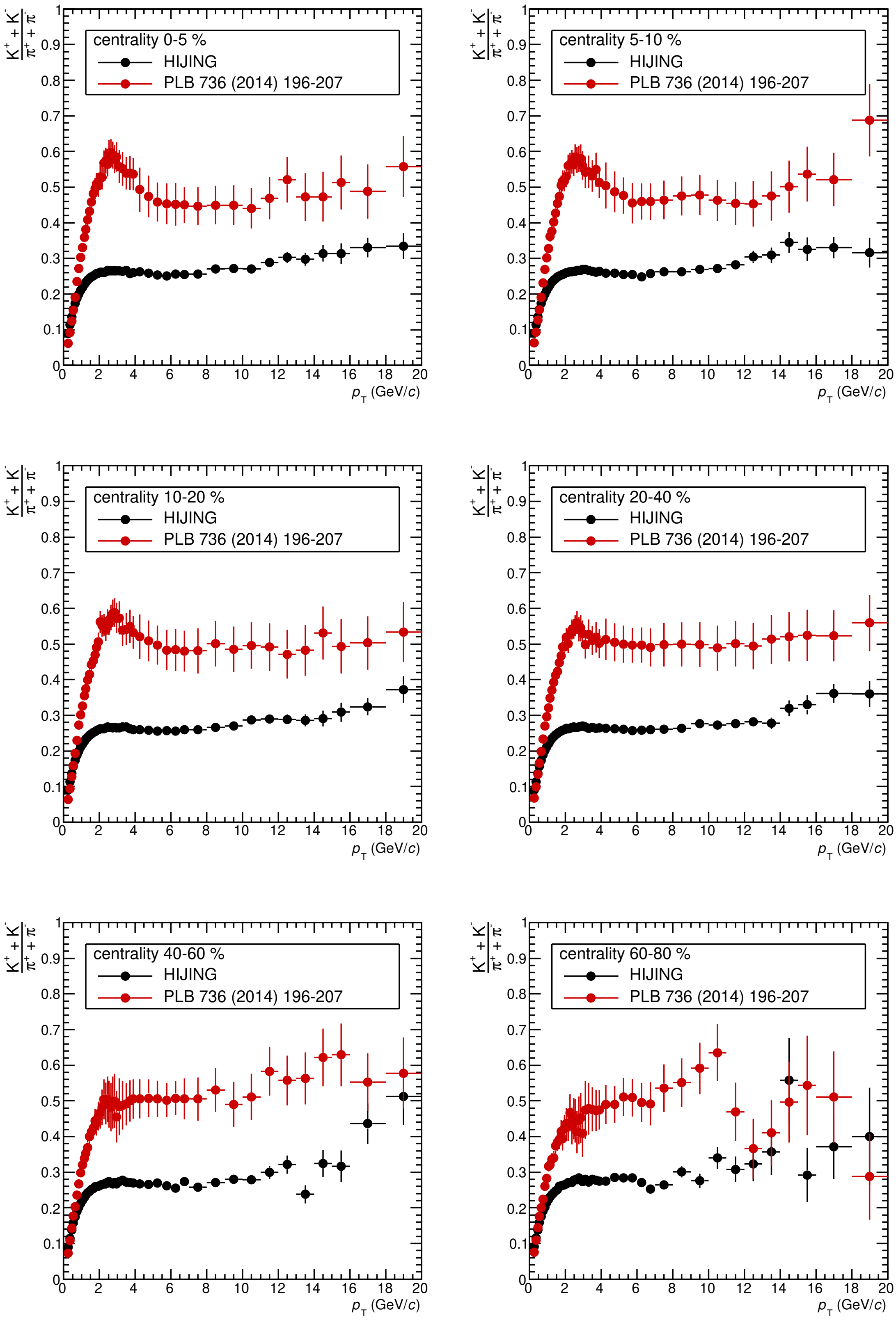

Figure 69: $K^{\pm}/\pi^{\pm}$ ratio in M.C. before re-weighting.

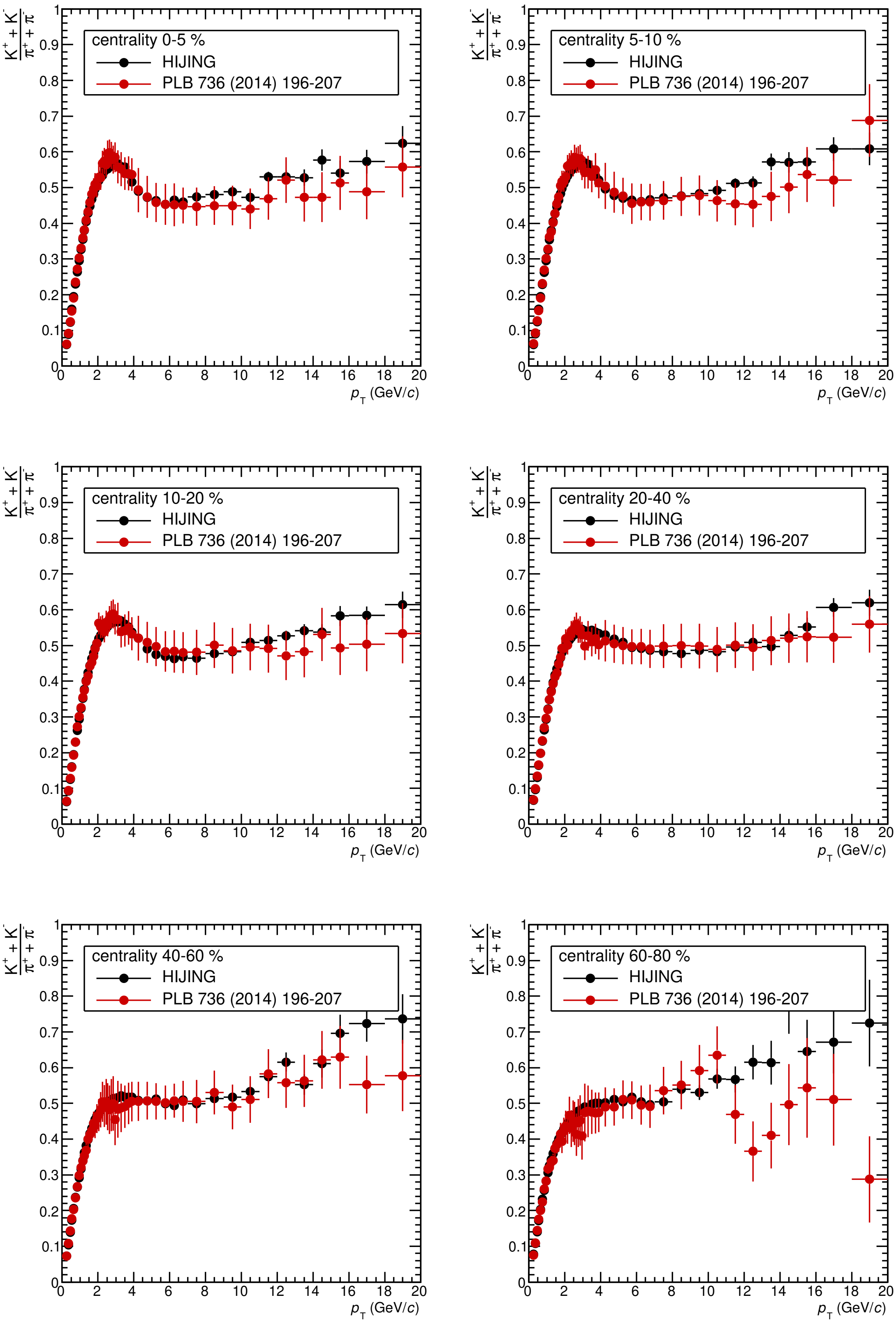

Figure 70: $K^{\pm}/\pi^{\pm}$ ratio in M.C. after re-weighting.

5 Systematic uncertainties for neutral mesons

5.1 Yield extraction

A systematic uncertainty of yield extraction was estimated by varying fitting functions, fitting ranges and integral regions. In total, 24 combinations were performed for each neutral mesons. The relative systematic uncertainty of the yield extraction is defined as standard deviation/mean value of 24 samples.

- Fitting function for signal : Gaussian/CrystalBall [67]
- Fitting function for background : polynomial 1/2
- Fitting ranges for π^0 : [0.06,0.22], [0.04,0.20], [0.08,0.24] GeV/c^2
- Fitting ranges for η : [0.4,0.7], [0.35,0.65], [0.45,0.75] GeV/c^2
- Integral region : [-3σ,+3σ], [-2σ,+2σ] around the peak

5.2 Global energy scale

The global energy scale was evaluated by energy to momentum ratio E/p of electrons (positrons) in data and M.C.. Criteria for $e^{\pm}$ identification are $-2 < \mathrm{n}\sigma_e < 3$ in dE/dx measured by TPC and matched with a PHOS cluster which pass dispersion cut (2.5σ). Here, the nσ_e represents accepted deviation in unit of standard deviation from the dE/dx value expected for the electron signal. Figure.71 shows electron E/p reaches 1 at high energy and is well reproduced by M.C.. According to this study, the discrepancy between data and M.C. in $E/p\pm$ 0.5% is assigned to an uncertainty of energy scale. The p_{T} of neutral meson is shifted by $\Delta p_{\mathrm{T}}/p_{\mathrm{T}} = \pm 0.005$ in TCM function (or Hagedorn function for η meson in pp) fitting, and the ratio to the function with $\Delta p_{\mathrm{T}}/p_{\mathrm{T}} = 0$ was taken. The larger side is assigned to the final systematic uncertainty of particle yields due to the global energy scale. In case of Pb–Pb collisions, the energy scale uncertainty

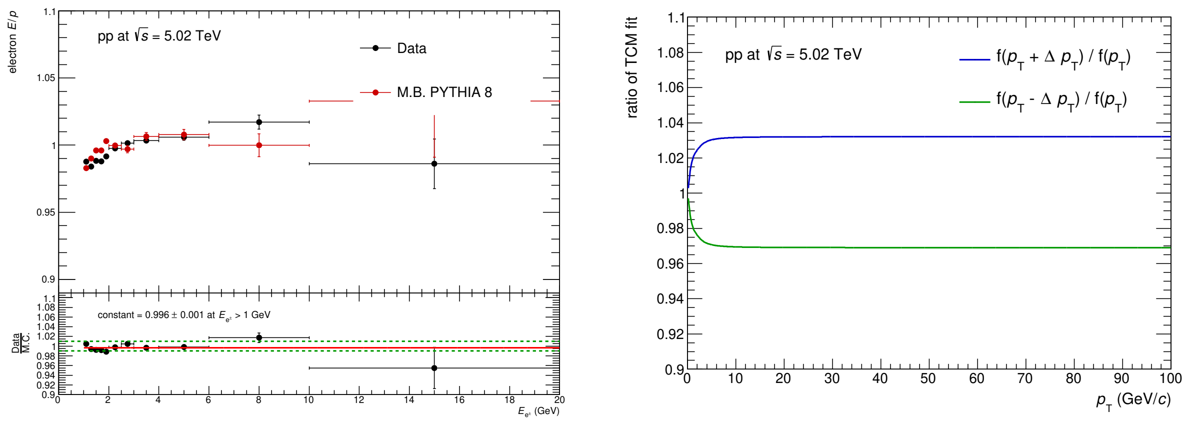

(a) E/p of $e^{\pm}$ as a function of energy measured by PHOS.

(b) The ratio of TCM fit to π^0 .

Figure 71: E/p of $e^{\pm}$ and the uncertainty of particle yield by the energy scale in pp collisions at $\sqrt{s}$ = 5.02 TeV.

due to the discrepancy of peak position between data and M.C. ($\Delta p_{\mathrm{T}}/p_{\mathrm{T}} \sim 0.01$ for centrality 0-10 %, $\Delta p_{\mathrm{T}}/p_{\mathrm{T}} \sim 0.005$ for centrality 10-40 %) was added quadratically.

5.3 Non-linearity of energy measurement in simulation

The non-linear response of the energy measurement was studied in pp collisions at $\sqrt{s} = 5.02$ TeV taken in 2015 data, described in section B.8.6.

5.4 Trigger efficiency

The systematic uncertainty related to the trigger efficiency was estimated by varying fitting range at plateau region on Figure 53 and 67b. They have plateau region at 0.597 ± 0.015 for PHOS L0 trigger in pp collisions (2017) and at 0.45 ± 0.02 for PHOS L1H/M trigger in Pb–Pb collisions at $\sqrt{s_{\rm NN}} = 5.02$ TeV, respectively. Since neutral meson yields are corrected by logical-OR (i.e. $\varepsilon^{\rm trg}_{\rm NM} = \varepsilon^{\rm trg}_{\gamma 1} + \varepsilon^{\rm trg}_{\gamma 2} - \varepsilon^{\rm trg}_{\gamma 1} \times \varepsilon^{\rm trg}_{\gamma 2}$), the uncertainty of trigger efficiency for 1 photon is analytically propagated to the uncertainty of their yields at high $p_{\rm T}$.

5.5 Timing cut efficiency

There were data taking period when a bunch space of each pp collision was 1000 ns which was much wider than timing resolution of PHOS. These runs allow us to estimate systematic uncertainty of TOF cut efficiency. The idea is defined by Eq.24. The deviation from unity in the ratio is considered as a systematic uncertainty of TOF cut.

$$\text{ratio} = \frac{\pi^0 \text{ yield at BS} = 25 \text{ ns corrected by } \varepsilon^1_{\rm TOF} \times \varepsilon^2_{\rm TOF}}{\pi^0 \text{ yield at BS} = 1000 \text{ ns } (\varepsilon_{\rm TOF} = 1)} \tag{24}$$

As shown by Figure.72a, it is found to be 2% in pp collisions at $\sqrt{s} = 5.02$ TeV, not depending

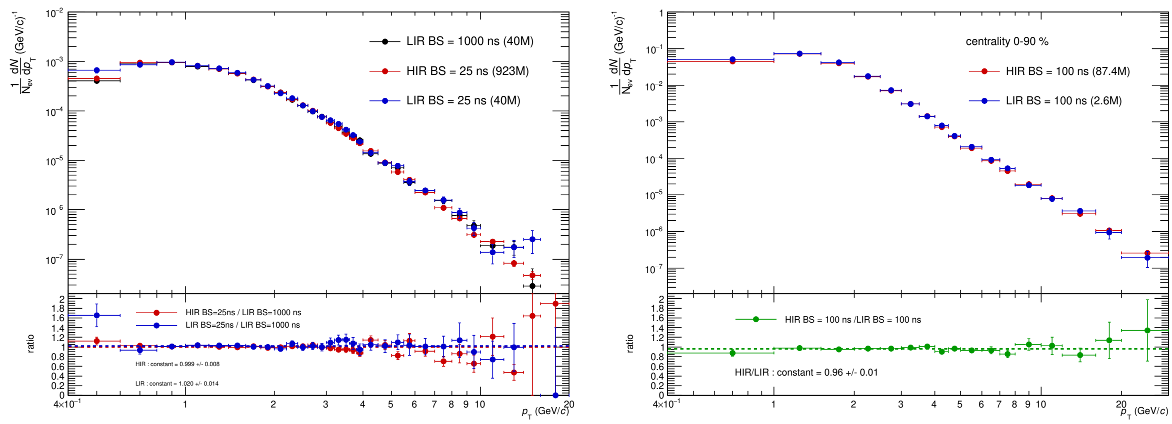

(a) The syst. unc. of TOF in pp.

(b) The syst. unc. of TOF in Pb–Pb

Figure 72: The ratio of π^0 raw yields in high intensity runs to those in low intensity runs.

on $p_{\rm T}$. The same approach was applied for Pb–Pb analysis, but the nominal bunch space (BS) was 100 ns. It is found to be 4% in Pb–Pb collisions at $\sqrt{s_{\rm NN}} = 5.02$ TeV.

5.6 PID cut efficiency

In order to check photon identification cut on PHOS, each PID cut efficiency as a function of photon energy was evaluated. i.e. Charged Particle Veto (2.5σ) and dispersion cut (2.5σ) were tested. Especially in pp collisions, the CPV cut efficiency is very close to unity, because average charged track multiplicity in pp collisions is expected to be $5 \sim 7$ tracks at mid-rapidity [68]. Hence, the probability of random matching between a photon hit and a charged particle is small.

The deviation from unity in the ratio Data/M.C. is considered as systematic uncertainty of PID cut, which is $\sim 2\%$ without depending on photon energy in all centralities.

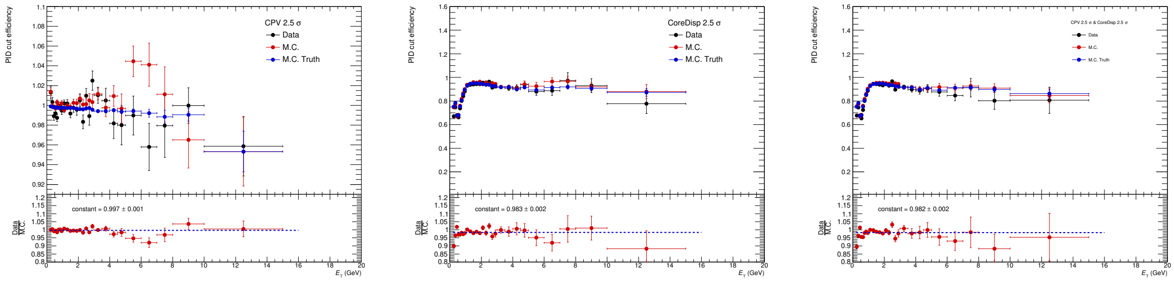

(a) CPV cut (b) Dispersion cut (c) CPV and Dispersion cut

Figure 73: PID cut efficiency as a function of photon energy in pp collisions at $\sqrt{s} = 5.02$ TeV.

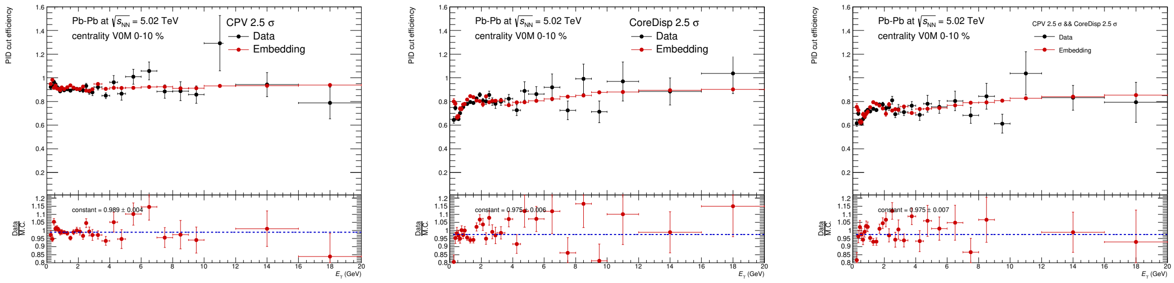

(a) CPV cut (b) Dispersion cut (c) CPV and Dispersion cut

Figure 74: PID cut efficiency as a function of photon energy in Pb–Pb collisions at $\sqrt{s_{\rm NN}} = 5.02$ TeV centrality 0-10%.

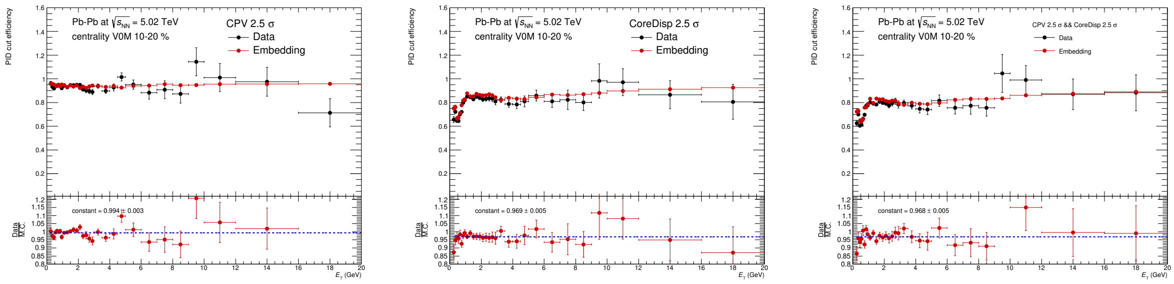

(a) CPV cut (b) Dispersion cut (c) CPV and Dispersion cut

Figure 75: PID cut efficiency as a function of photon energy in Pb–Pb collisions at $\sqrt{s_{\rm NN}} = 5.02$ TeV centrality 10-20%.

5.7 Feed down from strange hadrons

The systematic uncertainty of feed down correction to π^0 is inherited from the systematic uncertainty of the measured $K^{\pm}/\pi^{\pm}$ ratio [61]. Typically, the systematic uncertainty of K/π ratio is about 10 % at the maximum. Thus, it is feed down correction $\times$ 0.1 in both pp and Pb–Pb collisions.

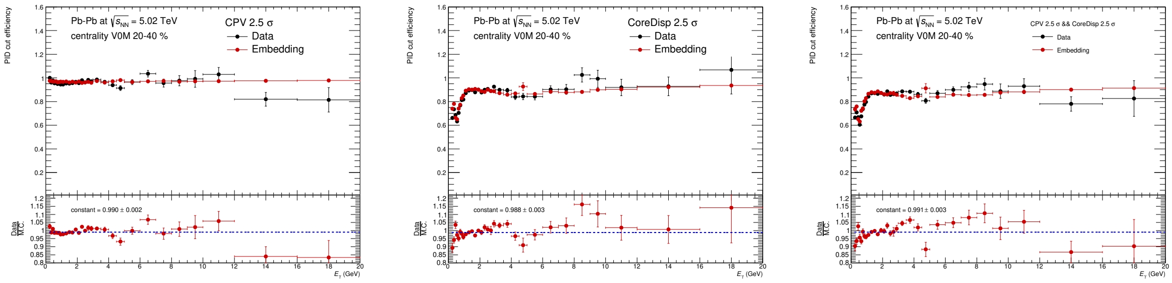

(a) CPV cut (b) Dispersion cut (c) CPV and Dispersion cut

Figure 76: PID cut efficiency as a function of photon energy in Pb–Pb collisions at $\sqrt{s_{\mathrm{NN}}} = 5.02$ TeV centrality 20-40%.

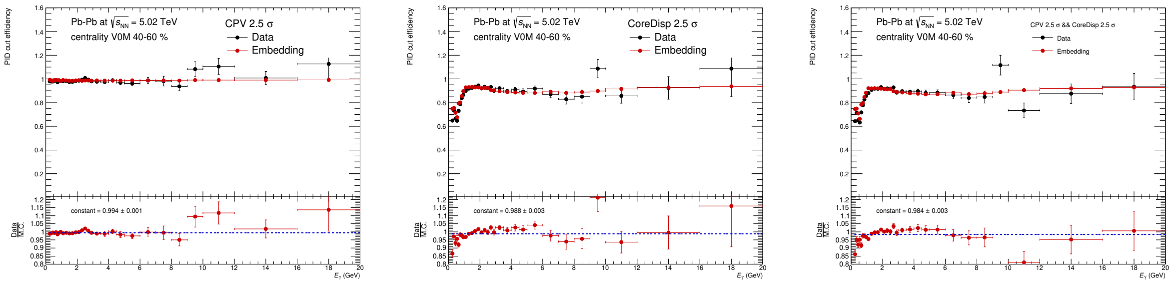

(a) CPV cut (b) Dispersion cut (c) CPV and Dispersion cut

Figure 77: PID cut efficiency as a function of photon energy in Pb–Pb collisions at $\sqrt{s_{\mathrm{NN}}} = 5.02$ TeV centrality 40-60%.

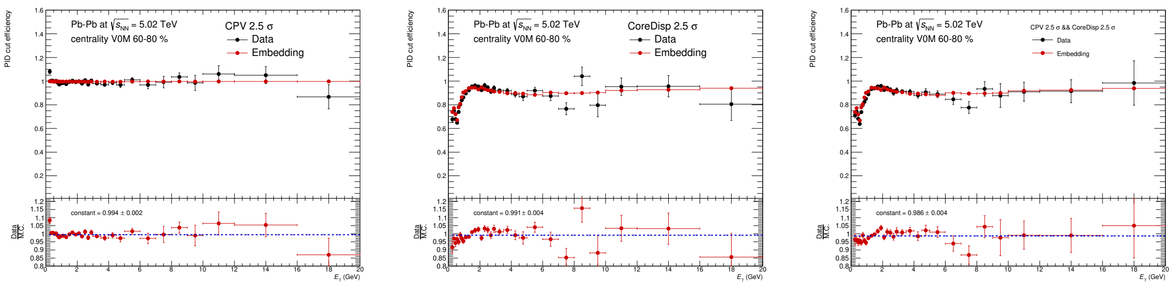

(a) CPV cut (b) Dispersion cut (c) CPV and Dispersion cut

Figure 78: PID cut efficiency as a function of photon energy in Pb–Pb collisions at $\sqrt{s_{\mathrm{NN}}} = 5.02$ TeV centrality 60-80%.

5.8 Acceptance of PHOS detector

This estimation was done in 2015 data of pp collisions at $\sqrt{s} = 5.02$ TeV by varying the distance to the closest bad channel (0 or 1 cell), which is described in section B.8.7. Typically, it is 1.5 % for neutral mesons.

5.9 Material budget

This uncertainty is common in pp and Pb–Pb data, as ALICE detector did not change during Run2 operation. The systematic uncertainty of the material budget has been estimated by comparing π^0 yields between magnetic field ON and OFF taken in 2017 data (LHC17d). As converted e^+e^- pairs do not bend without magnetic field, the e^+e^- pair is reconstructed as same as a photon candidate. This results in increase of the reconstructed π^0 yields and allows us to estimate description of the material budget in simulation. Note that there are TOF and TRD in front of PHOS M4 (a half module). As shown by Fig.79, π^0 yields at B = 0.0 T is higher those in 0.5 T and well described by M.C in M123 (1.01 ± 0.02). However, there are large statistical error bars in M4 (1.11 ± 0.21). Thus, I decided to exclude M4 from my analyses and the systematic uncertainty of the material budget is 2% from this study.

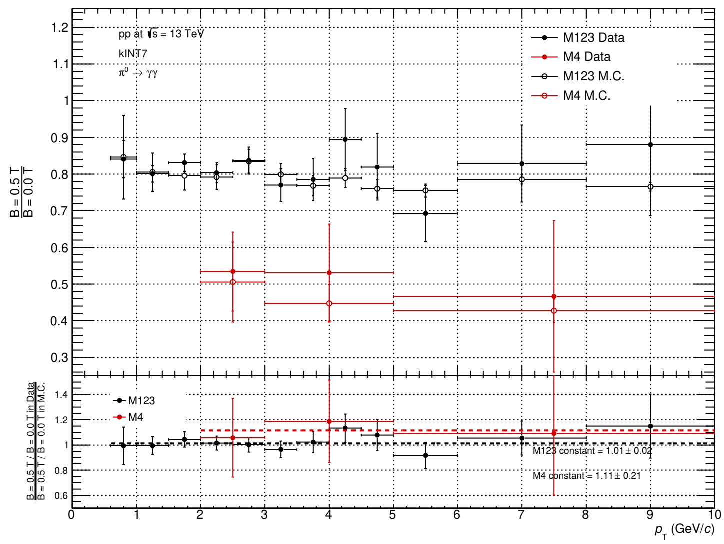

Figure 79: top : ratio of π^0 yields at B = 0.5 T to those at B = 0.0 T in data and M.C.. bottom : Double ratio of π^0 yields

5.10 Summary of systematic uncertainties

Total systematic uncertainties for π^0 and η mesons are summarized in this section.

5.10.1 Summary of systematic uncertainties in pp collisions at $\sqrt{s} = 5.02$ TeV

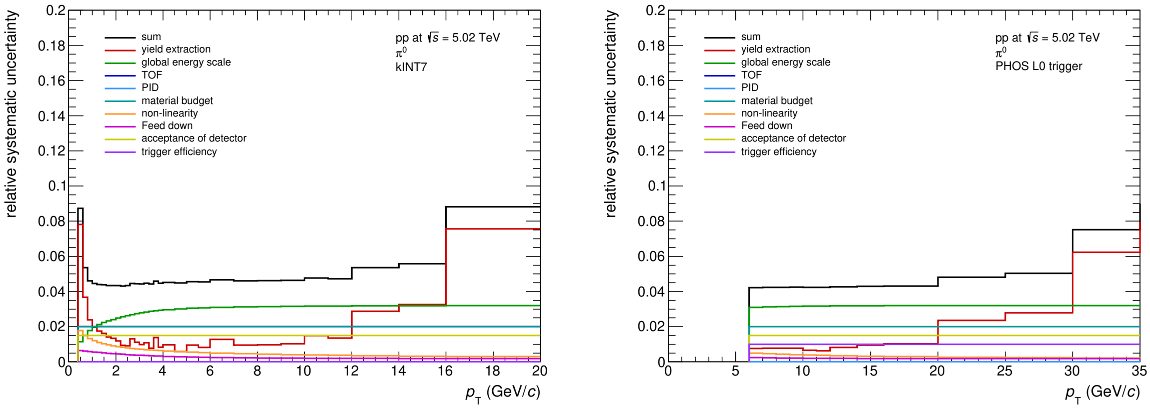

(a) kINT7 (b) kPHI7

Figure 80: The summary of systematic uncertainties of the π^0 measurement in pp collisions at $\sqrt{s} = 5.02$ TeV

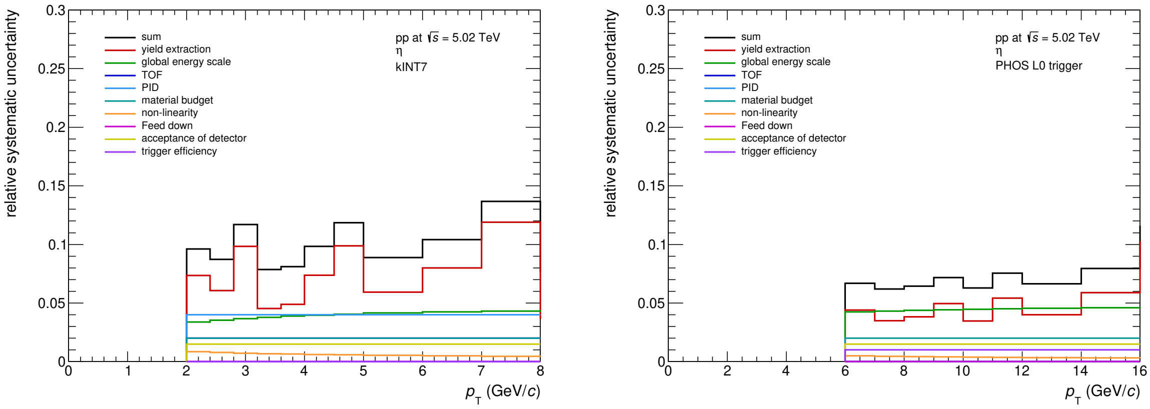

(a) kINT7 (b) kPHI7

Figure 81: The summary of systematic uncertainties of the η measurement in pp collisions at $\sqrt{s} = 5.02$ TeV

5.10.2 Summary of systematic uncertainties in Pb–Pb collisions at $\sqrt{s_{\mathrm{NN}}} = 5.02$ TeV

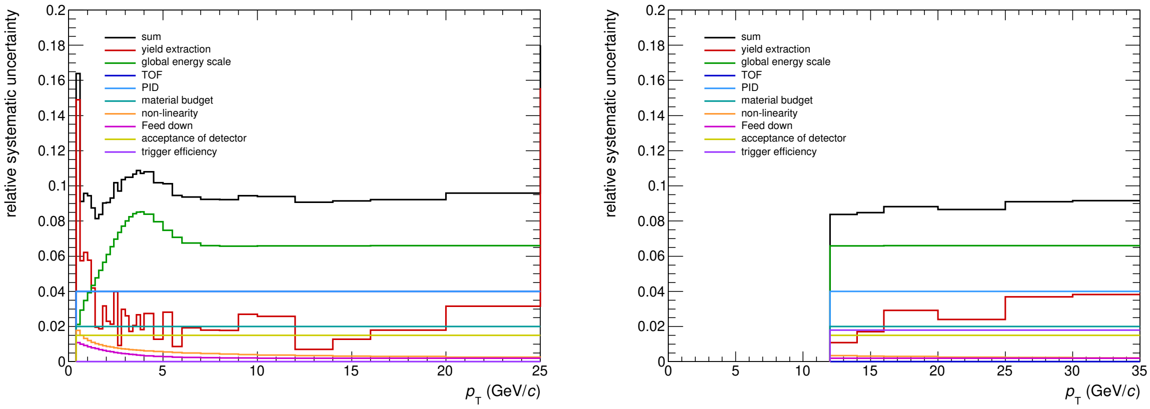

(a) kINT7 (b) kPHI7

Figure 82: The summary of systematic uncertainties of the π^0 measurement in Pb–Pb collisions at $\sqrt{s_{NN}}$ = 5.02 TeV (0-5 %)

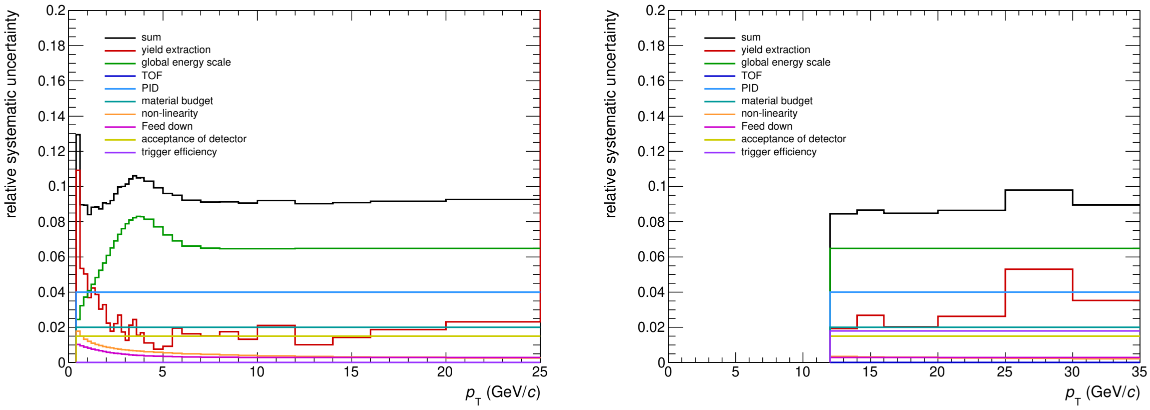

(a) kINT7 (b) kPHI7

Figure 83: The summary of systematic uncertainties of the π^0 measurement in Pb–Pb collisions at $\sqrt{s_{NN}}$ = 5.02 TeV (5-10 %)

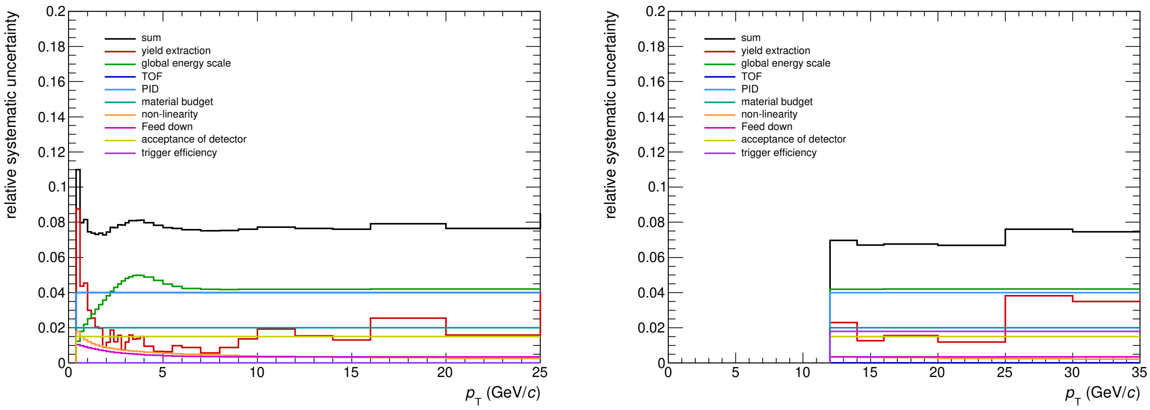

(a) kINT7 (b) kPHI7

Figure 84: The summary of systematic uncertainties of the π^0 measurement in Pb–Pb collisions at $\sqrt{s_{NN}}$ = 5.02 TeV (10-20 %)

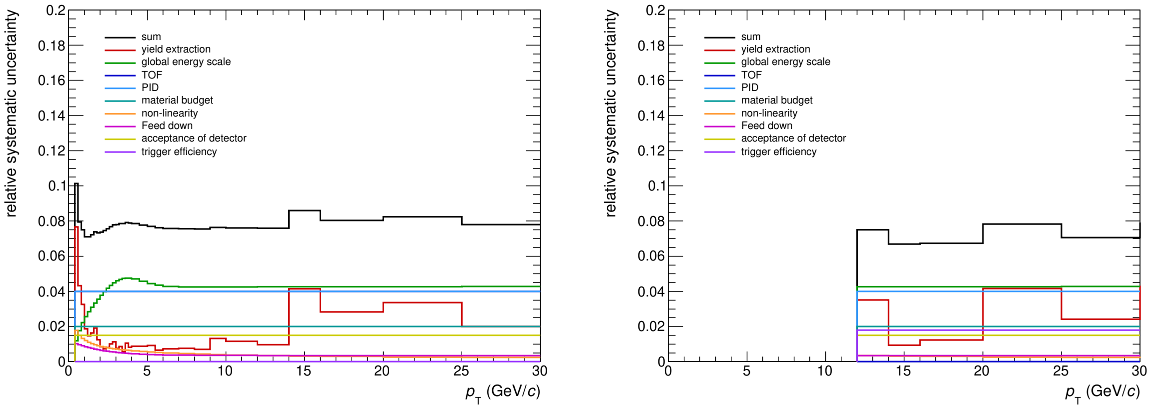

(a) kINT7 (b) kPHI7

Figure 85: The summary of systematic uncertainties of the π^0 measurement in Pb–Pb collisions at $\sqrt{s_{NN}} = 5.02$ TeV (20-40 %)

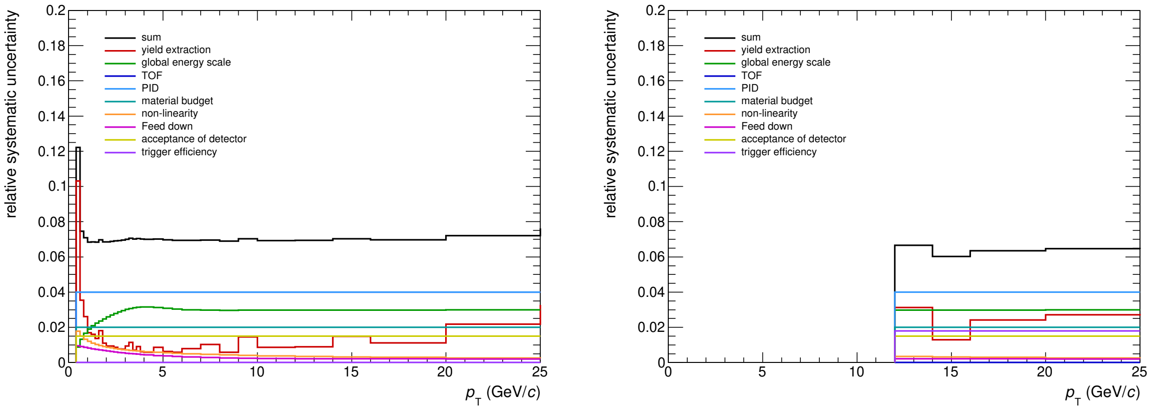

(a) kINT7 (b) kPHI7

Figure 86: The summary of systematic uncertainties of the π^0 measurement in Pb–Pb collisions at $\sqrt{s_{NN}} = 5.02$ TeV (40-60 %)

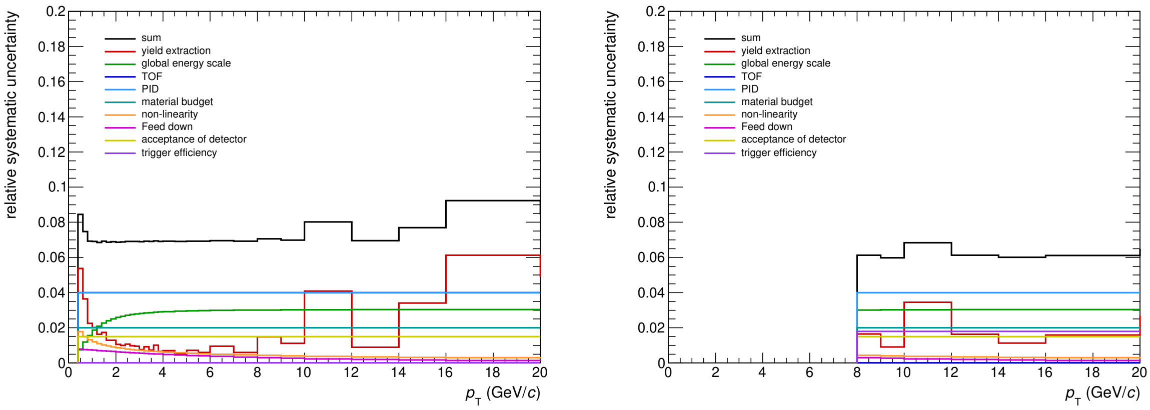

(a) kINT7 (b) kPHI7

Figure 87: The summary of systematic uncertainties of the π^0 measurement in Pb–Pb collisions at $\sqrt{s_{NN}} = 5.02$ TeV (60-80 %)

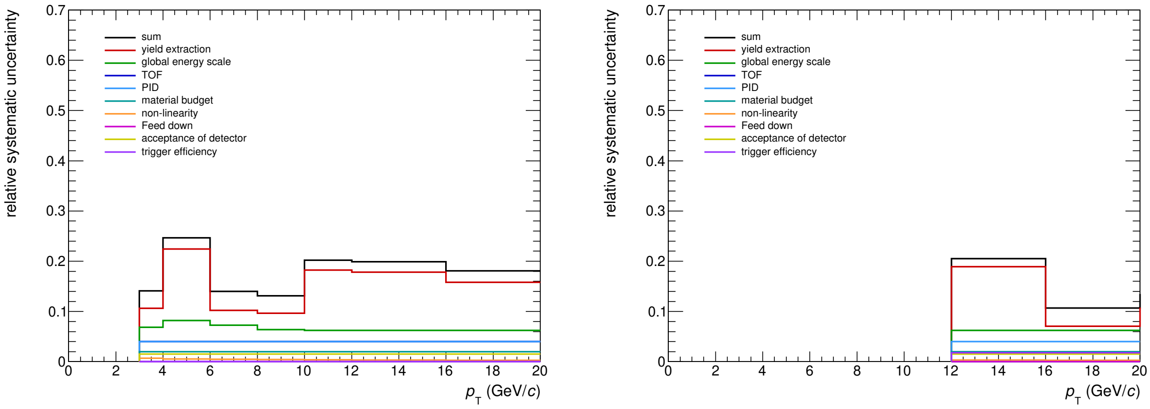

(a) kINT7

(b) kPHI7

Figure 88: The summary of systematic uncertainties of the η measurement in Pb–Pb collisions at $\sqrt{s_{\mathrm{NN}}} = 5.02$ TeV (0-10 %)

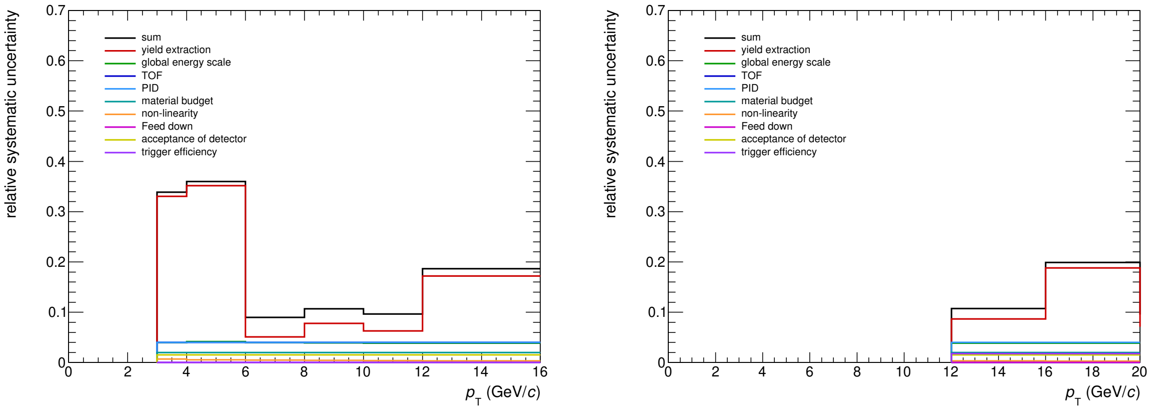

(a) kINT7

(b) kPHI7

Figure 89: The summary of systematic uncertainties of the η measurement in Pb–Pb collisions at $\sqrt{s_{\mathrm{NN}}} = 5.02$ TeV (10-20 %)

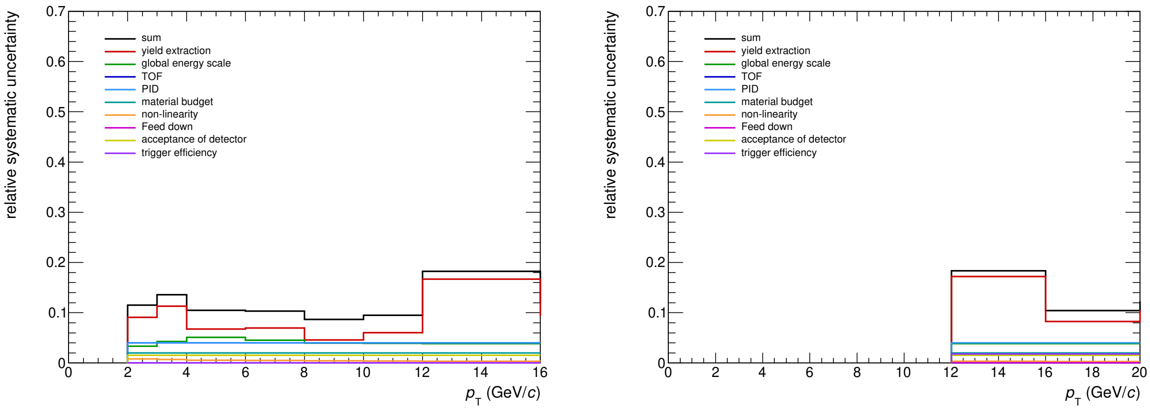

(a) kINT7

(b) kPHI7

Figure 90: The summary of systematic uncertainties of the η measurement in Pb–Pb collisions at $\sqrt{s_{\mathrm{NN}}} = 5.02$ TeV (20-40 %)

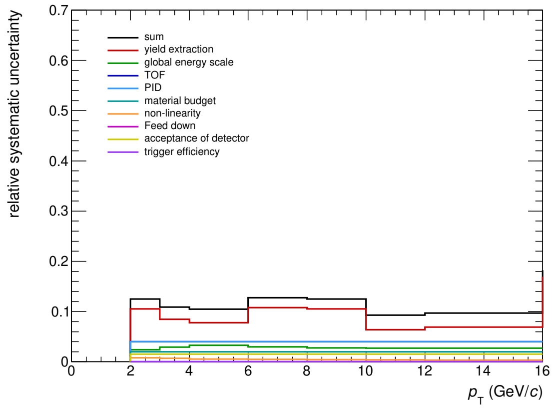

(a) kINT7

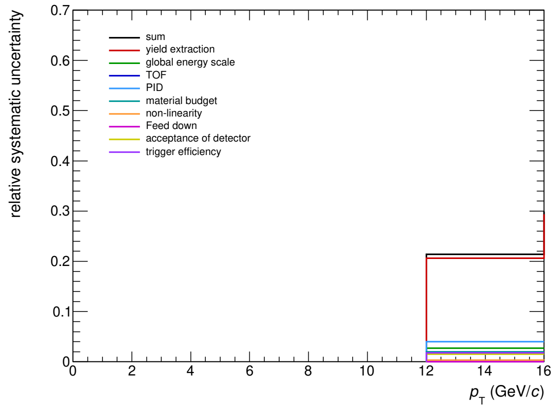

(b) kPHI7

Figure 91: The summary of systematic uncertainties of the η measurement in Pb–Pb collisions at $\sqrt{s_{\mathrm{NN}}} = 5.02$ TeV (40-60 %)

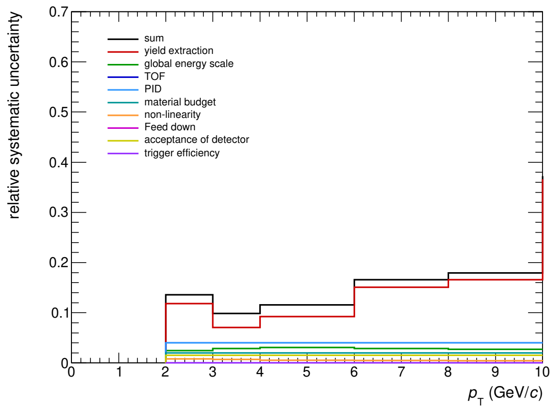

(a) kINT7

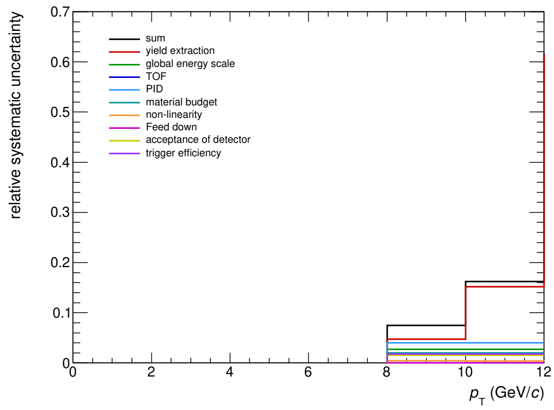

(b) kPHI7

Figure 92: The summary of systematic uncertainties of the η measurement in Pb–Pb collisions at $\sqrt{s_{\mathrm{NN}}} = 5.02$ TeV (60-80 %)

6 Results and discussions for neutral mesons

Results of neutral mesons analyses are summarized in this section. Production cross sections, invariant yield, particle ratio η/π^0, and nuclear modification factor R_{AA} are described. In all figures, vertical bars represent statistical error and boxes indicate the systematic uncertainty.

6.1 Invariant cross section of particles

The production cross section of π^0 and η mesons have been measured in pp collisions at $\sqrt{s}$ = 5.02 TeV. Neutral mesons spectra are fitted by either two-component model (TCM) function [69, 70, 71] or Hagedorn function [72]. Two-component model function is :

$$E\frac{d^3\sigma}{dp^3} = A_e \exp\left(-\frac{E_{\mathrm{Tkin}}}{T_e}\right) + A\left(1+\frac{p_{\mathrm{T}}^2}{T^2\cdot n}\right)^{-n}, \tag{25}$$

where A_e, T_e, A, T and n are free parameters for fitting and $E_{\mathrm{Tkin}} = \sqrt{p_{\mathrm{T}}^2+m^2} - m$ is transverse kinetic energy (m is mass of particle). The exponential term is for soft, and the power-law is for hard particle production. Hagedorn function is :

$$E\frac{d^3\sigma}{dp^3} = A\left(1+\frac{p_{\mathrm{T}}}{p_0}\right)^{-n}, \tag{26}$$

$$\left(1+\frac{p_{\mathrm{T}}}{p_0}\right)^{-n} \to \begin{cases} \exp\left(-\frac{n}{p_0}p_{\mathrm{T}}\right) & \text{for } p_{\mathrm{T}} \ll p_0 \\ p_{\mathrm{T}}^{-n} & \text{for } p_{\mathrm{T}} \to \infty \end{cases}$$

where A, p_0 and n is free parameters for fitting. Hagedorn function behaves exponential at low p_{T} and power-law at high p_{T}. Fitting parameters are listed in Table. 1, 2, 3, 4.

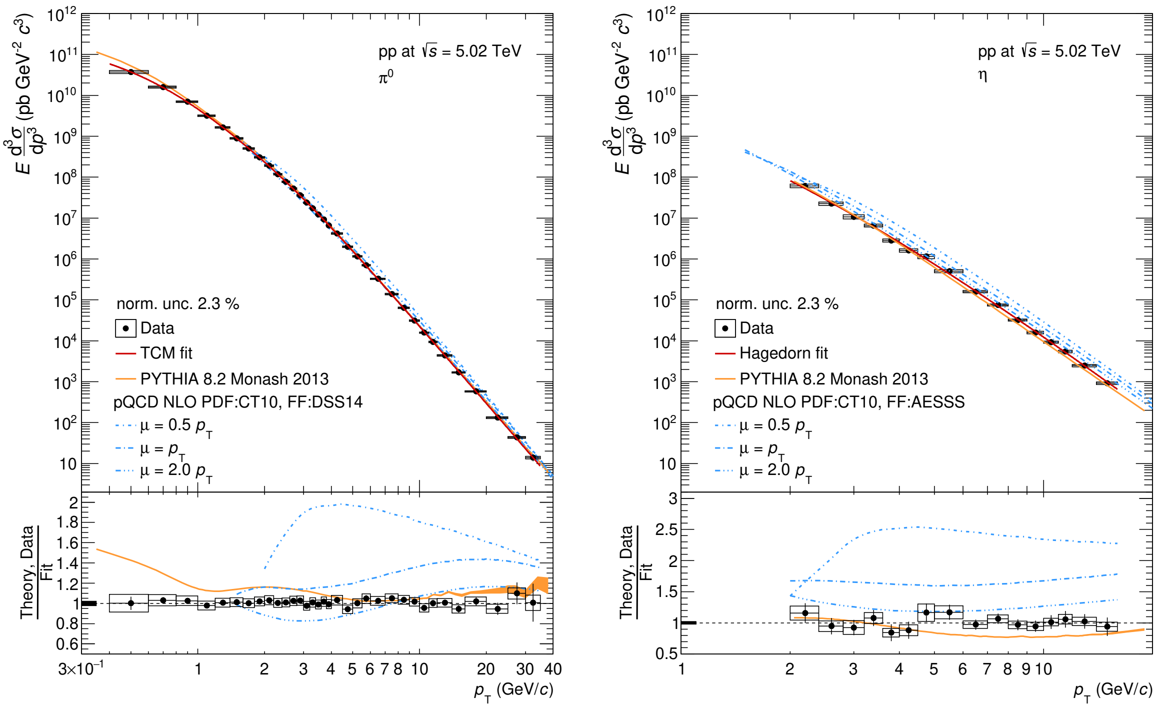

(a) The production cross section of π^0

(b) The production cross section of η

Figure 93: Production cross sections of neutral mesons in pp collisions at $\sqrt{s}$ = 5.02 TeV

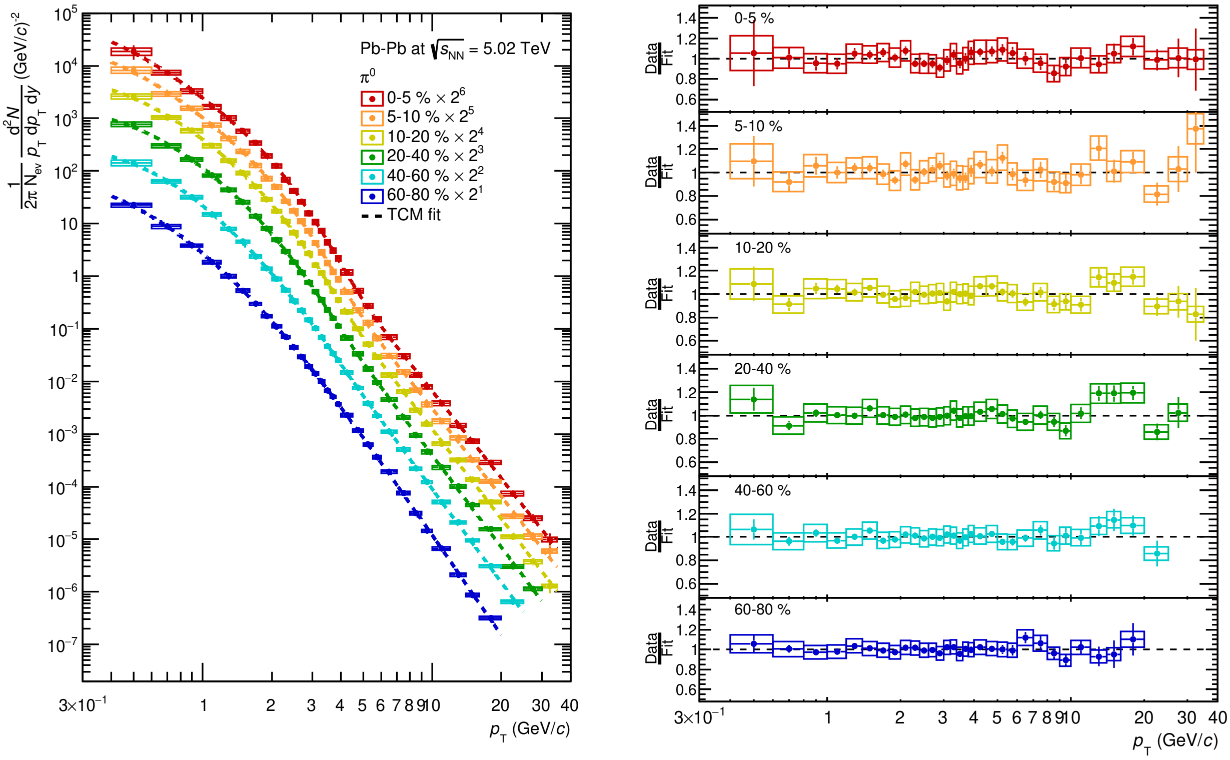

(a) The invariant yield of π^0

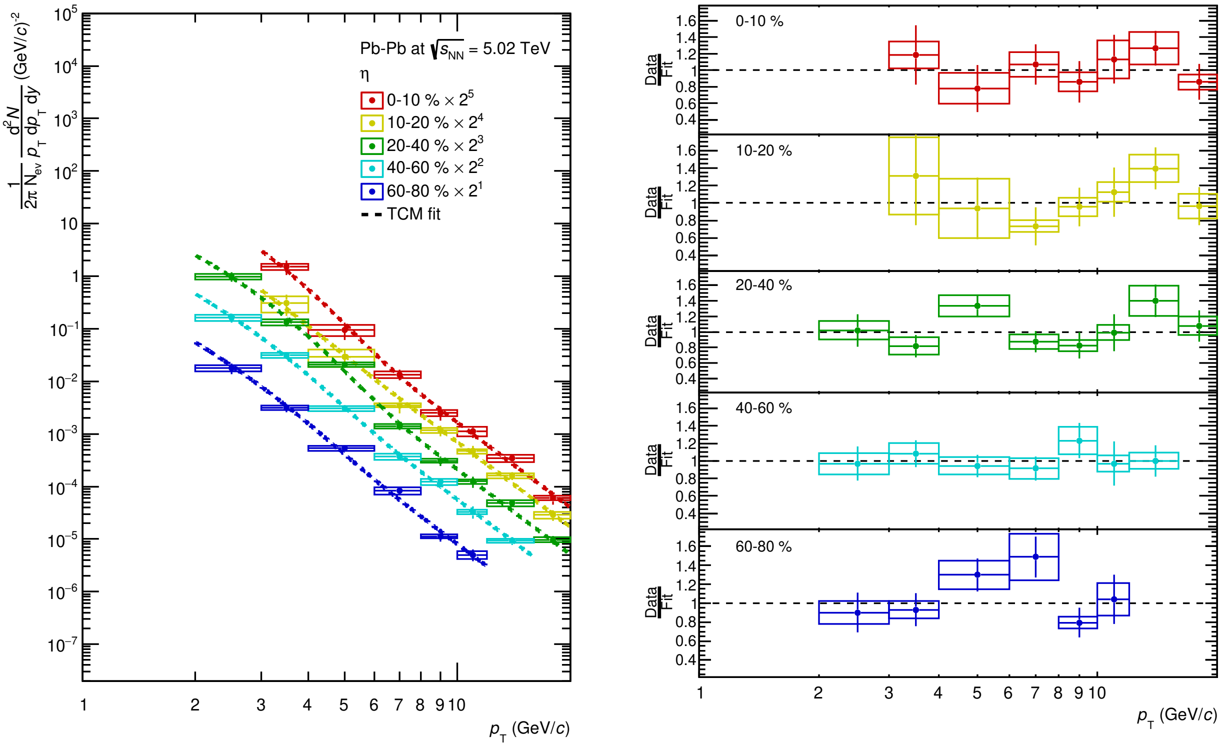

(b) The invariant yield of η

Figure 94: Invariant yields of neutral mesons in Pb–Pb collisions at $\sqrt{s_{NN}} = 5.02$ TeV

Table 1: Fitting parameters of TCM function in pp collisions at $\sqrt{s} = 5.02$ TeV

particle	A_e (pb GeV^{-2} c^3)	T_e (GeV/c)	A (pb GeV^{-2} c^3)	T (GeV/c)	n
π^0	$(2.57 \pm 0.58) \times 10^{11}$	0.18 ± 0.02	$(0.16 \pm 0.04) \times 10^{11}$	0.67 ± 0.03	3.16 ± 0.02

Table 2: Fitting parameters of Hagedorn function in pp collisions at $\sqrt{s} = 5.02$ TeV

particle	A (pb GeV^{-2} c^3)	p_0 (GeV/c)	n
η	$(1.58 \pm 0.58) \times 10^{11}$	0.96 ± 0.08	6.7 ± 0.1

Table 3: Fitting parameters of TCM function for π^0 in Pb–Pb collisions at $\sqrt{s_{\mathrm{NN}}} = 5.02$ TeV

centrality (%)	A_e (GeV^{-2} c^3)	T_e (GeV/c)	A (GeV^{-2} c^3)	T (GeV/c)	n
0-5	187 ± 26	0.39 ± 0.01	1526 ± 1055	0.29 ± 0.05	2.75 ± 0.04
5-10	144 ± 22	0.39 ± 0.01	1026 ± 500	0.33 ± 0.04	2.78 ± 0.04
10-20	105 ± 15	0.39 ± 0.01	421 ± 129	0.39 ± 0.03	2.85 ± 0.03
20-40	40.7 ± 7.4	0.40 ± 0.01	233 ± 52	0.41 ± 0.02	2.89 ± 0.03
40-60	5.9 ± 1.9	0.43 ± 0.02	92 ± 16	0.44 ± 0.02	2.93 ± 0.03
60-80	78 ± 36	0.16 ± 0.03	5.9 ± 2.8	0.64 ± 0.06	3.17 ± 0.04
0-10	185 ± 24	0.39 ± 0.01	1062 ± 466	0.32 ± 0.03	2.76 ± 0.03
0-90	43.7 ± 7.1	0.39 ± 0.01	163 ± 43	0.41 ± 0.02	2.88 ± 0.02

Table 4: Fitting parameters of TCM function for η in Pb–Pb collisions at $\sqrt{s_{\mathrm{NN}}} = 5.02$ TeV

centrality (%)	A_e (GeV^{-2} c^3)	T_e (GeV/c)	A (GeV^{-2} c^3)	T (GeV/c)	n
0-10	6.1 ± 2.9	0.55	202 ± 27	0.36	2.68
10-20	0.78 ± 2.0	0.55	171 ± 21	0.36	2.68
20-40	3.1 ± 0.6	0.55	103 ± 10	0.36	2.68
40-60	0.81 ± 0.25	0.55	55.5 ± 6.2	0.36	2.68
60-80	0.15 ± 0.07	0.55	15.8 ± 2.1	0.36	3.68
0-90	2.6 ± 1.5	0.55 ± 0.05	112 ± 89	0.36 ± 0.05	2.68 ± 0.10

Especially, η meson spectra in Pb–Pb collisions have only $6 \sim 7$ data points, that leads poor quality of the fitting or divergence. Therefore, centrality classes are merged into 0-90 % to get the full statistics of data and fitted by TCM function. When η meson spectra in different centrality classes are fitted by TCM, T_e, T and n are fixed to those in centrality 0-90 % to avoid divergence of the fitting. Hence, yield parameters A_e and A are free parameters in each centrality class.

Figure 95 shows the ratio of p_{T} spectra of π^0 at $\sqrt{s_{\mathrm{NN}}} = 5.02$ TeV to those at $\sqrt{s_{\mathrm{NN}}} = 2.76$ TeV [73, 74] in Pb–Pb (color filled marker) and pp (black open marker) collisions for same centrality classes. Ratios of spectra increase with p_{T} in both pp and Pb–Pb collisions which means harder p_{T} spectra at higher collision energy.

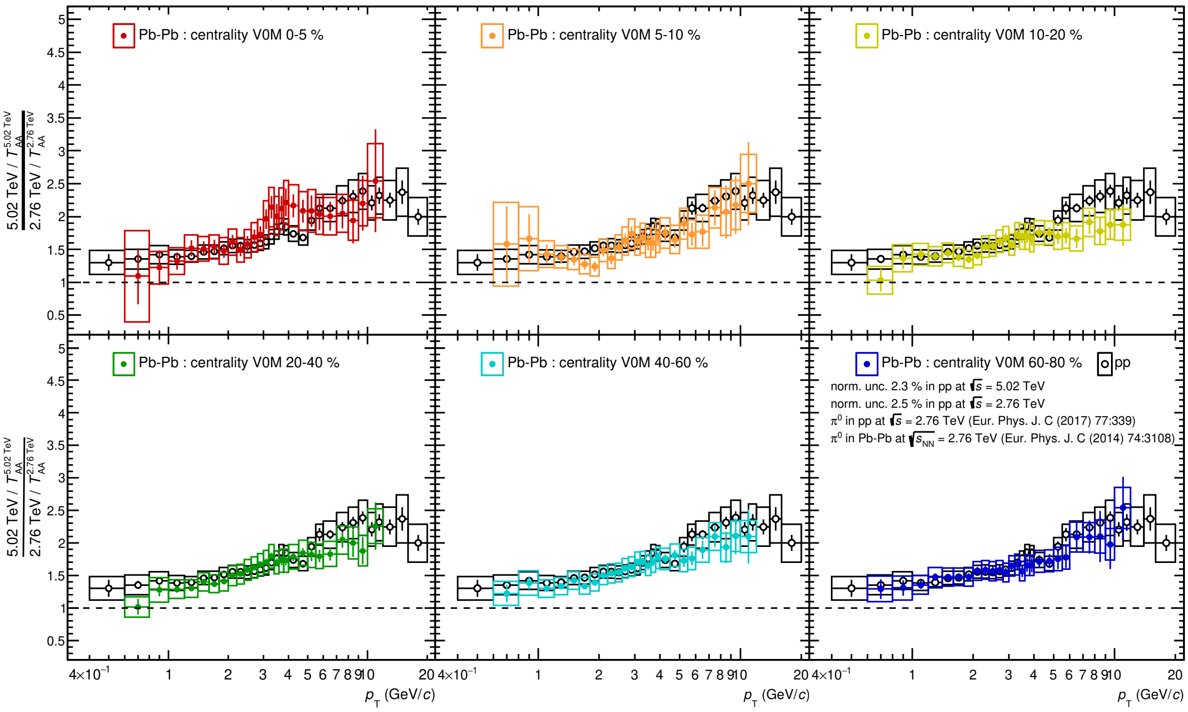

Figure 95: Comparison of p_{T} spectra for π^0 between $\sqrt{s_{\mathrm{NN}}} = 5.02$ and 2.76 TeV in Pb–Pb collisions

6.2 Particle ratio

η/π^0 ratios have been measured in pp and Pb–Pb collisions at $\sqrt{s_{\mathrm{NN}}} = 5.02$ TeV for different centrality classes, as shown by Figure 96 and Figure97. As, the statistical uncertainty is large, no centrality dependence of η/π^0 ratios in Pb–Pb collisions is observed. In order to reduce statistical and systematic uncertainties, all centrality (Figure.97b) have been combined in Pb–Pb collisions. The η/π^0 ratio is found to be $0.507 \pm 0.017(\text{stat.}) \pm 0.008(\text{syst.})$ in pp collisions and $0.491 \pm 0.022(\text{stat.}) \pm 0.017(\text{syst.})$ at $p_{\mathrm{T}} > 3.6$ GeV/c in centrality 0-90% Pb–Pb collisions at $\sqrt{s_{\mathrm{NN}}} = 5.02$ TeV. The measured η/π^0 ratios may be claimed to be consistent with published ALICE results [74, 75, 76, 77] within experimental uncertainties, although the ratio in pp collisions at $\sqrt{s} = 5.02$ TeV is a bit higher than that in pp collisions at $\sqrt{s} = 8$ TeV [78].

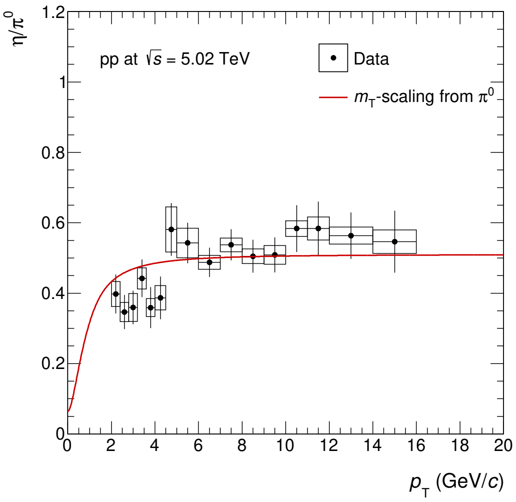

Figure 96: The η/π^0 ratio in pp collisions at $\sqrt{s} = 5.02$ TeV

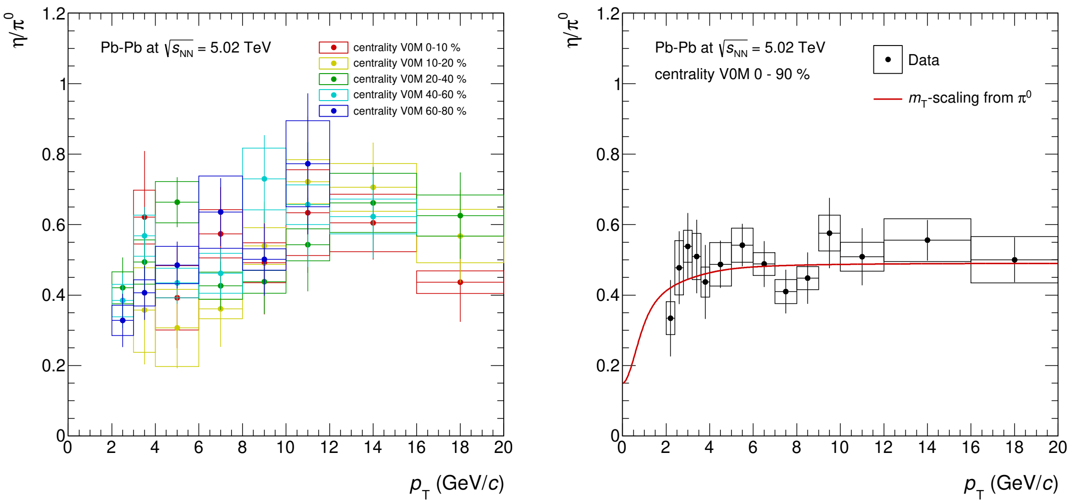

(a) η/π^0 in different centrality classes

(b) η/π^0 in centrality 0-90 %

Figure 97: η/π^0 ratios in Pb–Pb collisions at $\sqrt{s_{\mathrm{NN}}} = 5.02$ TeV

6.3 Nuclear modification factors R_{AA} of neutral mesons

Since neutral mesons spectra have been measured in both pp and Pb–Pb collisions at $\sqrt{s_{\mathrm{NN}}} =$ 5.02 TeV, nuclear modification factors R_{AA} in different centrality class have been determined. The typical values of the nuclear overlap function T_{AA} used in this thesis are summarized in Table.5. These are taken from the reference [79]. Boxes around unity is the total normalization uncertainty, namely, square root of the quadratic sum of systematic uncertainty of T_{AA} and systematic uncertainty of normalization for spectra in pp collisions. R_{AA} reaches 0.13 at $p_{\mathrm{T}} = 5-6$ GeV/c in central Pb–Pb collisions for both π^0 and η mesons and increase with p_{T}.

Table 5: Geometrical parameters in Pb–Pb collisions at $\sqrt{s_{\mathrm{NN}}} = 5.02$ TeV [79]

centrality	T_{AA} (mb^{-1})	syst. T_{AA} (mb^{-1})	N_{coll}	syst. N_{coll}	N_{part}	syst. N_{part}
0-5 (%)	25.92	0.37	1752	28	382.3	2.4
5-10 (%)	20.22	0.52	1367	37	329.1	5
10-20 (%)	14.27	0.36	964.8	25	260.2	5.2
20-40 (%)	6.872	0.21	464.5	15	158.5	3.1
40-60 (%)	2.046	0.05	138.3	3.1	70.61	1.1
60-80 (%)	0.4173	0.014	28.21	0.81	23.34	0.43

6.3.1 Collision energy $\sqrt{s_{\mathrm{NN}}}$ dependence

R_{AA} of π^0 mesons in Pb–Pb collisions at $\sqrt{s_{\mathrm{NN}}} = 5.02$ and 2.76 TeV are compared on Figure 98. In spite of the fact that p_{T} spectra become harder at higher collision energy both in pp and Pb–Pb collisions, R_{AA} is found to be the same at two collision energies. This indicates the larger parton energy-loss at the higher collision energy.

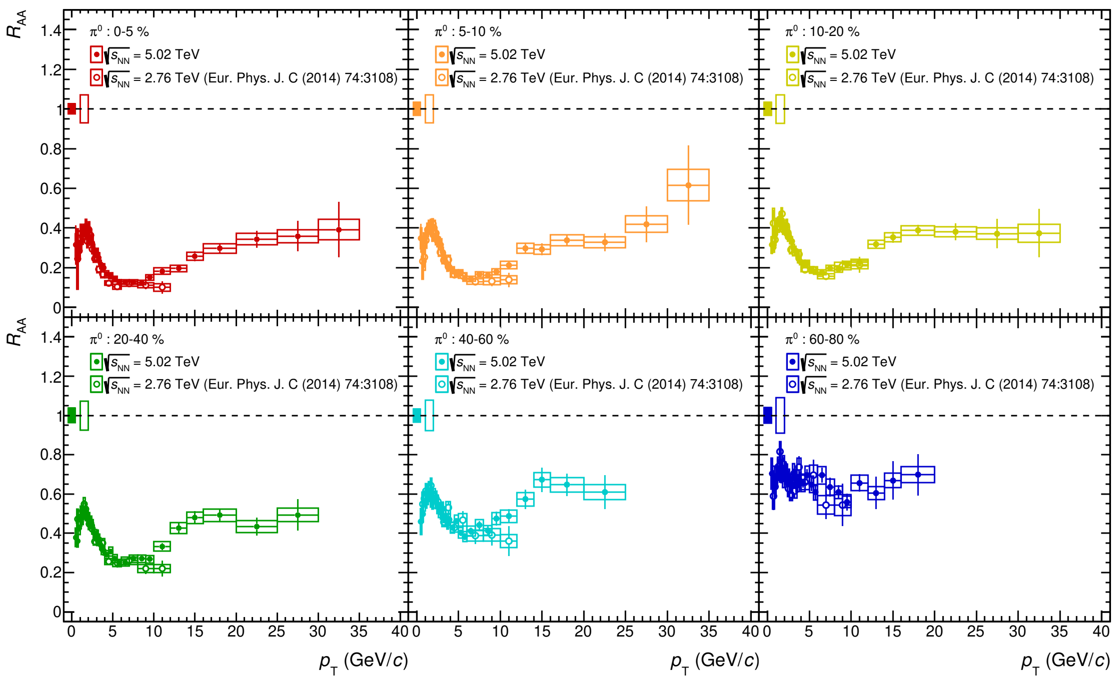

Figure 98: R_{AA} of π^0 in Pb–Pb collisions at $\sqrt{s_{\mathrm{NN}}} = 5.02$ and 2.76 TeV

There is one more possibility to compare the p_{T} spectrum and R_{AA} of π^0 in central collisions

(0-10%) with higher statistics [76]. Those were recorded in 2011, so called LHC11h period, in Pb–Pb collisions at $\sqrt{s_{\mathrm{NN}}} = 2.76$ TeV. As published results are available up to $p_{\mathrm{T}} = 20$ GeV/c, the comparison has been performed at only $p_{\mathrm{T}} < 20$ GeV/c here. Considering the large experimental uncertainties for both results, comparisons on Figure 99 again indicate the harder p_{T} spectrum at higher collision energy, but the same suppression level at two collision energies up to $p_{\mathrm{T}} = 20$ GeV/c.

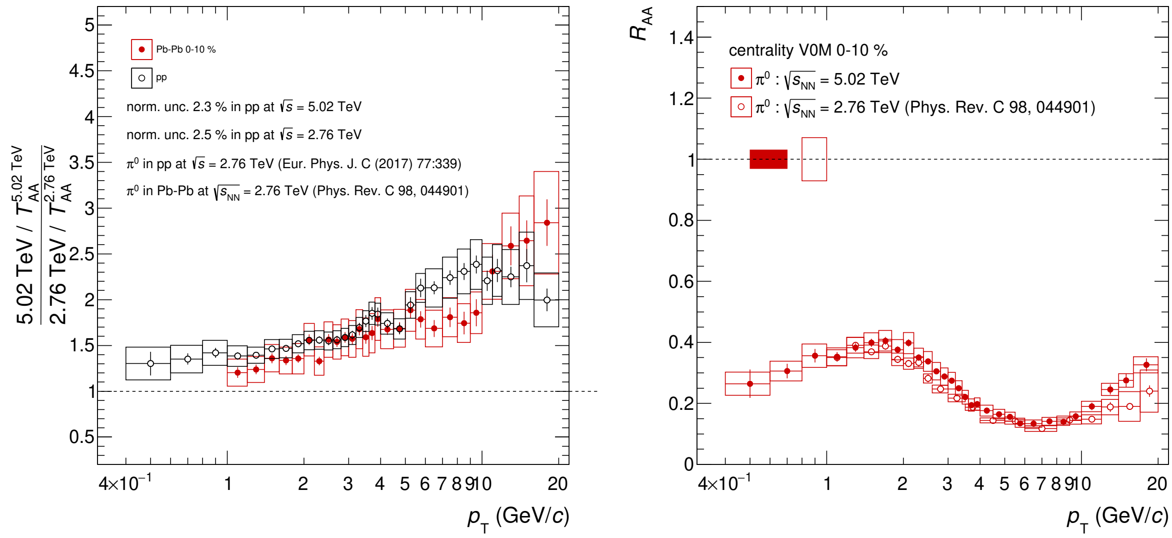

(a) The ratio of p_{T} spectrum for π^0.

(b) R_{AA} for π^0.

Figure 99: Comparison of the ratio of p_{T} spectrum and R_{AA} in Pb–Pb collisions at $\sqrt{s_{\mathrm{NN}}} = 5.02$ and 2.76 TeV (2011 sample)

6.3.2 Comparison to theoretical models

R_{AA} of π^0 and η mesons are compared to theoretical models (Figure 100). The prediction including both radiative and elastic energy-loss in the hydrodynamically expanding QCD medium by M.Djordjevic [26] shows quantitatively good agreement with data in all centrality classes for both π^0 and η mesons. The model based on the same approach in the constant-temperature QCD medium without the evolution by M.Djordjevic [25] also gives good agreement again. This can be interpreted as that the evolution of the medium affects the azimuthal anisotropy v_2 of hadrons, rather than to R_{AA}, as she explains [26, 25]. Models by M.Djordjevic aim to reproduce R_{AA} and v_2 for hadrons simultaneously in her framework. So, it might be interesting to see them for comprehensive studies in the future.

6.3.3 Hadron species dependence

R_{AA} of π^0 and η mesons are consistent with each other within experimental uncertainties at $p_{\mathrm{T}} > 4$ GeV/c. However, it seems R_{AA} for η meson is systematically higher than that of π^0 at low p_{T}, which is similar to those previously measured in Pb–Pb collisions at $\sqrt{s_{\mathrm{NN}}} = 2.76$ TeV [76, 80].
R_{AA} for different hadron species in central Pb–Pb collisions at $\sqrt{s_{\mathrm{NN}}} = 5.02$ TeV are summarized on Figure 102. The suppression of neutral and charged [81] pions is consistent with each other, as expected (centrality classes 0-5 and 5-10% were merged into 0-10% for $\pi^{\pm}$ and $K^{\pm}$). The comparison indicates the similar suppression pattern between η and $K^{\pm}$ [81] mesons for whole p_{T} range, but seems to differ from pions at $p_{\mathrm{T}} < 4$ GeV/c. This is explained by that both η and $K^{\pm}$ mesons consist of a strange quark and an up, down quark, while pions contain up, down quarks. However, with the present accuracy of the η meson measurement, it is not enough to determine whether the suppression is different/same for π^0 and η at low p_{T}. On the other hand, comparing R_{AA} between π^0 and D mesons [82], the suppression of D mesons is clearly weaker than that of π^0 mesons at $p_{\mathrm{T}} < 10$ GeV/c. This is because of smaller energy-loss for charm quarks than for up and down quarks due to its heavier mass. At high p_{T}, the parton energy-loss does not depend on the quark mass [84, 85] and thus, R_{AA} is the same for light and heavy flavor hadrons. $B^{\pm}$ mesons which contain a bottom quark and a light quark have been measure in centrality class 0-100% by CMS [83] by triggering muons from from $B^{\pm} \to J/\psi K^{\pm} \to \mu^+\mu^- K^{\pm}$ at high p_{T}. So, it would be interesting to see R_{AA} of charm-hadrons and bottom-hadrons at low p_{T} in Run3 at $\sqrt{s_{\mathrm{NN}}} = 5.5$ TeV.

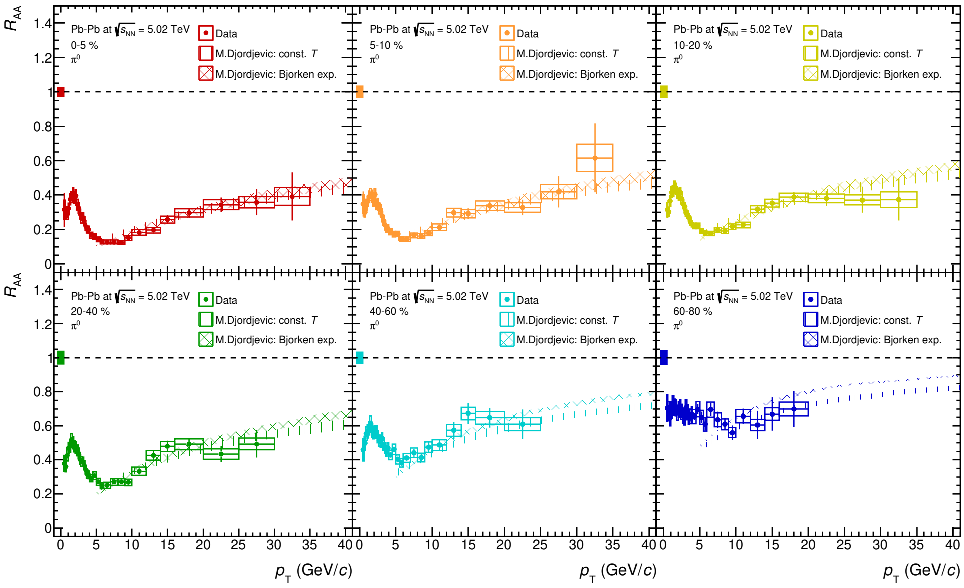

(a) For π^0 mesons.

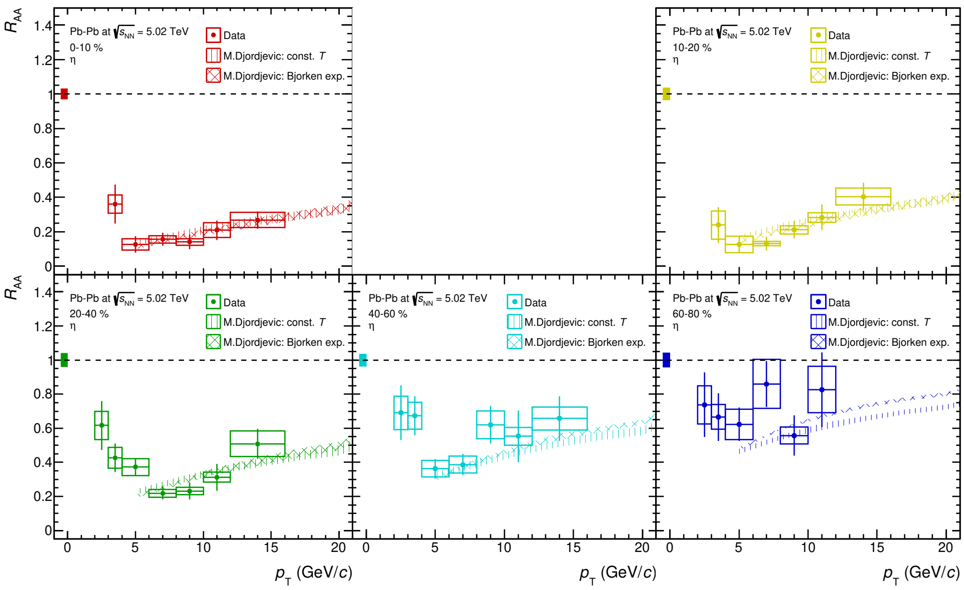

(b) For η mesons.

Figure 100: Comparison of R_{AA} with theoretical models in Pb–Pb collisions at $\sqrt{s_{NN}}$ = 5.02 TeV

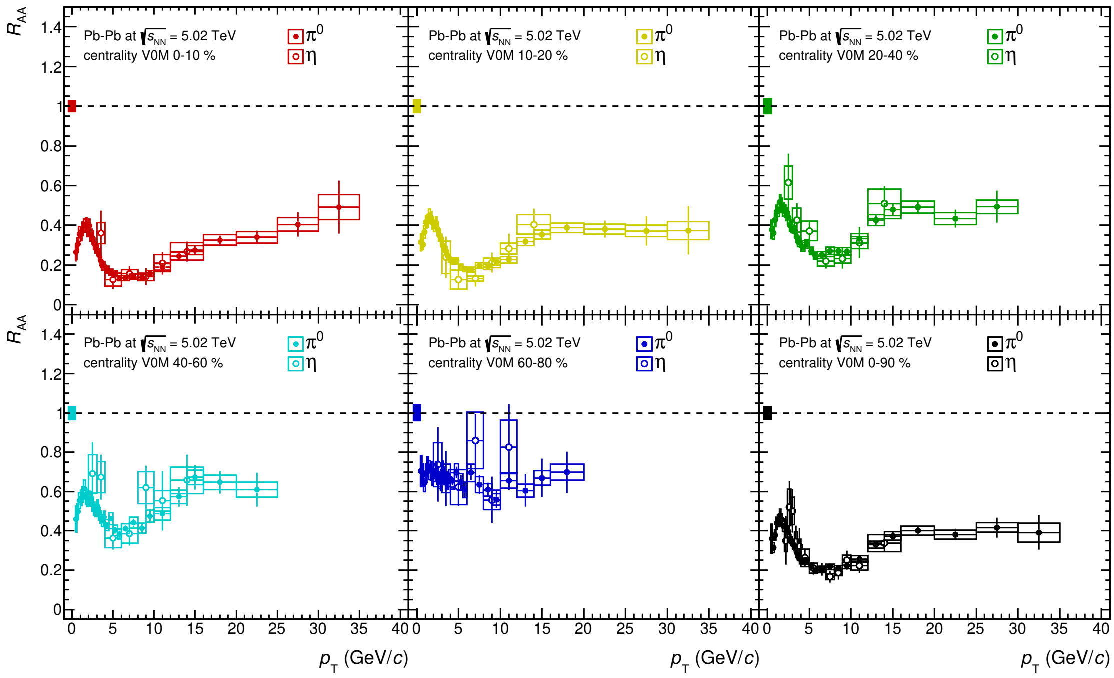

Figure 101: Comparison of R_{AA} between π^0 and η in Pb–Pb collisions at $\sqrt{s_{NN}} = 5.02$ TeV for different centrality classes.

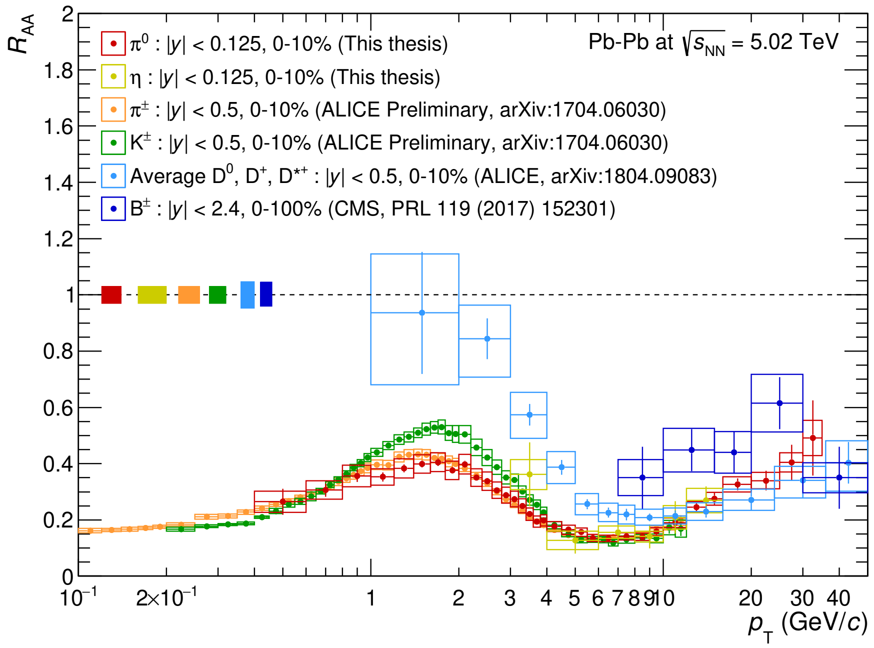

Figure 102: R_{AA} of π^0, η, $\pi^\pm$, $K^\pm$, D and $B^\pm$ mesons in central (0-10%) Pb–Pb collisions at $\sqrt{s_{NN}} = 5.02$ TeV [81, 82, 83]

6.3.4 Comparison of R_{AA} and R_{pA} at $\sqrt{s_{NN}} = 5.02$ TeV

Comparing the suppression of high p_T hadrons between A–A and p–A collisions can distinguish whether the suppression is initial state or final state effects. Figure 103 shows there is no suppression in p–Pb collisions [77], while the strong suppression is observed in Pb–Pb collisions. This demonstrates that the strong suppression observed in Pb–Pb collisions is not related to initial state effect, but to the formation of hot and dense QCD medium.

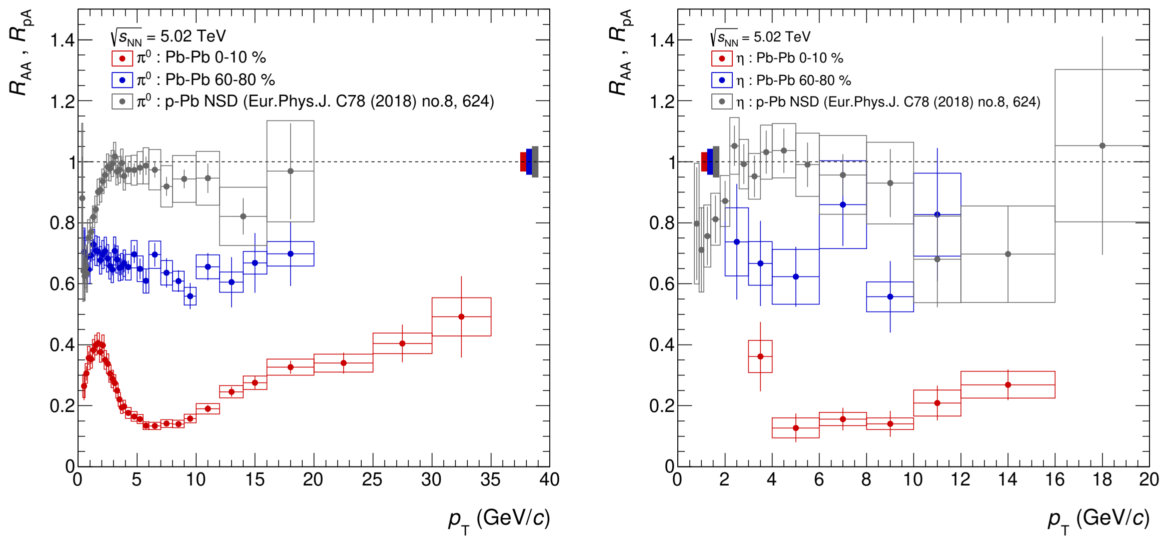

(a) R_{AA} and R_{pA} of π^0

(b) R_{AA} and R_{pA} of η

Figure 103: R_{AA}, R_{pA} of π^0 and η mesons

7 Analyses for direct photon

Detailed descriptions for the direct photon γ^{dir} measurement by using measured π^0 and η mesons are described in this section.

7.1 Analysis strategy

First of all, the inclusive photon γ^{inc} spectrum has to be measured as :

$$E\frac{d^3N_{\gamma^{\text{inc}}}}{dp^3} = \frac{1}{2\pi} \times \frac{1}{p_{\text{T}}}\frac{dN}{dp_{\text{T}}} \times P \times \frac{1}{\Delta y} \times \frac{1}{\varepsilon} \times \frac{1}{N_{\text{ev}}}, \tag{27}$$

where P is photon purity in the total number of clusters. The photon purity is estimated by a data driven approach described in section 7.7.

Direct photons γ^{dir} are defined as produced photons not originating from hadron decays as follows :

$$\gamma^{\text{dir}} = \gamma^{\text{inc}} - \gamma^{\text{decay}} = \gamma^{\text{inc}} \cdot \left(1 - \frac{1}{R_\gamma}\right), \tag{28}$$

where γ^{inc} indicates inclusive photons and γ^{decay} denotes decay photons from hadrons. In order to observe direct photon signals, it is convenient to introduce a variable R_γ which is the ratio of inclusive photons yields to decay photons yields.

$$R_\gamma = \frac{\gamma^{\text{inc}}}{\gamma^{\text{decay}}} = \frac{(\gamma^{\text{inc}}/\pi^0)_{\text{data}}}{(\gamma^{\text{decay}}/\pi^0)_{\text{cocktail}}} \tag{29}$$

The π^0 spectrum is inserted in R_γ because experimentally systematic uncertainties related to the energy measurement cancel out in the ratio. The cocktail simulation (mixture of hadrons which decay into photons such as π^0, η, ω, η', ρ and ϕ e.t.c.) is used to determine decay photon yields. Thus, neutral mesons measurements described in the previous section are important inputs to this cocktail simulation. Finally, if $R_\gamma > 1$, inclusive photon yields in data are larger than decay photon yields, which means the excess of direct photon signals beyond decay photon yields. If R_γ is consistent with unity within experimental uncertainties, upper limits at the 90% confidence level (C.L.) are set. The invariant yield of direct photon is obtained by :

$$\frac{1}{2\pi\ N_{\text{ev}}}\frac{d^2N_{\gamma^{\text{dir}}}}{p_{\text{T}}\ dp_{\text{T}}\ dy} = \frac{1}{2\pi\ N_{\text{ev}}}\frac{d^2N_{\gamma^{\text{inc}}}}{p_{\text{T}}\ dp_{\text{T}}\ dy} \times \left(1 - \frac{1}{R_\gamma}\right) \tag{30}$$

In case of upper limits on direct photon yields at the 90% confidence level, mean data point + 1.28σ is considered at each p_{T} bin.

7.2 Raw yields of clusters

At first, raw yields of cluster have been constructed as shown by Figure 104. Only the core-dispersion cut was applied to clusters in pp and both CPV and core-dispersion cuts was used in Pb–Pb collisions.

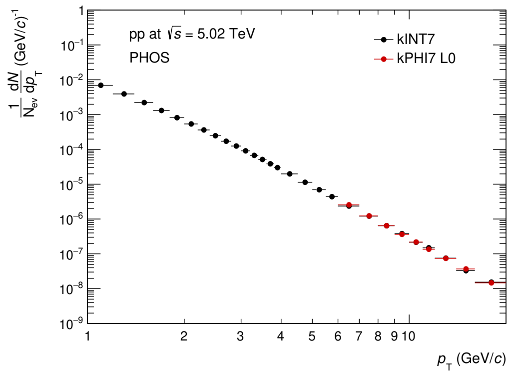

(a) $\frac{1}{N_{\mathrm{ev}}}\frac{dN}{dp_{\mathrm{T}}}$ in pp collisions.

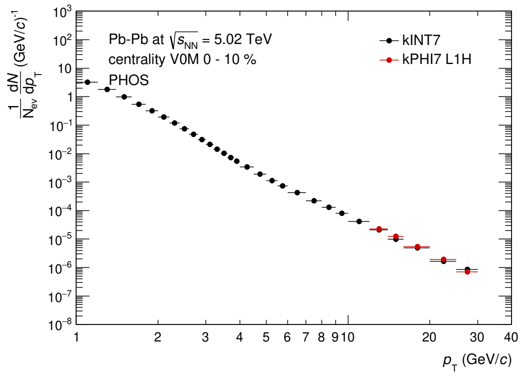

(b) $\frac{1}{N_{\mathrm{ev}}}\frac{dN}{dp_{\mathrm{T}}}$ in Pb–Pb collisions for 0-10%.

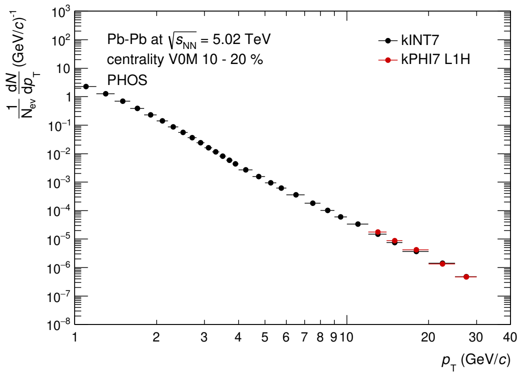

(c) $\frac{1}{N_{\mathrm{ev}}}\frac{dN}{dp_{\mathrm{T}}}$ in Pb–Pb collisions for 10-20%.

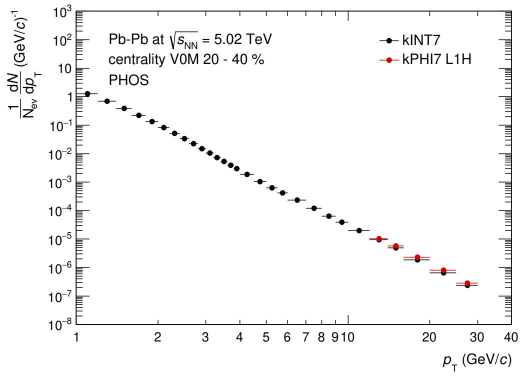

(d) $\frac{1}{N_{\mathrm{ev}}}\frac{dN}{dp_{\mathrm{T}}}$ in Pb–Pb collisions for 20-40%.

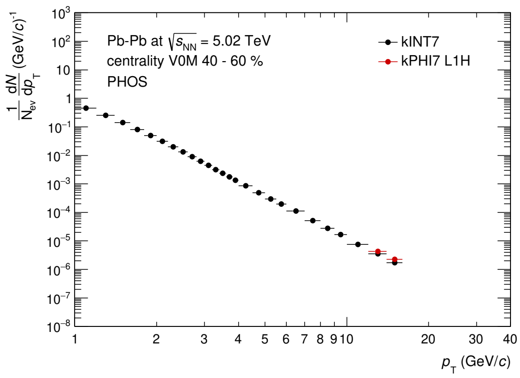

(e) $\frac{1}{N_{\mathrm{ev}}}\frac{dN}{dp_{\mathrm{T}}}$ in Pb–Pb collisions for 40-60%.

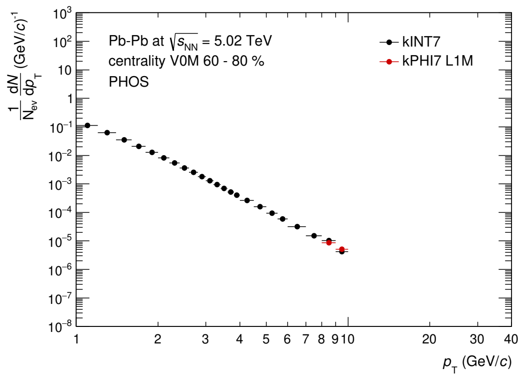

(f) $\frac{1}{N_{\mathrm{ev}}}\frac{dN}{dp_{\mathrm{T}}}$ in Pb–Pb collisions for 60-80%.

Figure 104: Raw yields of clusters in pp and Pb–Pb collisions at $\sqrt{s_{\mathrm{NN}}} = 5.02$ TeV

7.3 Acceptance × reconstruction efficiency

The acceptance × reconstruction efficiency has been measured by the same procedure as neutral mesons analyses, namely the single γ simulation in pp and the embedded simulation (single γ events + real underlying events) in Pb–Pb collisions. One should keep different active area of the PHOS detector in different data taking periods in mind. As single γ simulation on only the PHOS detector was employed, there is no tracking information in single γ simulation for pp case. Thus, only the dispersion cut was applied to clusters in pp collisions for both data and M.C.. However, the CPV cut efficiency in pp collisions is close to 100% due to the low multiplicity environment $\frac{dN_{\mathrm{ch}}}{dy} = 5 \sim 7$ at mid-rapidity [68]. On the other hand, after embedding photons into real underlying events, track matching between a cluster and a track was available in Pb–Pb case. Late conversion electrons ($\gamma \to e^+e^-$ outside of TPC) are also considered as photon signals, because they can not be rejected by the CPV cut. Efficiencies are plotted on Figure 105. The higher efficiency is observed in peripheral collisions due to the small overlapping probability between clusters, as expected.

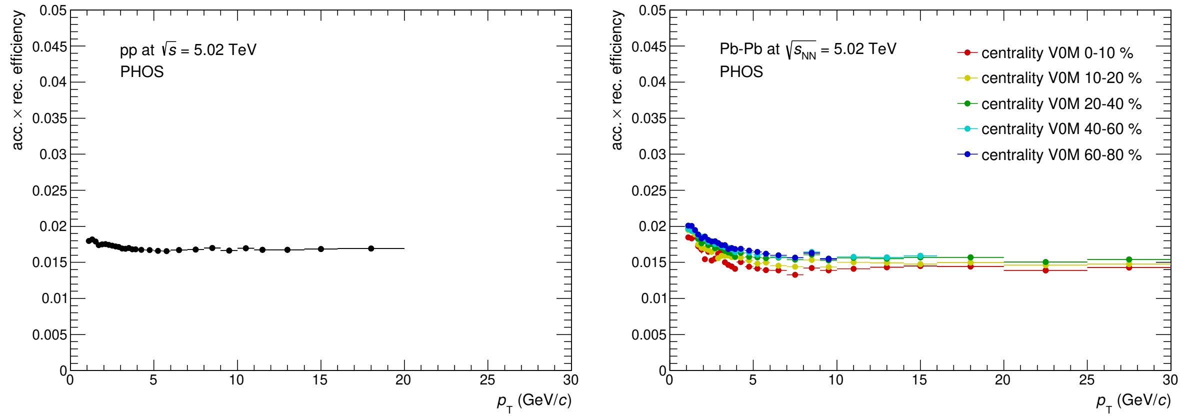

(a) The efficiency in pp collisions.

(b) The efficiency in Pb–Pb collisions.

Figure 105: Acceptance × reconstruction efficiencies in pp and Pb–Pb collisions at $\sqrt{s_{\mathrm{NN}}} = 5.02$ TeV

7.4 TOF cut efficiency

This is the same as the neutral mesons analysis, but corrected by $1/\varepsilon_{\mathrm{TOF}}$.

7.5 Trigger efficiency

This is the same as the neutral mesons analysis, but corrected by $1/\varepsilon_{\mathrm{trg}}$.

7.6 Feed down correction for $K^0_S \to \pi^0\pi^0 \to 4\gamma$

Photons from strange hadron decays were subtracted based on PYTHIA and HIJING event generator for pp and Pb–Pb respectively. $K^{\pm}/\pi^{\pm}$ has been already tuned for the π^0 measurement explained in the previous section. They are about 5-6% at low p_{T} and 2-3% at high p_{T}.

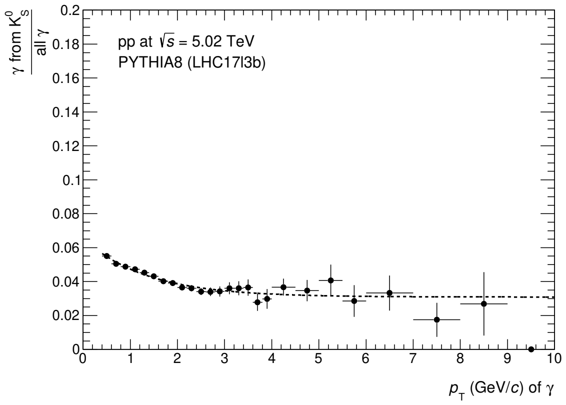

(a) The feed down correction in pp collisions.

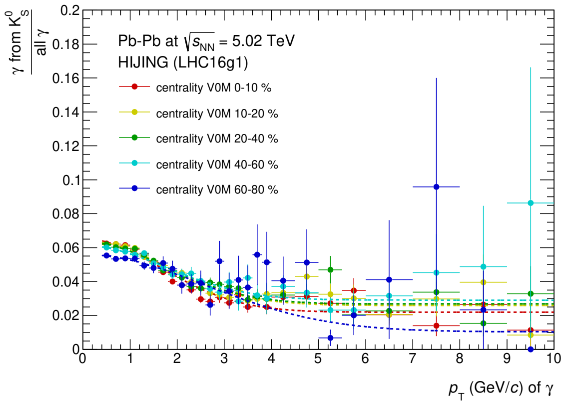

(b) The feed down correction in Pb–Pb collisions.

Figure 106: Feed down corrections from K^0_S in pp and Pb–Pb collisions at $\sqrt{s_{\rm NN}} = 5.02$ TeV

7.7 Photon purity

In order to measure inclusive and direct photons spectra, the photon purity has been estimated by a data driven approach. The definition of photon purity is a fraction of the number of photon clusters in the total number of clusters.

7.7.1 Data driven approach for photon purity estimation

The total number of cluster $N_{\rm cluster}$ can be expressed as $N_{\rm cluster} = N_\gamma + N_{e^\pm} + N_{\pi^\pm} + N_{K^\pm} + N_p + N_{\bar{p}} + N_n + N_{\bar{n}} + N_{K^0_L} + \cancel{N_{\mu^\pm}} + \cancel{N_\nu} + \cancel{N_{\bar{\nu}}}$. It is known that $\bar{p}/p \sim 1$ in high-energy hadron collisions [86] and $N_p \sim N_n$ based on isospin symmetry. In this analysis, there are 4 independent PID cuts (no PID, CPV, Disp, and CPV+Disp). Then, a system 31 can be constructed to estimate particle composition in PHOS clusters.

$$\begin{pmatrix} N_{\rm all} \\ N_{\rm CPV} \\ N_{\rm Disp} \\ N_{\rm both} \end{pmatrix} = \begin{pmatrix} 1 & C_{\rm ch} + C_{\rm nh} & 2 & 1 \\ \varepsilon_\gamma^{\rm CPV} & \varepsilon_{\pi^\pm}^{\rm CPV} C_{\rm ch} + \varepsilon_\gamma^{\rm CPV} C_{\rm nh} & \varepsilon_{\bar{p}}^{\rm CPV} + \varepsilon_\gamma^{\rm CPV} & \varepsilon_{e^\pm}^{\rm CPV} \\ \varepsilon_\gamma^{\rm Disp} & \varepsilon_{\pi^\pm}^{\rm Disp} (C_{\rm ch} + C_{\rm nh}) & 2\varepsilon_{\bar{p}}^{\rm Disp} & \varepsilon_{e^\pm}^{\rm Disp} \\ \varepsilon_\gamma^{\rm CPV} \times \varepsilon_\gamma^{\rm Disp} & (\varepsilon_{\pi^\pm}^{\rm CPV} C_{\rm ch} + \varepsilon_\gamma^{\rm CPV} C_{\rm nh}) \times \varepsilon_{\pi^\pm}^{\rm Disp} & (\varepsilon_{\bar{p}}^{\rm CPV} + \varepsilon_\gamma^{\rm CPV}) \times \varepsilon_{\bar{p}}^{\rm Disp} & \varepsilon_{e^\pm}^{\rm CPV} \times \varepsilon_{e^\pm}^{\rm Disp} \end{pmatrix} \begin{pmatrix} N_\gamma \\ N_{\pi^\pm} \\ N_{\bar{p}} \\ N_{e^\pm} \end{pmatrix} \tag{31}$$

where $C_{\rm ch} = 1 + K^\pm/\pi^\pm + p/\pi^\pm$ (sum of relative $\pi^\pm$, $K^\pm$ and p contributions) and $C_{\rm nh} = 0.5 \times K^\pm/\pi^\pm + p/\pi^\pm$ (sum of relative K^0_L and n contributions) as a function of $p_{\rm T}^{\rm cluster}$ on PHOS. ε^i_X is efficiency of PID cut i for particle X. Charged particles are identified by dE/dx in TPC. It has been reported that electrons/positrons from semi-leptonic decays of heavy flavor hadrons becomes larger at the higher collision energy at LHC [87], compared to RHIC. So, electrons/positrons contributions has to be taken into account. Here, anti-protons contribution is different from protons because of detector response. Protons behave as minimum ionizing particles (MIP) in an electro-magnetic calorimeter. On the other hand, anti-protons can deposit higher energy because of annihilation. Finally, $N_\gamma, N_{\pi^\pm}, N_{\bar{p}}, N_{e^\pm}$ are obtained by solving system 31. Adding/removing $C_{\rm nh}$ is considered as a systematic uncertainty of photon purity. To evaluate the CPV cut efficiency for charged particles, the mixed event technique was used to subtract random matchings. The distance between a PHOS cluster in a current event and a charged particle in another event is measured to make a random matching distribution (Figure 107). Then, the CPV cut efficiency for charged particles (i.e. how many charged particles can survive after applying the CPV cut) is defined as :

$$\varepsilon_{\rm ch}^{\rm CPV} = \frac{\text{Number of entries beyond a criterion in the real matching distribution}}{\text{Number of all entries in the real matching distribution}}, \tag{32}$$

and the dispersion cut efficiency for charged particles is defined as :

$$\varepsilon_{\rm ch}^{\rm Disp} = \frac{\text{Number of particles with Disp cut}}{\text{Number of charged particles without Disp cut}} \tag{33}$$

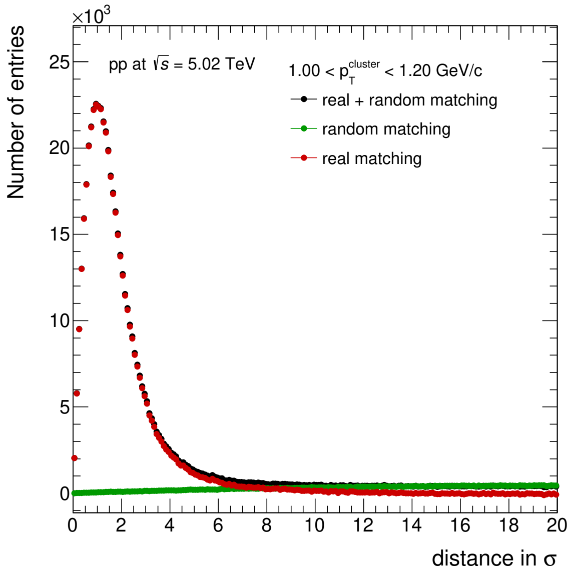

Figure 107: The distance between a cluster on PHOS and a charged particle in pp collisions at $\sqrt{s}$ = 5.02 TeV.

7.7.2 Photon purity in pp collisions at $\sqrt{s}$ = 5.02 TeV

Figure 108 shows particle ratios on PHOS that are inputs for $C_{\rm ch}$ and $C_{\rm nh}$. Figure 109 shows PID cut efficiencies for different particles. The matching criterion between a charged particle with a cluster on PHOS is $r < 2\sigma$ for evaluation of the dispersion cut efficiency. Especially for $e^{\pm}$, $0.8 < E/p < 1.2$ was applied to get higher electron purity. To avoid statistical fluctuation at high $p_{\rm T}$ ($p_{\rm T} > 4$ GeV/c), each efficiency is fitted by constant and used as matrix elements. The particle abundance on PHOS is summarized on Figure 110. The photon purity is 90 % with the dispersion cut and 97 % with the CPV and the dispersion cuts at high $p_{\rm T}$. Electrons and positrons converted from photons outside of TPC, so-called late conversion electrons, can not be tracked, because there is no tracking detector there. Therefore, late conversion electrons denoted by L.C. $e^{\pm}$ are treated as photon signals in M.C. truth.

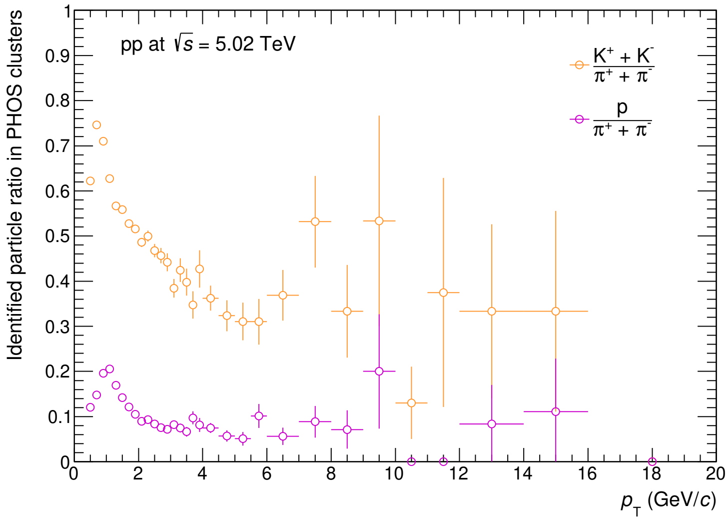

Figure 108: Measured particle ratios on PHOS in pp collisions at $\sqrt{s} = 5.02$ TeV.

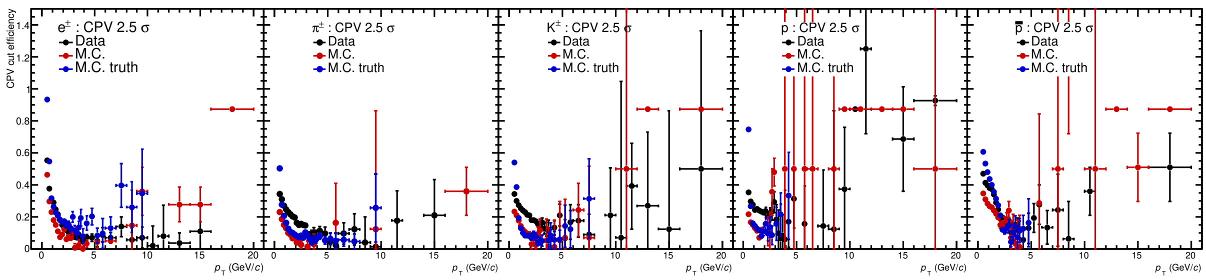

(a) CPV cut efficiency for charged particles.

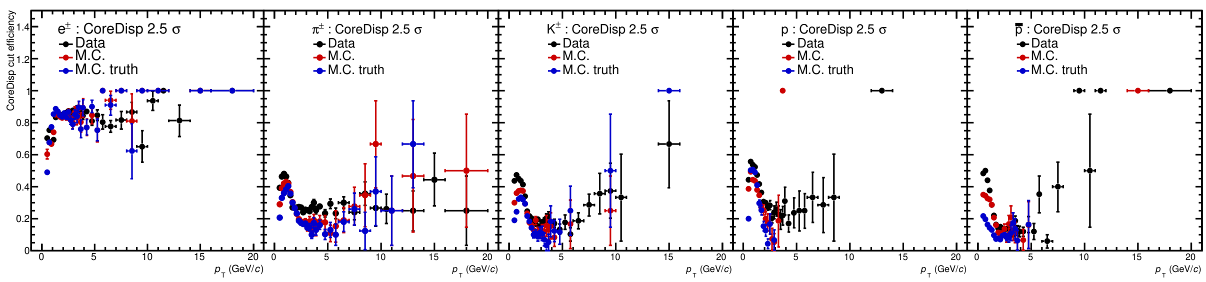

(b) CoreDisp cut efficiency for charged particles.

Figure 109: PID cut efficiencies for identified charged particles in pp collisions at $\sqrt{s} = 5.02$ TeV. From left to right, $e^{\pm}$, $\pi^{\pm}$, $K^{\pm}$, p and $\bar{p}$. Black for data, red for M.C. DDA, blue for M.C. truth.

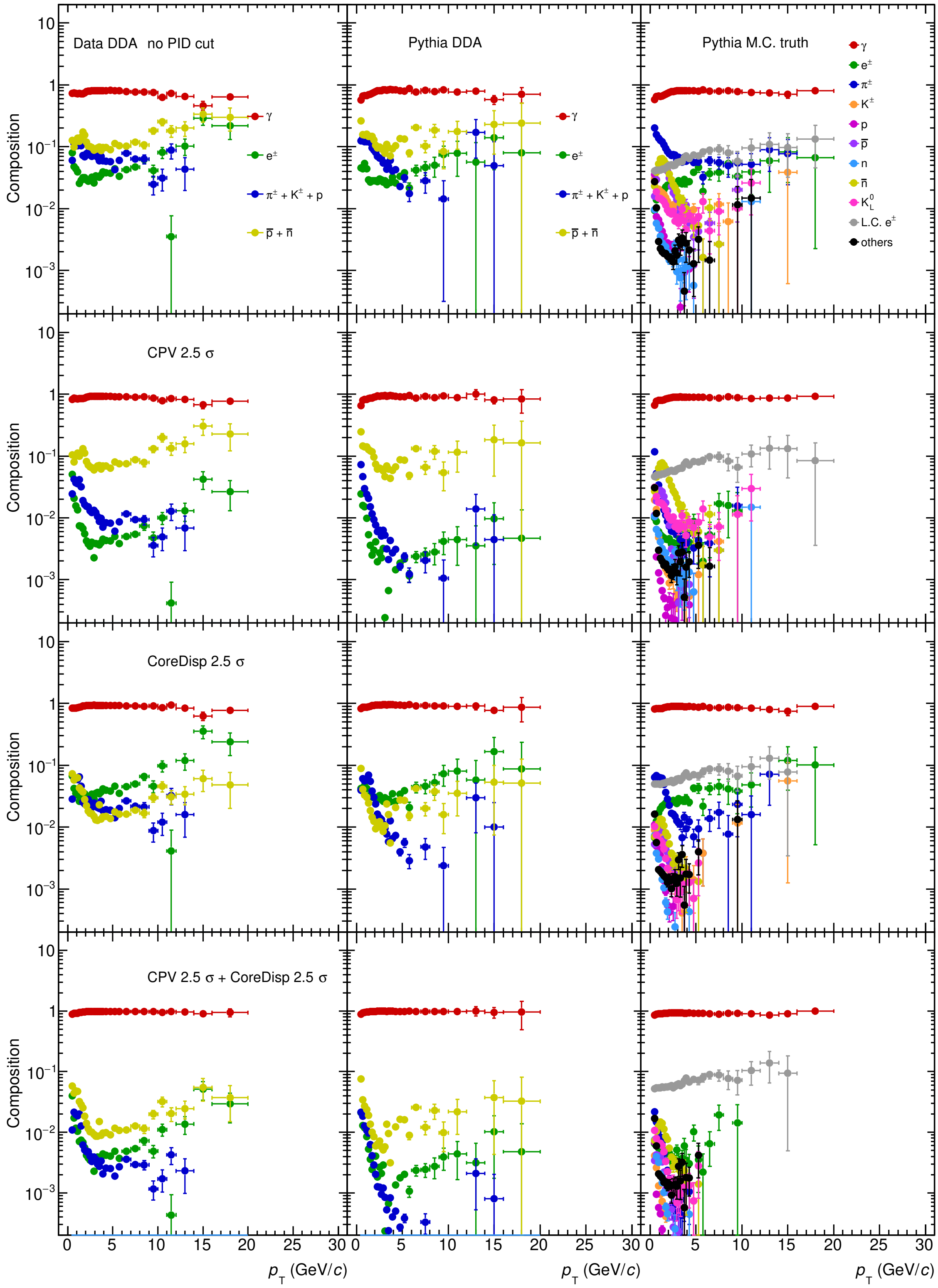

Figure 110: The summary of particle abundance on PHOS in pp collisions at $\sqrt{s} = 5.02$ TeV for $C_{\rm nh} = 0$.

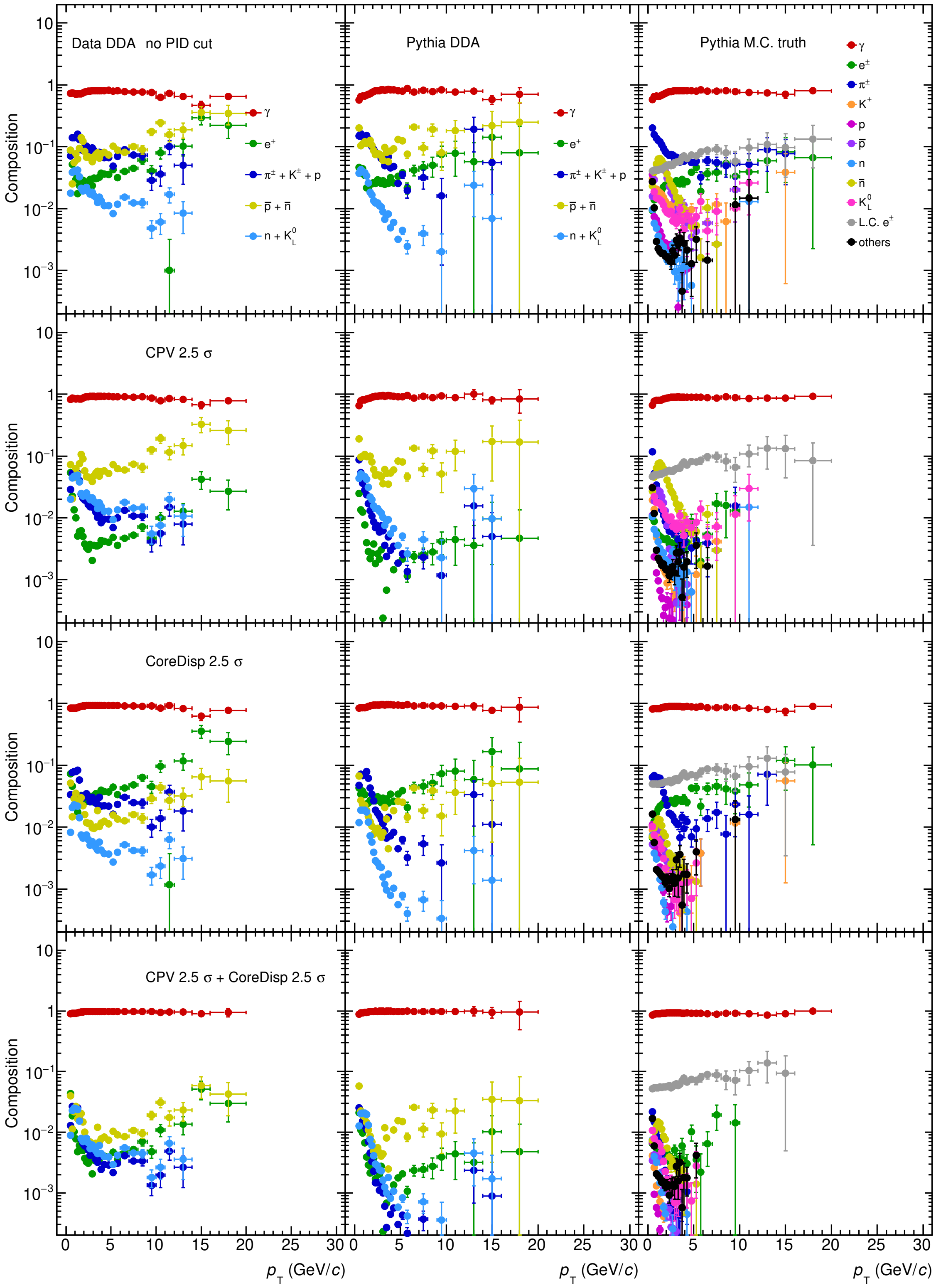

Figure 111: The summary of particle abundance on PHOS in pp collisions at $\sqrt{s} = 5.02$ TeV for $C_{\mathrm{nh}} = 0.5 \times K^{\pm}/\pi^{\pm} + p/\pi^{\pm}$.

1373 7.7.3 Photon purity in Pb–Pb collisions at $\sqrt{s_{\mathrm{NN}}}$ = 5.02 TeV

The procedure is the same as the pp case.

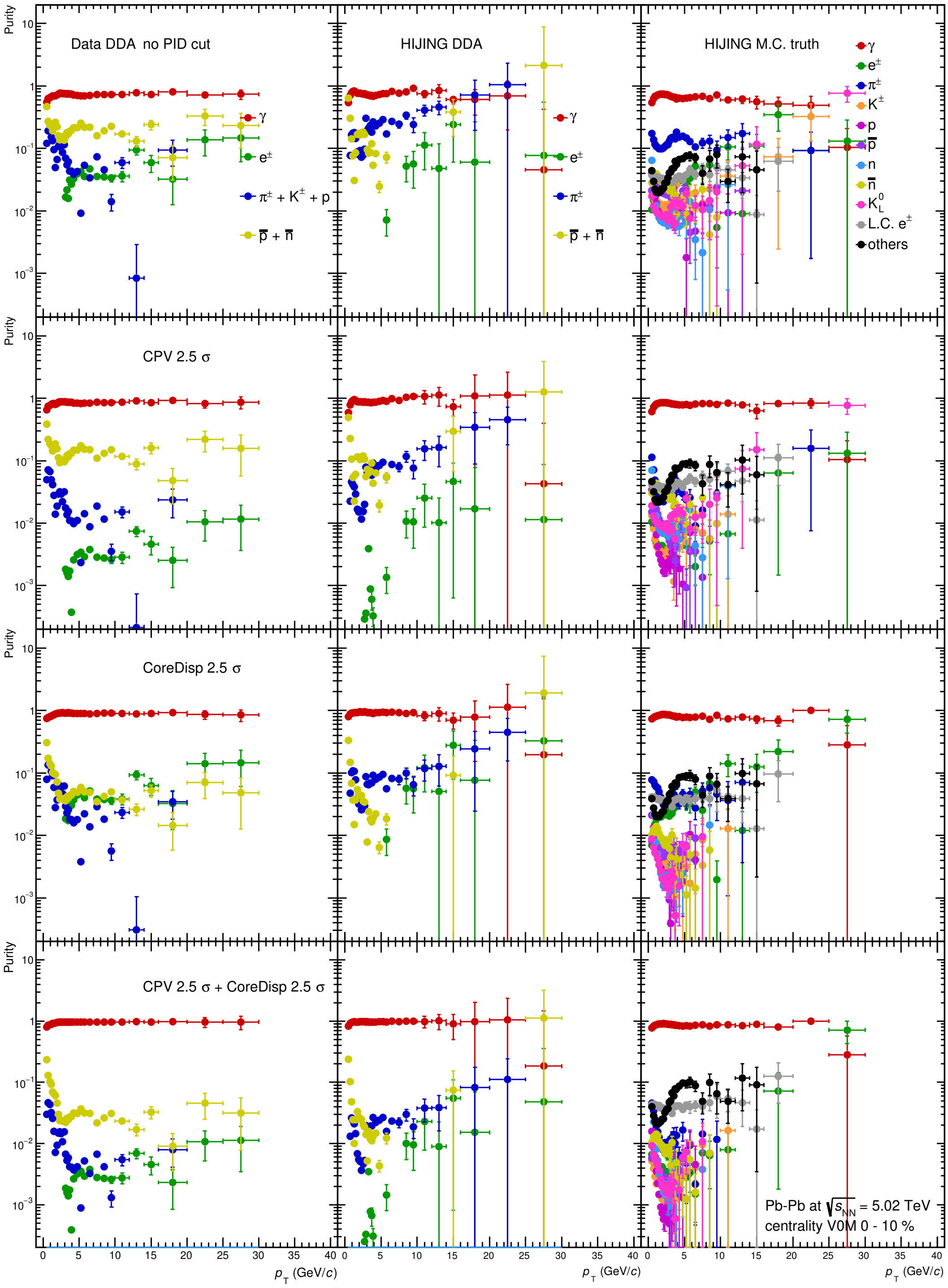

Figure 112: The summary of particle abundance on PHOS in 0-10% Pb–Pb collisions at $\sqrt{s_{\mathrm{NN}}}$ = 5.02 TeV for $C_{\mathrm{nh}} = 0$.

1374

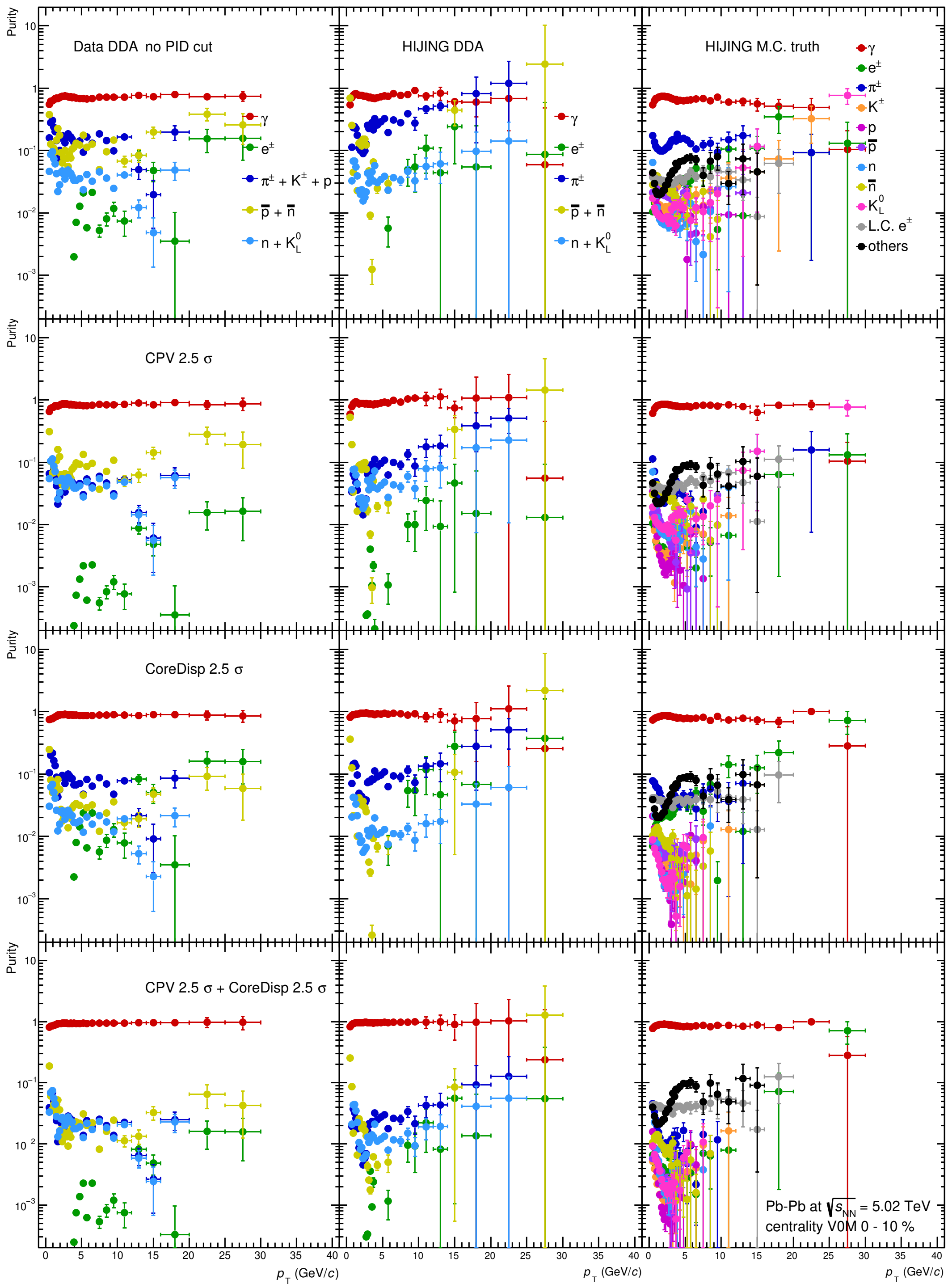

Figure 113: The summary of particle abundance on PHOS in 0-10% Pb–Pb collisions at $\sqrt{s_{\rm NN}}$ = 5.02 TeV for $C_{\rm nh} = 0.5 \times K^{\pm}/\pi^{\pm} + p/\pi^{\pm}$.

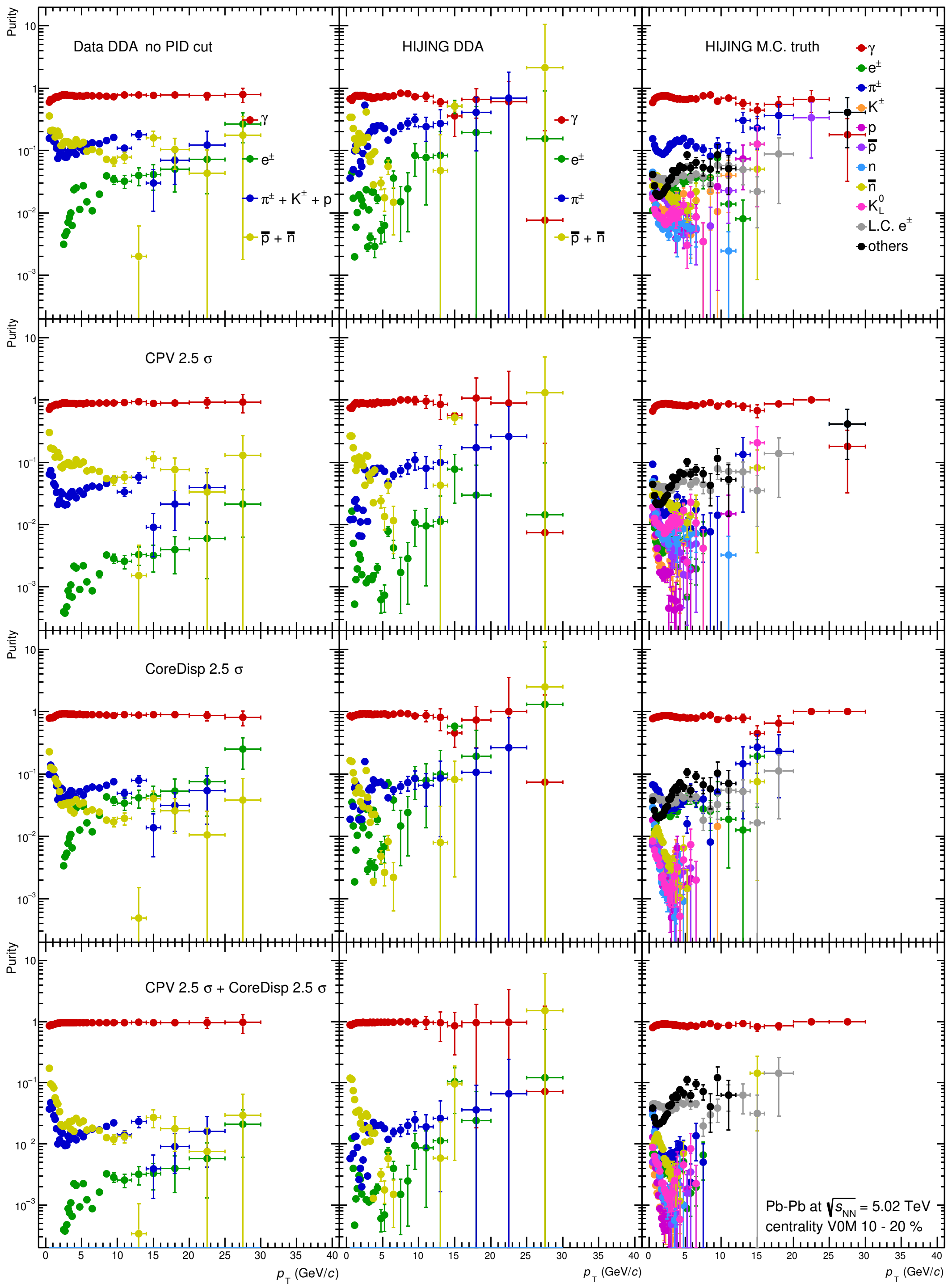

Figure 114: The summary of particle abundance on PHOS in 10-20% Pb–Pb collisions at $\sqrt{s_{\mathrm{NN}}}$ = 5.02 TeV for $C_{\mathrm{nh}} = 0$.

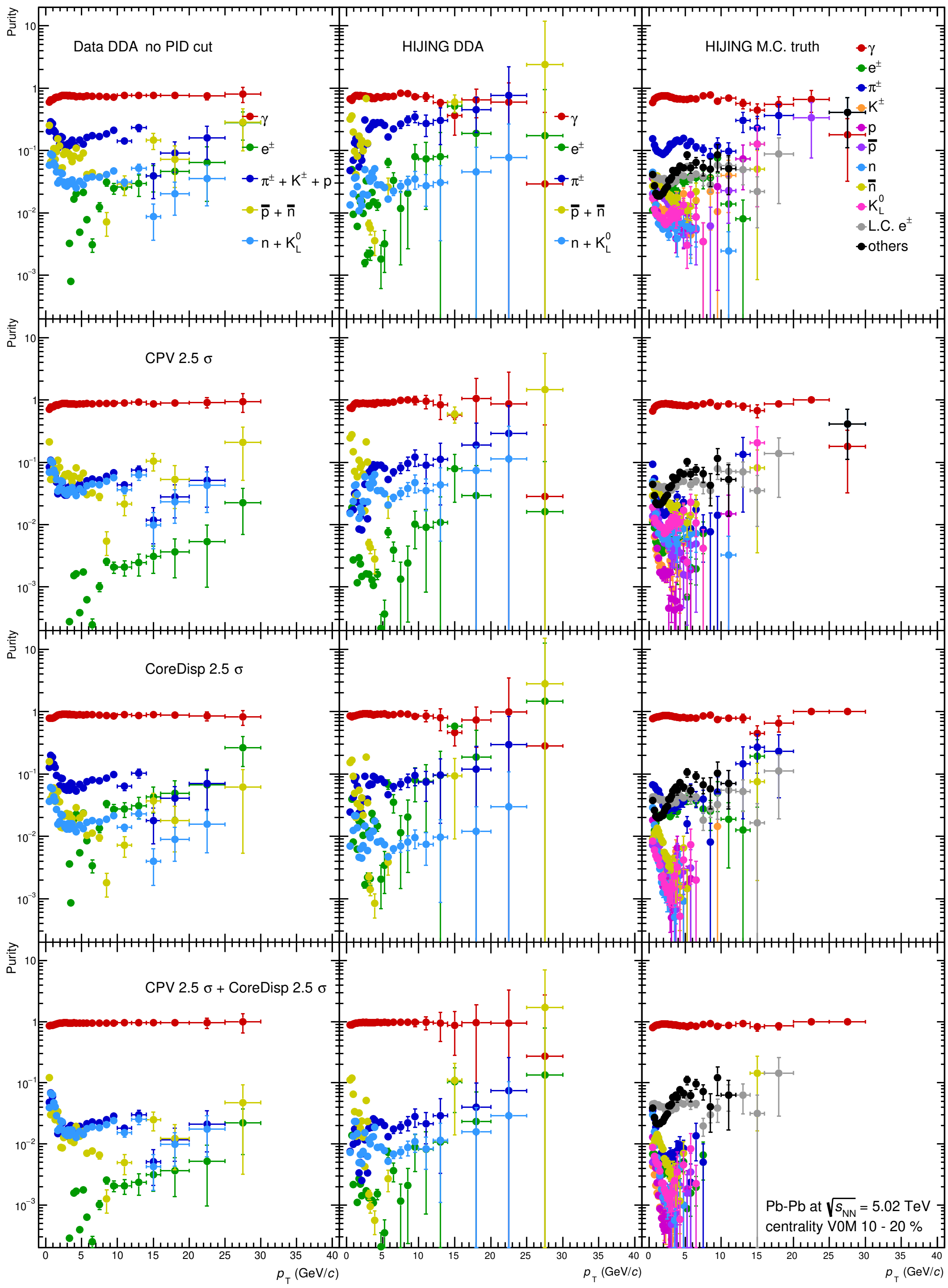

Figure 115: The summary of particle abundance on PHOS in 10-20% Pb–Pb collisions at $\sqrt{s_{\rm NN}}$ = 5.02 TeV for $C_{\rm nh} = 0.5 \times K^{\pm}/\pi^{\pm} + p/\pi^{\pm}$.

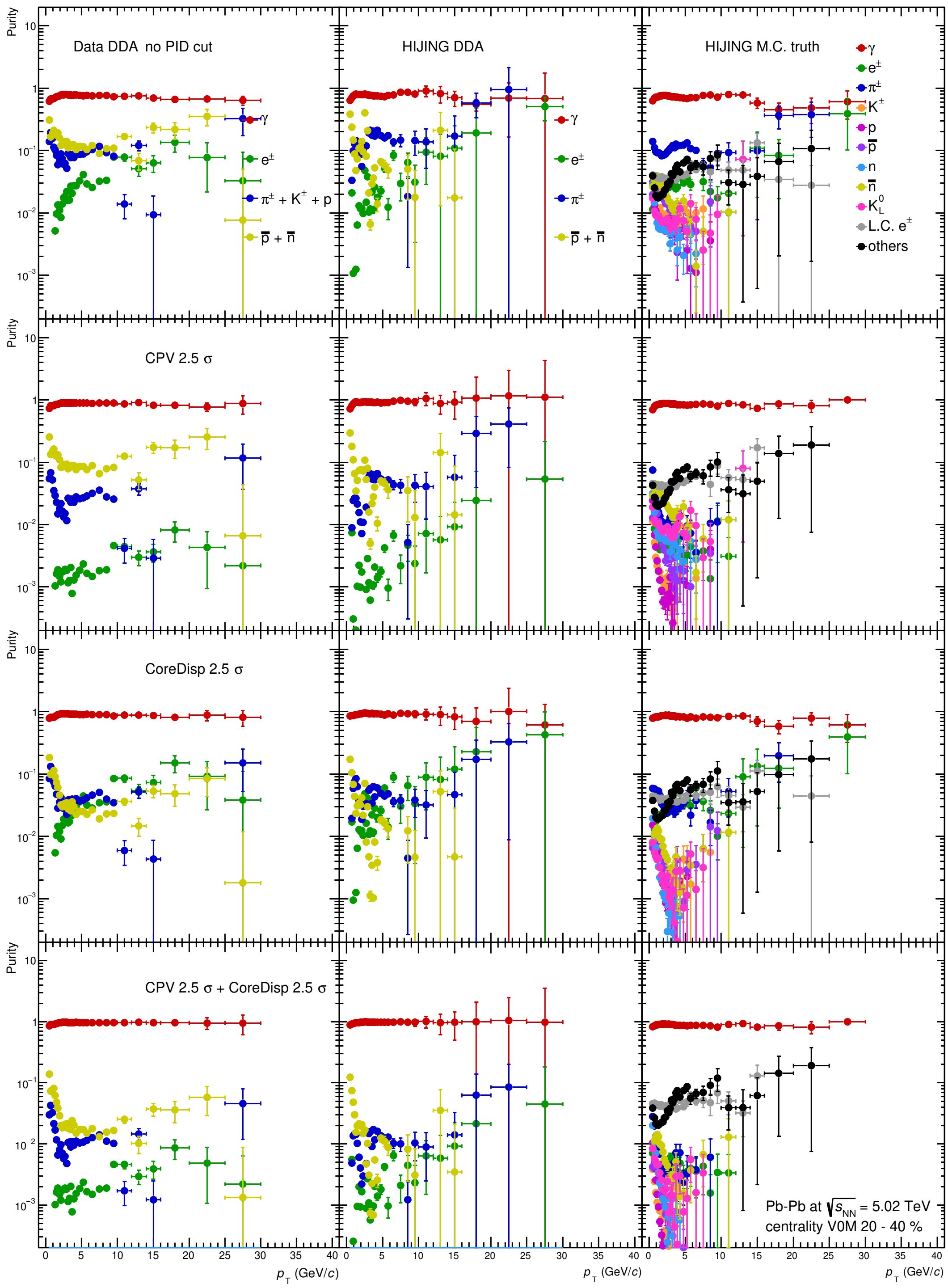

Figure 116: The summary of particle abundance on PHOS in 20-40% Pb–Pb collisions at $\sqrt{s_{\rm NN}}$ = 5.02 TeV for $C_{\rm nh} = 0$.

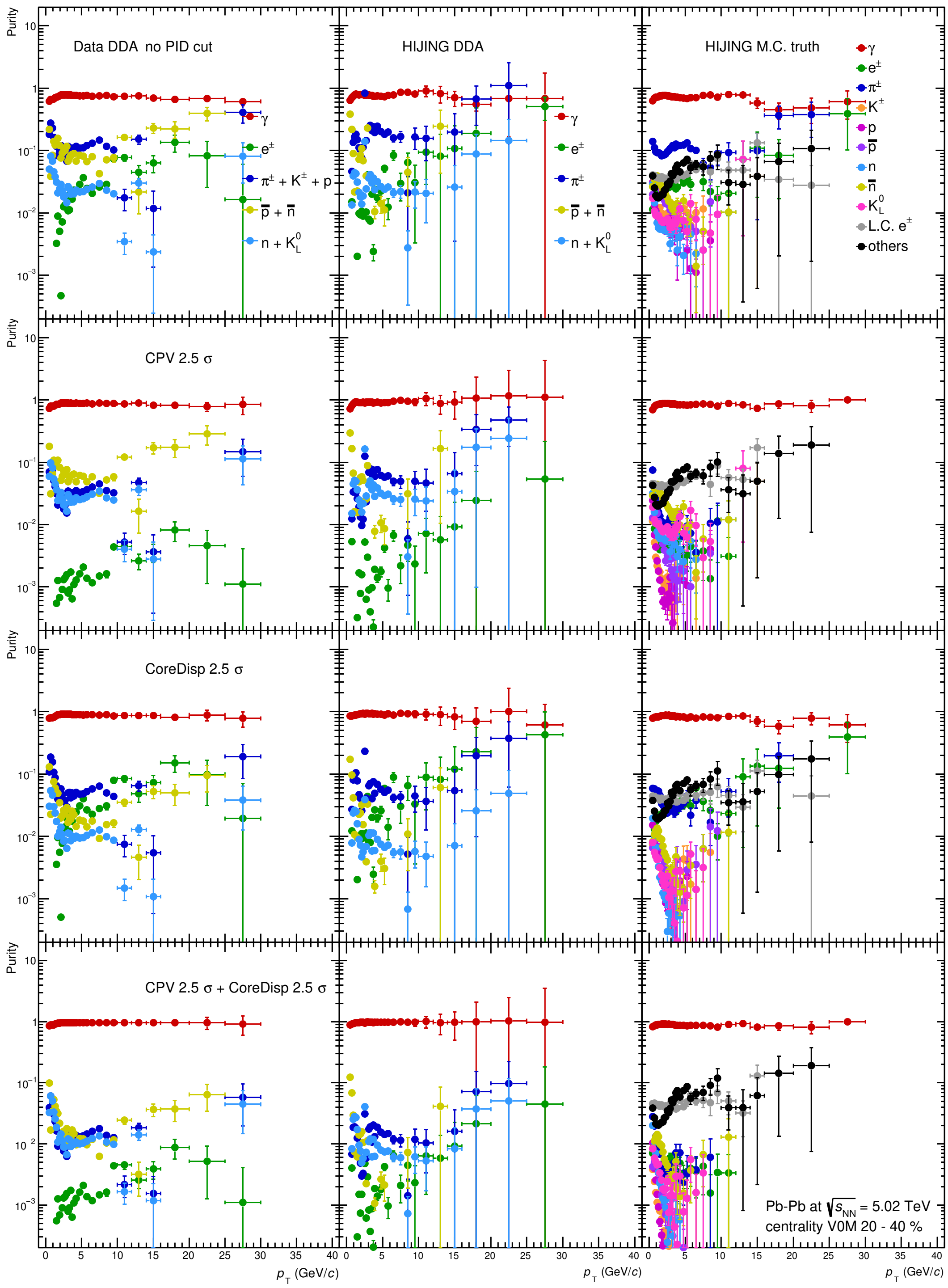

Figure 117: The summary of particle abundance on PHOS in 20-40% Pb–Pb collisions at $\sqrt{s_{\rm NN}}$ = 5.02 TeV for $C_{\rm nh} = 0.5 \times K^{\pm}/\pi^{\pm} + p/\pi^{\pm}$.

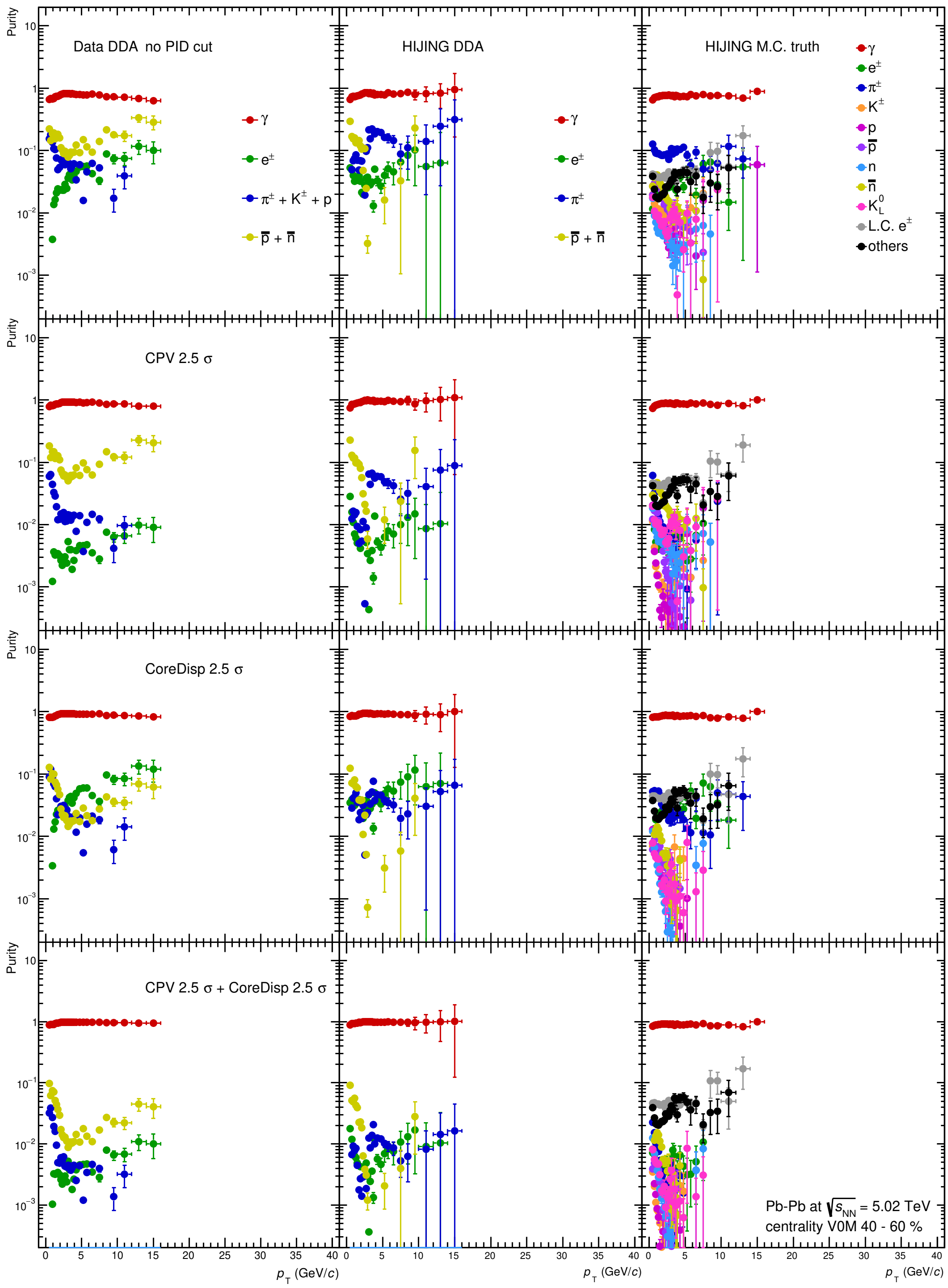

Figure 118: The summary of particle abundance on PHOS in 40-60% Pb–Pb collisions at $\sqrt{s_{\rm NN}}$ = 5.02 TeV for $C_{\rm nh} = 0$.

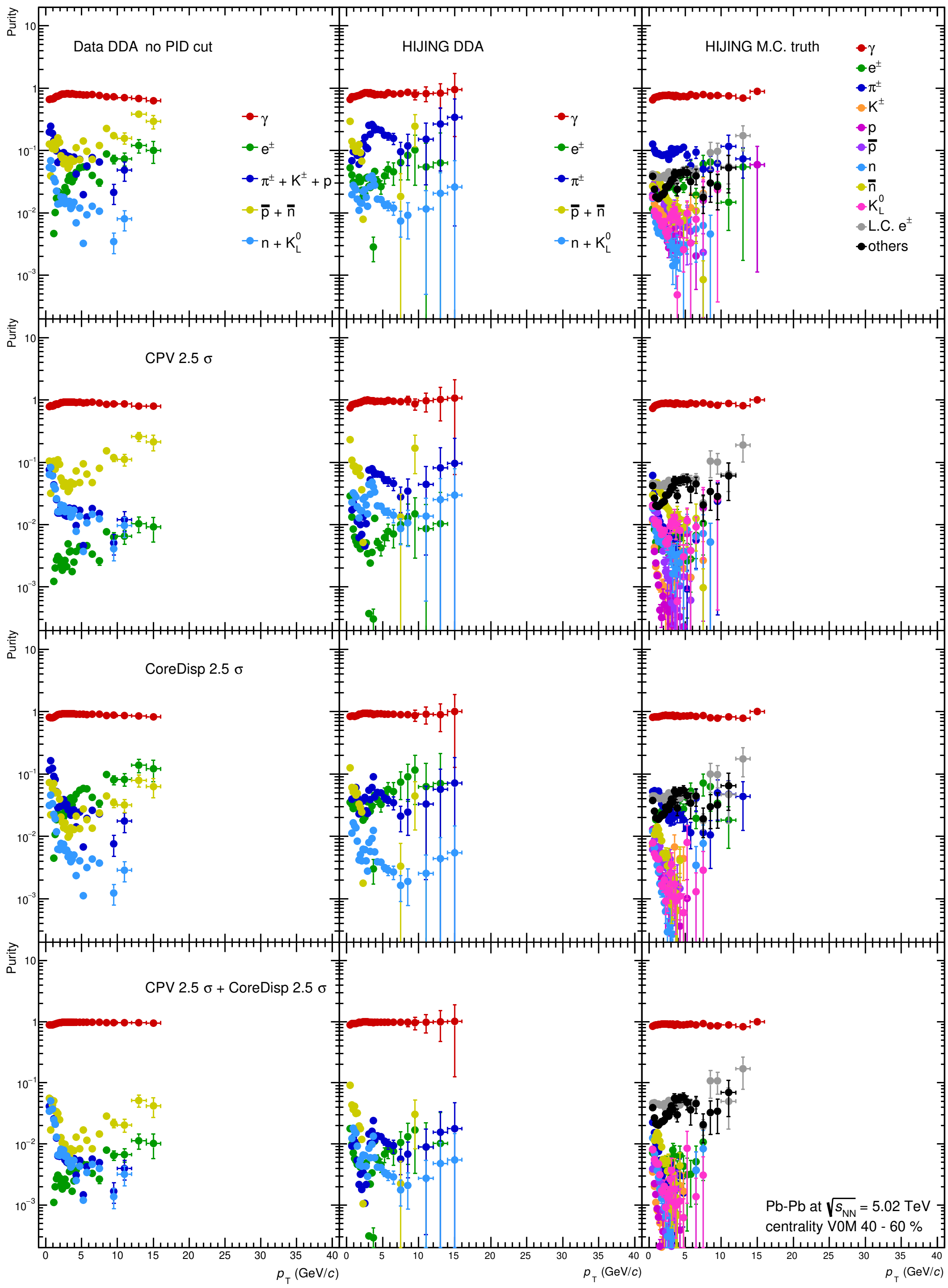

Figure 119: The summary of particle abundance on PHOS in 40-60% Pb–Pb collisions at $\sqrt{s_{\rm NN}}$ = 5.02 TeV for $C_{\rm nh} = 0.5 \times K^{\pm}/\pi^{\pm} + p/\pi^{\pm}$.

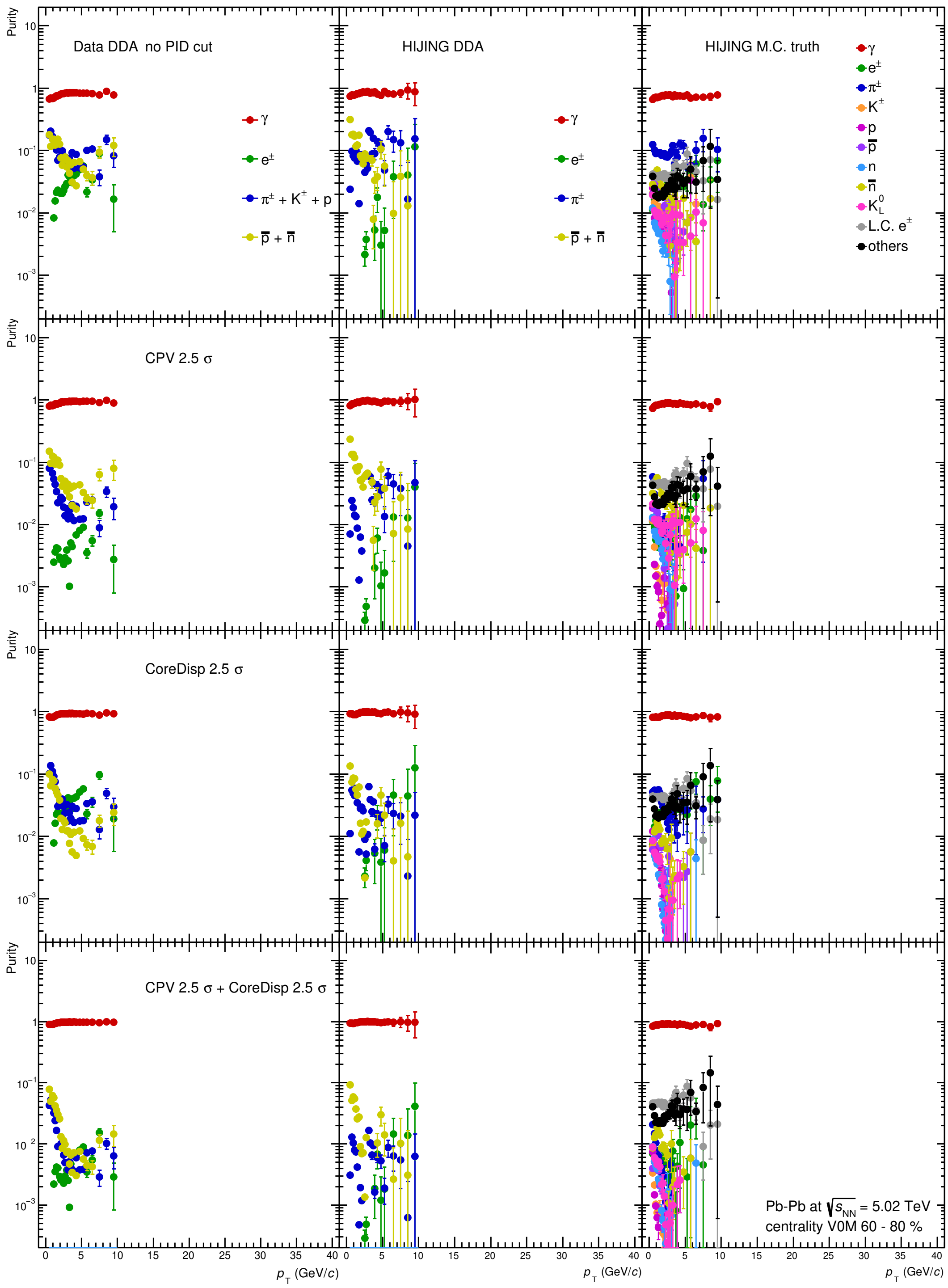

Figure 120: The summary of particle abundance on PHOS in 60-80% Pb–Pb collisions at $\sqrt{s_{\rm NN}}$ = 5.02 TeV for $C_{\rm nh} = 0$.

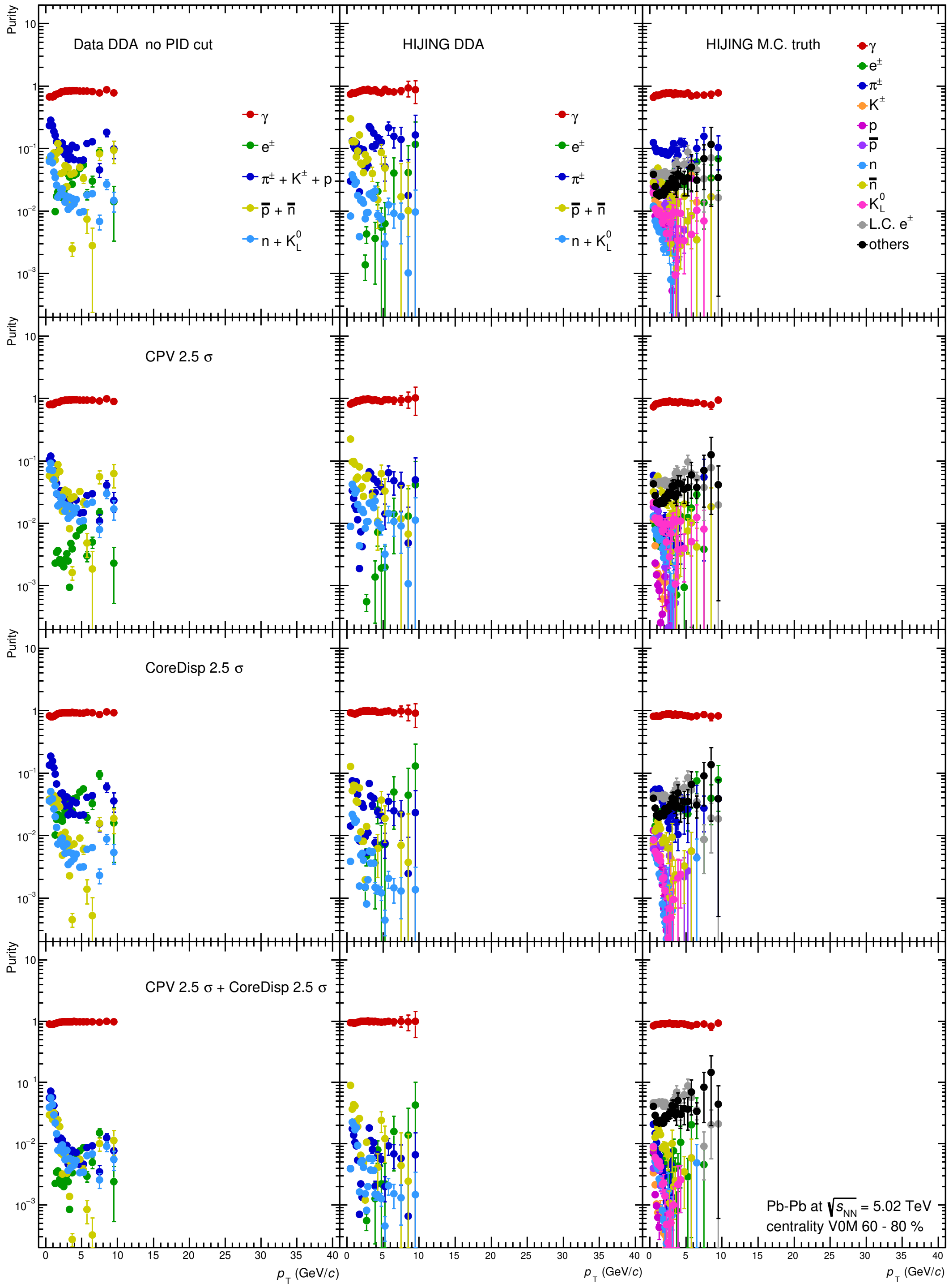

Figure 121: The summary of particle abundance on PHOS in 60-80% Pb–Pb collisions at $\sqrt{s_{\mathrm{NN}}}$ = 5.02 TeV for $C_{\mathrm{nh}} = 0.5 \times K^{\pm}/\pi^{\pm} + p/\pi^{\pm}$.

7.8 Photon cocktail simulation

The cocktail simulation is used to determine decay photon yield from hadrons. Measured p_{T} spectra of hadrons desctibed in section 6 are inputs to the cocktail simulation. Technically, TPythia6Decayer in ROOT6 framework based on PYTHIA 6.4 [88] with flat p_{T}, azimuthal angle and rapidity distribution is used for decay simulation. The source of cocktail simulation considered in this thesis is summarized in Table.6.

Non-measured particles (ω and η') are scaled from the π^0 spectrum using m_{T} scaling [89]. The

Table 6: Particles which decay into photons

Particle	mass (MeV/c^2)	decay channel	branching ratio (%)
π^0	135	$\gamma\gamma$	98.8
		γe^+e^-	1.2
η	547	$\gamma\gamma$	39.2
		$\gamma\pi^+\pi^-$	4.8
		γe^+e^-	4.9×10^{-3}
ω	782	$\pi^0\gamma$	8.3
		$\eta\gamma$	4.6×10^{-4}
η'	958	$\gamma\gamma$	2.2
		$\rho^0\gamma$	29.1
		$\omega\gamma$	2.8

m_{T} is called transverse mass which is defined by $m_{\mathrm{T}} = \sqrt{p_{\mathrm{T}}^2 + m^2}$. The relation to the invariant yield is:

$$\frac{1}{p_{\mathrm{T}}}\frac{d^2N}{dp_{\mathrm{T}}dy} = \frac{1}{m_{\mathrm{T}}}\frac{d^2N}{dm_{\mathrm{T}}dy}$$

The meaning of m_{T} scaling is that particle yields at the same m_{T} can be scaled from light hadron yields (e.g. $\pi^{\pm,0}$ for mesons or p for baryons) by a constant coefficient C_h. Therefore, one can write kinematic relation between π and particle of interest (h) as following:

$$\begin{aligned} p_{\mathrm{T},\pi}^2 + m_\pi^2 &= p_{\mathrm{T},h}^2 + m_h^2 \\ p_{\mathrm{T},\pi}^2 &= p_{\mathrm{T},h}^2 + m_h^2 - m_\pi^2 \end{aligned}$$

Finally, the invariant $p_{\mathrm{T},h}$ spectrum for particle h can be obtained by:

$$f_h(p_{\mathrm{T},h}) = C_h \times f_\pi(\sqrt{p_{\mathrm{T},h}^2 + m_h^2 - m_\pi^2})$$

where, f_π represents parameterization of invariant p_{T} spectrum of reference particle π. Typically, $\omega/\pi^0 = 0.85$ [90] and $\eta'/\pi^0 = 0.40$ [88].

7.8.1 Cocktail simulation in pp at $\sqrt{s} = 5.02$ TeV

7.8.2 Cocktail simulation in Pb–Pb at $\sqrt{s_{\mathrm{NN}}} = 5.02$ TeV

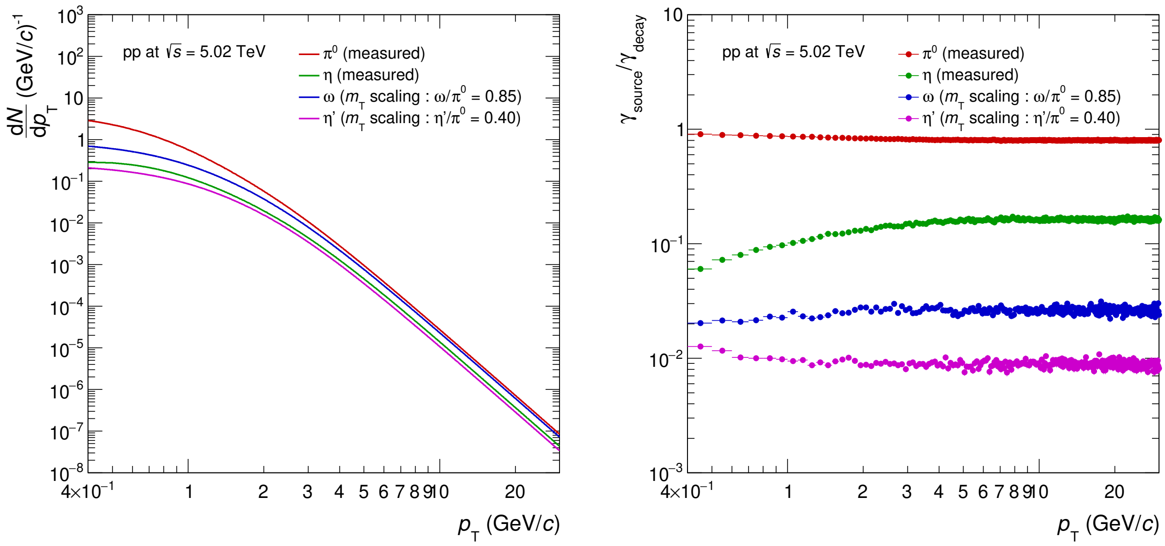

(a) The input p_{T} spectra from different mesons. (b) The fraction of each decay photon source.

Figure 122: The decay photon cocktail in pp collisions at $\sqrt{s} = 5.02$ TeV

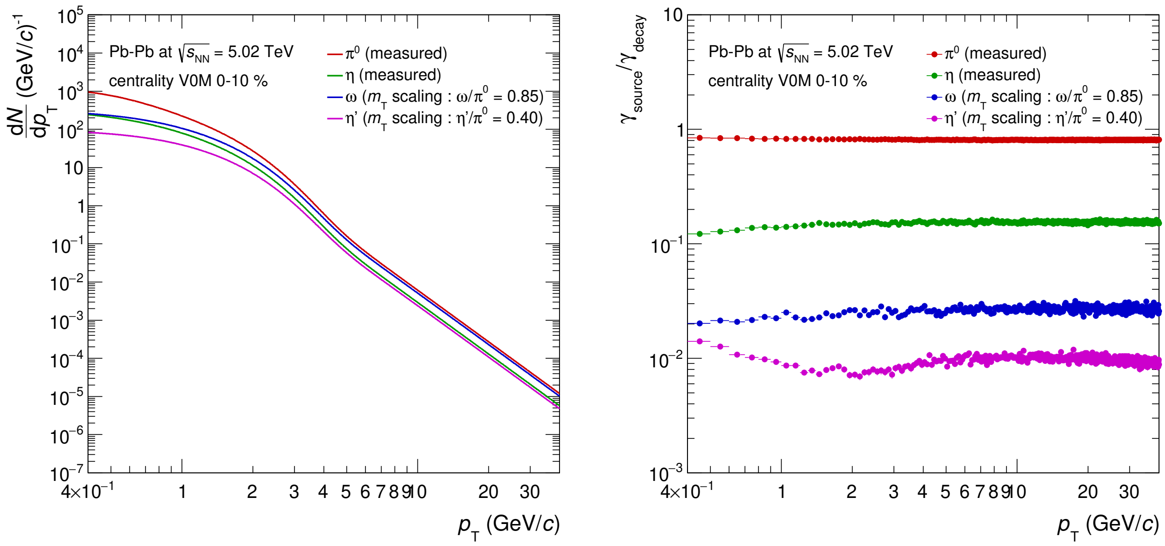

(a) The input p_{T} spectra from different mesons. (b) The fraction of each decay photon source.

Figure 123: The decay photon cocktail in Pb–Pb collisions at $\sqrt{s} = 5.02$ TeV centrality 0-10 %

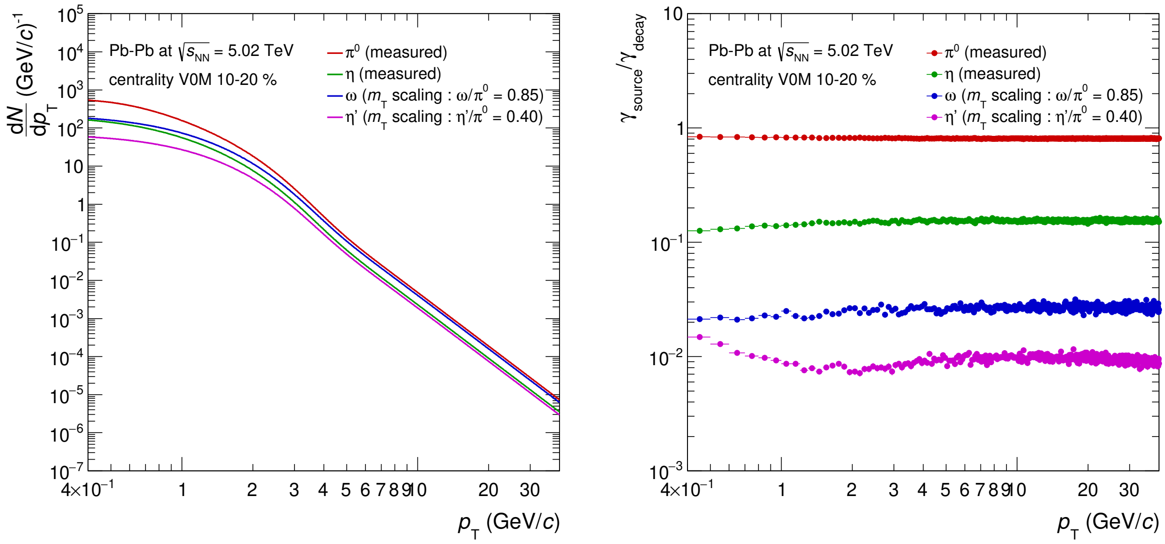

(a) The input p_T spectra from different mesons. (b) The fraction of each decay photon source.

Figure 124: The decay photon cocktail in Pb–Pb collisions at $\sqrt{s}$ = 5.02 TeV centrality 10-20 %

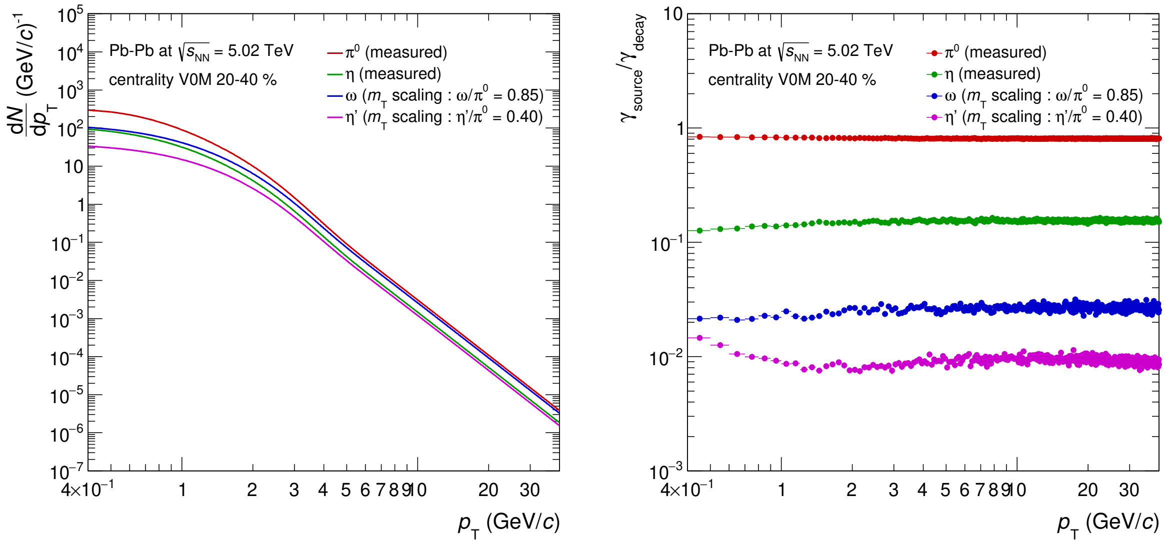

(a) The input p_T spectra from different mesons. (b) The fraction of each decay photon source.

Figure 125: The decay photon cocktail in Pb–Pb collisions at $\sqrt{s}$ = 5.02 TeV centrality 20-40 %

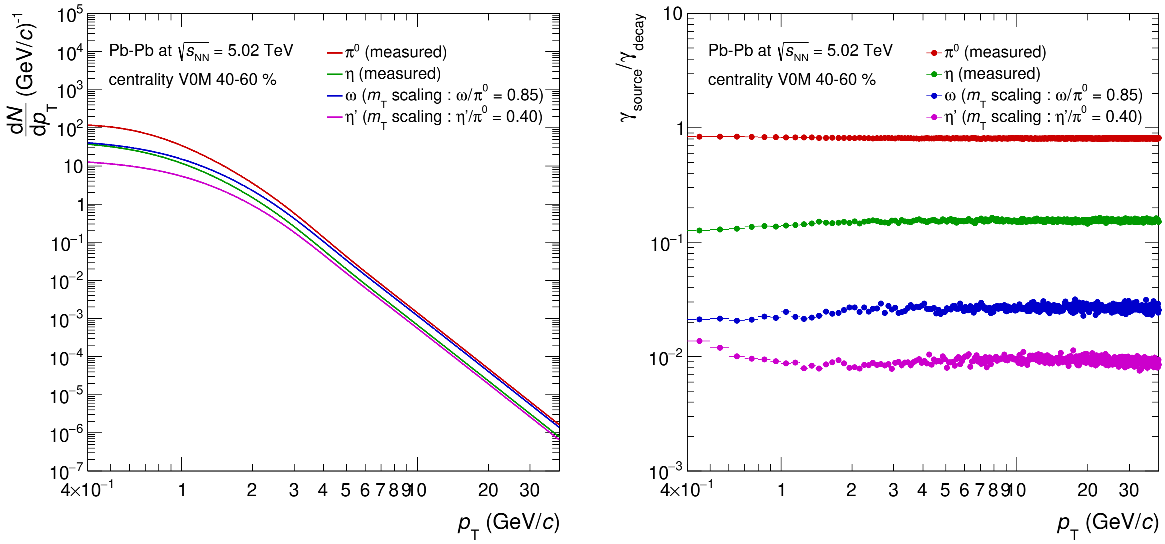

(a) The input p_T spectra from different mesons.

(b) The fraction of each decay photon source.

Figure 126: The decay photon cocktail in Pb–Pb collisions at $\sqrt{s}$ = 5.02 TeV centrality 40-60 %

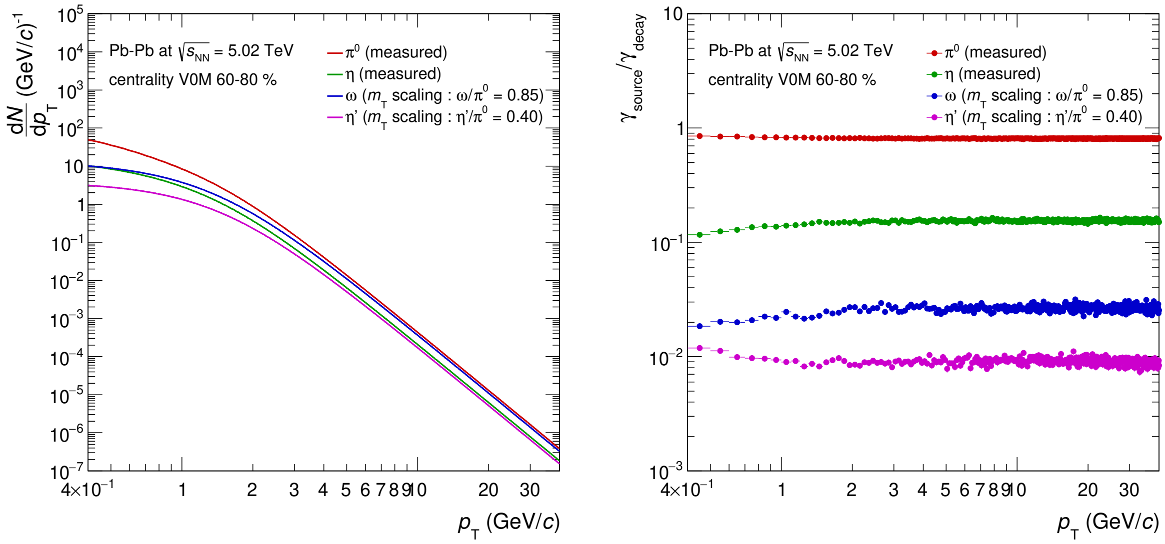

(a) The input p_T spectra from different mesons.

(b) The fraction of each decay photon source.

Figure 127: The decay photon cocktail in Pb–Pb collisions at $\sqrt{s}$ = 5.02 TeV centrality 60-80 %

8 Systematic uncertainties for photon measurements

Systematic uncertainties for photon measurements are summarized in this section. Systematic uncertainties from the PID cut, the triggering, the global energy scale, the non-linearity, the acceptance of the PHOS detector and the material budget are common with neutral mesons measurements.

8.1 Photon purity

The systematic uncertainty of the photon purity is divided into two components. One is data driven approach (DDA) method itself. This has to be evaluated in M.C., because the true particle abundance is known. The other is due to the different assumption of the particle composition.

8.1.1 Data Driven approach method itself

The uncertainty due to the method itself was estimated by comparing photon purity between M.C. truth and DDA in M.C., since the true particle abundance is known in M.C.. This was performed in PYTHIA simulation (pp collisions) to avoid cluster overlappings under the high multiplicity environment. As shown by Figure 128, it is found to be $\sim 4\%$ at low p_{T} and almost vanishes (0.2%) at high p_{T}. The uncertainty of the DDA method itself is treated as common in pp and Pb–Pb collisions.

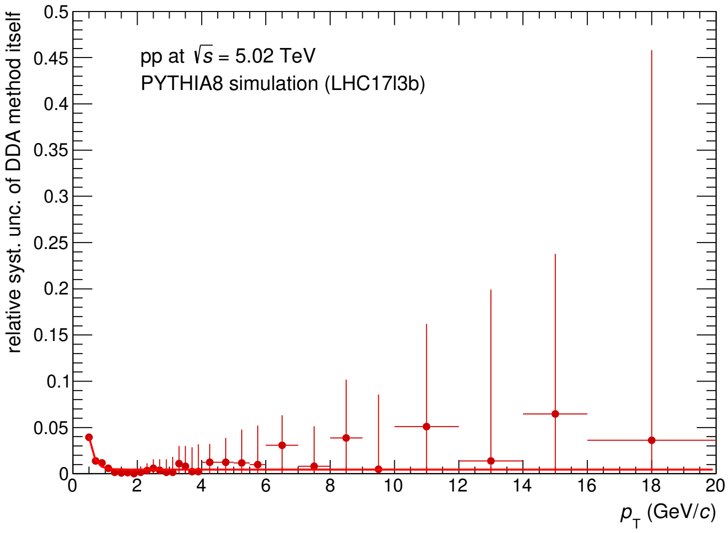

Figure 128: Systematic uncertainties of the DDA method itself.

8.1.2 Different assumption of particle composition

In the DDA, the system 31 was constructed to obtain the number of particles on PHOS under different assumptions of hadron contributions. This was evaluated by adding/removing neutral hadron components in system 31. The deviation from unity in the ratio $\frac{\gamma\text{ purity with }C_{\mathrm{nh}}}{\gamma\text{ purity without }C_{\mathrm{nh}}}$ is considered as the systematic uncertainty due to the different assumption.

8.2 Cocktail simulation

Mainly, there are two systematic uncertainties in the cocktail simulation. They are due to the different input parameterization of the measured π^0 spectrum and particle ratios.

8.2.1 Shape of input π^0 spectrum

The input π^0 spectrum is parameterized by TCM function described in the prevision section. In order to take into account different parameterization, the measured π^0 spectra in pp collisions at $\sqrt{s} = 5.02$ TeV is alternatively fitted by the modified Hagedorn function [29, 91, 92] developed by the PHENIX collaboration at RHIC.

$$E\frac{d^3\sigma}{dp^3} = A\left(\exp(-(ap_{\mathrm{T}} + bp_{\mathrm{T}}^2)) + \frac{p_{\mathrm{T}}}{p_0}\right)^{-n} \tag{34}$$

When $a \rightarrow 0$ and $b \rightarrow 0$, the modified Hagedorn function becomes the original Hagedorn function. On the other hand, the modified Hagedorn function does not fit to π^0 spectra measured for wide p_{T} range in central Pb–Pb collision at $\sqrt{s_{\mathrm{NN}}} = 5.02$ TeV due to a kink at $p_{\mathrm{T}} = 4 \sim 5$ GeV/c. In other wards, the TCM function is necessary for describing hadron productions for such wide p_{T} range in central Pb–Pb collisions. Hence, a simplified TCM-inspired function was tried for alternative parameterizations of input π^0 spectra.

$$E\frac{d^3\sigma}{dp^3} = A_e \exp\left(-\frac{p_{\mathrm{T}}}{T_e}\right) + A\left(1 + \frac{p_{\mathrm{T}}^2}{T^2}\right)^{-n} \tag{35}$$

The systematic uncertainty due to different π^0 paramterization was evaluated by the γ/π^0 ratio in the cocktail simulation. The deviation from unity in the double ratio $\frac{(\gamma/\pi^0)_{\mathrm{alt}}}{(\gamma/\pi^0)_{\mathrm{def}}}$ in the cocktail simulation is considered as the systematic uncertainty of the shape of the input π^0 spectrum. However, since $(1+\frac{p_{\mathrm{T}}^2}{T^2})^{-n}$ is similar to the original TCM function, alternative parameterizations for π^0 spectra fitted by Eq. 35 give too small difference from default ones in Pb–Pb collisions. Thus, the systematic uncertainty due to the shape of the input π^0 spectrum in Pb–Pb collisions is inherited from that in pp collisions. It is 4 % at low p_{T} and decreases with p_{T} down to 0.4 %.

8.2.2 Particle ratios

The uncertainty due to particle ratios are originating from measured particle ratios. The η/π^0 and ω/π^0 are varied 0.50 ± 0.02 and 0.85 ± 0.15 respectively. As relative contributions to total decay photon yields (15% for photons from η mesons and 2.5% for photons from ω mesons) are known, the relative systematic uncertainty can be analytically estimated as :

$$\frac{\pm 0.02}{0.50} \times 0.15 \approx \pm 0.60\% \text{ for photons decayed from } \eta \text{ mesons} \tag{36}$$

$$\frac{\pm 0.15}{0.85} \times 0.025 \approx \pm 0.44\% \text{ for photons decayed from } \omega \text{ mesons} \tag{37}$$

They were also estimated directly in the cocktail simulation, as shown on Figure 129, which gives similar values to the analytical calculations, as expected. The uncertainty from η'/π^0 is negligible, as the relative contribution of decay photons decayed from η' mesons to total the decay photon is less than 1%.

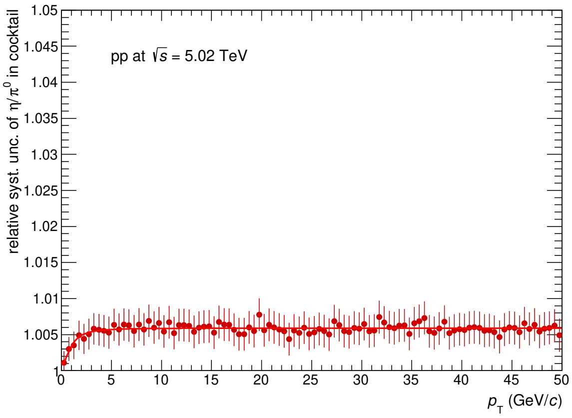

(a) The systematic uncertainty due to the η/π^0 in the cocktail simulation.

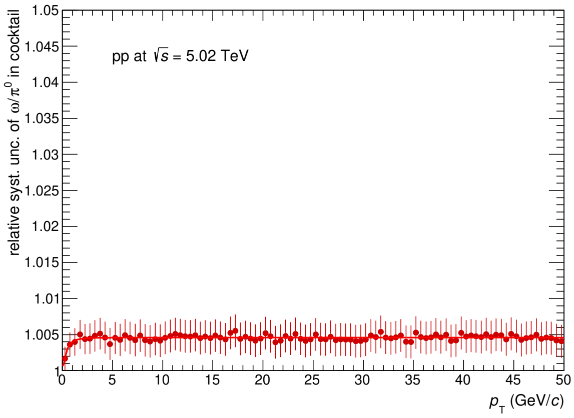

(b) The systematic uncertainty due to the ω/π^0 in the cocktail simulation.

Figure 129: Systematic uncertainties due to particle ratios in the cocktail simulation

8.3 Summary of systematic uncertainties for inclusive photons γ^{inc}

The summary of systematic uncertainties for inclusive photons γ^{inc} is plotted in this section.

8.3.1 Summary of systematic uncertainties for γ^{inc} in pp collisions at $\sqrt{s} = 5.02$ TeV

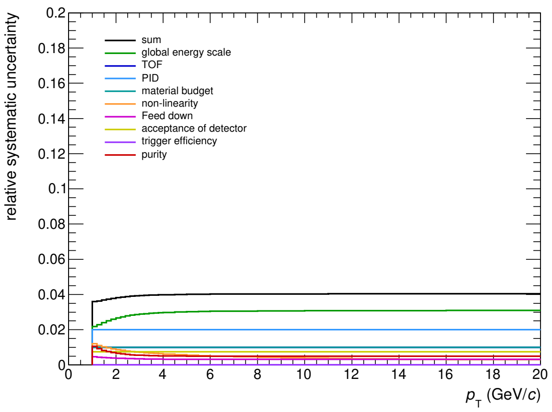

(a) For INT7

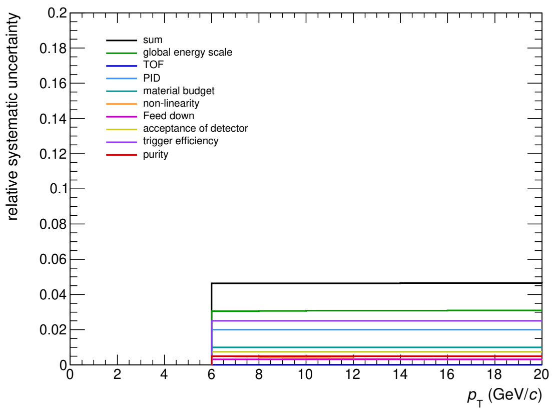

(b) For PHI7

Figure 130: Systematic uncertainties for γ^{inc} in pp collisions at $\sqrt{s} = 5.02$ TeV.

8.3.2 Summary of systematic uncertainties for $\gamma^{\rm inc}$ in Pb–Pb collisions at $\sqrt{s_{\rm NN}} = 5.02$ TeV

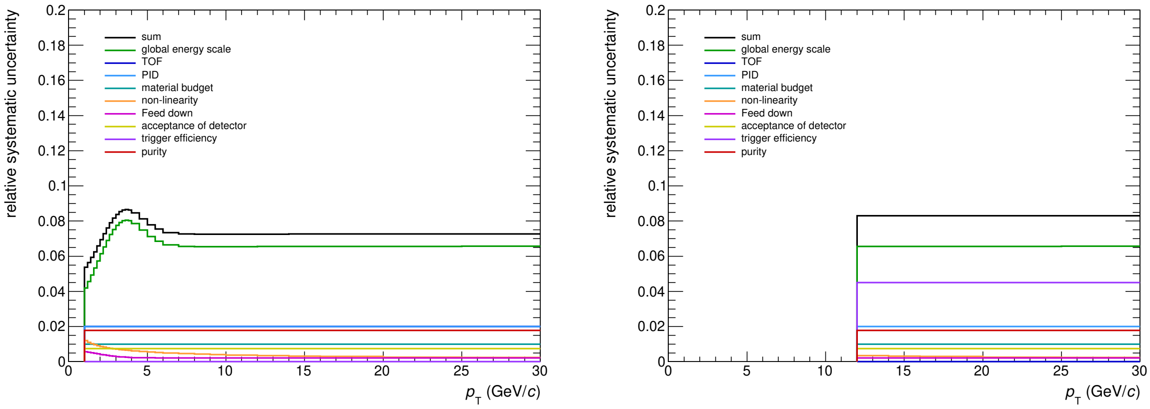

(a) For INT7 (b) For PHI7

Figure 131: Systematic uncertainties for $\gamma^{\rm inc}$ in Pb–Pb collisions at $\sqrt{s_{\rm NN}} = 5.02$ TeV for centrality 0-10%.

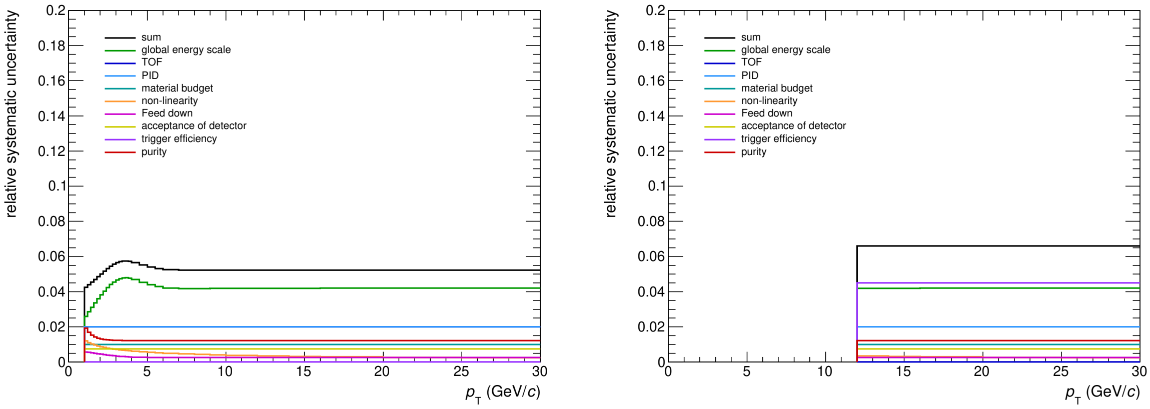

(a) For INT7 (b) For PHI7

Figure 132: Systematic uncertainties for $\gamma^{\rm inc}$ in Pb–Pb collisions at $\sqrt{s_{\rm NN}} = 5.02$ TeV for centrality 10-20%.

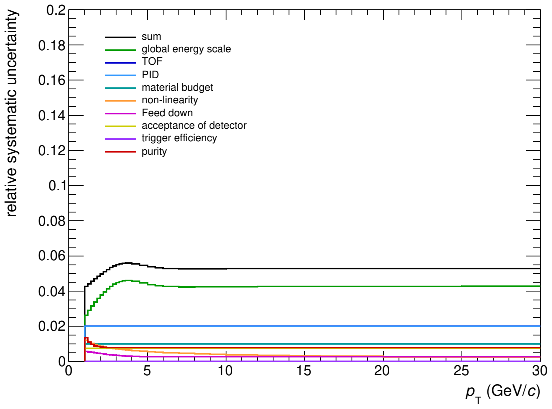

(a) For INT7

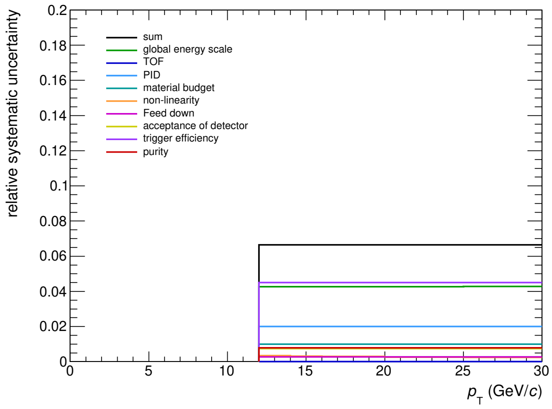

(b) For PHI7

Figure 133: Systematic uncertainties for γ^{inc} in Pb–Pb collisions at $\sqrt{s_{\text{NN}}}$ = 5.02 TeV for centrality 20-40%.

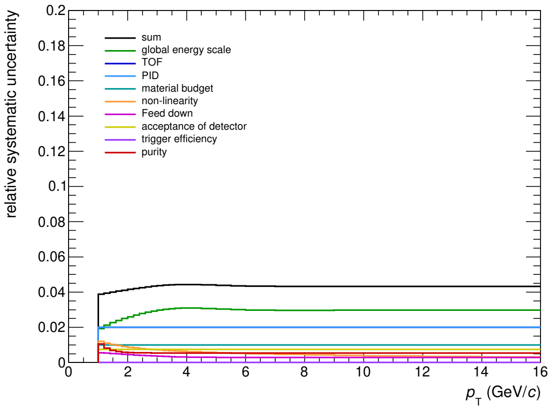

(a) For INT7

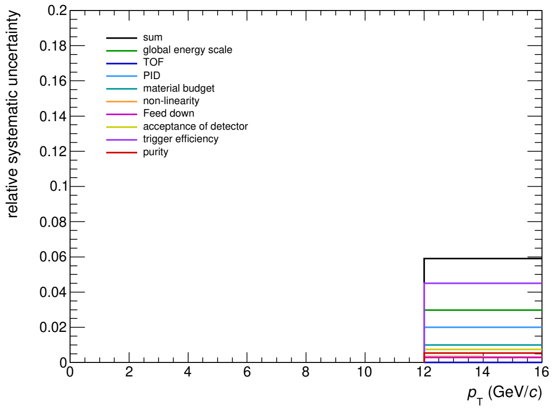

(b) For PHI7

Figure 134: Systematic uncertainties for γ^{inc} in Pb–Pb collisions at $\sqrt{s_{\text{NN}}}$ = 5.02 TeV for centrality 40-60%.

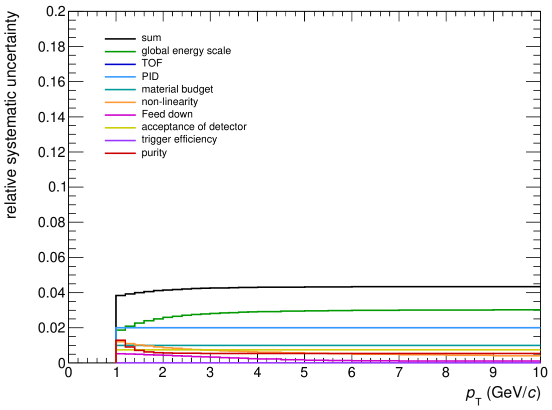

(a) For INT7

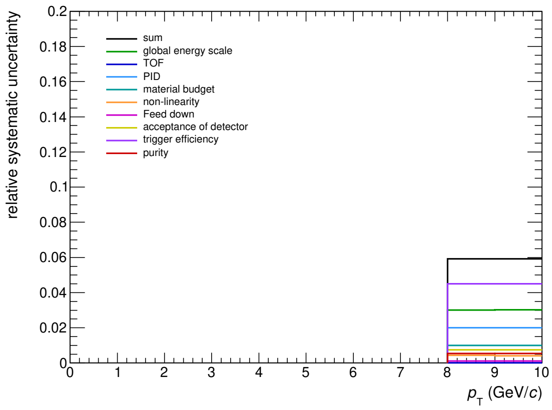

(b) For PHI7

Figure 135: Systematic uncertainties for γ^{inc} in Pb–Pb collisions at $\sqrt{s_{\text{NN}}}$ = 5.02 TeV for centrality 60-80%.

9 Results and discussions for photons

Results toward the direct photons measurement are described in this section. Inclusive photon spectra γ^{inc}, $\gamma^{\text{inc}}/\pi^0$ ratios in data and cocktail simulation, R_γ which is the double ratio of $\gamma^{\text{inc}}/\pi^0$ and finally, direct photon spectra.

9.1 Results on inclusive photons γ^{inc}

As a first step for the direct photons measurement, inclusive photon spectra have been measured in pp and Pb–Pb collisions at $\sqrt{s_{\text{NN}}} = 5.02$ TeV.

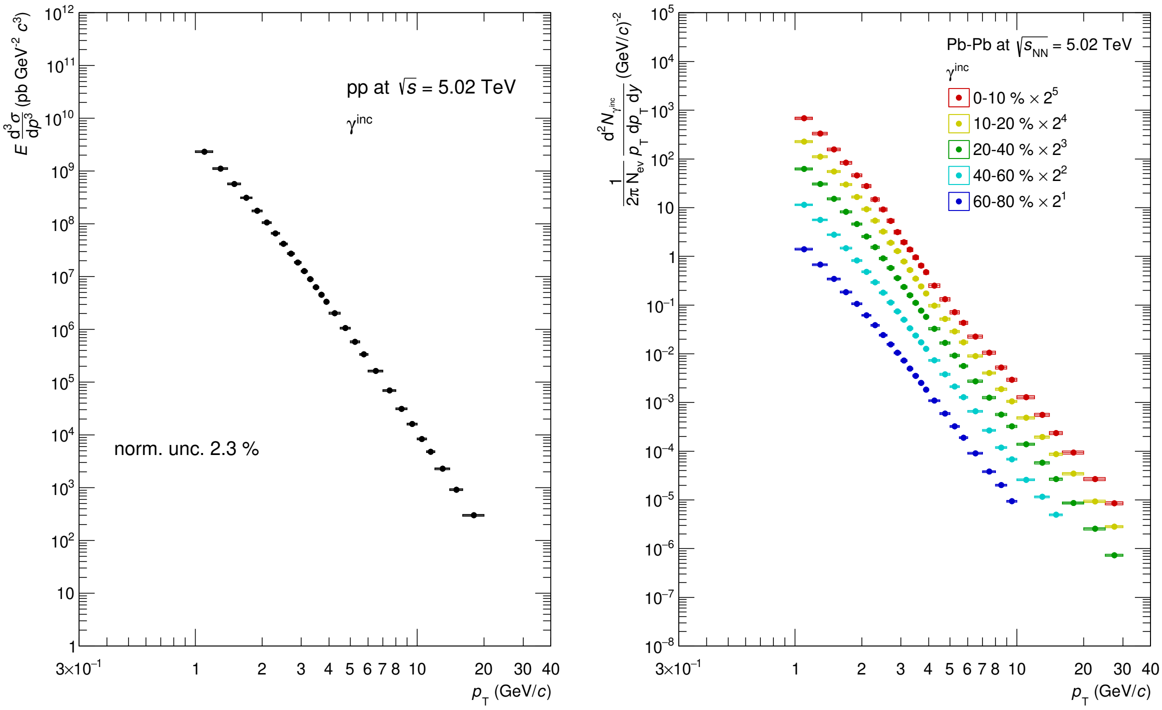

(a) The production cross section of inclusive photons in pp collisions at $\sqrt{s} = 5.02$ TeV.

(b) Invariant yields of inclusive photons in Pb–Pb collisions at $\sqrt{s_{\text{NN}}} = 5.02$ TeV.

Figure 136: Inclusive photons spectra in pp and Pb–Pb collisions at $\sqrt{s_{\text{NN}}} = 5.02$ TeV.

9.2 Results on direct photons γ^{dir}

9.2.1 $\gamma^{\text{inc}}/\pi^0$ ratio

Neutral mesons and inclusive photons have been measured as described in previous sections. Secondly, the ratio of inclusive photon yields to π^0 yields are constructed in data and cocktail simulation from known sources respectively for pp and Pb–Pb collisions (Figure 137). The main advantage of $\gamma^{\text{inc}}/\pi^0$ ratio is to cancel out the systematic uncertainty of energy measurement, namely global energy scale and non-linear response in M.C., that are dominant sources in the PHOS detector.

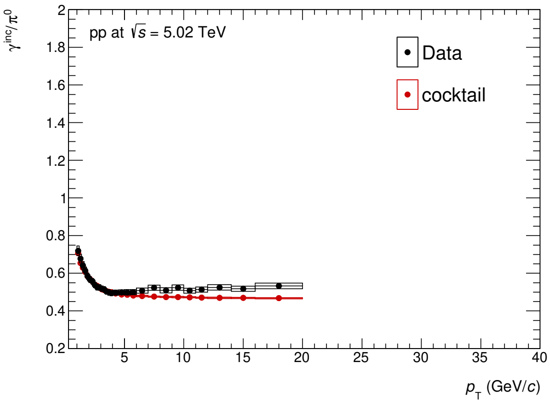

(a) The $\gamma^{\text{inc}}/\pi^0$ ratio in pp collisions.

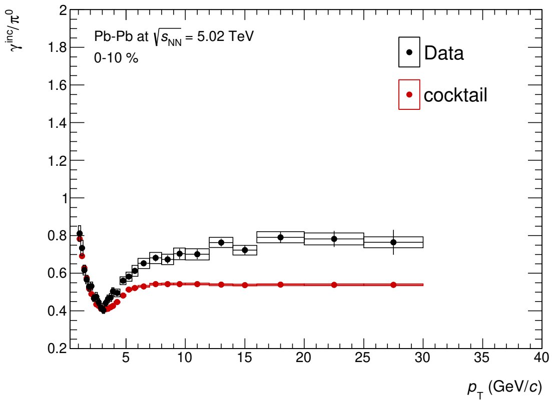

(b) The $\gamma^{\text{inc}}/\pi^0$ ratio in 0-10% Pb–Pb collisions.

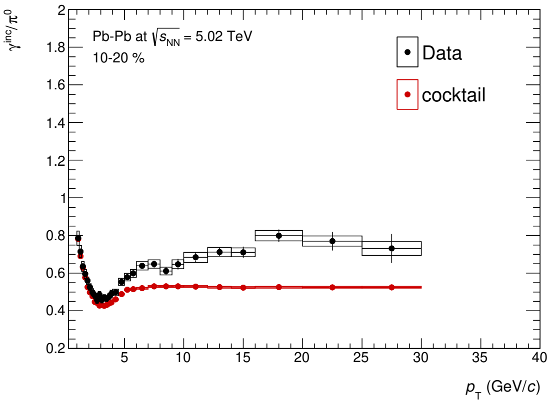

(c) The $\gamma^{\text{inc}}/\pi^0$ ratio in 10-20% Pb–Pb collisions.

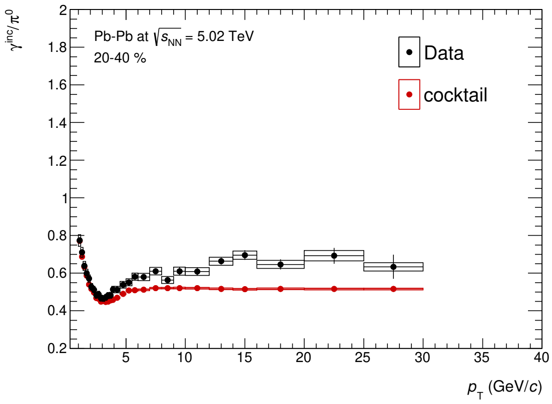

(d) The $\gamma^{\text{inc}}/\pi^0$ ratio in 20-40% Pb–Pb collisions.

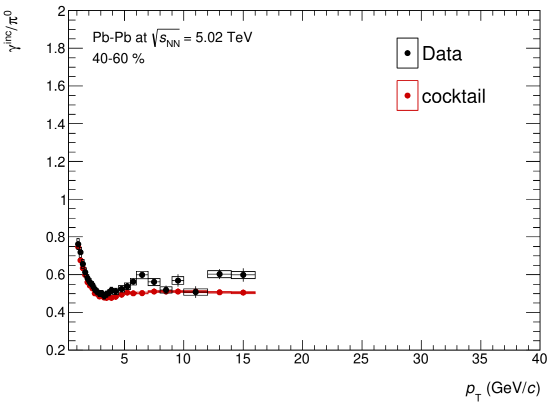

(e) The $\gamma^{\text{inc}}/\pi^0$ ratio in 40-60% Pb–Pb collisions.

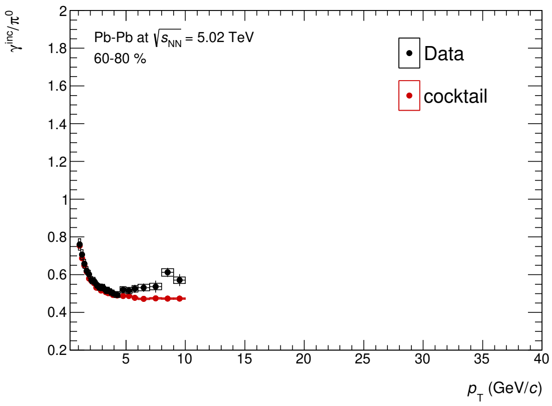

(f) The $\gamma^{\text{inc}}/\pi^0$ ratio in 60-80% Pb–Pb collisions.

Figure 137: $\gamma^{\text{inc}}/\pi^0$ ratios in pp and Pb–Pb collisions at $\sqrt{s_{\text{NN}}} = 5.02$ TeV.

9.2.2 Direct photon excess ratio R_γ

As plotted on Figure 138, R_γ becomes larger with the event multiplicity (i.e. central collisions) at high p_T. This is explained by the suppression of neutral mesons in central collisions, while the direct photon is transparent probe for the QCD medium. Therefore, the excess of prompt photons that are produced by initial hard scatterings between partons becomes significant at higher p_T in central collisions. R_γ for the pQCD NLO calculation is defined as :

$$R_\gamma^{\mathrm{NLO}} = 1 + N_{\mathrm{coll}} \cdot \frac{\gamma^{\mathrm{dir}}_{\mathrm{NLO}}}{\gamma^{\mathrm{decay}}_{\mathrm{cocktail}}} \tag{38}$$

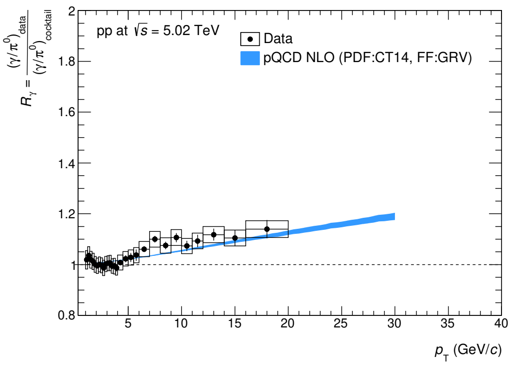

(a) R_γ in pp collisions.

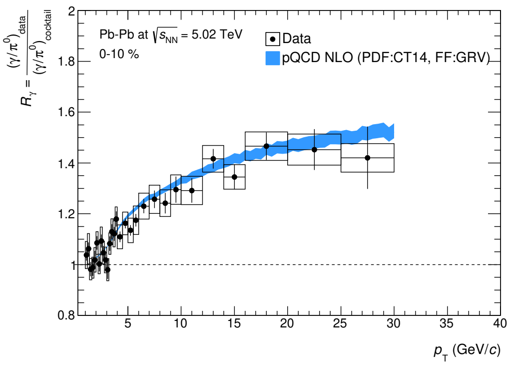

(b) R_γ in 0-10% Pb–Pb collisions.

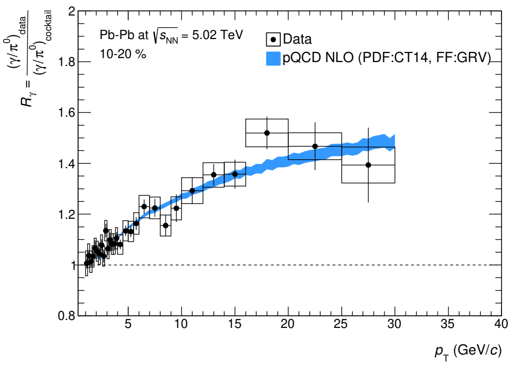

(c) R_γ in 10-20% Pb–Pb collisions.

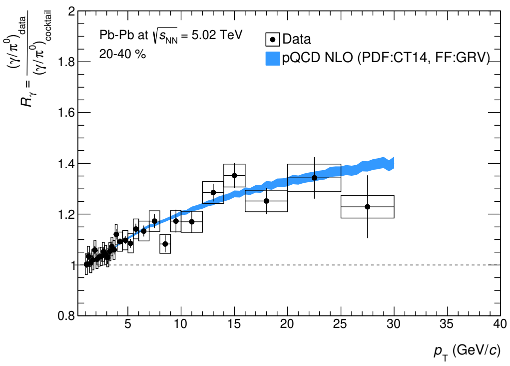

(d) R_γ in 20-40% Pb–Pb collisions.

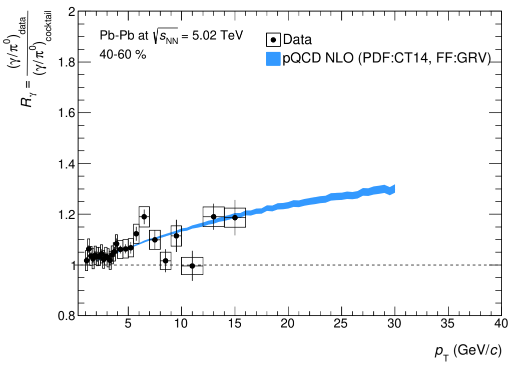

(e) R_γ in 40-60% Pb–Pb collisions.

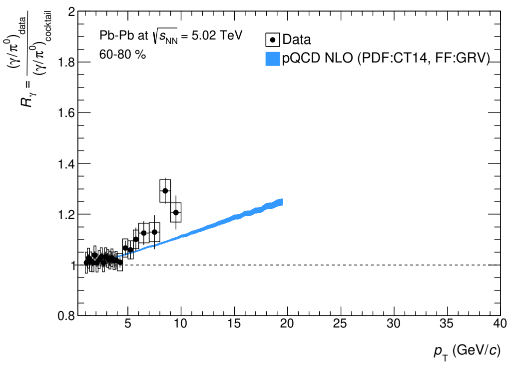

(f) R_γ in 60-80% Pb–Pb collisions.

Figure 138: R_γ in pp and Pb–Pb collisions at $\sqrt{s_{\mathrm{NN}}} = 5.02$ TeV.

9.2.3 Direct photon spectra

Finally, direct photon spectra or upper limits at the 90% confidence level have been extracted as shown by Figure 139. The pQCD calculation basically describes prompt photon yields at high p_{T} well in both pp and Pb–Pb collisions.

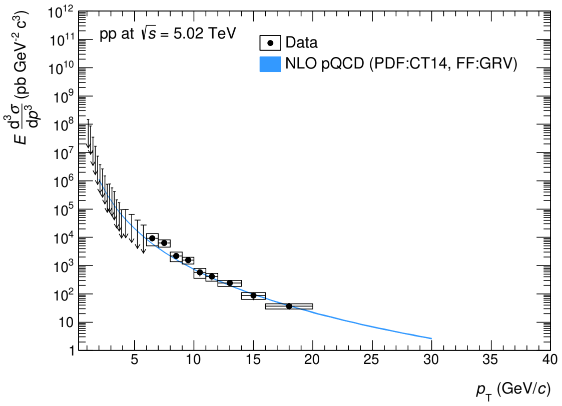

(a) The production cross section of direct photons in pp collisions.

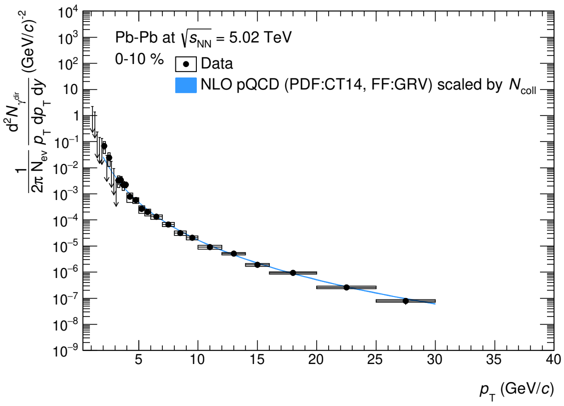

(b) The invariant yield of direct photons in 0-10% Pb–Pb collisions.

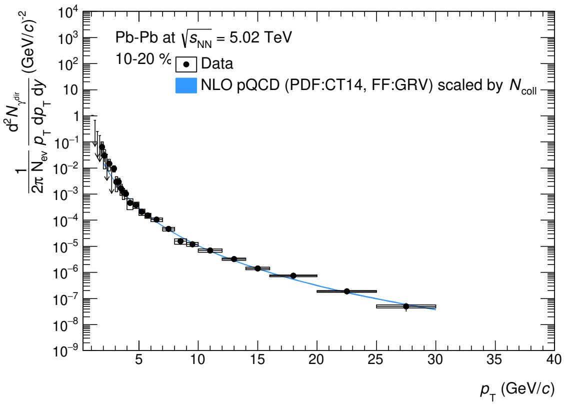

(c) The invariant yield of direct photons in 10-20% Pb–Pb collisions.

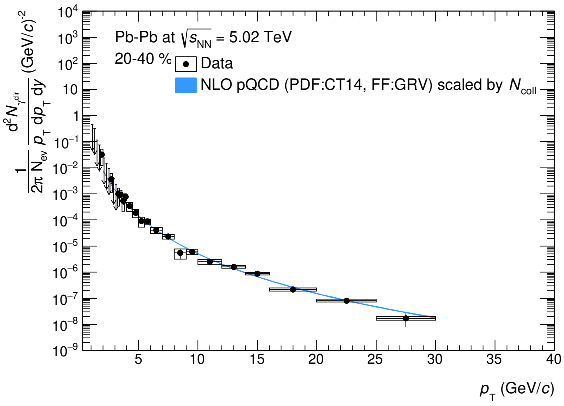

(d) The invariant yield of direct photons in 20-40% Pb–Pb collisions.

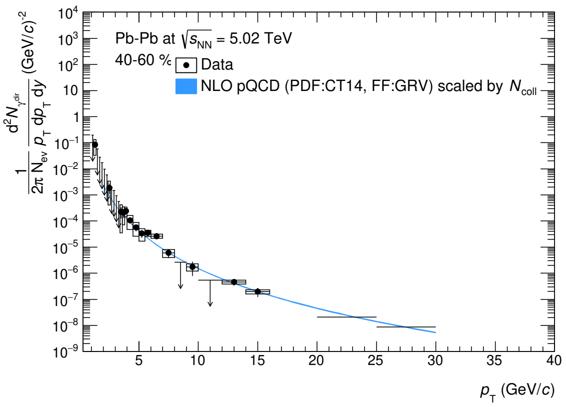

(e) The invariant yield of direct photons in 40-60% Pb–Pb collisions.

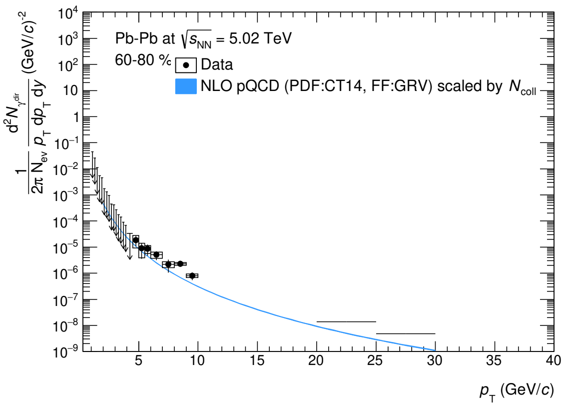

(f) The invariant yield of direct photons in 60-80% Pb–Pb collisions.

Figure 139: Direct photon spectra in pp and Pb–Pb collisions at $\sqrt{s_{\mathrm{NN}}} = 5.02$ TeV.

9.2.4 R_{AA} of direct photons

In this thesis, only upper limits on direct photon yields at the 90% confidence level have been set at low p_{T}. Nevertheless, a few data points on R_{γ} (Figure 138b) and the invariant yield of direct photons (Figure 139b) in central collisions show larger value than the pQCD calculation at low p_{T}. Hence, it is interesting to see R_{AA} of direct photons. As shown by Figure 140, direct photon yields beyond the pQCD calculation which can describe prompt photon yields by a factor of up to about 4 is observed at $p_{\mathrm{T}} < 4$ GeV/c. This can be interpreted as an indication of thermal photon emissions from the hot and dense medium in central Pb–Pb collisions. Focusing on R_{AA} at high p_{T} region, hadron yields are strongly suppressed, while it is consistent with unity for direct photons. The resulting R_{AA} emphasizes the observed strong hadron suppression is related to final state effects due to the formation of hot and dense colored medium. Additionally, the experimental fact that R_{AA} of direct photons is consistent with unity at high p_{T} proves successful Glauber modeling in terms of the collision geometry.

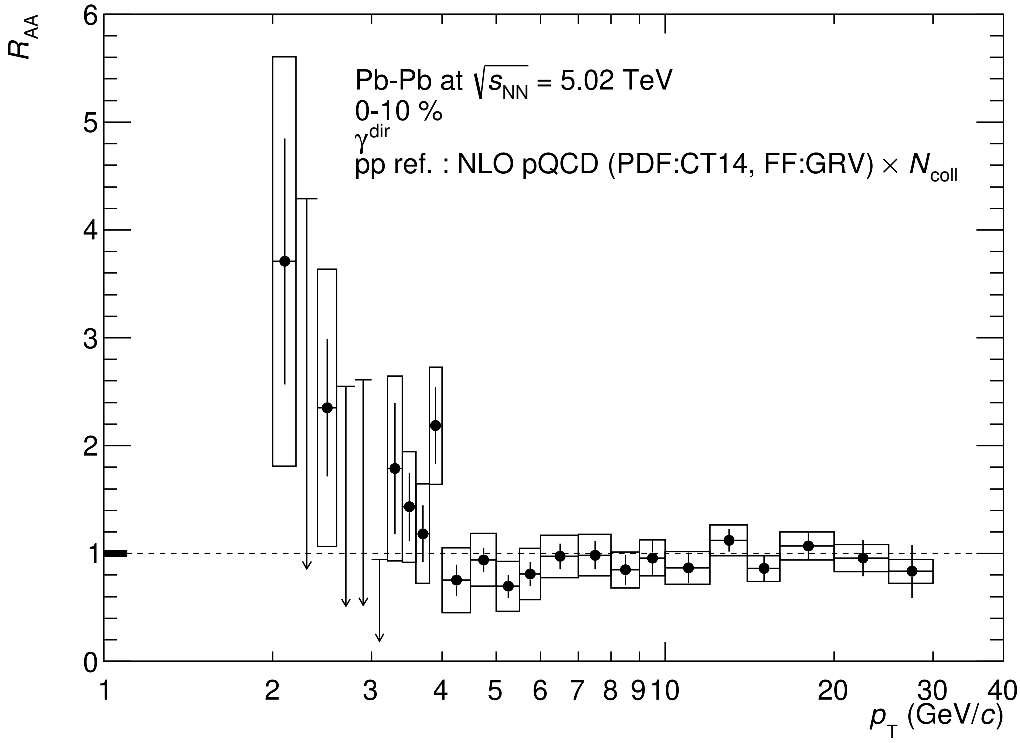

Figure 140: R_{AA} of direct photons in Pb–Pb collisions at $\sqrt{s_{\mathrm{NN}}} = 5.02$ TeV for centrality 0-10%.

9.2.5 Effective temperature $T_{\rm eff}$ extraction

The inverse slope of an exponential fit at low $p_{\rm T}$ regime is interpreted as the average temperature over all the space-time evolution. As written in the previous section (9.2.4), $p_{\rm T}$ spectra of prompt photons at high $p_{\rm T}$ agree with the pQCD calculation, which justifies these measurements. Moreover, there is indication of excess due to thermal emissions from the QGP at low $p_{\rm T}$ beyond the pQCD calculation in central Pb–Pb collisions (0-10%). Therefore, there is a possibility to fit data points at low $p_{\rm T}$ by the exponential function $A \times \exp(-p_{\rm T}/T_{\rm eff})$ and modified Hagedorn function. Namely, the global fitting function is :

$$\frac{1}{2\pi\ N_{\rm ev}} \frac{d^2 N_{\gamma^{\rm dir}}}{p_{\rm T}\ dp_{\rm T}\ dy} = A \times \exp(-p_{\rm T}/T_{\rm eff}) + B \times \left(1 + \frac{p_{\rm T}^2}{p_0^2}\right)^{-n}, \tag{39}$$

where parameters B, p_0 and n for prompt photons at high $p_{\rm T}$ are fixed by the pQCD calculation to reduce the number of degrees of freedom. So, free parameters are A and $T_{\rm eff}$. Both data points and upper limits at the 90% C.L. are included in the fitting. The obtained effective temperature

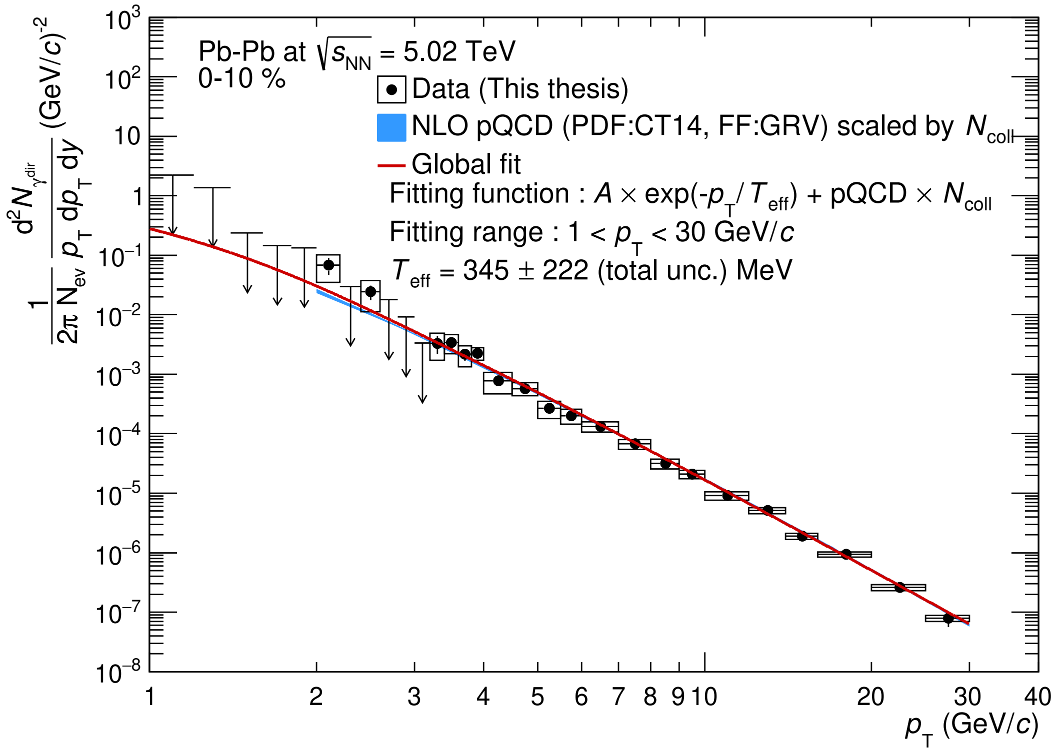

Figure 141: The $p_{\rm T}$ spectrum of direct photons in Pb–Pb collisions at $\sqrt{s_{\rm NN}}$ = 5.02 TeV for centrality 0-10% and the TCM fit to data.

$T_{\rm eff}$ is 345 ± 222(total unc.) MeV in Pb–Pb collisions at $\sqrt{s_{\rm NN}}$ = 5.02 TeV for centrality 0-10%. The statistical and systematic uncertainty of the $T_{\rm eff}$ are not separated, because upper limits on direct photon yields at the 90 % C.L. are set based on the quadratic sum of them. For references, it has been reported that $T_{\rm eff}$ = 239 ± 25(stat.) ± 7(syst.) MeV [30] via real photons in 0-20 % central Au–Au collisions at $\sqrt{s_{\rm NN}}$ = 0.2 TeV at RHIC by PHENIX, and $T_{\rm eff}$ = 294 ± 12(stat.) ± 47(syst.) MeV [31] in 0-20 % central Pb–Pb collisions at $\sqrt{s_{\rm NN}}$ = 2.76 TeV with ALICE at the LHC.

10 Conclusion

The measurement of neutral mesons and direct photons in pp and Pb–Pb collisions at $\sqrt{s_{\rm NN}}$ = 5.02 TeV has been performed in ALICE with the PHOS detector. $p_{\rm T}$ spectra and nuclear modification factors $R_{\rm AA}$ of π^0 meson in $0.4 < p_{\rm T} < 35$ GeV/c and η meson in $2.0 < p_{\rm T} < 16$ GeV/c have been measured in pp and Pb–Pb collisions at $\sqrt{s_{\rm NN}} = 5.02$ TeV. This is the first measurement of the suppression of π^0 at such high $p_{\rm T}$ regime. π^0 and η mesons show the same suppression pattern at $p_{\rm T} > 4$ GeV/c in all centrality classes. The suppression pattern between η and $K^{\pm}$ mesons seems to be similar at low $p_{\rm T}$, though the uncertainty for η meson is large. It is found that $p_{\rm T}$ spectrum of π^0 becomes harder than that at $\sqrt{s_{\rm NN}} = 2.76$ TeV in both pp and Pb–Pb collisions. Nevertheless, the suppression of π^0 meson in Pb–Pb collisions compared to pp collisions is the same level between $\sqrt{s_{\rm NN}} = 2.76$ and 5.02 TeV, which is by a factor of up to 8. This indicates the larger energy-loss at the higher collision energy. Comparing the light and heavy flavor hadrons, namely π^0 and D mesons, the suppression of D mesons at $p_{\rm T} < 10$ GeV/c is weaker than that of π^0, which is interpreted as the smaller energy-loss for charm quarks than for up, down quarks. The suppression pattern of η meson seems to be similar to $K^{\pm}$ meson consisting of a strange quark, though uncertainties for the η meson measurement is large.
The direct photon measurement is complicated due to the huge background of decay photons from hadrons. By using measured $p_{\rm T}$ spectra of π^0, η mesons and $m_{\rm T}$-scaled $\omega(782)$, $\eta'(958)$ mesons as inputs to the cocktail simulation, decay photon yields have been estimated and statistically subtracted from inclusive photon spectra. Direct photon excess ratios R_γ show clear prompt photon signals originating from initial hard scatterings at high $p_{\rm T}$. The prompt photon production is described by the pQCD NLO calculation well in both pp and Pb–Pb collisions at $\sqrt{s_{\rm NN}} = 5.02$ TeV. Direct photon spectra or upper limits at the 90 % of C.L. have been extracted up to $p_{\rm T} = 30$ GeV/c in central Pb–Pb collisions. The resulting $R_{\rm AA}$ of direct photons which is consistent with unity at high $p_{\rm T}$ justifies the measurement and proves the successful Glauber modeling for the collision geometry. Focusing on $R_{\rm AA}$ of direct photon at low $p_{\rm T}$ in central collisions, a few data points show the excess beyond the pQCD calculation by a factor of up to 4. This indicates thermal photon emissions from the hot and dense QCD medium. The obtained effective temperature $T_{\rm eff}$ is 345 ± 222(total unc.) MeV in Pb–Pb collisions at $\sqrt{s_{\rm NN}}$ = 5.02 TeV for centrality 0-10%. This is the first measurement and setting upper limits on the direct photons in pp and Pb–Pb collisions at $\sqrt{s_{\rm NN}} = 5.02$ TeV.

Acknowledgement

First of all, I would like to express my greatest appreciation to Prof. Toru Sugitate who supervised me in my master and Ph.D courses. He supported my long stay at CERN with his research grant and told me strategy how to survive in a large experiment. My deepest appreciation goes to Dr. Yuri Kharlov. He gave me a lot of appropriate help for not only analyses, but also PHOS commissioning at CERN during LS1 and operation during Run2. Successful data taking of PHOS in Run2 could not be done without his leadership, this thesis either. Dr. Dmitri Peressounko who is a coordinator in PHOS analyses group together with Dr. Yuri Kharlov helped me with calibration of data and simulation. I deeply thank Alexander Vinogradov, Iouri Sibiryak, Dmitri Alexandrov who are PHOS experts for repairing and checking PHOS quality everyday. I am grateful to Prof. Kenta Shigaki who allowed me to have dinner at excellent restaurants with him in Geneva, Frascati, Amsterdam, wherever he was. I also thank Prof. Kensuke Homma, Prof. Takahiro Miyoshi and Dr. Yorito Yamaguchi. They gave me a lot of important comments and discussion about laser experiments and the plasma simulation at our meeting. Especially, Dr. Yorito Yamagaguchi taught me a lot of important physical topics in photon and dilepton as transparent probes in heavy-ion collisions. I would like to thank Dr. Yosuke Watanabe, Dr. ShinIchi Hayashi, Dr. Satoshi Yano, Dr. Daisuke Watanabe, Dr. Tsubasa Okubo, Dr. Kazuya Nagashima, Yosuke Ueda, Kosei Yamakaya and Akihide Nobuhiro for fruitful discussions and a pleasant life with them in Hiroshima and CERN.

A Zero Suppression study in Run2

A new noise reduction system has been introduced in PHOS readout since Run2. This is based on minimum sequence of samples (MINSEQ) in ALTRO chip [93]. MINSEQ is set to 3 samples in PHOS readout in Run2. It means data is readout only if consecutive ALTRO sample is longer than 3 samples. This mechanism successfully reduces noise by a factor of $3 \sim 4$ compared to Run1. Data size of noise scan was $2 \sim 3$ kBytes in Run1, but it is 0.8 kBytes in Run2. ZS threshold is set to 3 ADC counts. However, ZS threshold is effectively increased due to MINSEQ. In order to test this effect, effective ZS threshold was varied in M.C. and tuned for reproducing standard cluster cut efficiency and PID cut efficiency. As shown by Fig.142, standard cluster cuts play rolls only at $E_{\gamma} < 1$ GeV where an electro-magnetic shower evolution is not well defined and ZS at 20 MeV can reproduce data very well (the best). Fig.143 shows that ZS at 20 MeV is the best again.

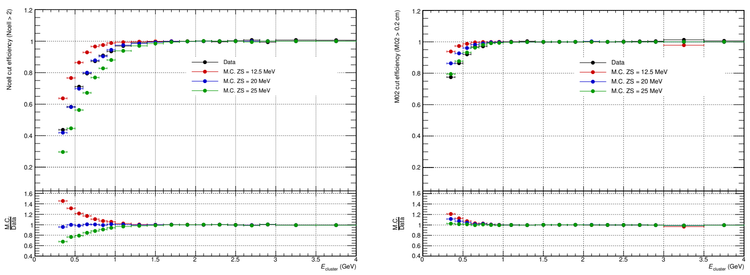

(a) Ncell cut efficiency vs. E_{γ} (b) M02 cut efficiency vs. E_{γ} (c) M20 cut efficiency vs. E_{γ}

Figure 142: standard cluster cut efficiency as a function of photon energy. (12.5 MeV is default value in M.C.) Note these cuts are not apply in my analysis.

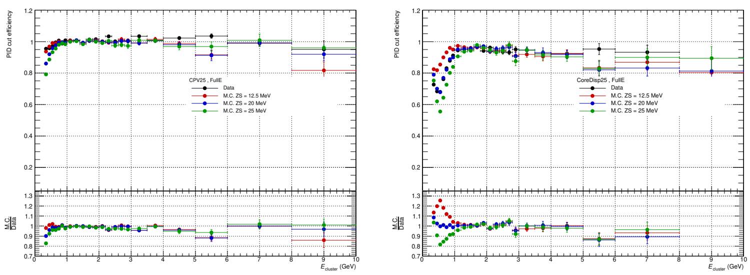

(a) CPV cut efficiency vs. E_{γ} (b) Dispersion cut efficiency vs. E_{γ} (c) CPV and Dispersion cut efficiency vs. E_{γ}

Figure 143: γ-ID cut efficiency as a function of photon energy. (12.5 MeV is default value in M.C.)

B pp collisions at $\sqrt{s} = 5.02$ TeV in 2015

The LHC provided proton-proton collisions at $\sqrt{s} = 5.02$ TeV in 2015 and 2017. ALICE took 100 M events (~ 2 nb^{-1}) triggered by V0AND in November of 2015. On the other hand, as described in section 3.1, ~ 10 times more V0AND events which corresponds to 19 nb^{-1} were recorded in 2017. Although data in 2015 have been also analyzed, it is just considered as a "guideline" for this thesis. This small pp data recorded in early period gave me a great opportunity to estimate systematic uncertainties at early stage and allowed me to save my time for 2017 data analyses. Hereafter, LHC15n represents pp data in 2015.

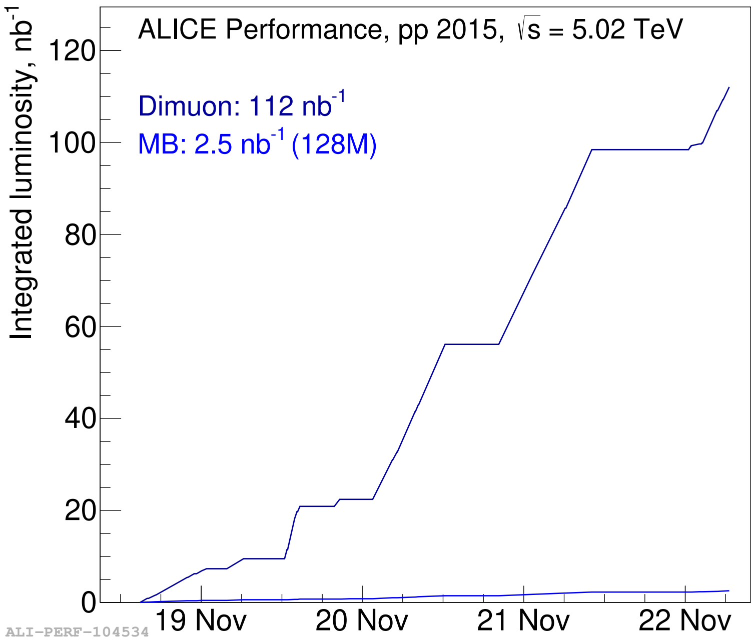

Figure 144: Integrated luminosity in pp collisions at $\sqrt{s} = 5.02$ TeV in 2015.

B.1 Date sets and QA

B.1.1 Date sets in pp collisions at $\sqrt{s} = 5.02$ TeV

run list in pp collisions at $\sqrt{s} = 5.02$ TeV in 2015 is following:

LHC15n

244628, 244627, 244618, 244617, 244542, 244540, 244531, 244484, 244483, 244482, 244481, 244480, 244453, 244421, 244418, 244416, 244411, 244377, 244364, 244359, 244355, 244351, 244343, 244340.

M.C. productions used in this analysis are following:

- LHC16h8a + LHC16k5a PYTHIA8 for LHC15n
- LHC16h8b + LHC16k5b PYTHIA6 for LHC15n
- LHC16h3 PYTHIA8 jet-jet for LHC15n
- LHC17i7 single particle (π^0, η, γ) simulation for LHC15n/o

B.1.2 event selection

Following event cuts have been applied in order to select physics events both in data and M.C..

- physics selection to reject beam-gas interaction
- the number of charged track associated with primary vertex > 0
- pileup rejection by SPD
- $|Z_{\mathrm{vtx}}| < 10$ cm

B.1.3 minimal cluster selection

- E > 0.2 GeV (to extract photon signal as much as possible at low energy)
- M02 > 0.1 cm is applied only E > 1 GeV (to extract photon signal as much as possible at low energy)
- |TOF| < 12.5 ns in pp

As a first check of PHOS data, an average cluster energy and an average number of hits are plotted (Fig.145). Average values stay stable in all runs.

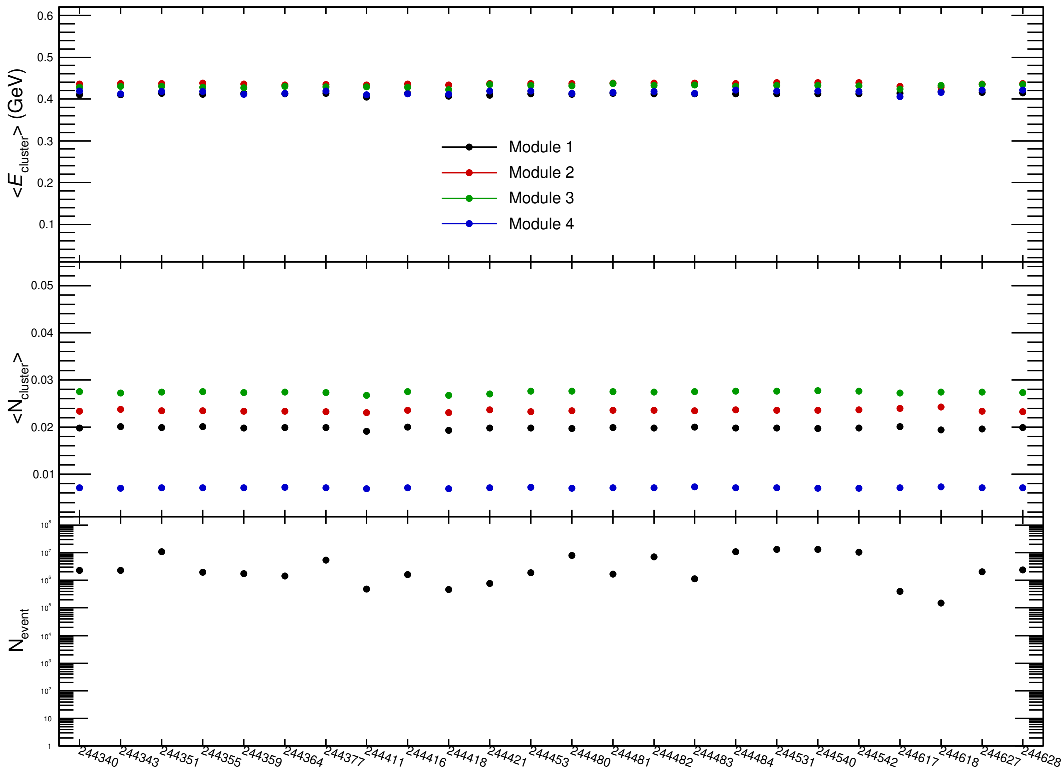

Figure 145: average cluster energy and number of hits in each run on PHOS in LHC15n.

B.1.4 π^0 peak parameters vs. run numbers

π^0 peak parameters are plotted (Fig.146) run-by-run to verify that PHOS was stable in this period. As a result, M1,2,3 are all stable. Especially, π^0 peak could not be seen well on M4, because M4 has limited detector acceptance. A peak position in M1,2,3 are consistent within statistical error bar. There are poor statistics in some runs where π^0 peak is not so clear. Note that M4 was excluded from the beginning because a systematic uncertainty of material budget is large in front of M4 due to TOF + TRD, which is not suitable for the precise photon measurement.

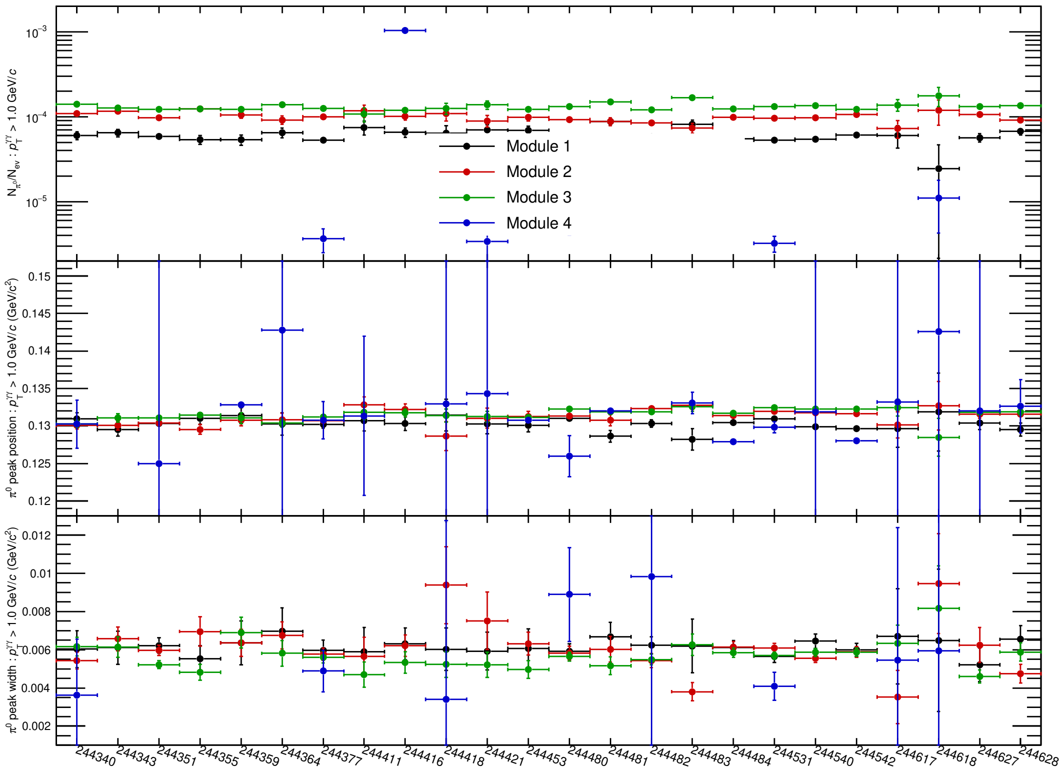

Figure 146: π^0 yield, peak position and sigma in each run in LHC15n.

B.2 Trigger QA

B.2.1 Distance between fired TRU channels and clusters

B.2.2 Energy distribution of matched clusters

B.3 Raw yield extraction

Unfortunately, η measurement was not possible due to the small statistics in LHC15n.

B.4 Acceptance $\times$ reconstruction efficiency

At first, peak positions and peak widths have been compared between data and M.C..

B.5 Trigger efficiency

PHOS trigger allows us to measure high energy photons/electrons efficiently in ALICE. An energy threshold of PHOS L0 trigger in LHC15n period was set to 3 GeV in sum of 4x4 FastOR. Due to the poor TRU acceptance in LHC15n period, trigger efficiency $\varepsilon_{\mathrm{trg}}$ is saturated at about 0.28 ± 0.02 at high p_{T} .

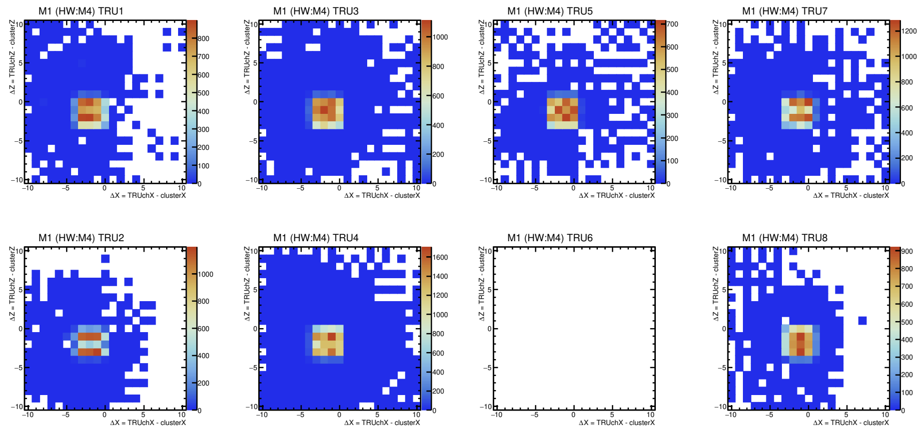

(a) The distance between fired TRU channels and cluster position on M1 in LHC15n.

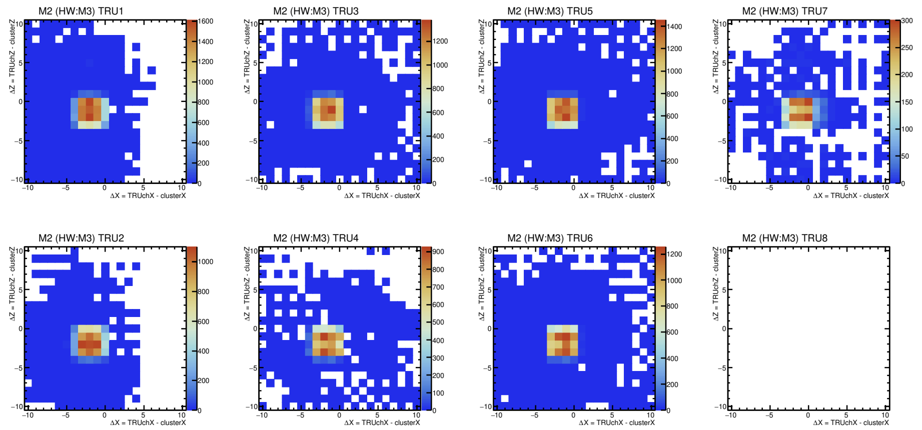

(b) The distance between fired TRU channels and cluster position on M2 in LHC15n.

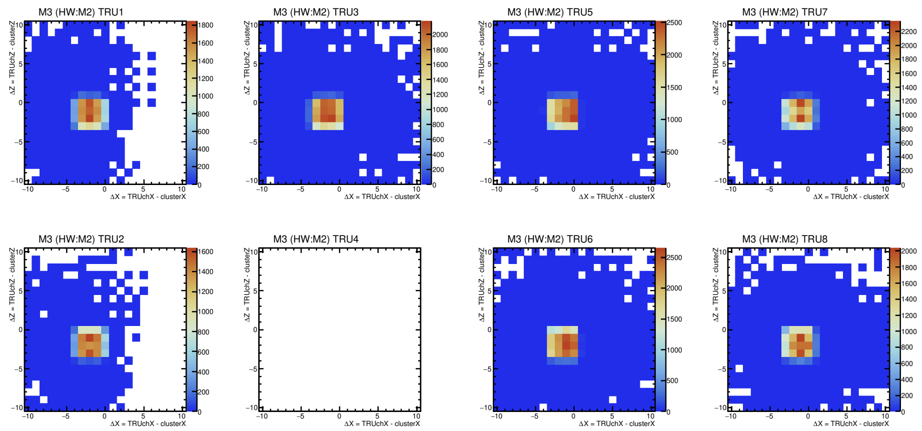

(c) The distance between fired TRU channels and cluster position on M3 in LHC15n.

Figure 147: The distance between fired TRU channels and cluster position in different module for $E_{\text{cluster}} > 3$ GeV in LHC15n. Note that M4 is excluded from my analysis from the very beginning.

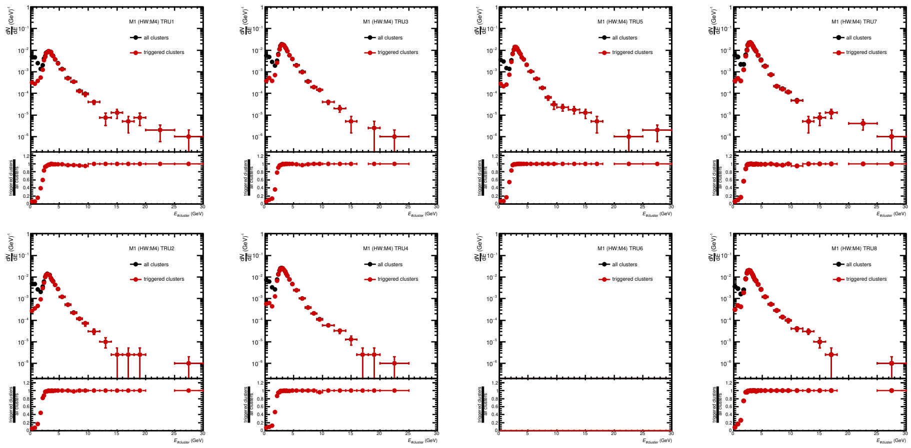

(a) Energy distribution on M1 in LHC15n.

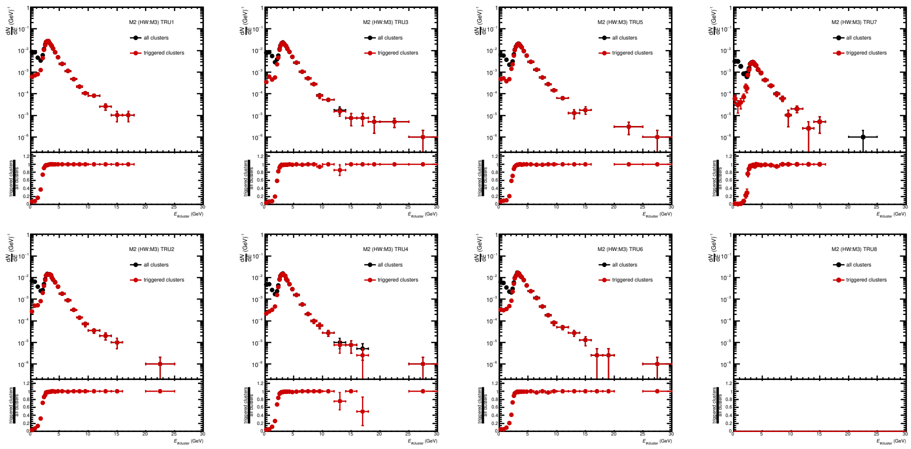

(b) Energy distribution on M2 in LHC15n.

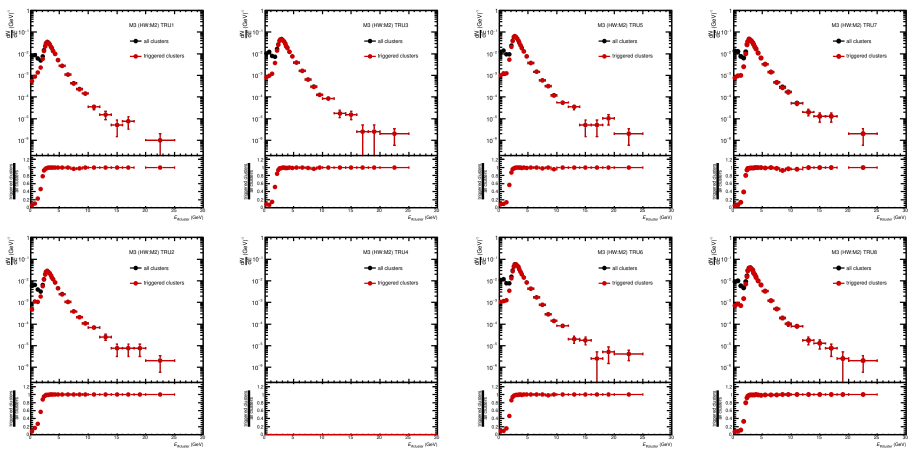

(c) Energy distribution on M3 in LHC15n.

Figure 148: Energy distribution of all clusters and triggered clusters and ratios in LHC15n. Note that M4 is excluded from my analysis from the very beginning.

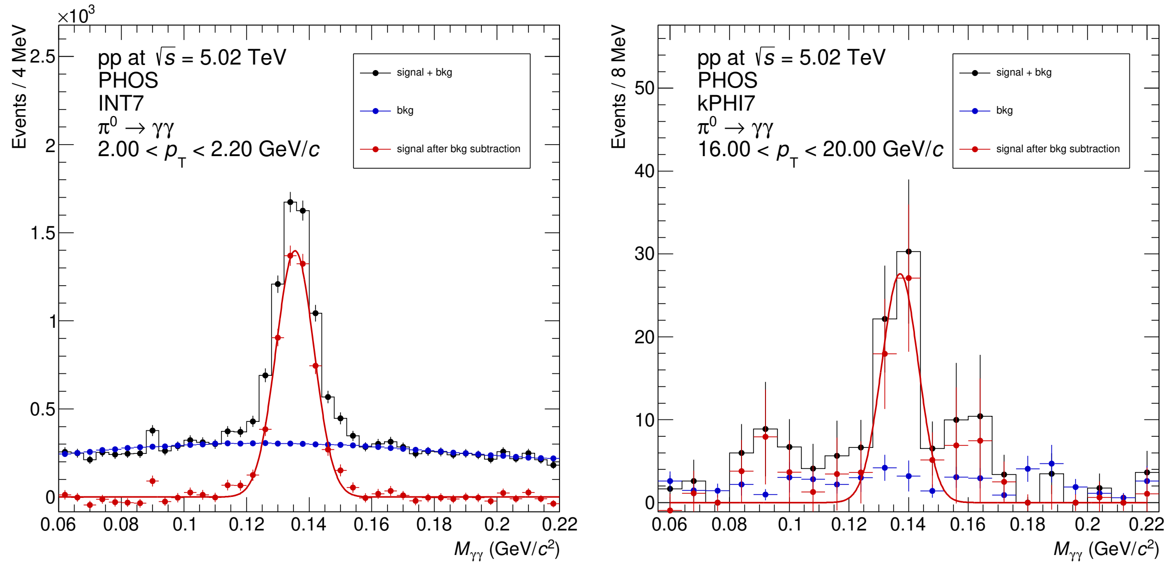

(a) Invariant mass distribution in kINT7.

(b) Invariant mass distribution in kPHI7.

Figure 149: π^0 peak in kINT7 and kPHI7. An energy threshold of PHOS L0 trigger was 3 GeV in 2015

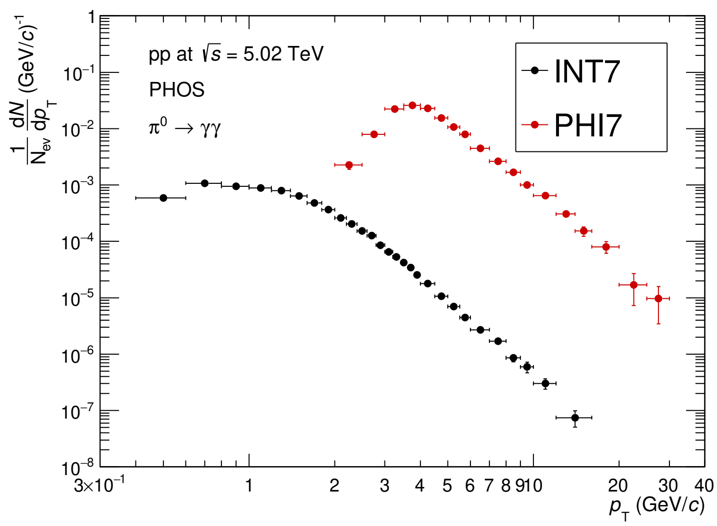

Figure 150: Raw yields of π^0 in LHC15n.

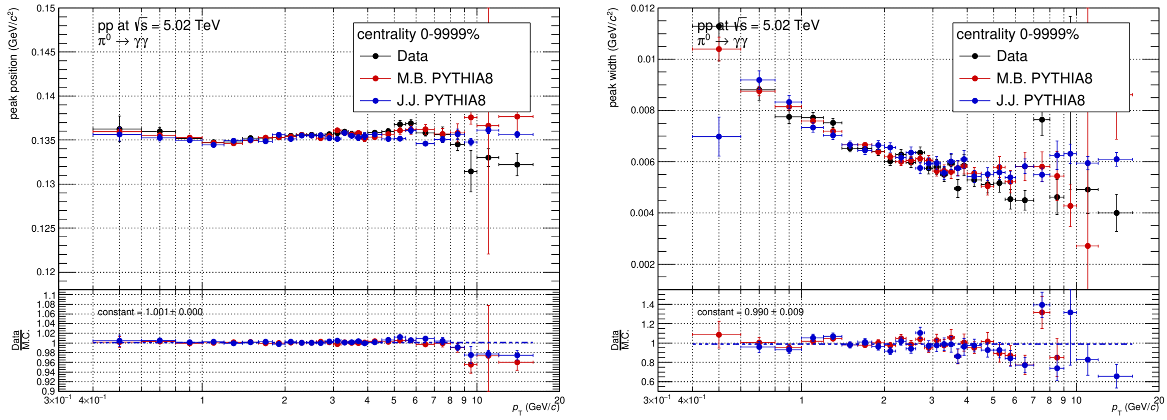

(a) π^0 peak position. (b) π^0 peak width.

Figure 151: peak parameters of π^0 in data and M.C. as a function of p_{T} .

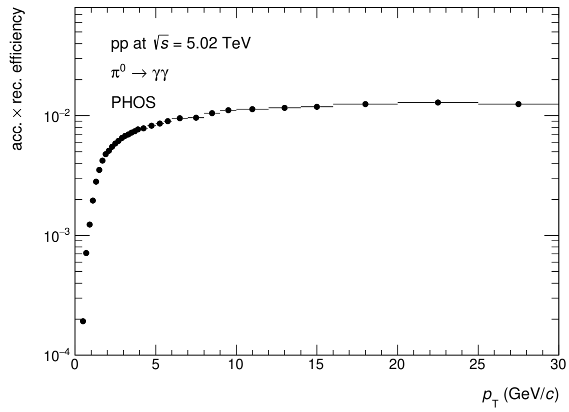

Figure 152: The acceptance $\times$ reconstruction efficiency of π^0

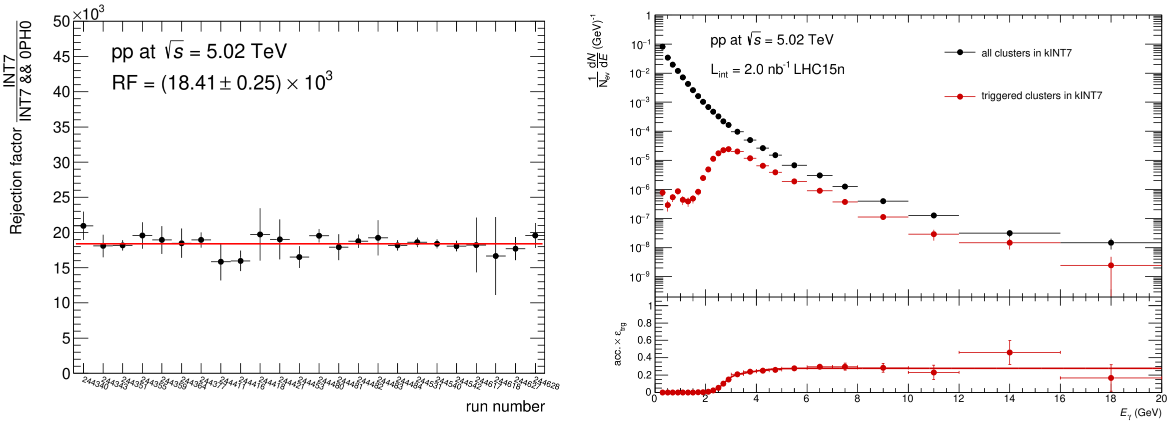

(a) rejection factor (b) trigger efficiency

Figure 153: The rejection factor and trigger efficiency of PHOS L0 trigger in LHC15n data.

B.6 Timing cut

Timing cut ($|\mathrm{TOF_{cluster}}| < 12.5$ ns) was applied at cluster level to reject clusters from other BCs. Thus, TOF cut efficiency efficiency ($\varepsilon_{\mathrm{TOF}}$) as a function of photon energy has to be measured. where, $\mathrm{N}^{\mathrm{triggered\ BC}}_{\mathrm{TOF}\ \gamma}$ is the number of photons after TOF cut in the triggered BC and $\mathrm{N}^{\mathrm{triggered\ BC}}_{\mathrm{all}\ \gamma}$ is the number of photons in the triggered BC respectively. Then, histograms are filled with the number of photons weighted by the inverse of $\varepsilon_{\mathrm{TOF}}$ as a function of photon energy after TOF cut. Since $\varepsilon_{\mathrm{TOF}}$ is measured as a function of photon energy, $\frac{1}{\varepsilon^{1}_{\mathrm{TOF}} \times \varepsilon^{2}_{\mathrm{TOF}}}$ is necessary at neutral mesons level which are reconstructed from 2 photons.

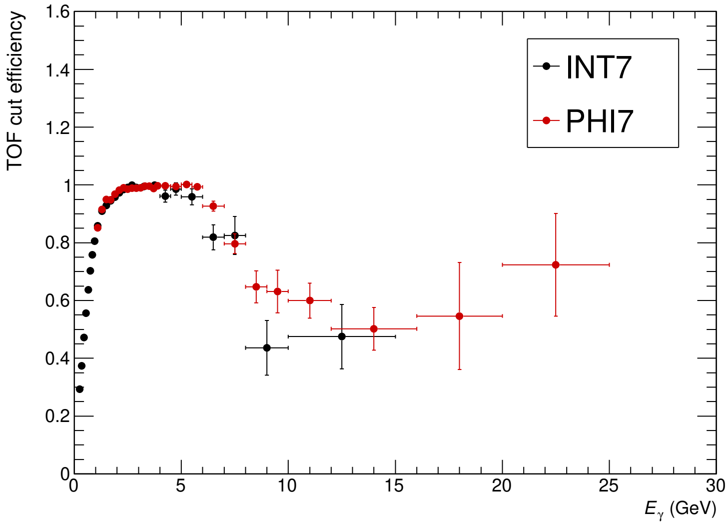

Figure 154: TOF cut efficiency as a function of photon energy in LHC15n data sample.

B.7 Feed down from strange hadrons

The same approach as in 2017 data was applied.

B.8 Systematic uncertainties in pp collisions at $\sqrt{s} = 5.02$ TeV in LHC15n

B.8.1 Yield extraction of neutral mesons

Fitting function, range and integration range were varied to estimate systematic uncertainty of yield extraction. This estimation was performed by the fully corrected yields. R.M.S./mean value in each p_{T} bin is considered as the uncertainty of yield extraction.

- Fitting function [Gaussian,crystallball] for signal and [pol1,pol2] for background
- Fitting range [0.06,0.22], [0.04,0.20], [0.08,0.24] GeV/c^2 for π^0
- Fitting range [0.40,0.70], [0.35,0.65], [0.45,0.75] GeV/c^2 for η
- Integration range [$\pm 3\sigma$,$\pm 2\sigma$]

B.8.2 PID cut

No PID cut was applied in pp analysis.

B.8.3 TOF cut

There were data taking period when a bunch space of each pp collision was 1000 ns which was much wider than timing resolution of PHOS. These runs allow us to estimate systematic uncertainty of TOF cut efficiency. The idea is defined by Eq.24. The deviation from unity in the ratio is considered as a systematic uncertainty of TOF cut. It is found to be 4% from Fig.155 in kINT7 events recorded in LHC15n period, not depending on $p_{\rm T}$.

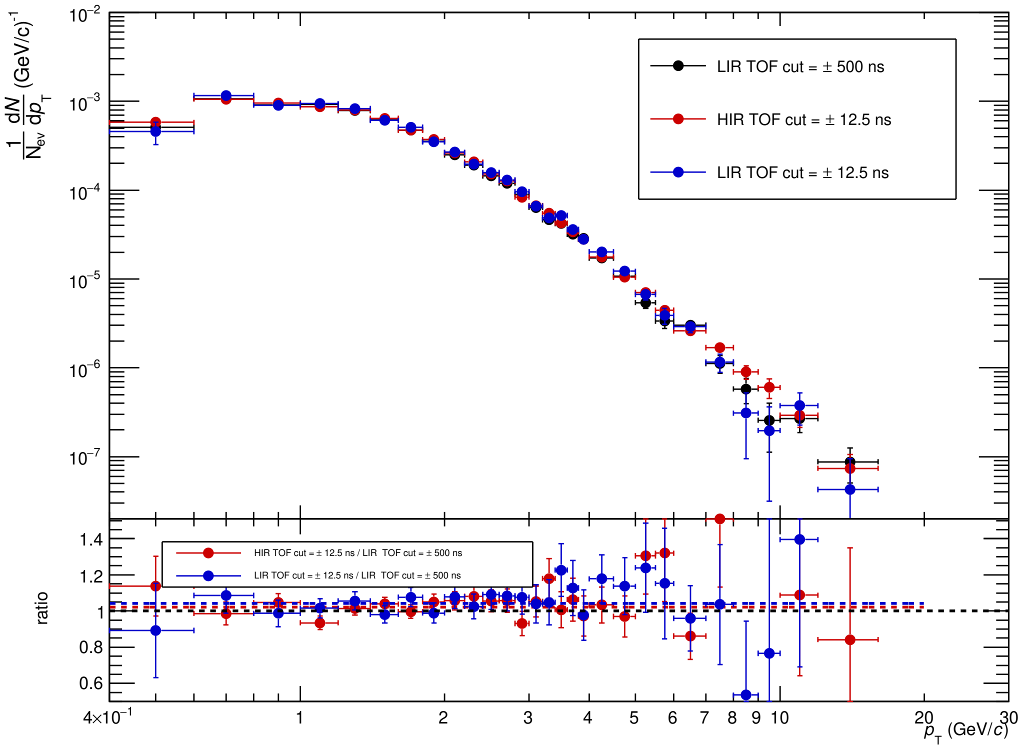

Figure 155: The ratio of π^0 yield in BS = 25 ns to one in BS = 1000 ns triggered by kINT7 in pp collisions at $\sqrt{s} = 5.02$ TeV.

B.8.4 Feed-down correction

The systematic uncertainty of K/π ratio in pp collisions at $\sqrt{s} = 2.76$ TeV is $\sim 10\%$ [61] at the maximum. Therefore, the final systematic uncertainty of π^0 yields from feed down correction is $0.3 \sim 0.6\%$, decreasing with $p_{\rm T}$.

B.8.5 Global energy scale

The same approach was performed as described in section 5.2.

B.8.6 Non-linearity of energy response

The peak position measured by PHOS depends on $p_{\rm T}$. This is due to $p_{\rm T}$ slope of particle spectrum and finite energy resolution of the PHOS detector. The important effect is, so called, non-linearity of energy response. One has to tune non-linearity and reproduce peak position in M.C. for efficiency calculation. However, it is too difficult to understand non-linearity response which may come from APD response and/or light yield of a crystal in simulation. A simple non-linearity model defined by Eq.40 to correct the measured energy was used in this analysis.

$$E_{\mathrm{corr}} = E \cdot f(E),\ \ f(E) = 1 + \frac{a}{1 + E^2/b^2} \tag{40}$$

where, E_{corr} is corrected energy and E is energy before non-linearity correction. Parameters a,b were varied in M.C. to find the best combination that can reproduce π^0 peak position. The ratio of π^0 peak position in data to that in M.C. was fitted by a 0th-order polynomial function and χ^2/ndf were obtained, shown on Fig.156. The best parameters are $a = -0.06$, $b = 0.7$. Combinations (a,b) at $\chi^2/\mathrm{ndf} < 2$ were taken into account to estimate uncertainty of non-linearity. The systematic ucertainty of non-linearity was estimated by R.M.S/mean value with different nonlinearity function shown by Fig.157. The systematic ucertainty of non-linearity is 2% at low p_{T} and deacring with p_{T} (Fig.156b).

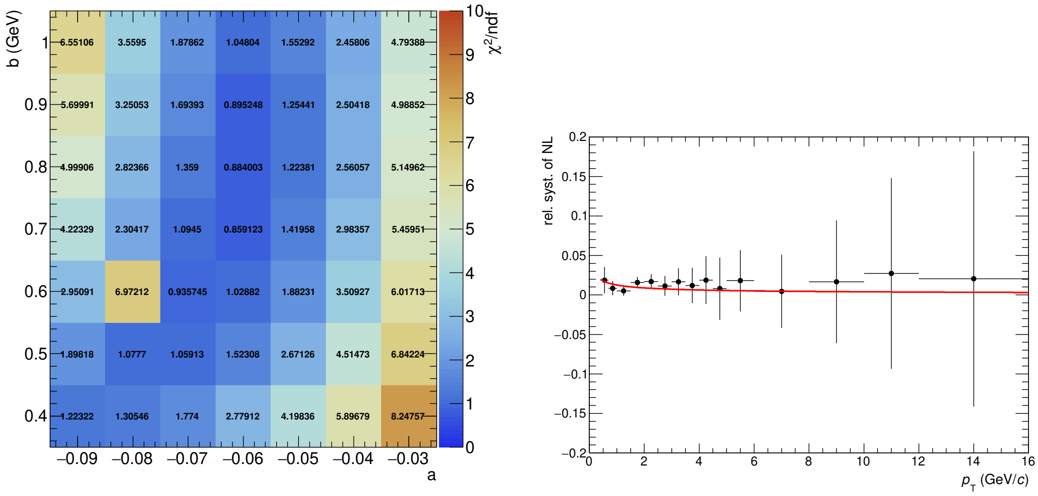

(a) The correlation of a,b.

(b) The systematic uncertainty of NL.

Figure 156: χ^2/ndf of fitting to the ratio of π^0 peak position in data to that in M.C. at different parameters a,b.

B.8.7 Acceptance of detector

The systematic uncertainty of acceptance was estimated by varying the distance to the bad channel (0 cell or 1cell). 0 cell is default value in my analysis. The deviation from unity in the ratio of corrected yield of π^0 in different distance cut is considered as systematic uncertainty of acceptance. The deviation from unity is 1.5% and this value is systematic uncertainty of acceptance.

B.8.8 Material budget

This is common in all period and taken from section 5.9.

B.8.9 Summary of systematic uncertainties

Total systematic uncertainty is summarized on Fig.159.

B.9 Invariant differential cross section of π^0

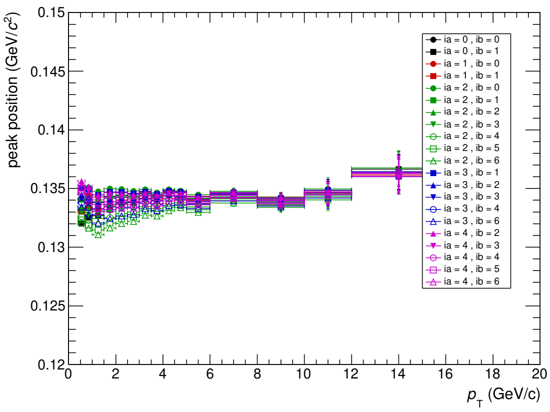

(a) π^0 peak position in different NL.

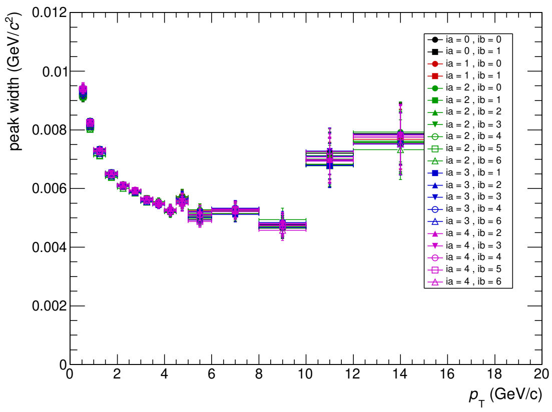

(b) π^0 peak width in different NL.

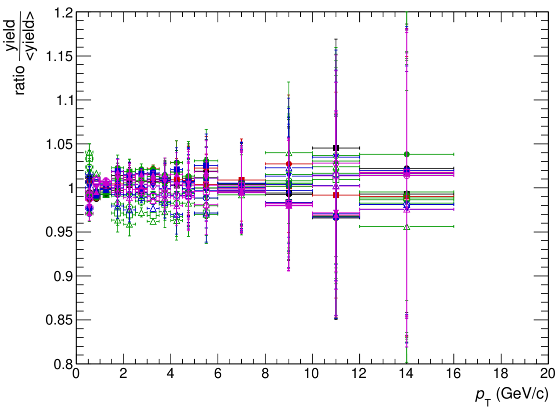

(c) The ratio of π^0 raw yield in different NL.

Figure 157: π^0 peak parameters in different NL.

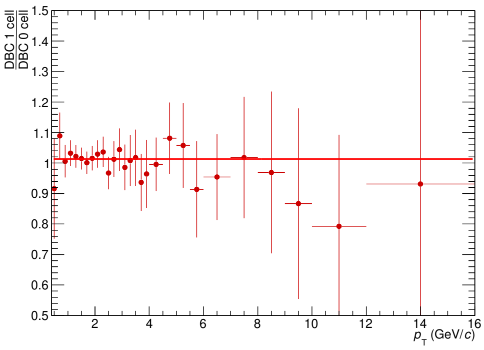

(a) The ratio of corrected yield in kINT7.

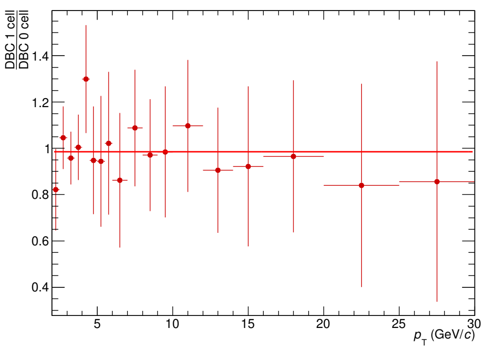

(b) The ratio of corrected yield in kPHI7.

Figure 158: The ratio of corrected yield in different distance cut.

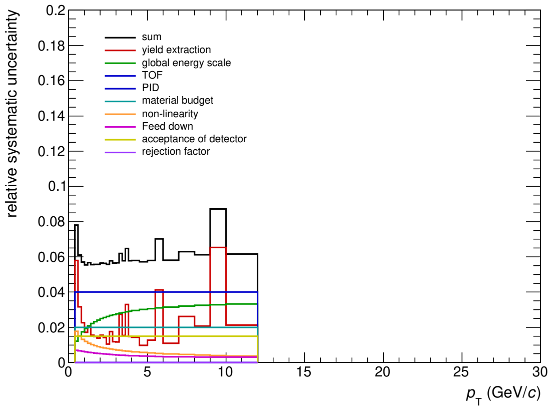

(a) Total systematic uncertainty in kINT7

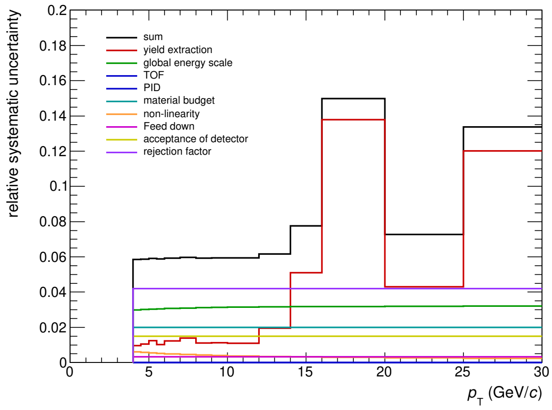

(b) Total systematic uncertainty in kPHI7

Figure 159: Summary of systematic uncertainties of π^0 measurement

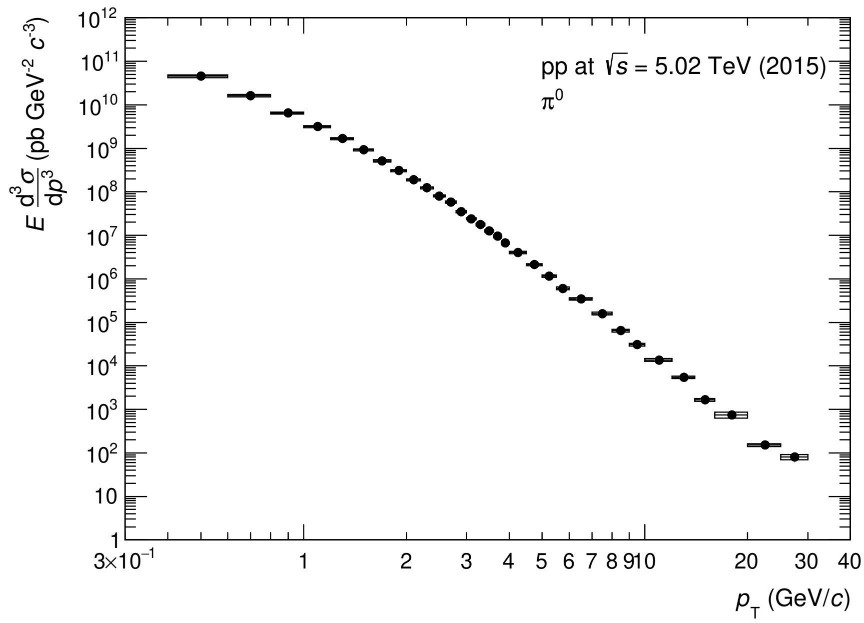

Figure 160: The invariant differential cross section of π^0 .

References

[1] J. D. Bjorken. Energy Loss of Energetic Partons in Quark - Gluon Plasma: Possible Extinction of High p(t) Jets in Hadron - Hadron Collisions. 1982.

[2] Szabocls Borsanyi, Zoltan Fodor, Christian Hoelbling, Sandor D. Katz, Stefan Krieg, and Kalman K. Szabo. Full result for the QCD equation of state with 2+1 flavors. *Phys. Lett.*, B730:99–104, 2014.

[3] A. Bazavov et al. The chiral and deconfinement aspects of the QCD transition. *Phys. Rev.*, D85:054503, 2012.

[4] Frithjof Karsch. Lattice results on QCD thermodynamics. *Nucl. Phys.*, A698:199–208, 2002.

[5] Gert Aarts. Introductory lectures on lattice QCD at nonzero baryon number. *J. Phys. Conf. Ser.*, 706(2):022004, 2016.

[6] Michael L. Miller, Klaus Reygers, Stephen J. Sanders, and Peter Steinberg. Glauber modeling in high energy nuclear collisions. *Ann. Rev. Nucl. Part. Sci.*, 57:205–243, 2007.

[7] CERN. Participants and spectators at the heavy-ion fireball. April,26 2013. CERN COURIER.

[8] S. S. Adler et al. High p_T charged hadron suppression in Au + Au collisions at $\sqrt{s}_{NN} = 200$ GeV. *Phys. Rev.*, C69:034910, 2004.

[9] J. Adams et al. Transverse momentum and collision energy dependence of high p(T) hadron suppression in Au+Au collisions at ultrarelativistic energies. *Phys. Rev. Lett.*, 91:172302, 2003.

[10] K. Aamodt et al. Suppression of Charged Particle Production at Large Transverse Momentum in Central Pb-Pb Collisions at $\sqrt{s_{NN}} = 2.76$ TeV. *Phys. Lett.*, B696:30–39, 2011.

[11] Serguei Chatrchyan et al. Study of high-pT charged particle suppression in PbPb compared to *pp* collisions at $\sqrt{s_{NN}} = 2.76$ TeV. *Eur. Phys. J.*, C72:1945, 2012.

[12] Georges Aad et al. Measurement of charged-particle spectra in Pb+Pb collisions at $\sqrt{s_{\mathsf{NN}}} =$ 2.76 TeV with the ATLAS detector at the LHC. *JHEP*, 09:050, 2015.

[13] F. Abe et al. Transverse Momentum Distributions of Charged Particles Produced in $\bar{p}p$ Interactions at $\sqrt{s} = 630$ GeV and 1800 GeV. *Phys. Rev. Lett.*, 61:1819, 1988.

[14] M. Jacob and P. Landshoff. THE INNER STRUCTURE OF THE PROTON. *Sci. Am.*, 242:46–55, 1980.

[15] J. W. Cronin, Henry J. Frisch, M. J. Shochet, J. P. Boymond, R. Mermod, P. A. Piroue, and Richard L. Sumner. Production of hadrons with large transverse momentum at 200, 300, and 400 GeV. *Phys. Rev.*, D11:3105–3123, 1975.

[16] M. Arneodo et al. The A dependence of the nuclear structure function ratios. *Nucl. Phys.*, B481:3–22, 1996.

[17] J. J. Aubert et al. The ratio of the nucleon structure functions $F2_n$ for iron and deuterium. *Phys. Lett.*, 123B:275–278, 1983.

[18] M. Gyulassy, P. Levai, and I. Vitev. NonAbelian energy loss at finite opacity. *Phys. Rev. Lett.*, 85:5535–5538, 2000.

[19] Ivan Vitev. Testing the mechanism of QGP-induced energy loss. *Phys. Lett.*, B639:38–45, 2006.

[20] Magdalena Djordjevic and Miklos Gyulassy. Heavy quark radiative energy loss in QCD matter. *Nucl. Phys.*, A733:265–298, 2004.

[21] R. Baier, Yuri L. Dokshitzer, Alfred H. Mueller, S. Peigne, and D. Schiff. Radiative energy loss and p(T) broadening of high-energy partons in nuclei. *Nucl. Phys.*, B484:265–282, 1997.

[22] R. Baier, Yuri L. Dokshitzer, Alfred H. Mueller, S. Peigne, and D. Schiff. Radiative energy loss of high-energy quarks and gluons in a finite volume quark - gluon plasma. *Nucl. Phys.*, B483:291–320, 1997.

[23] Magdalena Djordjevic and Ulrich W. Heinz. Radiative energy loss in a finite dynamical QCD medium. *Phys. Rev. Lett.*, 101:022302, 2008.

[24] Magdalena Djordjevic. Theoretical formalism of radiative jet energy loss in a finite size dynamical QCD medium. *Phys. Rev.*, C80:064909, 2009.

[25] Dusan Zigic, Igor Salom, Jussi Auvinen, Marko Djordjevic, and Magdalena Djordjevic. Joint R_{AA} and v_2 predictions for $Pb + Pb$ collisions at the LHC within DREENA-C framework. 2018.

[26] Dusan Zigic, Igor Salom, Marko Djordjevic, and Magdalena Djordjevic. DREENA-B framework: first predictions of R_{AA} and v_2 within dynamical energy loss formalism in evolving QCD medium. 2018.

[27] M. Gyulassy, P. Levai, and I. Vitev. Jet tomography of Au+Au reactions including multigluon fluctuations. *Phys. Lett.*, B538:282–288, 2002.

[28] A. Adare et al. Enhanced production of direct photons in Au+Au collisions at $\sqrt{s_{NN}} = 200$ GeV and implications for the initial temperature. *Phys. Rev. Lett.*, 104:132301, 2010.

[29] A. Adare et al. Detailed measurement of the e^+e^- pair continuum in $p + p$ and Au+Au collisions at $\sqrt{s_{NN}} = 200$ GeV and implications for direct photon production. *Phys. Rev.*, C81:034911, 2010.

[30] A. Adare et al. Centrality dependence of low-momentum direct-photon production in Au+Au collisions at $\sqrt{s_{_{NN}}} = 200$ GeV. *Phys. Rev.*, C91(6):064904, 2015.

[31] Jaroslav Adam et al. Direct photon production in Pb-Pb collisions at $\sqrt{s_{\rm NN}} = 2.76$ TeV. *Phys. Lett.*, B754:235–248, 2016.

[32] R. Albrecht et al. Transverse momentum distributions of neutral pions from nuclear collisions at 200 AGeV. *Eur. Phys. J. C*, 5(nucl-ex/9805007. IKP-MS-98-05-01. 2):255–267. 13 p, May 1998. Accepted for publication in Eur.Phys.J.C, 13 pages including 16 figures Report-no: IKP-MS-980501.

[33] R. Albrecht et al. Limits on the production of direct photons in 200-A/GeV S-32 + Au collisions. *Phys. Rev. Lett.*, 76:3506–3509, 1996.

[34] D. K. Srivastava and B. Sinha. Single photons from S + Au collisions at the CERN Super Proton Synchrotron and the quark - hadron phase transition. *Phys. Rev. Lett.*, 73:2421–2424, 1994.

[35] A. Dumitru, U. Katscher, J. A. Maruhn, Horst Stoecker, W. Greiner, and D. H. Rischke. Pion and thermal photon spectra as a possible signal for a phase transition. *Phys. Rev.*, C51:2166–2170, 1995.

[36] M. M. Aggarwal et al. Centrality dependence of neutral pion production in 158-A-GeV Pb-208 + Pb-208 collisions. *Phys. Rev. Lett.*, 81:4087–4091, 1998. [Erratum: Phys. Rev. Lett.84,578(2000)].

[37] M. M. Aggarwal et al. Observation of direct photons in central 158-A-GeV Pb-208 + Pb-208 collisions. *Phys. Rev. Lett.*, 85:3595–3599, 2000.

[38] A. Adare et al. Azimuthally anisotropic emission of low-momentum direct photons in Au+Au collisions at $\sqrt{s_{NN}} = 200$ GeV. *Phys. Rev.*, C94(6):064901, 2016.

[39] Shreyasi Acharya et al. Direct photon elliptic flow in Pb-Pb collisions at $\sqrt{s_{\rm NN}} = 2.76$ TeV. *Phys. Lett.*, B789:308–322, 2019.

[40] Oliver S. Bruning, P. Collier, P. Lebrun, S. Myers, R. Ostojic, J. Poole, and P. Proudlock. LHC Design Report Vol.1: The LHC Main Ring. 2004. `https://cds.cern.ch/record/782076`.

[41] O. Buning, P. Collier, P. Lebrun, S. Myers, R. Ostojic, J. Poole, and P. Proudlock. LHC Design Report. 2. The LHC infrastructure and general services. 2004. `http://cds.cern.ch/record/815187`.

[42] M. Benedikt, P. Collier, V. Mertens, J. Poole, and K. Schindl. LHC Design Report. 3. The LHC injector chain. 2004. `https://cds.cern.ch/record/823808`.

[43] by Cian O'Luanaigh. Heavy metal: Refilling the lead source for the LHC. Feb 2013.

[44] Fabienne Marcastel. CERN's Accelerator Complex. La chaîne des accélérateurs du CERN. Oct 2013. General Photo.

[45] K. Aamodt et al. The ALICE experiment at the CERN LHC. *JINST*, 3:S08002, 2008.

[46] Betty Bezverkhny Abelev et al. Performance of the ALICE Experiment at the CERN LHC. *Int. J. Mod. Phys.*, A29:1430044, 2014.

[47] P.Cortese et al. *Technical Design Report of forward detectors FMD, T0 and V0*, CERN-LHCC-2004-025, 2004. `https://cds.cern.ch/record/781854`.

[48] E. Abbas et al. Performance of the ALICE VZERO system. *JINST*, 8:P10016, 2013.

[49] Jaroslav Adam et al. Determination of the event collision time with the ALICE detector at the LHC. *Eur. Phys. J. Plus*, 132(2):99, 2017.

[50] K Aamodt et al. Alignment of the ALICE Inner Tracking System with cosmic-ray tracks. *JINST*, 5:P03003, 2010.

[51] G.Dellecasa et al. *Technical Design Report of ITS*, CERN-LHCC-99-012, 1999. `http://cds.cern.ch/record/391175`.

[52] Christian Lippmann. Upgrade of the ALICE Time Projection Chamber. 2014. `https://cds.cern.ch/record/1622286/`.

[53] The ALICE Collaboration. Addendum to the Technical Design Report for the Upgrade of the ALICE Time Projection Chamber. 2015. `http://cds.cern.ch/record/1984329/`.

[54] G.Dellecasa et al. *Technical Design Report of TPC*, CERN-LHCC-2000-001, 2000. `http://cds.cern.ch/record/451098`.

[55] V.Manko et al. *Technical Design Report of PHOS*, CERN-LHCC-99-004, 1999. `http://cds.cern.ch/record/381432`.

[56] D. V. Aleksandrov et al. A high resolution electromagnetic calorimeter based on lead-tungstate crystals. *Nucl. Instrum. Meth.*, A550:169–184, 2005.

[57] C. Zhao, L. Liu, K. Røed, D. Rohrich, Y. Kharlov, L. Bratrud, J. Alme, and T. B. Skaali. Performance of the ALICE PHOS trigger and improvements for RUN 2. *JINST*, 8:C12028, 2013.

[58] T. C. Awes, F. E. Obenshain, F. Plasil, S. Saini, S. P. Sorensen, and G. R. Young. A Simple method of shower localization and identification in laterally segmented calorimeters. *Nucl. Instrum. Meth.*, A311:130–138, 1992.

[59] Christian Wolfgang Fabjan et al. ALICE: Physics performance report, volume II. *J. Phys.*, G32:1295–2040, 2006.

[60] Martino Gagliardi, Jesus Guillermo Contreras Nuno, Christoph Mayer, and Satoshi Yano. ALICE luminosity determination for pp collisions at $\sqrt{s} = 5$, 8 and 13 TeV. *ALICE public note*, 2016.

[61] Betty Bezverkhny Abelev et al. Production of charged pions, kaons and protons at large transverse momenta in pp and Pb − Pb collisions at $\sqrt{s_{\rm NN}}$ =2.76 TeV. *Phys. Lett.*, B736:196–207, 2014.

[62] Betty Bezverkhny Abelev et al. K^0_S and Λ production in Pb-Pb collisions at $\sqrt{s_{NN}} = 2.76$ TeV. *Phys. Rev. Lett.*, 111:222301, 2013.

[63] Jaroslav Adam et al. Measurement of pion, kaon and proton production in proton − proton collisions at $\sqrt{s} = 7$ TeV. *Eur. Phys. J.*, C75(5):226, 2015.

[64] Jaroslav Adam et al. Centrality dependence of the pseudorapidity density distribution for charged particles in Pb-Pb collisions at $\sqrt{s_{\rm NN}} = 5.02$ TeV. *Phys. Lett.*, B772:567–577, 2017.

[65] Ehab Abbas et al. Centrality dependence of the pseudorapidity density distribution for charged particles in Pb-Pb collisions at $\sqrt{s_{\rm NN}} = 2.76$ TeV. *Phys. Lett.*, B726:610–622, 2013.

[66] Particle Data Group. Statistics. `http://pdg.lbl.gov/2017/reviews/rpp2017-rev-statistics.pdf`.

[67] M.J. Oreglia. A Study of the Reactions $\psi' \to \gamma\gamma\psi$. *PhD. thesis.* `http://www.slac.stanford.edu/pubs/slacreports/slac-r-236.html`.

[68] Jaroslav Adam et al. Pseudorapidity and transverse-momentum distributions of charged particles in proton–proton collisions at $\sqrt{s} = 13$ TeV. *Phys. Lett.*, B753:319–329, 2016.

[69] A. A. Bylinkin and A. A. Rostovtsev. Role of quarks in hadroproduction in high energy collisions. *Nucl. Phys.*, B888:65–74, 2014.

[70] A. A. Bylinkin and M. G. Ryskin. Secondary hadron distributions in two component model. *Phys. Rev.*, D90(1):017501, 2014.

[71] Alexander Bylinkin, Nadezda S. Chernyavskaya, and Andrei A. Rostovtsev. Predictions on the transverse momentum spectra for charged particle production at LHC-energies from a two component model. *Eur. Phys. J.*, C75(4):166, 2015.

[72] R. Hagedorn. Thermodynamics of strong interactions. 1971.

[73] Betty Bezverkhny Abelev et al. Neutral pion production at midrapidity in pp and Pb-Pb collisions at $\sqrt{s_{\mathrm{NN}}} = 2.76\,\mathrm{TeV}$. *Eur. Phys. J.*, C74(10):3108, 2014.

[74] Shreyasi Acharya et al. Production of π^0 and η mesons up to high transverse momentum in pp collisions at 2.76 TeV. *Eur. Phys. J.*, C77(5):339, 2017. [Eur. Phys. J.C77,no.9,586(2017)].

[75] B. Abelev et al. Neutral pion and η meson production in proton-proton collisions at $\sqrt{s} =$ 0.9 TeV and $\sqrt{s} = 7$ TeV. *Phys. Lett.*, B717:162–172, 2012.

[76] Shreyasi Acharya et al. Neutral pion and η meson production at mid-rapidity in Pb-Pb collisions at $\sqrt{s_{NN}} = 2.76$ TeV. *Phys. Rev.*, C98(4):044901, 2018.

[77] Shreyasi Acharya et al. Neutral pion and η meson production in p-Pb collisions at $\sqrt{s_{\mathrm{NN}}} =$ 5.02 TeV. *Eur. Phys. J.*, C78(8):624, 2018.

[78] Shreyasi Acharya et al. π^0 and η meson production in proton-proton collisions at $\sqrt{s} = 8$ TeV. *Eur. Phys. J.*, C78(3):263, 2018.

[79] ALICE Collaboration. Centrality determination in heavy ion collisions. *ALICE public note*, 2018. `http://cds.cern.ch/record/2636623/`.

[80] Jaroslav Adam et al. Centrality dependence of the nuclear modification factor of charged pions, kaons, and protons in Pb-Pb collisions at $\sqrt{s_{\mathrm{NN}}} = 2.76$ TeV. *Phys. Rev.*, C93(3):034913, 2016.

[81] Nicolò Jacazio. Production of identified charged hadrons in Pb–Pb collisions at $\sqrt{s_{NN}} =$ 5.02 TeV. *Nucl. Phys.*, A967:421–424, 2017.

[82] S. Acharya et al. Measurement of D^0, D^+, D^{*+} and D_s^+ production in Pb-Pb collisions at $\sqrt{\mathrm{s_{NN}}} = 5.02$ TeV. *JHEP*, 10:174, 2018.

[83] Albert M Sirunyan et al. Measurement of the $B^{\pm}$ Meson Nuclear Modification Factor in Pb-Pb Collisions at $\sqrt{s_{NN}} = 5.02$ TeV. *Phys. Rev. Lett.*, 119(15):152301, 2017.

[84] Simon Wicks, William Horowitz, Magdalena Djordjevic, and Miklos Gyulassy. Elastic, inelastic, and path length fluctuations in jet tomography. *Nucl. Phys.*, A784:426–442, 2007.

[85] Magdalena Djordjevic, Bojana Blagojevic, and Lidija Zivkovic. Mass tomography at different momentum ranges in quark-gluon plasma. *Phys. Rev.*, C94(4):044908, 2016.

[86] K. Aamodt et al. Midrapidity antiproton-to-proton ratio in pp collisions at $\sqrt{s} = 0.9$ and 7 TeV measured by the ALICE experiment. *Phys. Rev. Lett.*, 105:072002, 2010.

[87] Betty Abelev et al. Measurement of electrons from semileptonic heavy-flavour hadron decays in pp collisions at $\sqrt{s} = 7$ TeV. *Phys. Rev.*, D86:112007, 2012.

[88] Torbjorn Sjostrand, Stephen Mrenna, and Peter Z. Skands. PYTHIA 6.4 Physics and Manual. *JHEP*, 05:026, 2006.

[89] P. K. Khandai, P. Shukla, and V. Singh. Meson spectra and m_T scaling in $p + p$, d+Au, and Au + Au collisions at $\sqrt{s_{NN}} = 200$ GeV. *Phys. Rev.*, C84:054904, 2011.

[90] A. Adare et al. Production of ω mesons in $p + p$, d+Au, Cu+Cu, and Au+Au collisions at $\sqrt{s_N N} = 200$ GeV. *Phys. Rev.*, C84:044902, 2011.

[91] A. Adare et al. Measurement of neutral mesons in p+p collisions at $\sqrt{s}$= 200 GeV and scaling properties of hadron production. *Phys. Rev.*, D83:052004, 2011.

[92] A. Adare et al. Heavy Quark Production in $p + p$ and Energy Loss and Flow of Heavy Quarks in Au+Au Collisions at $\sqrt{s_{NN}} = 200$ GeV. *Phys. Rev.*, C84:044905, 2011.

[93] CERN. ALICE TPC readout chip user manual. *CERN EP/ED*, 2002.